Technical University of Munich

Physics Department

Max-Planck-Institute for Physics

Master's thesis to obtain the degree of

Master of Science (M. Sc.)

Studies of Quantum Entanglement in the $\Upsilon(4S) \rightarrow B^0\overline{B}^0$ system at Belle II using $B^0 \rightarrow D^{(*)-}\pi^+$ decays

Submitted by

Maximilian Kei Hattenbach

Munich, April 11th, 2025

Supervisor: Prof. Dr. Allen Caldwell

Advisor: Dr. Hans-Günther Moser

Abstract

This thesis presents a study of quantum entanglement in the $\Upsilon(4S) \to B^0\overline{B}^0$ system using the hadronic $B^0 \to D^{(*)-}\pi^+$. As it is the first study of such kind at Belle II, this work is focused on establishing an analysis framework, which enables testing disentanglement in hadronic B^0 modes. A novel event generator model has been implemented within `basf2` to create a Signal MC samples with 1 Mio. $B\overline{B}$ events, corresponding to an integrated luminosity of 1ab^{-1} which are reconstructed in $B^0 \to D^{(*)-}\pi^+$ decays.

The model of partial spontaneous disentanglement is implemented, where a fraction ζ of $B^0\overline{B}^0$ pairs disentangle right at production. The implementation is proven to be successful, as the model is sensitive to such entanglement effects. Fits to Δt distributions for different values of ζ_{gen} in Signal MC samples return consistently the correct values for free parameter ζ within uncertainties. A subsequent Toy Monte Carlo study once more shows the model's and fitting processes' suitability for disentanglement studies, although some biased behavior for parameter ζ could not be fully resolved. However, this thesis provides a proof-of-concept for future probes of entanglement at Belle II.

The question, whether unaccounted disentanglement effects introduce a bias in time-dependent CP violation measurements at Belle II is answered. Such effects in the region of $\zeta \sim \mathcal{O}(1-10\%)$ is absorbed in form of a bias of $1-2\%$ in wrong tag parameters. However, slight biases in these parameters do in general not translate to a shift in parameters A_{CP} and S_{CP}, thus the worry of an unaccounted systematic effect is for now mitigated.

Kurzfassung

Diese Arbeit untersucht die Quantenverschränkung im System $\Upsilon(4S) \to B^0\overline{B}^0$ unter Verwendung des hadronischen Zerfallkanals $B^0 \to D^{(*)-}\pi^+$. Da es sich um die erste Studie dieser Art am Belle II Experiment handelt, liegt der Fokus dieser Arbeit auf dem Etablieren eines Analyseframeworks, das Tests auf eine mögliche Aufhebung der Verschränkung in hadronischen B^0 Kanälen ermöglicht. Hierzu wurde ein neuartiges Event Generator Modell innerhalb von `basf2` implementiert, womit Signal MC Datensätze mit 1 Mio. $B\overline{B}$, korrespondierend zu einer integrierten Luminosität von $1\,\mathrm{ab}^{-1}$ erzeugt wurden. Diese werden in den Zerfällen $B^0 \to D^{(*)-}\pi^+$ rekonstruiert.

Ein Model partieller spontaner Aufhebung der Verschränkung wurde implementiert, bei dem ein Anteil ζ der $B^0\overline{B}^0$ Paare direkt bei der Produktion ihre Verschränkung verlieren. Die Implementierung erweist sich als erfolgreich, da sich das Model sensibel gegenüber Verschränkungseffekten zeigt. Fits an die Δt-Verteilungen für verschiedene Werte von ζ_{gen} in den Signal-MC-Samples reproduzieren konsistent die korrekten Werte des freien Parameters ζ innerhalb der statistischen Unsicherheiten. Eine anschließende Toy-Monte-Carlo-Studie bestätigt erneut die Eignung des Modells und des Fitverfahrens für Verschränkungsanalysen, auch wenn ein gewisser Bias im Parameter ζ nicht vollständig aufgelöst werden konnte. Insgesamt liefert diese Arbeit ein Proof-of-Concept für zukünftige Verschränkungsstudien bei Belle II.

Abschließend wird die Frage beantwortet, ob nicht berücksichtigte Effekte der Aufhebung der Verschränkung einen Bias in zeitabhängigen CP-Verletzungsmessungen bei Belle II hervorrufen könnten. Ferner wurden für partielle Aufhebungen der Verschränkung im Bereich von $\zeta \sim \mathcal{O}(1\text{–}10\%)$ Verzerrungen in Wrong Tag Fractions von etwa $1\text{–}2\%$ gemessen. Da kleine systematische Verschiebungen in diesen Parametern im Allgemeinen jedoch nicht zu einer Verzerrung in den CP-Verletzungsparametern A_{CP} und S_{CP} führen, kann die Sorge vor einem bislang unbeachteten systematischen Effekt vorerst abgemildert werden.

Contents

1 Introduction

The Standard Model (SM) of Particle Physics is the most successful and thoroughly tested theoretical framework describing the fundamental particles and their interactions. While it has withstood extensive experimental scrutiny, it is widely believed to be incomplete, as it leaves several fundamental questions unanswered.

The Standard Model fails to explain various phenomena such as the reason for the number of fermion generations to be exactly three, the mass hierarchy between those generations or the abundance of matter over antimatter in the universe. In fact, the SM offers a mechanism through CP violation, in which a fraction of the matter dominance can be described, however the predicted amount is several orders of magnitude too small to account for the observed asymmetry [1].

In the landscape of experimental high-energy physics, two approaches are pursued: the *high energy frontier* and the *intensity frontier*. The former aims to directly access new physics by producing New Physics (NP) particles at facilities e.g. the LHC, while the latter explores processes with known particles with precision measurements where potential deviations from Standard Model predictions may hint at NP. The Belle II experiment probes the intensity frontier and utilizes high-luminosity e^+e^- collisions at the next-generation SuperKEKB accelerator to study B meson decays with unprecedented precision.

As experimental precision improves, subtle quantum effects become accessible with increasing sensitivity such as quantum entanglement, a cornerstone of quantum mechanics. Entanglement describes a quantum state of a multi-particle system in which the constituent particles cannot be described independently, even when spatially separated. This non-local correlation between measurement outcomes was first highlighted in the famous Einstein-Podolsky-Rosen (EPR) paradox [2], and later given quantitative form through Bell's theorem [3], which provides a direct test for the completeness of quantum theory.

While the validity of quantum entanglement has been extensively studied in systems of photons and atoms, its investigation in the context of heavy, unstable particles such as kaons, D, and B mesons remains an active and compelling area of research [4]. These systems offer a unique opportunity to test the limits of quantum mechanics within the framework of the Standard Model, particularly in regimes where particles undergo both mixing and decay. Deviations from full quantum entanglement in e.g. the $B^0\overline{B}^0$ system may arise not only from subtle effects within the Standard Model but also from a broad spectrum of theories beyond the SM, including proposals from quantum gravity, dark energy, and string theory frameworks [5, 6]. Regardless of their underlying mechanism, such disentanglement phenomena could lead to distortions in the measured system, potentially biasing precision tests of the Standard Model — most notably in time-dependent CP violation measurements.

In this thesis, a study of quantum entanglement in the $B^0\bar{B}^0$ system is performed using the hadronic decay channel $B^0 \to D^{(*)-}\pi^+$. The analysis is a pure Signal Monte Carlo study on a data set corresponding to an integrated luminosity of 1 ab^{-1} at Belle II. Mainly, the model of partial disentanglement is investigated in which a fraction ζ of the $B^0\overline{B}^0$ pairs lose their entanglement and subsequently evolve independently. The main goal of this thesis is to design a framework which can be used for the first physics analysis of such kind at Belle II.

Thesis outline:

- Chapter 2 introduces the theoretical framework of the Standard Model, flavor physics, $B^0\bar{B}^0$ mixing, CP violation, a qualitative review of Quantum Mechanics and disentanglement models in $B^0\overline{B}^0$ systems.

- Chapter 3 presents the Belle II experiment, including the detector setup, software framework including Monte Carlo production and reconstruction algorithms.

- Chapter 4 lies out the analysis strategy, including resolution modeling and the final observed Δt distribution, event selection, signal reconstruction and validation of Signal MC.

- Chapter 5 focuses on the studies of disentanglement models, single Δt fits, toy MC, and absorption studies.

- Chapter 6 concludes with a summary of the findings and an outlook on current prospects for entanglement studies at Belle II.

2 Theory

This chapter provides the theoretical framework for the analysis. It starts by introducing the basic concepts of the Standard Model of Particle Physics, the most successful theory in modern physics. In the scope of this thesis, important processes and interactions are highlighted with a special focus on the field of Flavor Physics. Furthermore, the most general concepts and ideas of Quantum Entanglement and its mathematical treatment in the field of Quantum Mechanics are introduced. Finally, the physical models for disentanglement in $B^0\overline{B}^0$ systems are introduced.

2.1 The Standard Model

The Standard Model (SM) is the prevailing theoretical framework describing fundamental particles and their interactions, based on principles of quantum field theory and gauge symmetry [7, 8, 9][1]. It successfully unifies the electromagnetic, weak, and strong interactions, providing an accurate description of almost all known experimental results in particle physics. The theory categorizes particles into fermions, which constitute matter, and bosons, which mediate interactions. The elementary particles of the Standard Model are grouped into three families of fermions and a set of gauge bosons that mediate interactions. Fig. 2.1 shows all 12 fermions and 5 types of bosons with current values for mass (upper limits for neutrinos), their charge and spin. Fermions grouped into quarks and leptons are shown in purple and green, respectively. Gauge bosons are shown in red while the scalar Higgs boson in shown in yellow. Both fermions and bosons are highlighted in detail in the following.

Fermions: Fermions are Spin-$\frac{1}{2}$ particles and can be divided into two subgroups, quarks and leptons. Both fermion groups can be further categorized into three generations, with same properties besides a hierarchy in mass. For leptons, every generation consists of a charged lepton and

[1] Throughout this chapter, these references will be used without explicit citation, unless otherwise stated.

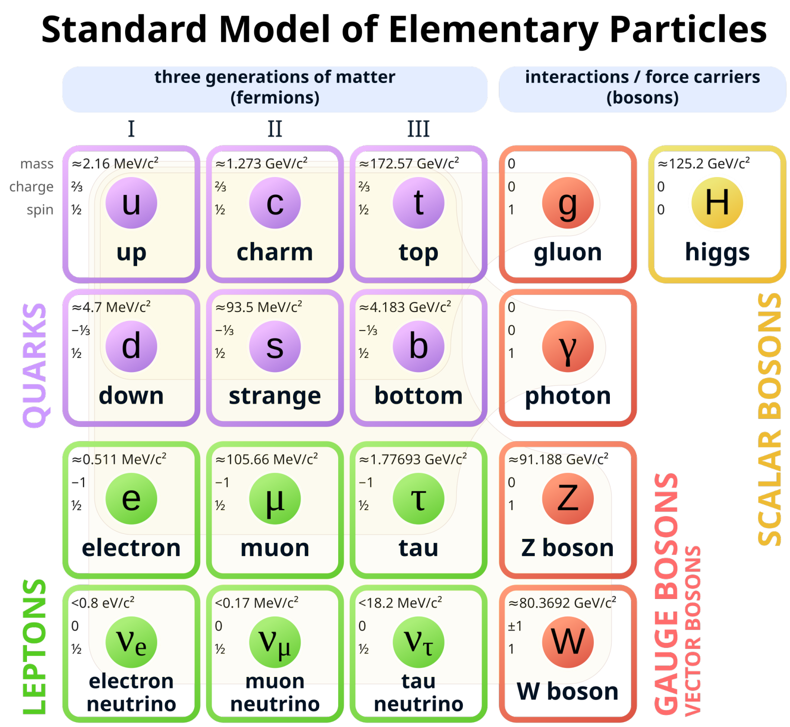

Figure 2.1: All particles in the Standard Model of Elementary particles. Fermions, consisting of quarks and leptons are grouped into 3 generations. Gauge bosons which mediate forces are shown in red. Finally, the only scalar boson, the Higgs is shown in yellow. [10]

a corresponding uncharged lepton, called neutrino which is massless in the SM[2]:

$$\begin{pmatrix} \nu_e \\ e^- \end{pmatrix}, \begin{pmatrix} \nu_\mu \\ \mu^- \end{pmatrix}, \begin{pmatrix} \nu_\tau \\ \tau^- \end{pmatrix}. \tag{2.1}$$

Every lepton generation carries a distinct lepton family number which is a conserved quantity. Finally, antileptons are charge conjugate particles with same mass, but with inverted sign of electric charge and lepton family number. Analogously, quarks are also paired in three generations of each one up-type and one down-type quark:

$$\begin{pmatrix} u \\ d \end{pmatrix}, \begin{pmatrix} s \\ c \end{pmatrix}, \begin{pmatrix} t \\ b \end{pmatrix}. \tag{2.2}$$

These particles carry a fraction of the electric charge. The same way leptons have corresponding antileptons, there is also an antiquarks for every quark. These antiquarks are of the same mass as

[2]Although, the SM predicts the neutrino masses to be zero evidence suggests a non-trivial neutrino mass. This is proven through observations of neutrino oscillations [11].

their corresponding quark, although the quantum numbers and charges listed in table 2.1 are of the opposite sign. In Tab. 2.1, selected quantum numbers are shown.

	B	I_3	S	Q/e
u	1/3	1/2	0	2/3
d	1/3	-1/2	0	-1/3
s	1/3	0	-1	-1/3
c	1/3	0	0	2/3
t	1/3	0	0	2/3
b	1/3	0	0	-1/3

Table 2.1: Baryon number (B), third component of the isospin (I_3), strangeness (S) and electric charge (Q/e) of the individual quark flavor.

Moreover, all quarks carry the charge of the strong force - color; red, green and blue whilst antiquarks carry anti-red, anti-green and anti-blue. The mediating particles of the strong force couple to these colors. Note that these fermions only appear in bound doublet and triplet bound states due to confinement. Doublets are called mesons and consist of a quark-antiquark pair, while triplets are called baryons and consist of three (anti)quarks. In addition, all multiquark systems have to be *colorless*, i.e. the colors of the bound quarks have to cancel out. In mesons a color carrying quark must be matched with its respective anticolor carrying antiquark. In baryons all three different (anti)colors have to appear in the bound state.

Gauge Bosons: Three of the four fundamental forces are the strong force, the electromagnetic force and the weak force listed descending order of strength. They are mediated by their exchange particles – called gauge bosons with Spin-1. Strong force is mediated by 8 gluons, electromagnetic force is mediated by photons and lastly, the $W^{\pm}$ bosons and Z^0 bosons mediate the weak force. Since gluons interact solely with particles carrying color charge, they interact with quarks and themselves. Within a strong process the color of quarks can be changed while the flavor remains conserved. The photon is a massless boson with an electrical charge of zero. It interact with every charged particle while conserving flavor. Finally, the weak force mediating charged $W^{\pm}$ bosons and neutral Z^0 bosons have masses of $m(W^{\pm}) = 80.3$ GeV/c^2 and $m(Z^0) = 91.2$ GeV/c^2, respectively [8]. The masses arise from Spontaneous Symmetry Breaking of the Higgs field. Charged weak interactions are responsible for flavor-changing processes with $W^{\pm}$ bosons mediating the process. These gauge bosons arise naturally from the symmetry principles underlying the SM.

The Higgs Boson: The SM has a single scalar field, the Higgs field with its corresponding boson H, which is responsible for spontaneous electroweak symmetry breaking and provides mass to fermions and weak bosons through the Higgs mechanism. Its discovery completed the experimental confirmation of the SM particle spectrum [12].

2.1.1 Standard Model Formalism

The Standard Model (SM) is a quantum field theory based on the gauge group:

$$\mathcal{G}_{\rm SM} = SU(3)_C \times SU(2)_L \times U(1)_Y, \tag{2.3}$$

where $SU(3)_C$ describes Quantum Chromodynamics (QCD), $SU(2)_L$ governs weak interactions, and $U(1)_Y$ corresponds to hypercharge.

The SM contains scalar Higgs doublet

$$H = (1,2)_{1/2}, \tag{2.4}$$

and the three generations of fermions transforming under $SU(2)_L$

$$\begin{aligned} Q_{Li} = (3,2)_{+1/6}, \quad u_{Ri} = (3,1)_{+2/3}, \quad d_{Ri} = (3,1)_{-1/3}, \\ L_{Li} = (1,2)_{-1/2}, \quad l_{Ri} = (1,1)_{-1}, \end{aligned} \tag{2.5}$$

where $i = 1,2,3$ accounts for three generations. Q_{Li} and L_{Li} represent left-handed quark and lepton doublets, while u_{Ri}, d_{Ri}, and l_{Ri} are right-handed singlets. Left-handed fields couple to the $SU(2)_L$ gauge bosons and thus participate in weak interactions. Right-handed fields do not, making the weak interaction chiral and maximally parity-violating.

The Standard Model Lagrangian is composed of three main parts:

$$\mathcal{L}_{\rm SM} = \mathcal{L}_{\rm kin} + \mathcal{L}_{\rm Yukawa} + \mathcal{L}_{\rm Higgs}. \tag{2.6}$$

Each term describes a fundamental aspect of particle interactions.

Kinetic Terms and Gauge Interactions

Gauge interactions are introduced through the covariant derivative:

$$D_\mu = \left(\partial_\mu + ig_s G^a_\mu t^a + igW^i_\mu \tau^i + ig' B_\mu Y\right). \tag{2.7}$$

Here, the first term corresponds to QCD with strong coupling g_s, gluon fields G^a_μ, and $SU(3)_C$ generators t^a ($a = 1, \ldots, 8$). The second term represents weak interactions with coupling g, weak bosons W^i_μ, and generators τ^i ($i = 1,2,3$) of $SU(2)_L$. The final term accounts for hypercharge with coupling g' and generator Y.

The kinetic terms respect a global flavor symmetry:

$$\mathcal{G}_{\text{flavor}} = U(3)_q^3 \times U(3)_l^2, \tag{2.8}$$

where

$$U(3)_q^3 = U(3)_Q \times U(3)_u \times U(3)_d, \tag{2.9}$$

$$U(3)_l^2 = U(3)_L \times U(3)_l, \tag{2.10}$$

which is only broken explicitly by Yukawa couplings.

Electroweak Symmetry Breaking and the Higgs Mechanism

The Higgs potential,

$$V(H) = \mu^2|H|^2 + \lambda|H|^4. \tag{2.11}$$

leads to spontaneous symmetry breaking (SSB) for $\mu^2 < 0$, with the vacuum expectation value:

$$\langle H \rangle = \frac{1}{\sqrt{2}} \begin{pmatrix} 0 \\ v \end{pmatrix}, \quad v \approx 246 \text{ GeV}. \tag{2.12}$$

As a result, the $W^\pm$ and Z^0 bosons acquire masses

$$M_W = \frac{gv}{2}, \quad M_Z = \frac{\sqrt{g^2 + g'^2}v}{2}, \quad M_\gamma = 0. \tag{2.13}$$

After symmetry breaking, the gauge group reduces to

$$\mathcal{G}_{SM} = SU(3)_C \times U(1)_{\text{em}}, \tag{2.14}$$

where $U(1)_{\text{em}}$ is the gauge goup for electromagnetic interaction.

Fermion Masses and the Yukawa Interaction

Fermion masses arise through the Yukawa interaction:

$$\mathcal{L}_{\text{Yukawa}} = -Y_u \bar{Q}_L \tilde{H} u_R - Y_d \bar{Q}_L H d_R - Y_l \bar{L}_L H e_R + \text{h.c.} \tag{2.15}$$

where $\tilde{H} = i\sigma^2 H^*$. After SSB,

$$m_f = \frac{y_f v}{\sqrt{2}}. \tag{2.16}$$

where m_f is the fermion mass, with index f denoting the type of fermion. The Yukawa sector introduces flavor structure and violates global flavor symmetry, leading to quark mixing discussed in the following section.

2.2 Flavor Physics

The Yukawa sector of the Standard Model, introduced earlier, not only generates fermion masses but also governs the flavor structure of quarks and leptons. In the quark sector, this leads to flavor mixing and a rich phenomenology including CP violation and meson oscillations.

In this section, the flavor structure of the SM is explored, for which the CKM Mechanism is introduced. Moreover, flavor symmetries, their breaking, and neutral meson mixing are presented, which play a crucial role in measuring SM parameters.

2.2.1 From Yukawa Couplings to the CKM Matrix

Consider the Yukawa Lagrangian from Eq. 2.15 and the Higgs vacuum expectation value after SSB in Eq. 2.12. As already established, the mass terms in the Yukawa Lagrangian yield

$$M_u = \frac{v}{\sqrt{2}} Y_u, \quad M_d = \frac{v}{\sqrt{2}} Y_d. \tag{2.17}$$

Since Y_u and Y_d are in general complex matrices, the mass matrices M_u and M_d are also complex and not necessarily diagonal. To obtain physical mass eigenstates, a unitary transformations on the left-handed quark fields is performed

$$u_L \to V_u u_L, \quad d_L \to V_d d_L, \tag{2.18}$$

where V_i is some unitary transformation matrix. This diagonalizes the mass matrices

$$M_u^{\text{diag}} = V_u^\dagger M_u V_u, \quad M_d^{\text{diag}} = V_d^\dagger M_d V_d. \tag{2.19}$$

While transformations for right-handed quarks do not affect the weak interaction, the left-handed rotation induces mixing in the charged weak current

$$\mathcal{L}_{CC} = \frac{g}{\sqrt{2}} \bar{u}_L \gamma^\mu W_\mu^+ d_L + \text{h.c.} \tag{2.20}$$

Expressing the fields in their mass eigenbasis, the interaction becomes:

$$\mathcal{L}_{CC} = \frac{g}{\sqrt{2}} \bar{u}_L V_{\text{CKM}} \gamma^\mu W_\mu^+ d_L + \text{h.c.}, \tag{2.21}$$

where the so-called Cabbibo-Kobayashi-Masukawa (CKM) Matrix has been substituted:

$$V_{\text{CKM}} = V_u^\dagger V_d. \tag{2.22}$$

named after Kobayashi and Masukawa who extended the Cabbibo Matrix to three quark generations. This unitary 3×3 matrix encodes the misalignment between up-type and down-type quark mass eigenstates. [7]

2.2.2 CKM Mechanism

In the Standard Model, the CKM is a unitary 3×3 matrix which can be written in its general form

$$V = \begin{pmatrix} V_{ud} & V_{us} & V_{ub} \\ V_{cd} & V_{cs} & V_{cb} \\ V_{td} & V_{ts} & V_{tb} \end{pmatrix}, \tag{2.23}$$

where subscripts denote quark flavors. The matrix elements' absolute values describe the strength of corresponding charged transition among quark flavors. As transitions within a generation have the most dominant contributions, absolute values of the diagonal matrix elements are close to unity, while the off-diagonals are relatively small. This becomes evident when looking at the so-called Wolfenstein parametrization

$$V = \begin{pmatrix} 1-\lambda^2/2 & \lambda & A\lambda^3(\rho - i\eta) \\ -\lambda & 1-\lambda^2/2 & A\lambda^2 \\ A\lambda^3(1-\rho-i\eta) & -A\lambda^2 & 1 \end{pmatrix} + \mathcal{O}(\lambda^4), \tag{2.24}$$

where λ, A, ρ, η are real so-called Wolfenstein parameters, with $\lambda = \sin\theta_c + \mathcal{O}(\lambda^2)$ where $\sin\theta_c$ is the Cabbibo angle. The current known values for these parameters are [13]

$$\begin{aligned} \lambda =& 0.221 \pm 0.001, \\ A =& 0.81 \pm 0.02, \\ \rho =& 0.14 \pm 0.03, \\ \eta =& 0.35 \pm 0.02. \end{aligned} \tag{2.25}$$

This results in the following hierarchy in the elements:

$$|A\lambda^3(\rho - i\eta)|, |A\lambda^3(1-\rho-i\eta)| \ll A\lambda^2 \ll \lambda.$$

The condition of unitarity provides strict mathematical boundaries which can be represented in a geometrical framework: the unitarity triangle. From unitarity, one gets $V^\dagger V = 1 = VV^\dagger$, which gives

$$V_{ij}V^*_{ik} = \delta_{jk}, \quad V_{ji}V^*_{ki} = \delta_{jk}. \tag{2.26}$$

For $j \neq k$ Eq. 2.26 give six further conditions:

$$V_{ij}V^*_{ik} = 0, \tag{2.27}$$

$$V_{jk}V^*_{ki} = 0. \tag{2.28}$$

Each of these conditions show a vanishing sum of three complex numbers, thus projecting a triangle on the complex plane. Two out of the six unitarity triangles consist of three sides with their lengths in the same order of magnitude in λ. They are given by

$$V_{ud}V_{td}^* + V_{us}V_{ts}^* + V_{ub}V_{tb}^* = 0. \tag{2.29}$$

$$V_{ud}V_{ub}^* + V_{cd}V_{cb}^* + V_{td}V_{tb}^* = 0. \tag{2.30}$$

Eq. 2.30 is especially interesting in studies of B meson decays, since element V_{cb} is particularly important [14]. For this reason, Eq. 2.30 is now referred to as *the* Unitarity Triangle. All sides of this triangle are roughly in the order of $\mathcal{O}(\lambda^3)$. As convention, the sides are normalized by the term $V_{cd}V_{cb}^*$. It reads

$$\frac{V_{ud}V_{ub}^*}{V_{cd}V_{cb}^*} + \frac{V_{td}V_{tb}^*}{V_{cd}V_{cb}^*} = -1. \tag{2.31}$$

Angles of the UT are noted in terms of α, β and γ, while Belle and Belle II Collaboration follow a slightly different notation ϕ_1, ϕ_2 and ϕ_3. The relation between the CKM matrix elements and the angles can be seen here

$$\phi_2 = \alpha = \arg\left(-\frac{V_{td}V_{tb}^*}{V_{ud}V_{ub}^*}\right), \tag{2.32}$$

$$\phi_1 = \beta = \arg\left(-\frac{V_{cd}V_{cb}^*}{V_{td}V_{tb}^*}\right), \tag{2.33}$$

$$\phi_3 = \gamma = \arg\left(-\frac{V_{ud}V_{ub}^*}{V_{cd}V_{cb}^*}\right). \tag{2.34}$$

The resulting unitarity triangle is shown in Fig. 2.2. Current constraints on the angles of the

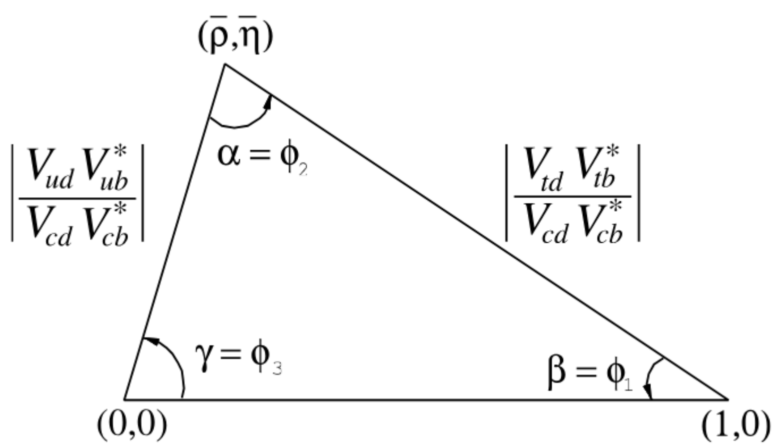

Figure 2.2: Sketch of Unitarity Triangle in the $(\bar{\rho}, \bar{\eta})$ plane. Sides are normalized to $V_{cd}V_{cb}^*$. Taken from Ref. [13].

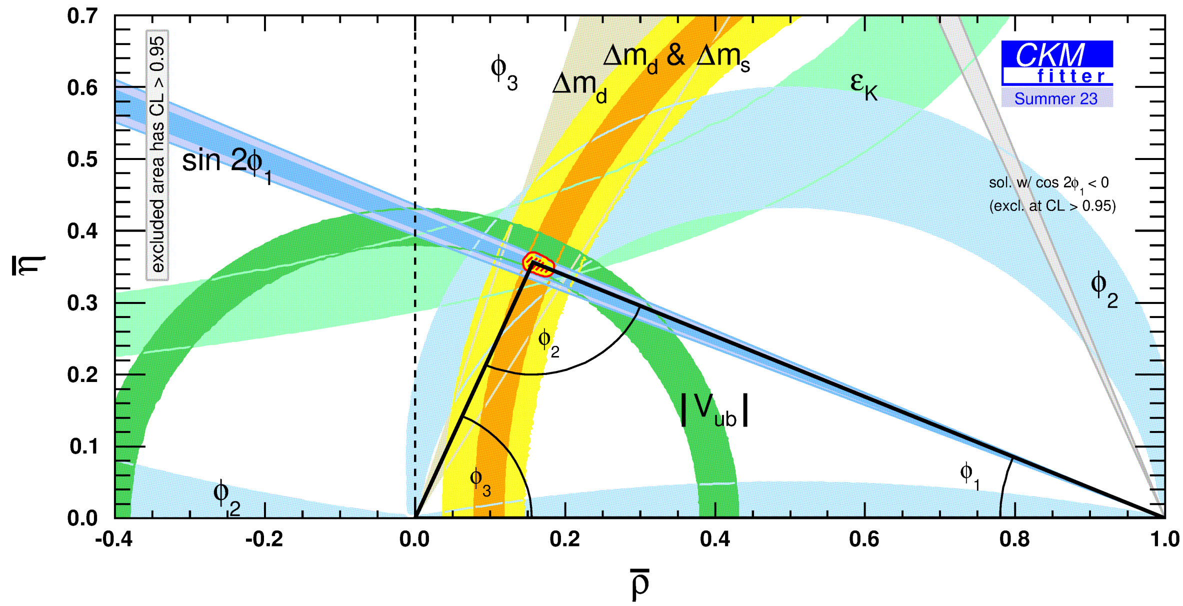

Figure 2.3: Current results for the constraints for the unitarity triangle. Prepared for the 2023 CKM workshop: Santiago de Compostela (September), Spain. [15]

unitarity triangle are shown in Fig. 2.3. Diverse measurements in angles, but also in CKM elements absolute values and mixing parameters such as Δm_d and Δm_s constrain the current UT. Ongoing measurements at B-factories Belle II and LHCb are working to further push the limits on the global values. The case of the UT not closing is a direct hint to physics beyond the standard model. This has been parameterized by C. Jarlskog for unnormalized UTs, the area of all six unitarity triangles are the same and independent of the phase redefinition of the quark fields. This allows for a phase independent measure of CP violation. This parameter is called the Jarlskog invariant

$$\mathrm{Im}[V_{ij}V_{ij}V_{ij}^{*}V_{ij}^{*}] = J \sum_{m,n=1}^{3} \epsilon_{ikm}\epsilon_{jln}. \tag{2.35}$$

In terms of Wolfenstein parameters, J can be rewritten to

$$J \approx A^2\lambda^6\eta. \tag{2.36}$$

Experiments have found the Jarlskog invariant to have a value around the order of 10^{-5}. This small value also explains why CP-violation measurements are so challenging. [1]

2.2.3 $B^0 - \bar{B}^0$ mixing

In 1955 Gell-Mann and Pais predicted neutral mesons and anti-mesons' oscillation [16], which was first discovered just one year later in the $K^0 - \bar{K}^0$ system [17]. It was not for another 32 years until mixing was also observed independently in neutral B's by the UA1 and ARGUS collaboration in 1987 [18, 19]. Following Feynman diagrams also referred to as *box diagrams* show the two dominant processes under which mixing can occur for neutral B mesons.

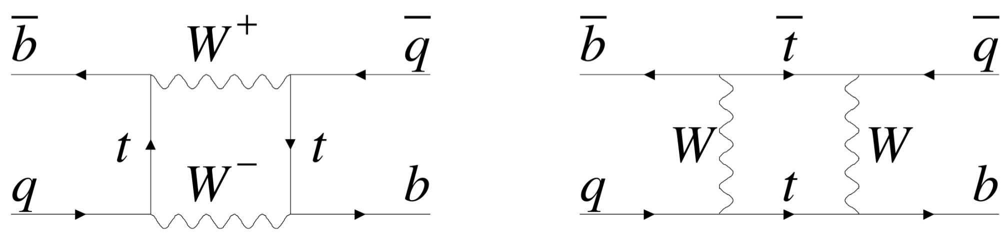

Figure 2.4: Leading order box diagrams for $B_q^0 \to \overline{B}_q^0$ transitions, with $q = d, s$. As the Yukawa coupling is proportional to quark mass, the dominant contribution in virtual particles comes from the top quark. [13]

In this Fig. 2.4 dominant box diagrams for the $B_q^0 \to \overline{B}_q^0$ transition are shown. The accompanying quarks q can be either d or s. The transition itself, although seemingly neutral, is mediated by two charged $W^{\pm}$ bosons. Due to the proportionality of Yukawa couplings to the fermion mass, the virtual quark contribution is dominated by the top quark.

Now, some useful formalism to build the mathematical framework concerning the $B^0 - \bar{B}^0$ system is introduced. This is the effective Hamiltonian

$$\begin{aligned}\mathcal{H}_{\text{eff}} &= \mathbf{M} - \frac{i\mathbf{\Gamma}}{2} \\ &= \begin{pmatrix} M_{11} & M_{12} \\ M_{21} & M_{22} \end{pmatrix} - \frac{i}{2}\begin{pmatrix} \Gamma_{11} & \Gamma_{12} \\ \Gamma_{21} & \Gamma_{22} \end{pmatrix},\end{aligned} \tag{2.37}$$

which governs the time evolution of neutral mesons. Here, $\mathbf{M}$ and $\mathbf{\Gamma}$ are 2×2 hermitian matrices representing mass and decay rate components, respectively. As CPT conservation holds for off-diagonal matrix elements they can be written as $M_{12} = M_{21}^*$ and $\Gamma_{12} = \Gamma_{21}^*$, while diagonal elements are expressed as $M_{11} = M_{22}$ and $\Gamma_{11} = \Gamma_{22}$. For matrix $\mathcal{H}_{\text{eff}}$ the eigenvalue problem has to be solved, which in itself is not hermitian anymore. Consequently, the eigenvalues of the matrix are complex and the eigenstates not orthogonal. As both B^0 and $\bar{B}^0$ are not stable and will decay after some time, probability is not conserved in this subspace spanned by the two mesons. In the following, the explicit formalism of the system's time-evolution is further investigated.

The mass eigenstates of $\mathcal{H}_{\text{eff}}$ can be written as a linear combination of B^0 and $\bar{B}^0$

$$|B_{L,H}\rangle = p\,|B^0\rangle \pm q\,|\bar{B}^0\rangle\,, \tag{2.38}$$

where subscript L and H stand for light and heavy, respectively. Prefactors p and q fulfill $|p|^2 + |q|^2 = 1$ and for normalization

$$\frac{q}{p} = \sqrt{\frac{M_{12}^* - \frac{i}{2}\Gamma_{12}^*}{M_{12} - \frac{i}{2}\Gamma_{12}}}, \tag{2.39}$$

while for CP conserving cases $p = q = 1/\sqrt{2}$. Finally, the eigenvalues read

$$m_1 - \frac{i}{2}\Gamma_1 = M_{11} - \frac{i}{2}\Gamma_{11} + \frac{q}{p}\left(M_{12} - \frac{i}{2}\Gamma_{12}\right), \tag{2.40}$$

$$m_2 - \frac{i}{2}\Gamma_2 = M_{11} - \frac{i}{2}\Gamma_{11} - \frac{q}{p}\left(M_{12} - \frac{i}{2}\Gamma_{12}\right). \tag{2.41}$$

Here, $m_{1,2}$ and $\Gamma_{1,2}$ are introduced, which correspond to the mass and decay width of B_L and B_H eigenstates and will from now on be written as $m_{L,H}$ and $\Gamma_{L,H}$. As already implied, the condition $m_H > m_L$ holds and thus $\Delta m_d = m_H - m_L > 0$. Also the decay width difference is non-trivial with $\Delta\Gamma = \Gamma_H - \Gamma_L$. The time evolution of a particle starting from B^0 at $t = 0$ can be written as

$$|B^0(t)\rangle = g_+(t)\,|B^0\rangle + \frac{q}{p}g_-(t)\,|\bar{B}^0\rangle\,, \tag{2.42}$$

where

$$g_\pm = \frac{1}{2}e^{-im_Lt}e^{-\frac{\Gamma_L}{2}t}\left(1 \pm e^{-\Delta mt}e^{\frac{\Delta\Gamma}{2}t}\right). \tag{2.43}$$

In the general matrix form, the time evolution of the two-state system can be written as

$$i\frac{d}{dt}\begin{pmatrix}|B^0(t)\rangle \\ |\bar{B}^0(t)\rangle\end{pmatrix} = \mathcal{H}_{eff}\begin{pmatrix}|B^0(t)\rangle \\ |\bar{B}^0(t)\rangle\end{pmatrix}, \tag{2.44}$$

with $\mathcal{H}_{\text{eff}}$ from Eq. 2.37. The non-unitary evolution is caused by the fact that B^0 and $\overline{B}^0$ decay into final states outside of the basis span by $|B^0\rangle$ and $|\overline{B}^0\rangle$. In general, the mass eigenstates $|B_L\rangle$ and $|B_H\rangle$ are no longer orthogonal. [9]

The mass difference Δm is an important parameter of the SM. The oscillation frequency imposes a powerful constraint on CKM matrix elements, such as ϕ_1 and ϕ_2 [20]. Experimentally Δm_d is accessible through time-dependent measurements.

2.2.4 CP Violation

At first, parity (P) and charge (C) symmetries were believed to be exact. However, in 1956 first evidence of parity violation was observed in the β decay of ^{60}Co [21]. As already described earlier, parity is maximally violated by the chiral nature of weak interaction. Also the C parity is violated in weak interactions. Furthermore, CP violation refers to the violation of not only P and C, but the product of these conjugations. CP violation was observed first in the K^0-$\bar{K}^0$ oscillation in 1964 [17].

To understand CP violation, first formalism of decay amplitudes is introduced. These decay amplitudes can be calculated by the sum of different processes, which contribute at different strengths. The amplitude for a decay of an arbitrary initial state A into the final state f is defined as:

$$A_f = \sum_k A_k e^{i\delta_k} e^{i\phi_k}, \tag{2.45}$$

$$\bar{A}_{\bar{f}} = \sum_k A_k e^{i\delta_k} e^{-i\phi_k}, \tag{2.46}$$

where δ_k denotes the strong phase and $\phi_k = \alpha, \beta, \gamma$ the weak phases. While weak phases are related to the initial state decaying via weak interaction, strong phases are related to the final states. In addition, Eq. 2.46 is the decay amplitude of the conjugated process, where not only the initial state but the final state is conjugated as well, resulting in the weak phase's negative sign. There are three classes of CP violating processes: *CP violation in decay*, *CP violation in mixing* and *mixing induced CP violation*.

CP violation in decay (also *Direct CP violation*) occurs in processes where ratio $\left|\frac{\bar{A}_{\bar{f}}}{A_f}\right|$ is not equal to 1. In such process there are at least two weak phases ϕ_k and strong phases δ_k that are non-trivial. In other words, two different amplitudes have to be involved in the decay. This can be easily seen when calculating the difference between the absolute value of these decay amplitudes, which yields [22]:

$$|\bar{A}_{\bar{f}}|^2 - |A_f|^2 \propto sin(\phi_1 - \phi_2) sin(\delta_1 - \delta_2). \tag{2.47}$$

The second class of CP violation is CP violation in mixing (also *indirect CP violation*). This occurs in processes involving neutral decaying particles such as neutral kaons or B mesons. For B mesons, if $\langle B_L | B_H \rangle$ is non-trivial, i.e. the states are not orthogonal, CP violation in mixing occurs. This is caused by the difference between CP eigenstates and mass eigenstates [22].

Lastly, when B^0 and its CP conjugated state $\bar{B}^0$ can decay into the same final state f mixing induced CP violation can be observed. This is caused by the interference of the two contributions to the same final state; a direct decay $B^0 \to f$ and mixed decay $\bar{B}^0 \to B^0 \to f$, for which resolution time-dependent analysis is necessary. The time-dependent amplitude yields:

$$A_f(t) = \frac{BF(\bar{B}^0(t) \to f) - BF(B^0(t) \to f)}{BF(\bar{B}^0(t) \to f) + BF(B^0(t) \to f)} = S_f sin(\Delta m t) - C_f cos(\Delta m t), \tag{2.48}$$

with $\Delta m = m_{B_H} - m_{B_L}$ and the real coefficients S_f and C_f. Note, that even in a process where no CP violation in decay nor mixing occurs, a mixing induced CP violation can be observed because of the interference term [22, 23].

2.3 B to charm decays

Most hadronic B meson decays are mediated via $b \to c$ transitions, as these are governed by the large magnitude of the CKM matrix element $|V_{cb}|$ compared to other b-quark transitions [14]. The large phase space available in B decays allows for a broad variety of possible final states. Despite the abundance of such decay channels, the charm sector remains challenging from both theoretical and experimental perspective.

Theoretical predictions turn out to be complicated due to the fact that the final states are purely hadronic, requiring non-perturbative QCD effects to be taken into account. While some decay modes such as $B^0 \to D^-\pi^+$ are considered relatively simple, they still demand careful treatment — although for this channel, certain QCD contributions can be computed from first principles. [14]

From the experiment's point of view, studies of these decays demand high-statistics data sets due to the small branching ratios, as well as excellent energy and momentum resolution, along with robust particle identification (PID) [20]. Meeting these requirements is demanding, however crucial because of their important role in calibration procedures for the detector and reconstruction algorithms [20].

2.3.1 Overview of $b \to c\bar{u}d$ transitions

Hadronic $b \to c\bar{u}d$ decays, such as $B \to D\pi$, are often described using the factorization ansatz. This approach separates short-distance QCD effects, calculable in perturbation theory, from long-distance effects that are treated non-perturbatively. In practical terms, this leads to decay amplitudes being approximated by products of form factors and decay constants.

Fig. 2.5 illustrates representative Feynman diagrams. The color-allowed topologies (a, c) dominate due to favorable color configurations, while the color-suppressed modes (b, d) are suppressed by a factor of $1/N_C$, where $N_C = 3$ is the number of QCD colors.

For the analysis in this thesis the focus will be on the channel $B^0 \to D^{(*)-}\pi^+$, which follows the topology shown in Fig. 2.5 c) for both D^{*-} and D^-. Here, the spectator quark is a d, which later combines with $\bar{c}$ after the $\bar{b} \to \bar{c}$ transition. The virtual W^+ boson results in a $u\bar{d}$ vertex, which constitutes to a π^+.

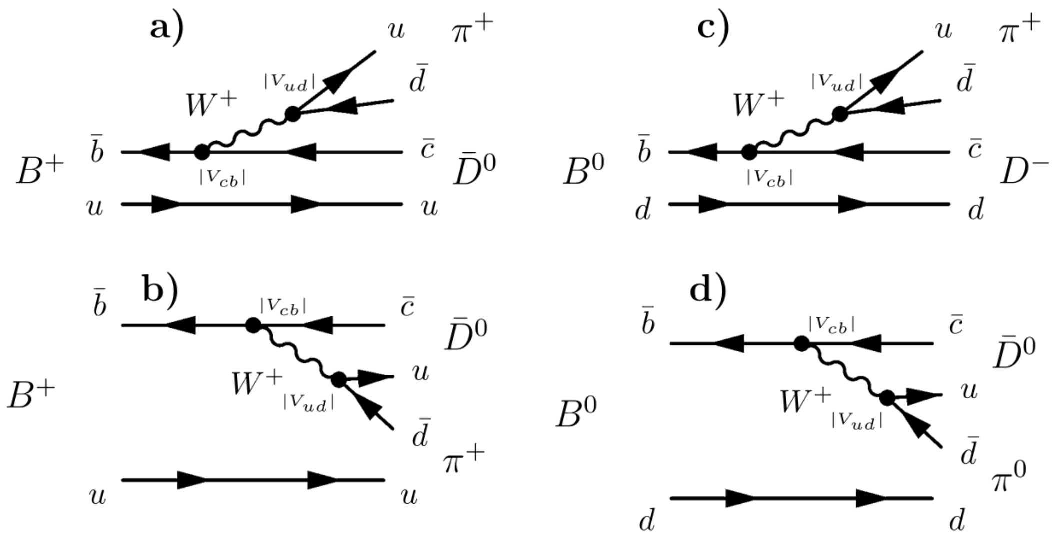

Figure 2.5: Feynman diagrams showing $B^+ \to \bar{D}^0\pi^+$ (a, b), $B^0 \to D^-\pi^+$ (c) and $B^0 \to \bar{D}^0\pi^0$ (d) modes. Diagrams a), c) are color-allowed, b) and d) are color-suppressed.

2.3.2 Tag-Side Interference effect

For a decay channel to exhibit a non-zero CP asymmetry, it must involve at least two interfering amplitudes with distinct weak phases. However, this condition alone does not guarantee a measurable CP violation effect. The primary focus in time-dependent CP asymmetry studies has traditionally been on interference effects occurring on the reconstructed B meson (B_{sig}) side. Nonetheless, as pointed out by authors of Ref. [24], an additional source of interference arises from the tag-side B meson (B_{tag}), where multiple amplitudes can contribute to the final state. This effect is dubbed the *tag-side interference* effect (TSI). If B_{tag}'s flavor at time of decay is not determined correctly, it could cause a systematic bias in the measured CP asymmetry of B_{sig}. While B_{tag} is reconstructed primarily in semi-leptonic and hadronic decay modes, only latter experiences interference effects as semi-leptonic decays via a single amplitude in the SM [14]. While TSI is an effect, as the name suggests, happening on the tag-side of course the physics is the same for signal-side. As this thesis analyzes hadronic decays as signal, the theory will be presented here to translate them later to signal-side.[3]

[3]It will be still called tag-side interference effect later, even when discussing the same effect on signal-side to avoid semantic confusion.

To illustrate the impact of TSI, consider the decay $B \to D^-\pi^+$ followed by $D^- \to K^+\pi^-\pi^-$. This final state is accessible via the favored $b \to cud$ transition in a B^0 meson. However, the same final state can also be reached from a B^0 that has undergone $B^0 - \bar{B}^0$ mixing first, followed by the doubly-CKM-suppressed $b \to ucd$ transition. The relative strength of these two amplitudes is determined by the ratio of CKM matrix elements, approximately given by:

$$\left|\frac{V_{ub}^* V_{cd}}{V_{cb} V_{ud}^*}\right| \approx 0.02, \tag{2.49}$$

with respect to the CKM-favored amplitude. Following Feynman diagrams in Fig. 2.6 show a CKM-favored amplitude (left) and a doubly CKM-suppressed amplitude for the decay mode $\overline{B}^0 \to D^{(*)+}\pi^-$. The amplitude ratio between the favored ($\overline{b} \to \overline{c}u\overline{d}$) and suppressed ($\overline{b} \to \overline{u}c\overline{d}$)

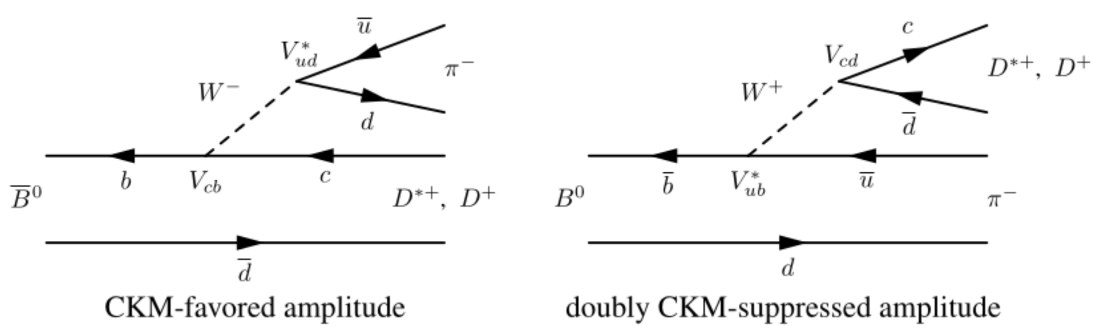

Figure 2.6: Feynman diagrams for CKM-favored amplitude (left) and doubly CKM-suppressed amplitude for decay mode $\overline{B}^0 \to D^{(*)+}\pi^-$. The ratio of these contribution is given by 2.49. Interference of both amplitudes two reach the final state causes the tag-side interference effect [14]. Figure taken from [25].

decay pathways can be expressed as:

$$\frac{\overline{A}_f}{A_f} = r_f e^{-i\phi_3 + i\delta_f}, \tag{2.50}$$

where r_f represents the relative magnitude of the suppressed decay amplitude, δ_f is the strong-phase difference between the two contributing amplitudes, and the weak phase ϕ_3. As B_{tag} is reconstructed from multiple decay modes, an effective ratio r'_f and phase difference δ'_f are introduced to account for different tag-side modes. This interference modifies the time-dependent CP asymmetry parameters S and C, which can be corrected by tuning the shape of the Δt distribution. These corrections would broaden/tighten the distribution while slightly reducing/increasing the amplitude, as shown in Ref. [24]. Consequently, for hadronic-tag events, CP asymmetry parameters can deviate from their true values.

There are two ways of mitigating systematic uncertainties arising from TSI: (i) restricting the analysis to semi-leptonic or leptonic tag events to eliminate TSI effects[4], (ii) utilizing control samples to directly measure the CKM-favored and suppressed decay ratios, along with their phase differences. Latter approach can be challenging as a new term in the Δt distribution of the $B^0\overline{B}^0$ system has to be introduced in Eq. 2.60 proportional to $\sin \Delta m \Delta t$. When looking at signal-side TSI formalism introduces new possible fit parameters. The sine-term is modeled by parameters r', δ' and $\phi = 2\phi_1 + \phi_3$. Notice how the sine-term is different to the additional sine-term introduced by disentanglement effects in Eq. 2.61 as Δt is not an absolute value. As a consequence, a non-zero contribution of TSI effects would lead to a asymmetric shift in the time-dependent asymmetry as can be seen in the following relation

$$a(\Delta t) = \frac{N_{OF}(\Delta t) - N_{SF}(\Delta t)}{N_{OF}(\Delta t) + N_{SF}(\Delta t)} = \cos \Delta m \Delta t + f_{\mathrm{TSI}} \cdot \sin \Delta m \Delta t, \tag{2.51}$$

where f_{TSI} is the strength of the effect, depending on TSI parameters. Finally, tag-side interference introduces an additional correction to the wrong-tag fraction w due to misidentification effects from $D^0 - \bar{D}^0$ oscillations. This modifies the effective mistagging fraction as:

$$w_{\mathrm{eff}} = w + \Delta w_{\mathrm{TSI}}, \tag{2.52}$$

where Δw_{TSI} depends on the decay modes involved and the degree of interference. Tag-side interference represents a subtle but significant effect in time-dependent analyses of neutral B mesons. While it does not introduce a bias in the absence of CP violation, it can alter the effective tagging efficiency and introduce systematic uncertainties [25]. For interference on signal-side, an important study will be pure Toy Monte Carlo studies, where data sets are sampled directly from the model PDFs. Thus, different TSI sizes can be tested in a clean environment to predict systematic impacts on mixing studies.

[4]This has been done by Go. *et al.* in Ref. [26] (See Sec. 2.5.2).

2.4 Quantum Entanglement

2.4.1 EPR-Type Entanglement

The concept of quantum entanglement, introduced by W. Heisenberg [27] and discussed critically in Einstein-Podolsky-Rosen (EPR) paradox [2], highlights the fundamental non-locality of quantum mechanics. The EPR paper challenged the completeness of quantum mechanics by suggesting that a hidden variable theory could provide a more fundamental description of reality. The paradox is typically illustrated using Spin-$\frac{1}{2}$ systems but can be generalized to two-state quantum systems, such as the neutral B-meson system.

In a typical entangled system, two quantum particles are prepared in a maximally entangled state, such as:

$$|\Psi\rangle = \frac{1}{\sqrt{2}}(|\uparrow\rangle_1 |\downarrow\rangle_2 - |\downarrow\rangle_1 |\uparrow\rangle_2), \tag{2.53}$$

where $|\uparrow\rangle$ and $|\downarrow\rangle$ represent the two possible outcomes of a measurement spin up and down, respectively. This antisymmetric EPR-like state ensures that the measurement of one particle's state determines the state of the other particle immediately, no matter the spatial separation. This property is what enables quantum non-locality tests. [2]

2.4.2 Bell Tests and the possibility of violations in the $B^0\overline{B}^0$ system

Bell's Theorem [3] provided a concrete mathematical framework to test the validity of local hidden variable theories against quantum mechanics. Bell derived an inequality that must be satisfied by any theory based on local realism, and its violation would provide strong evidence in favor of quantum mechanics.

In typical Bell tests, measurements are performed on two entangled particles using different measurement settings, ensuring that their correlations cannot be explained by local hidden variables. Experimental violations of Bell's inequalities in photon polarization, electron spin, and atomic systems have confirmed quantum mechanical predictions. Moreover, the neutral B meson system presents an interesting opportunity to test Bell inequalities in heavy flavor particle systems.

A generalized Clauser-Horne-Shimony-Holt (CHSH) inequality for a pair of entangled photons with two polarization measurement devices on both sides reads [28]:

$$S = E(\alpha, \beta) - E(\alpha, \beta') + E(\alpha', \beta) + E(\alpha', \beta') \leq 2, \tag{2.54}$$

where α, α' and β, β' are possible angle settings on the polarizers. $E(\alpha, \beta)$ represents the correlation coefficient of polarization measurement outcomes, defined as [3]

$$E_R(\alpha, \beta) = \frac{R_{++}(\alpha, \beta) + R_{--}(\alpha, \beta) - R_{+-}(\alpha, \beta) - R_{-+}(\alpha, \beta)}{R_{++}(\alpha, \beta) + R_{--}(\alpha, \beta) + R_{+-}(\alpha, \beta) + R_{-+}(\alpha, \beta)}, \tag{2.55}$$

where $R(\alpha, \beta)$ is the coincidence rate. If $S > 2$ is observed in experimental data, it would be a direct violation of Bell's inequality, ruling out any local hidden variable theory and confirming the inherently non-local nature of quantum mechanics. To move from entangled photons to the $B^0\overline{B}^0$ system, the polarization angles α, β have to be replaced by $\Delta m \Delta t$, thus the coincidence rate is now defined as

$$R_{B^0B^0}(t_1, t_2) = \frac{1}{4} e^{-2t'/\tau} e^{-\Delta t/\tau} \left(1 - e^{-\Delta/\tau} \cos \Delta m \Delta t\right). \tag{2.56}$$

The unnormalized correlation function takes on the form

$$E(t_1, t_2) = -e^{-2t'/\tau} e^{-\Delta/\tau} \cos \Delta m \Delta t. \tag{2.57}$$

Normalizing this equation to the undecayed $B^0\overline{B}^0$ pair, the correlation function in Eq. 2.55 becomes

$$E_R(\Delta t) = \cos \Delta m \Delta t, \tag{2.58}$$

and is only dependent on the mixing parameter Δm and the decay time difference Δt. The CHSH Inequality of Eq. 2.54 can be expressed as

$$S(\Delta t) = 3E_R(\Delta t) - E_R(3\Delta t) \leq 2. \tag{2.59}$$

Moreover, authors of Ref. [29, 30] have found the parameter $x = \Delta m/\Gamma$ to be a crucial parameter in Bell tests. Following their argument, x has to be smaller than a numerically determined value of $N = 2.0$, for $B^0\overline{B}^0$, $D^0\overline{D}^0$, $K^0\overline{K}^0$ and $B_s^0\overline{B}_s^0$. Experimental values show that $x = \Delta m/\Gamma$ is greater than this threshold only for the $B_s^0\overline{B}_s^0$ system with $x > 20.6$ [29], for the remaining neutral meson systems no CHSH inequality violation is expected. Unfortunately, Belle II is not designed to produce $B_s^0\overline{B}_s^0$, thus no bell tests can be performed at this experiment. Therefore, a different approach has to be taken to test quantum entanglement in $B^0\overline{B}^0$ systems directly. Thus, this thesis' focuses on special disentanglement models described in the following Sec. 2.5.

2.5 Models of Quantum Disentanglement in the $B^0\overline{B}^0$ system

In this section the physics models are presented that are studied in the analysis. The models are introduced as alternatives or extensions to the established Standard Model neutral B Meson mixing. The applied framework does not introduce new interactions or new particles, it only addresses the coherent oscillation of entangled B Meson pairs. Therefore, the following models can be in accordance with SM as well as Quantum Mechanics. First, the so-called *Spontaneous Disentanglement* (SD) Model is presented, followed by the *Partial Spontaneous Disentanglement* (PSD) Model in which the crucial parameter ζ determines the fraction of disentangled B meson pairs. The section closes with some remarks on the *Time Dependent Disentanglement* Model.

2.5.1 Spontaneous Disentanglement

Firstly, the probability of survival (oscillation) for a B^0 created at time $t = 0$ is defined as

$$P(t) = \frac{1}{2}e^{-\Gamma t}(1 \pm \cos \Delta m t), \tag{2.60}$$

with Δm the mass difference between the two mass eigenstates heavy and light, Γ the absolute decay width. Now, consider the case of Spontaneous Disentanglement. The two B mesons coming from the $\Upsilon(4S)$ resonance disentangle immediately after the pair production, hence, the independent oscillation of both neutral B mesons. This follows *Furry's Hypohesis*, in which an entangled two-state system transitions into individual definite states in a probabilistic manner [4]. Due to $\mathcal{C}$-parity conservation of the $\Upsilon(4S)$, the initial state of the B meson pair is still asymmetric with both particles in orthogonal states $|B^0\rangle$ and $|\overline{B}^0\rangle$ at $t = 0$. The PDF can be derived starting from

$$P_{\mathrm{SD}}(\Delta t) \propto \frac{1}{2}e^{-\Gamma t_2}(1 \pm \cos \Delta m t_2) \times \frac{1}{2}e^{-\Gamma t_2}(1 \pm \cos \Delta m t_2), \tag{2.61}$$

where $t_{1,2}$ is the absolute decay time of B_1 and B_2. By convention, $B_1 = B_{\mathrm{tag}}$ and $B_2 = B_{\mathrm{sig}}$ is chosen. After integrating over time t_1, and simplifying Eq. 2.61 reads:

$$P_{\mathrm{SD}}(\Delta t) = \frac{1}{8}e^{-\Gamma\Delta t}\left[2 \mp \left(1 + \frac{\Gamma^2}{\Gamma^2 + \Delta m^2}\right)\cos \Delta m \Delta t \pm \frac{\Gamma \Delta m}{\Gamma^2 + \Delta m^2}\sin \Delta m|\Delta t|\right]. \tag{2.62}$$

The main difference between the entangled PDF in Eq. 2.60 and 2.62 lies in the prefactor of the cosine, which serves as a damping term and the emergence of a sine-term with an absolute Δt in the argument. The rigorous derivation of the SD PDF in Eq. 2.62 can be found in Appendix A.1.

Additionally, the time-dependent asymmetries for fully entangled and SD case is defined

$$a(\Delta t) = \frac{N_{OF}(\Delta t) - N_{SF}(\Delta t)}{N_{OF}(\Delta t) + N_{SF}(\Delta t)} = \cos \Delta m \Delta t, \tag{2.63}$$

$$a_{SD}(\Delta t) = f_{cos} \cdot \cos \Delta m \Delta t + f_{sin} \cdot \sin \Delta m|\Delta t|. \tag{2.64}$$

where f_{cos} and f_{sin} are the prefactors of cosine and sine from Eq. 2.62 and the subscripts OF and SF stand for opposite flavor and same flavor, respectively. The additional sine-term in Eq. 2.64 leads to a phase shift in the asymmetry, in respect to Eq. 2.63. Following Fig. 2.7 show the PDFs and time-dependent asymmetries Eqs. 2.63 and 2.64 for the entangled and disentangled case, respectively. When looking at the Δt-distributions in Fig. 2.7, one can see a clear difference especially in the same flavor PDFs. For the fully disentangled case the blue distribution does not vanish at $\Delta t = 0$, as for the entangled case (blue distribution in left Fig. 2.7). This is a direct result of the disentangled oscillation. While for entangled $B^0\overline{B}^0$ pairs it would be impossible to be in the same state at the same time ($\Delta t = 0$), this constraint does not exist for disentangled pairs. The shapes of the red curves for both cases are seemingly similar, although the relative peak

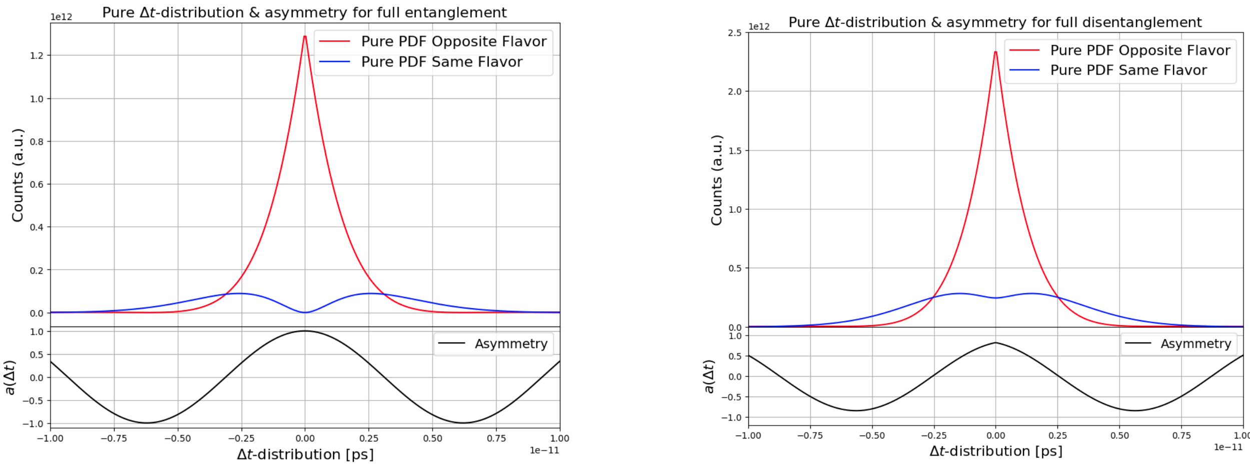

Figure 2.7: Δt-distribution and time-dependent asymmetry $a(\Delta t)$ for the case of full entanglement (left) and full disentanglement (right). The PDF for the case of the B mesons decaying in opposite flavor states and same flavor states are shown in red and blue, respectively. The plot on the bottom shows the time-dependent asymmetry from Eqs. 2.63 and 2.64 for entangled and disentangled case, respectively.

height at $\Delta t = 0$ is lower for the SD case due to probability conservation. When looking at the asymmetries for both cases the SD case shows a smaller amplitude and some phase shift compared to the entangled case in left Fig. 2.7.

2.5.2 Partial Spontaneous Disentanglement

Moving on to the Partial Spontaneous Disentanglement model. Here, the fraction of spontaneously disentangling $B^0\overline{B}^0$ pairs is reduced to only a fraction $\zeta \in [0, 1]$. The PSD model is constructed by an linear combination of the entangled PDF in Eq. 2.60 (P_{QM}) and the SD PDF in Eq. 2.61 thus reads:

$$P_{\text{PSD}}(\Delta t, \zeta) = (1-\zeta) \cdot P_{\text{QM}}(\Delta t) + \zeta \cdot P_{\text{SD}}(\Delta t). \tag{2.65}$$

This means for $\zeta = 0(1)$, P_{PSD} takes on the form of the fully (dis)entangled case. After a simple arithmetic exercise one gets the time-dependent combined PDF:

$$P_{\text{PSD}}(\Delta t, \zeta) = \frac{1}{8} e^{\Delta t/\tau} \left[2 \mp \left(2 - \frac{\zeta \Delta m^2 \tau^2}{1 + \Delta m^2 \tau^2} \right) \cos \Delta m \Delta t \pm \frac{\zeta \Delta m \tau}{\Delta m^2 \tau^2} \sin \Delta m |\Delta t| \right]. \tag{2.66}$$

This model has been studied at Belle by Go *et al.* [26][5]. In the study, the time-dependent asymmetry has been extracted by deconvolution of detector effects and correction for experimental effects. The analysis has been performed for 152×10^6 $B\overline{B}$ pairs taken at the $\Upsilon(4S)$

[5] This study also analyses a model proposed by *Pompeili and Selleri* [31] which is strongly disfavored by 5.1σ compared to the entangled model. This model will not be included in this thesis's analysis.

resonance. Different from the Belle II experiment with the SuperKEKB accelerator, the data has been taken on an asymmetric energy of 3.5 GeV and 8.0 GeV at the e^+e^- collider KEKB. Moreover, the fully reconstructed signal channels are the semi-leptonic channel $B^0 \to D^{*-}l^+\nu$ with $D^{*-} \to \overline{D}^0[K^+\pi^-(\pi^0)]\pi_s^-$ and $D^{*-} \to K^+\pi^-\pi^+\pi^-$. Conversely, the tag-side B's decay vertex and flavor are determined by a flavor tagger algorithm described in [32]. Go *et al.* apply a lepton-tag condition, i.e. only leptonic tags from highest purity are used. This has some advantages such as having no Tag-Side Interference effects in turn of losing statistics. Exclusively using tags of the highest purity reduces the wrong-tag fraction to a minimum.[6] Fig. 2.8 shows the time-dependent asymmetries for QM and SD model predictions and data. As SD is excluded by 13σ, consequently

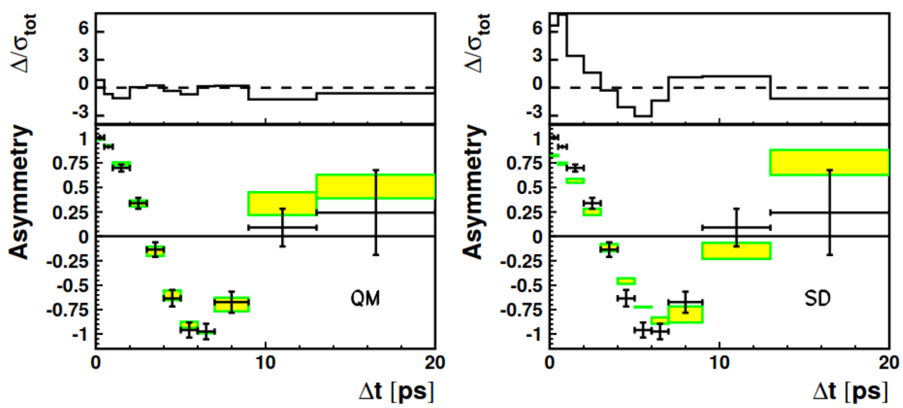

Figure 2.8: The plot on the bottom show time-dependent asymmetry for fully entangled QM model (left) and the fully disentangled model (right). The yellow boxes show the models' predictions for QM and SD case with $\pm 1\sigma$ region. Data points with error bars show the region of $\pm 1\sigma$. While QM is consistent with data, SD has been excluded with 13σ. Plots on the top show the pull distribution. [26]

the more realistic case of PSD is studied by fitting the time-dependent asymmetry with a free $\zeta_{B^0\overline{B}^0}$. For the fraction of PSD in the flavor basis $B^0 - \overline{B}^0$[7] they report a value of [26]

$$\zeta_{B^0\overline{B}^0} = 0.029 \pm 0.057, \tag{2.67}$$

consistent with full entanglement, though a small fraction of disentanglement in the $\mathcal{O}(1\%)$ could not be excluded, and a fraction of disentanglement in the $\mathcal{O}(10\%)$ could not be excluded on the 90% CL.

[6] For more details regarding selection, cuts and treatment of background, refer to Go *et al.* [26] directly.

[7] Throughout this thesis ζ is always defined in this flavor basis of the B meson, as long as not explicitly stated differently.

Multiple things will be different in this thesis's work as hadronic decay modes of the B^0 are studied. Using the semi-leptonic channel has been proposed as it offers a larger data set decreasing statistical uncertainty. Additionally, while the loss of statistics when applying the lepton tag condition has to be considered, the decrease of systematic uncertainty due to absence of TSI effects in semi-leptonic modes could turn out to be beneficial. As far as sensitivity estimations go for the parameter ζ at Belle II a simple extrapolation according to number of events is proposed.

2.5.3 Remarks on time-dependent disentanglement models

There are a variety of models describing possible ways of how quantum entanglement between the two B mesons could be lost. Theoretical works focus mostly on time-dependent disentanglement models, finding its origin in mathematical frameworks of so-called *Open Quantum Systems* with the *Lindblad* formalism [33]. These were later put into context of heavy flavor decays by e.g. Pompili & Selleri [31], Bertlmann *et al.* [34] and most recently Alok *et al.* [6], just to name a few. Currently, there are ongoing studies at Belle II searching for time-dependent disentanglement models, for example at the University Hawai'i. However, the search of time-dep. disentanglement relies on the measurement of the absolute decay times of both B mesons, for which novel techniques are currently under development. Here at Max-Planck-Institute for Physics's Belle II group, a focus has been set on studying disentanglement models using the decay time difference Δt. This approach has been motivated by the fact that the analysis stays model-independent, as absolute-time dependent effects are integrated out. Therefore, they can be modeled in terms of the fraction of disentanglement parameter $\zeta = f(\Lambda)$, with Λ being a universal parameter of disentanglement. Moving forward, the model independent definition of ζ will be used.

3 The Belle II Experiment

Belle II is a project consisting of the SuperKEKB accelerator and Belle II detector located at the research laboratory KEK in Tsukuba, Japan. To reach higher luminosities the KEKB accelerator has been upgraded to SuperKEKB. Likewise, the Belle detector has been upgraded to Belle II. The primary goal of this project is the search for NP in the flavor sector of the SM. Additionally, this B factory will improve measurements of SM parameters, provide unprecedented access to the τ-sector and allows for Dark Matter searches. The following chapter focuses on the apparatus of the Belle II experiment and the Belle II Analysis Software Framework. Information used in this chapter is taken from references [20, 35].

3.1 The SuperKEKB accelerator

SuperKEKB is an asymmetric e^-e^+-collider with a circumference of 3km, designed to reach instantaneous luminosities of $\mathcal{L} = 6 \cdot 10^{35}$ cm^{-2}s^{-1}. After production of the particles, the beams are accelerated in the electron-positron linear accelerator. Then the e^+ and e^- are injected into the low energy storage ring (LER) and into the high energy storage ring (HER), respectively. The positron and electron beams with 4 GeV and 7 GeV, respectively, result in a center of mass (CM) collision energy of $\sqrt{s} = 10.58$ GeV. These beams are brought to collision at the interaction point which is located inside the Belle II detector. The CM has the same energy as the $\Upsilon(4S)$ resonance, which is slightly above the energy threshold necessary for B meson pair production. Hence, the electron-positron-pair annihilates partly into the $\Upsilon(4S)$ resonance which then decays in 96% of the cases into an $B\bar{B}$-pair [36]:

$$e^-e^+ \to \Upsilon(4S) \to B\bar{B}. \tag{3.1}$$

3.2 The Belle II Detector

The Belle II detector consists of seven sub-detectors used for the measurement of numerous quantities. They are aligned concentrically around the collision axis in several layers. To account for the boost of the $\Upsilon(4S)$ the acceptance is asymmetric in the polar angles between 17° and 150°. The detector can be divided into an inner layer and an outer layer of sub-detectors, the latter is being reused from the predecessor Belle. The reused sub-detectors are the K_L and μ detector (KLM), the electromagnetic calorimeter (ECL) and the solenoid. The inner layer consists of the Aerogel Ring-Imaging Cerenkov Detector (ARICH), the Time of Propagation Detector (TOP), the Central Drift Chamber (CDC) and lastly the Silicon Vertex Detector (SVD) and Pixel Detector (PXD). Hereinafter, the sub-detectors are introduced starting from the innermost to the outermost sub-detector (In the Fig. 3.2: from the left to the right).

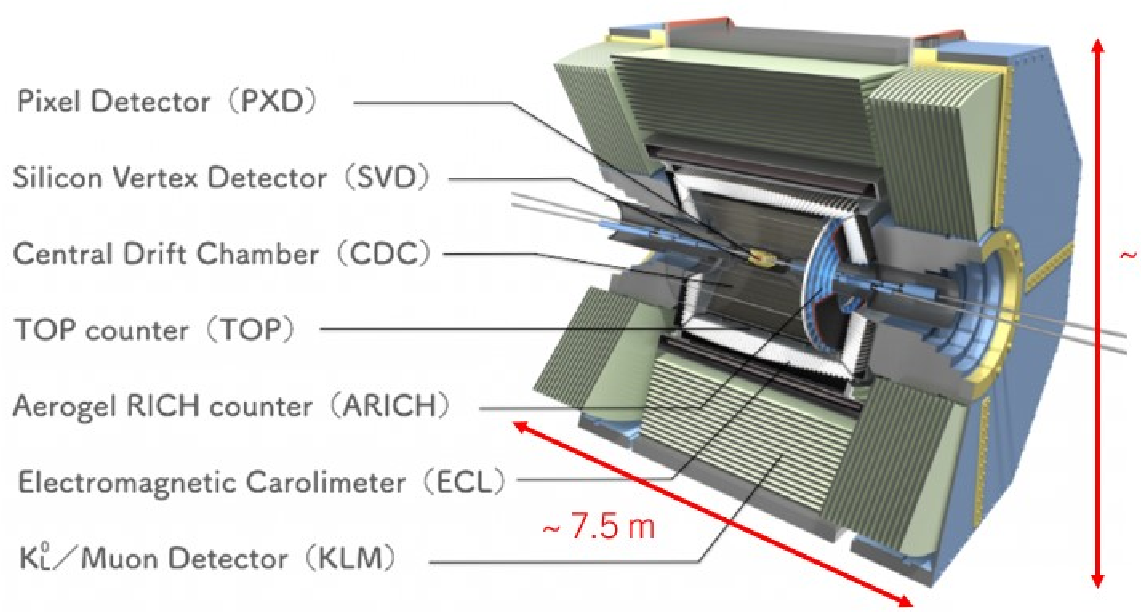

Figure 3.1: Three dimensional realistic schematic view of the Belle II detector. The sub-detectors are marked accordingly to the device and in the order of the innermost to the outermost part, from the top to the bottom [37].

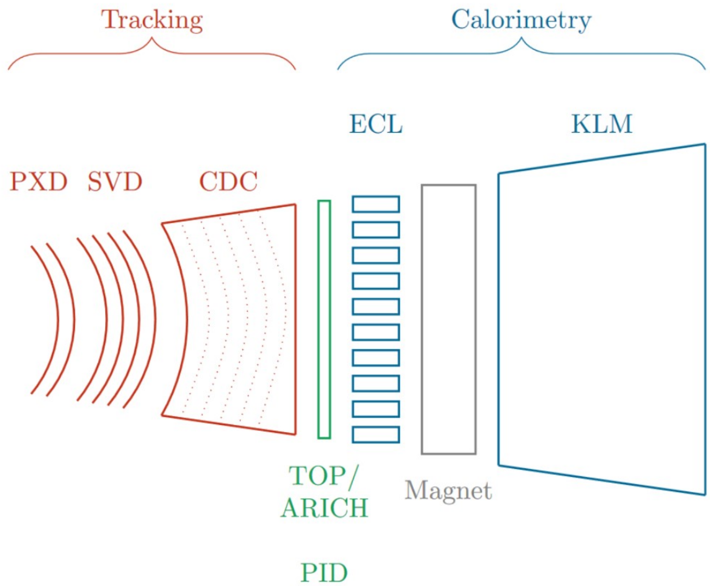

Figure 3.2: Simplified two dimensional schematic view of the Belle II detector, made out of 7 sub-detectors: PXD, SVD, CDC, TOP, ARICH, ECL and KLM. The colors red, green and blue depict the primary task of the devices that are tracking, particle identification (PID) and calorimetry, respectively [38].

3.2.1 Sub-detectors

Vertex Detector (VXD)

Just around the beam pipe the VXD is located. It consists of two detectors: the Silicon Vertex Detector (SVD) and Pixel Vertex Detector (PXD). The latter is the innermost detector, installed right around the beam pipe. Combined data from these subsystems and the CDC enables the vertex reconstruction of decayed B mesons. As already mentioned, the PXD is located right around the beryllium beam pipe. The sensors used in this detector system are based on technology called Depleted Field Effect Transistor (DEPFET) [39]. This device is made out of two layers with radii 14mm and 22mm with the interaction point at its center, illustrated in Fig. 3.3. The SVD is composed of four silicon layers placed in radii between 38mm and 140mm from the beam pipe, while three layers of forward sensors are orientated towards the IP, as can be seen in Fig. 3.4.

Central Drift Chamber (CDC)

The CDC is a cylindrical chamber filled with an 1:1 gas mixture of He-C_2H_6. Charged particles passing through the chamber ionize the gas, where wires inside the chamber can detect the avalanche created by ionized electrons. By this mechanism the trajectory of charged particles can

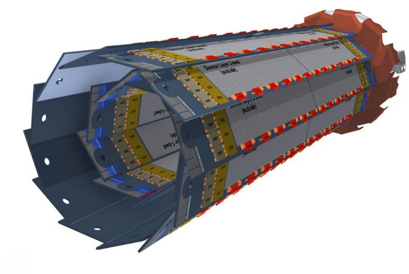

Figure 3.3: The PXD has a structure composed out of two concentrically arranged layers of sensors, in the shape of a windmill [40].

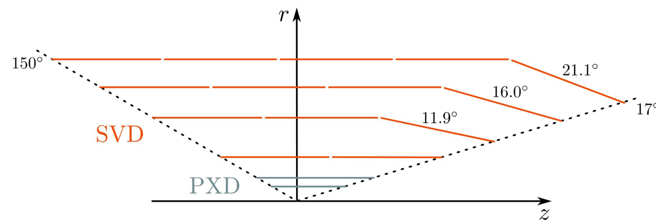

Figure 3.4: Schematic view of the Belle II VXD made out of two layers of the PXD and four layers of the SVD. [41]

be determined from the knowledge about the positions of ionizations. In combination with the strong magnetic field the charged particles' momenta are determined by considering their curvature. Moreover, the SVD and CDC are important for particle identification as they measure the ionization rates $\frac{dE}{dx}$. The measurements in the drift chamber also contribute to the trigger system.

Time of Propagation Detector (TOP) and Aerogel Ring-Imaging Cerenkov Detector (ARICH)

Information of charged particles' kinematics gathered from TOP and ARICH are also essential for particle identification. In the forward end cap region the ARICH is located. In a Cerenkov radiator made out of aerogel, incoming charged particles produce Cerenkov light. These photons can be registered in a photon detector. Incoming pions and kaons differ in mass. Thus, the angle of the emitted light differs. ARICH can separate pions from kaons up to a maximum momentum of 4 GeV/c.

The TOP is located in the barrel region of the Belle II detector. Incoming beams of charged particles emit Cerenkov light in quartz which is guided to the end of the crystal. A detector registers photons and measures the time of propagation in the TOP. From this measurement the particles' velocities are calculated. Fig. 3.5 shows the working principle of the TOP detector.

Superconducting Solenoid

The superconducting solenoid measures 4.4 m in length and 3.4 m in diameter. It creates a strong magnetic field of $B = 1.5$ T, which bends the trajectory of charged particles. This is used in the CDC for momentum measurements.

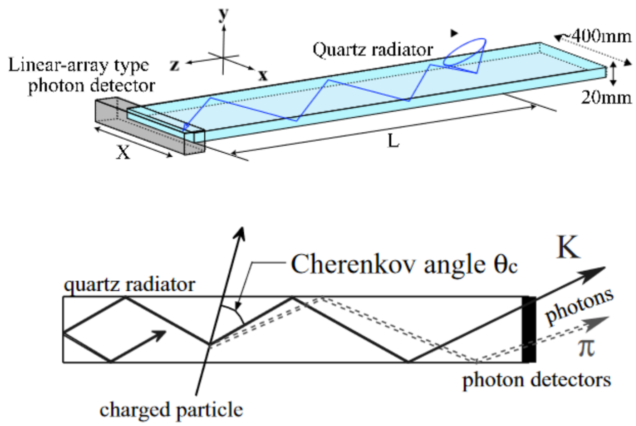

Figure 3.5: Top: general overview of the TOP detector. Bottom: Schematic view of the TOP. The incoming charged particles $K^{\pm}$ and $\pi^{\pm}$ emit Cerenkov light, which is then guided by the quartz radiator to the end of the crystal. Depending on the path the time until the photon reaches the detector differs [35].

Electromagnetic Calorimeter (ECL)

The ECL is crucial for measurements of photon energies and angular coordinates as well as for detection of clusters made by neutral pions with high momenta. Together with the KLM, the calorimeter generates signals for trigger processes. Due to their high light output, thallium-doped caesium iodide (CsI(Tl)) scintillation crystals are used for this detector, maximizing the rate of photons.

K_L and μ Detector (KLM)

The outermost detector, located at the barrel and end cap around the superconducting solenoid is the KLM, which is made out of alternating layers of 4.7 cm thick iron and scintillator detectors. It is used to detect long-lived Kaons K_L^0 and muons, with Kaons creating a hadronic shower when passing through iron plates, triggering the detector. Muons - the only charged leptons penetrating the KLM - and minimally ionizing charged hadrons with momentum above 0.6 GeV$/c$ are detected by depositing ionization energy.

3.3 Simulation and Analysis Software at Belle II

At Belle II a variety of software is used for event and detector simulations, reconstruction and data analysis. The software used in the scope of this thesis is the Belle II Software Framework `basf2`. In the following section the Event Simulation process, starting from the decay models in `EvtGen`, simulation of non-signal events and radiation using `PYTHIA 8.2` and `PHTOS` and finally the simulation of the detector response using `Geant4` will be presented. In the second part, tools used in the analysis such as Track and Vertex Reconstruction and the process of Flavor Tagging are presented. Most general information about `basf2` is taken from [20].

3.3.1 Event Simulation

For the study of B decays at Belle II, Signal Monte Carlo (MC) data generation is an essential component. This process is facilitated using the event generator `EvtGen`, a versatile tool specifically designed for simulating particle decays. The generation of Signal MC data involves several steps: implementing decay models, compiling the necessary `C++` code, generating the simulated events, and validating the output against known standards. Each step ensures that the generated events accurately reflect the expected physical behavior and detector responses. The information about EvtGen is taken from Ref. [42] if not stated otherwise.

`EvtGen` operates within the framework of the Belle II Analysis Software Framework, which integrates various software packages for a seamless simulation workflow. The MC samples are produced to emulate physical processes originating from e^+e^- collisions at the $\Upsilon(4S)$ resonance, followed by the decay into B meson pairs. These decays proceed into the final states of interest as well as other background processes. To capture the complexities of particle interactions and detector behavior, multiple software tools are used:

1. `EvtGen` This event generator models the decay chains of B mesons into exclusive final states. It utilizes a dedicated decay file (*dec file*) containing the decay chain specifications and branching fractions for each step in the process. `EvtGen` begins by simulating the production of $B\bar{B}$-meson pairs and proceeds through their subsequent decays according to the specified decay file. For neutral B mesons, the oscillation is modeled before further decay.

2. `PYTHIA 8.2`: Since `EvtGen` exclusively handles decays into exclusive final states, `PYTHIA 8.2` complements it by simulating non-resonant processes, e.g. hadronization, for any final states not explicitly covered in the dec file. This ensures that the simulated events account for all possible outcomes in a realistic manner.

3. `PHOTOS`: To get closer to reality in simulations, `PHOTOS` is employed to simulate final-state radiation (FSR). This accounts emitted photons during particle decays, which can significantly

impact the final state's kinematics.

4. `Geant4`: The simulated particles and their interactions with the Belle II detector are modeled using `Geant4`. This software incorporates a detailed description of the detector's geometry, material composition, and physics processes. This enables a realistic simulation of particle tracking, energy deposition, and detector responses. The inclusion of beam background effects further enhances the accuracy of simulated events to match experimental conditions.

3.3.2 EvtGen Model

A new `EvtGen` Model is used to generate spontaneously disentangled events. The model has been developed in collaboration with Alexei Sibidanov (University of Hawai'i). This subsection will provide a description of the idea of the `VSS_BMIX_SD` model. It is developed using the existing `VSS_BMIX` as example, which is used to handle Standard Model $\Upsilon(4S) \to B^0\bar{B}^0$ events with subsequent B^0 mixing. As the name already suggests this model handles decays of the type Vector to Scalar-Scalar. In this usage case $\Upsilon(4S)$ is a $C = -1$ vector particle decaying into to scalar particles with a adjustable fraction of coherent/independent mixing. The parameter $C = -1$ corresponds to η parameter used in the derivation in Appendix A.2. For coherent mixing, refer to Ref. [42] as there were no changes made for that part. The independent mixing is governed by the physics explained in theory chapter's section 2.2.3. The `VSS_BMIX_SD` model can be used as follows:

```
Decay Upsilon(4S)
1.0 B0 anti-B0 myB0 myanti-B0 VSS_BMIX_SD dm zeta;
Enddecay
```

Here `dm` corresponds to the physical oscillation parameter Δm in units of ps^{-1}, and `zeta` the fraction of disentangled events in the PSD model. When setting `zeta` to zero, this model returns the already established `VSS_BMIX`. As also remarked in [42] this new model is similar to the previous `VSS_MIX` model, however has no longer the need of manually setting the ratios of mixed and unmixed events using branching fractions. The correct distributions will also be provided for events including a fraction of disentangled events, i.e. `zeta` $\neq 0$. After the modeling of the oscillation, the decays follow the classic decays given in dec-files `1143040100.dec` and `1143062100.dec`.

3.3.3 Track Reconstruction

Track reconstruction is used to reconstruct charged particles from primary and secondary vertices. It is needed for vertex reconstruction and detector alignment for precise studies of time-dependent CP violation measurements and systematic uncertainty studies. In `basf2` track reconstruction is a two-step procedure, starting with *track finding* and then *track fitting*. Track finding requires pattern recognition of clusters in PXD/SVD and CDC wire hits to assign them to one charged particle. The identified clusters and wires belonging to one track are passed on to the track fitting step. Here, the trajectory of each particle is obtained by track fitting from the hit positions. The track fitting is based on `GENFIT` tracking framework, the Kalman filter optimized for Belle II, as well as multivariate methods [20].

A charged particle propagating in a uniform magnetic field follows a helical trajectory characterized by five parameters, which are - by convention - defined at a reference point P along the trajectory. At Belle II, this reference point is chosen as the so-called *Point of closest approach* to the interaction point, determined by extrapolating the track to the z axis. The five track parameters utilized in the Belle II tracking software are:

- d_0: The signed transverse distance from the IP to the point of closest approach. The sign convention is defined such that, when moving along the track in the direction of the particle's momentum, the sign is positive (negative) if the IP is to the right (left) of the track at the point of closest approach.

- z_0: The signed longitudinal distance from the IP to the point of closest approach along the beam axis.

- ϕ_0: The azimuthal angle of the track at the point of closest approach.

- $\tan\lambda$: The tangent of the dip angle, defined as the angle between the track's momentum at the point of closest approach and the transverse plane.

- ω: The track curvature, whose sign corresponds to the charge of the particle.

These track parameters are fundamental to reconstructing particle trajectories and obtaining precise measurements of decay vertices. Fig. 3.6 illustrates the impact parameters d_0 and z_0 within the Belle II detector system. Impact parameters d_0 and z_0 are collected in bins of the pseudo-momentum. To quantify the precision of track reconstruction impact parameter resolutions σ^{d_0} and σ^{z_0} can be defined as:

$$\sigma^{d_0} = \sqrt{a^2 + \frac{b^2}{p\beta\sin^{3/2}\theta}}, \quad \sigma^{z_0} = \sqrt{a^2 + \frac{b^2}{p\beta\sin^{5/2}\theta}}, \tag{3.2}$$

where a is the intrinsic detector resolution, b the multiple scattering coefficient in units of [GeV μm] and the denominators in the equations the so-called pseudo momenta. Latter, account for effects of multiple scattering. By fitting a Gaussian to the binned impact parameters the resolution parameters from Eq. 3.2 can be estimated.

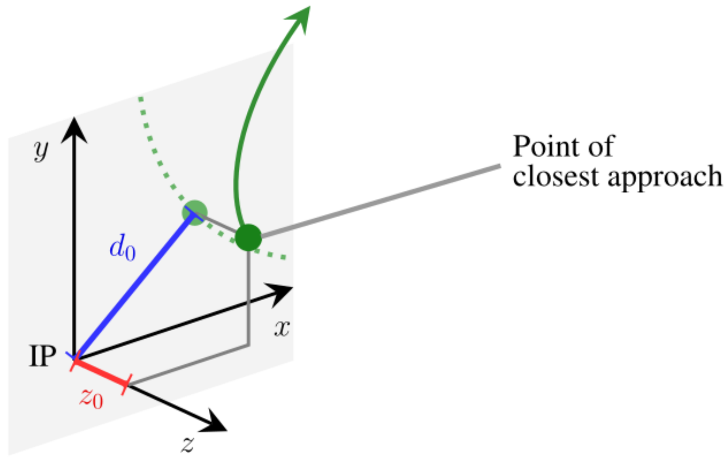

Figure 3.6: Schematic view of track reconstruction parameters. Solid green line shows the particle's track with the dashed green line showing its projection on the xy plane. Impact parameters d_0, z_0 are the distance between origin and Point of closest approach on xy plane and the z coordinate of the Point of closest approach, respectively. [25]

3.3.4 Vertex Reconstruction

Vertex reconstruction describes a technique where reconstructed parameters of decaying particles are used to determine the decay or interaction vertex. In this procedure the vertex position is reconstructed and the momentum as well as the invariant mass of the decaying particle is reevaluated. Difference in decay time and decay length can also be calculated by a vertex fitter. At Belle II, there are two main vertex reconstruction techniques, namely the Kinematic Fit library (`KFit`) developed at Belle and the Reconstruction in an Abstract Vertices Environment (`RAVE`), a standalone software from CMS and finally the `TreeFitter` from the BaBar Collaboration. KFit and RAVE are used for kinematic fits, while latter also serves for geometric fits. Moreover, TreeFitter is used for entire decay chain fitting. [20]

In kinematic fits, known properties of specific decay chains are applied to improve measurements, while kinematic constraints are acquired from Lagrangian Multipliers [20]. As usual for many fitting processes, a χ^2 function is defined which is minimized iteratively in order to obtain parameter estimates on physical quantities. This procedure is usually applied in order to determine decay vertex positions. Through residual fits on the vertex's' coordinate components can give limits on the spatial resolution.

Entire decay chains are fitted using the TreeFitter where trees are parameterized and fitted globally. Sharing information across the whole tree even allows for access to modes rich in neutral and missing particles. As the entire chain is parameterized, naive χ^2 minimization is suboptimal

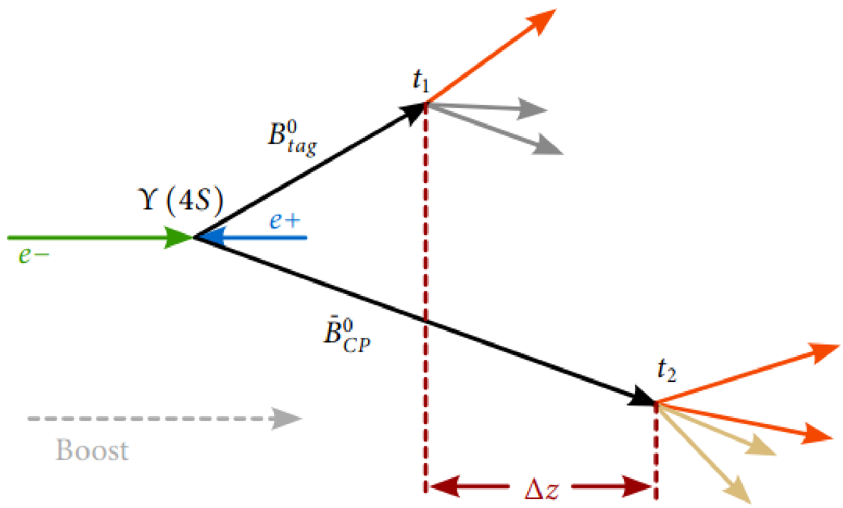

Figure 3.7: Production of two entangled B mesons from the $\Upsilon(4S)$ resonance. B_{tag} and B_{CP} (B_{sig}) propagate in an entangled state until B_{tag} decays at $\Delta z = 0$. B_{CP} oscillates further until it decays into final state Δz. [43]

due to high computation lengths. Instead, Kalman filtering algorithm is applied which brings down computation times significantly [20].

Moving on to a crucial application of vertex reconstruction in time-dependent CP violation measurements - the tag-side B vertex fitting. The sensitivity on the vertex position has to be sufficient to resolve neutral B meson oscillations. The difference between the tag-side and signal-side B is defined as

$$\Delta t = t_{\text{sig}} - t_{\text{tag}} = \frac{\Delta z}{\beta\gamma c}. \tag{3.3}$$

with t_{sig} and t_{tag} the absolute decay times of the fully reconstructed signal-side B and the tag-side B, respectively. Δz is defined as the decay vertex positions' difference of the two B mesons along boost direction. As the tag-side B's vertex sensitivity dominates the resolution of Δt a precise determination of the vertex position plays in important role in mitigating uncertainty. Following sketch illustrates the evolution of both B mesons on tag-, and signal-side until their subsequent decays. After their pair production in the $\Upsilon(4S)$ resonance, the tag-side B decays at $\Delta z = 0$, while signal-side B_{CP} (B_{sig}) decays at Δz. The difference in decay time is calculated using Eq. 3.3. In order to further optimize the χ^2 function's minimization, weights are introduced. These weights are constraints imposed upon the D meson's decay vertex. For this, an ellipsoid region is defined around the beam spot orientated along the boost direction in which the B^0 is more likely to decay than the D. For decay vertices outside this defined region the tracks originating from that point are assigned to the D. The following figure illustrates this beam spot constraint: More detailed description of the tag-side B meson's reconstruction can be found in Sec. 4.4.2.

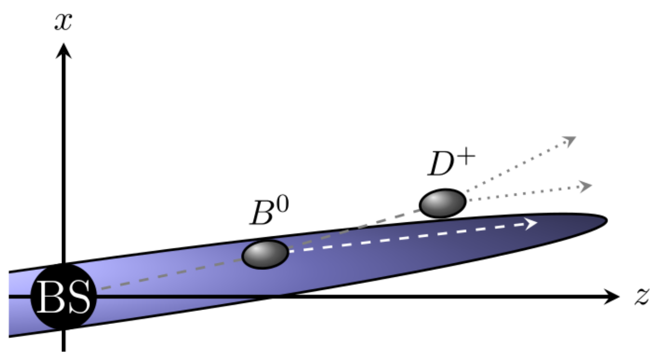

Figure 3.8: Schematic view of the tag-side B decay vertex in zx plane. A ellipsoid region centered around the beam-spot (BS) along the boost direction is defined. While B^0 decays more likely inside this region, decay vertices outside this region are more likely to be D mesons (here, D^+). [20]

3.3.5 Flavor Tagging

As already introduced, at Belle II the B mesons are produced in pairs, in our case $B^0\overline{B}^0$. After one B is fully reconstructed in the signal channel (signal side) the remaining reconstructed tracks and neutral ECL and KLM clusters belong to the other B meson on the so-called tag-side. Especially, in measurements involving CP-violation and B meson mixing require the determination of the B_{tag}'s flavor as this consequently dictates the flavor of B_{sig} at the time of B_{tag}'s decay. The procedure is done using so called flavor tagging algorithms, short - *Flavor Taggers.*
To determine the flavor of a decaying B meson, one can resort to so-called flavor-specific decays, e.g. $B^0 \to D^- l^+ \nu_l$. These types of decays result in a final state, which can exclusively be reached from a specific B^0 state[1]. However, due to the huge amount of possible flavor-specific modes, full reconstruction for many of them are dubbed unfeasible. Thus, the flavor tagger resorts to sophisticated inclusive techniques to exploit information provided by signatures in flavor-specific decays.
Already at Belle and BaBar experiments different flavor taggers have been developed. For the more challenging experimental environment of Belle II new flavor taggers had to be developed, while lessons from previous work have been incorporated.

[1]This is true to a good approximation. The effect of Tag-Side interference is caused by doubly CKM-suppressed amplitude contributions which are considered as systematic uncertainty. See section 2.3.2 for more.

Flavor Tagging Parameters

To quantify the flavor tagger some variables which will later be included in the observable PDF are introduced here. Firstly, the efficiency needs to be quantified, which is defined as the ratio between the number of events where the flavor tagger (N^{tag}) can assign a flavor to over all events (N):

$$\varepsilon = \frac{N^{\text{tag}}}{N}. \tag{3.4}$$

The case of the tag decision to be wrong is expressed by the fraction w, that can be used to express the number of tag-side B^0 mesons:

$$N^{\text{tag}}_{B^0} = \varepsilon(1-w)N_{B^0} + \varepsilon w N_{\overline{B}_0}, \tag{3.5}$$

$$N^{\text{tag}}_{\overline{B}^0} = \varepsilon(1-w)N_{\overline{B}^0} + \varepsilon w N_{B_0}. \tag{3.6}$$

Consequently, the observed asymmetry in CP-violation can be defined in terms of eqs. 3.5 and 3.6

$$a^{\text{obs}}_{CP} = \frac{N^{\text{tag}}_{B^0} - N^{\text{tag}}_{\overline{B}^0}}{N^{\text{tag}}_{B^0} + N^{\text{tag}}_{\overline{B}^0}} = (1-2w)\frac{N_{B^0} - N_{\overline{B}^0}}{N_{B^0} + N_{\overline{B}^0}}.. \tag{3.7}$$

The statistical uncertainty for this value is given by

$$\delta a_{CP} = \frac{\delta a^{\text{obs}}_{CP}}{1-2w} \overset{N^{\text{tag}}_{B^0} \approx N^{\text{tag}}_{\overline{B}^0}}{=} \frac{1}{\sqrt{N^{\text{tag}}}(1-2w)}. \tag{3.8}$$

Here the asymmetry is diluted by the term $(1-2w)$ which is the so-called dilution factor

$$r \equiv |1-2w|, \tag{3.9}$$

where $r = 0$ means no flavor information, hence $w = 0.5$, and $r = 1$ means a tag with full certainty, hence $w = 0, 1$. Now, substitute the denominator by introducing N^{eff}, the effective number of tagged events. With this quantity, Eq. 3.8 becomes

$$\delta a_{CP} = \frac{1}{\sqrt{N^{\text{eff}}}} = \frac{1}{\sqrt{\varepsilon_{\text{eff}} \cdot N}}, \tag{3.10}$$

where ε_{eff} is the effective tagging efficiency, defined as

$$\varepsilon_{\text{eff}} = \varepsilon \cdot r^2. \tag{3.11}$$

Above relations show that maximizing the effective efficiency results in a minimization of statistical uncertainty. Therefore, in CP-violation analyses the fits are performed in bins of the dilution factor r. The strength of flavor discrimination is maximal for r close to 1. This method is also applied when calibrating the flavor tagger. [25] The r-bins intervals are chosen to be

$$[0.000, 0.100, 0.250, 0.450, 0.600, 0.725, 0.875, 1.000]. \tag{3.12}$$

In the final step, the fact that a possible deviation arises for both w and ε when $q = \pm 1$ has to be considered. This is caused by the detector's charge-asymmetric performance. Thus, Eq. 3.4 and w are extended to

$$\varepsilon = \frac{\varepsilon_{B^0} + \varepsilon_{\overline{B}^0}}{2}, \quad w = \frac{w_{B^0} + w_{\overline{B}^0}}{2}, \tag{3.13}$$

where w_{B^0} is the fraction of true B^0 wrongly tagged as $\overline{B}^0$. The differences read

$$\Delta\varepsilon = \varepsilon_{B^0} - \varepsilon_{\overline{B}^0}, \quad \Delta w = w_{B^0} - w_{\overline{B}^0}. \tag{3.14}$$

To account for the charge-asymmetry the r-bins are multiplied by $q = \pm 1$.

4 Analysis Strategy

This chapter is divided into three parts. First, the physics model introduced in the theory chapter's Sec. 2.5 is reevaluated in terms of detector, kinematic and reconstruction effects. This step is crucial to get from the purely physics model to the real observable model. In the second part the analysis strategy is presented, which includes the choice of the decay modes, their reconstruction and the applied selection. Here, the methods presented Chapter 3 are used. Finally, a naive Signal MC validation is presented. Aim of this chapter is, to get the proper observable model and the reconstructed Signal MC data, so studies on quantum entanglement can be performed later.

4.1 Observable PDF

Thus far, when discussing the shape of disentanglement models' PDF only pure physics has been considered. To get from theoretical prediction to measurable quantities under real conditions, one has to take imperfect knowledge about the flavor of B_{tag}, detector response and kinematic smearing into account. The detector effects are modeled by the *Resolution Function* $\mathcal{R}(\delta\Delta t, \sigma_{\Delta t})$ which is a distribution of residuals $\delta\Delta t = \Delta t - \Delta t^{\mathrm{MC}}$, defined as the discrepancy between reconstructed and true decay time difference. The reason that $\Delta t \neq \Delta t^{\mathrm{MC}}$ is due to the combined uncertainty on the vertex position as well as tracks coming from intermediate charm decays on tag-side. In addition, all other inefficiencies have to be accounted for, which will be done first by incorporating flavor tagger parameters defined in Sec. 3.3.5.

4.1.1 Flavor Tagger parameters in the PDF

Before moving on to the resolution function and its impact on the observable PDF, Flavor Tagger parameters have to be included in the models' PDFs, following the approach of Ref. [25]. The flavor tagging parameters defined in Sec. 3.3.5 included for the SD as well as the PSD Δt distributions in Eqs. 2.61 and 2.65 give

$$\begin{aligned} P^{\text{obs}}_{SD}(\Delta t; q_{\text{sig}}, q_{\text{tag}}) =& \frac{\varepsilon}{8} \cdot e^{-\Gamma\Delta t} \cdot [2 \cdot (1 - q_{\text{tag}}\Delta w + q_{\text{tag}}\mu(1-2w)) \\ & - [q_{\text{tag}} \cdot (1-2w) + \mu \cdot (1 - q_{\text{tag}}\Delta w)] \cdot q_{\text{sig}} \\ & \times [f_{cos} \cos \Delta m \Delta t + f_{sin} \sin \Delta m |\Delta t|], \end{aligned} \tag{4.1}$$

where $\mu = \Delta\varepsilon/(2\varepsilon)$, and q_{tag} and q_{sig} are the flavor of the tag-side and signal-side B meson, respectively. The prefactors of trigonometric functions f_{cos} and f_{sin} follow the definition in Eq. 2.61. Finally, the Δt distribution for PSD in Eq. 2.65 can be extended the exact same way as in Eq. 4.1, with the only difference in the prefactors f_{cos} and f_{sin} depending on ζ.

4.1.2 Resolution function

Proceeding with inclusion of the detector response, the resolution function is presented here. The choice of the resolution function's nominal parametrisation follows the approach in Ref. [44]. An alternative parametrisation, namely the BaBar shape has been also investigated [44]. Though it requires fewer parameters that can be left to float in the fit, it has been shown to be less accurate and introduces a small bias to mixing parameter Δm_d.

The nominal resolution function parametrisation is defined as sum of a core and outlier (OL) part

$$R(\delta\Delta t; \sigma_{\Delta t}) = (1 - f_{\text{OL}}) R_{\text{core}}(\delta\Delta t; \sigma_{\Delta t}) + f_{\text{OL}} R_{\text{OL}}(\delta\Delta t; \sigma_{\Delta t}), \tag{4.2}$$

with f_{OL} the fraction of outlier events. Moreover, $R_{\text{core}}(\delta\Delta t; \sigma_{\Delta t})$ is the sum of two single Gaussians $G(x; \mu; \sigma)$ and a Gaussian convoluted with the right- and left-side exponential tail $\exp_{\pm}(x)$, with $x > 0$ or $x < 0$:

$$\begin{aligned} R_{\text{core}}(\delta\Delta t; \sigma_{\Delta t}) =& (1 - f_{\text{tail}}) \cdot G(\delta\Delta t; \mu_{\text{main}} \cdot \sigma_{\Delta t}, s_{\text{main}} \cdot \sigma_{\Delta t}) \\ & + f_{\text{tail}}(1 - f_{\text{exp}}) \cdot G(\delta\Delta t; \mu_{\text{tail}} \cdot \sigma_{\Delta t}, s_{\text{tail}} \cdot \sigma_{\Delta t}) \\ & + f_{\text{tail}} \cdot f_{\text{exp}} \cdot G(\delta\Delta t; \mu_{\text{tail}} \cdot \sigma_{\Delta t}, s_{\text{tail}} \cdot \sigma_{\Delta t}) \\ & \otimes ((1 - f_{\text{R}})\exp_{\text{L}}(\delta\Delta t/c \cdot \sigma_{\Delta t}) + f_{\text{R}}\exp_{\text{R}}(-\delta\Delta t/c \cdot \sigma_{\Delta t})) \end{aligned} \tag{4.3}$$

where $\sigma_{\Delta t}$ is the vertex fit uncertainty on Δt. The indices *main* and *tail* describe the mean and width of the tight (main) and wide (tail) Gaussian, respectively, while the constant c models the length of exponential tails. The three parameters f_{exp}, f_{tail} and f_{R} account for the fractions of events belonging to either exponential part, tail part (both, Gaussian and exponential tail) or right exponential tail. Due to small tail contributions at small $\sigma_{\Delta t}$, f_{tail} is defined as a function of $\sigma_{\Delta t}$ [44]

$$f_{\mathrm{tail}}(\sigma) = f_{\mathrm{max}} \cdot \mathrm{erf}(\sigma, \mu = f_{\mu}), \tag{4.4}$$

where erf is the error function, which guarantees a smooth transition between small and large tail fractions for $\sigma_{\Delta t}$. Conversely, the OL part of Eq. 4.2 is defined as a single Gaussian with its mean at the origin and dependence on $\sigma_{\Delta t}$ [44]

$$R_{\mathrm{OL}}(\delta\Delta t; \sigma) = G(\delta\Delta t, 0, \sigma_{\mathrm{OL}}). \tag{4.5}$$

The analytical convolution of the resolution function with the physics PDF from Secs. 2.5.1 and 2.5.2 is a crucial step to obtain the observed PDF. A general derivation of such convolution is shown in Appendix A.3. Finally, the kinematic approximation can be included to the PDF to get the full observed PDF.

4.1.3 Kinematic approximation

Moving on to the so-called kinematic approximation. Its inclusion is a crucial step towards obtaining the full observed PDF. The goal of the kinematic approximation is to bridge the difference between the true decay time difference $\Delta\tau$ in center-of-mass system (CMS) and the measured decay time difference Δt in lab frame [44]. This is achieved by considering $B^0\overline{B}^0$ system's motion in the CMS with respect to the boost direction. For different angles with respect to the boost direction the measured decay time difference experiences an asymmetry which has to be accounted for.

This effect is illustrated schematically in Fig. 4.1, where the B mesons' motion in CMS is shown schematically on the left. The mesons decay back-to-back both moving with the same angle θ^* with respect to the boost direction. Right plot shows the same flavor Δt^{MC}-distribution for different $\theta = 45°, 90°$ and $135°$ in orange, blue and green, respectively. The colors in both figures correspond to each other. For this plot all detector and imperfections regarding the flavor tagging process are still not included. Here, a sizable difference can be seen for different θ in regard to the Δt^{MC}-distribution. Though, the symmetry is conserved when $\theta = 90°$, asymmetry arises for $\theta = 45°$ and $135°$.

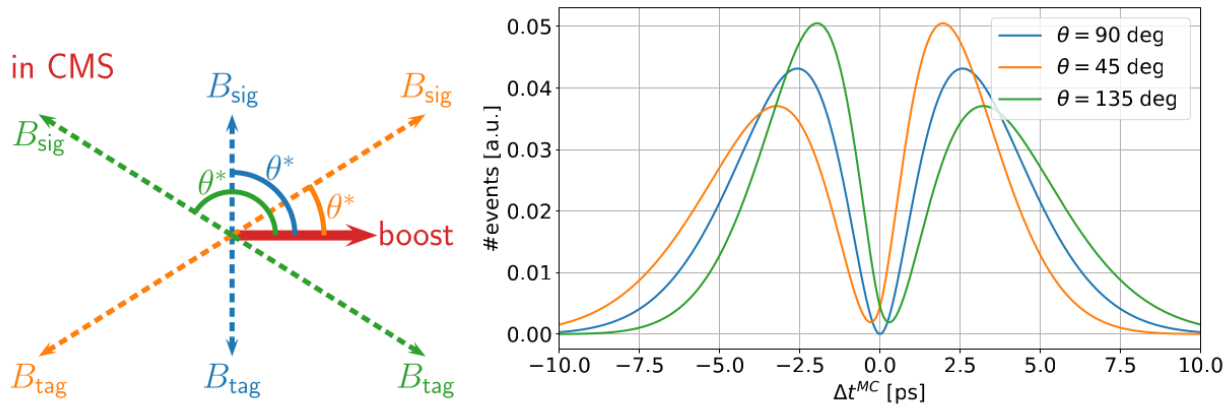

Figure 4.1: The sketch on the left shows the B_{sig} and B_{tag} for three different cases of θ^* in the center-of-mass system (CMS). The red arrow shows the direction of the boost. B_{sig} and B_{tag} decay back-to-back with θ^* with respect to the boost direction. Right plot shows the Δt^{MC} distribution for $\theta = 45°, 90°$ and $135°$ in orange, blue and green, respectively. The colors in both figures correspond to each other. [44]

Key parameters for this process are:

- $\Delta\tau \in (-\Sigma\tau, \Sigma\tau)$, the true decay time difference between B_{tag} and B_{sig} defined as $\Delta\tau = \tau_{\text{sig}} - \tau_{\text{tag}}$,
- $\Sigma\tau \in (0, +\infty)$, the sum of the true decay time of B_{tag} and B_{sig},
- $\cos\theta = \cos\theta^* \in (-1, 1)$, the cosine of the polar angle of B_{sig} with respect to $\Upsilon(4S)$'s boost direction in $\Upsilon(4S)$'s rest frame.

This set of three parameters describe the $B^0\overline{B}^0$ system for rotational invariance along azimuthal angle ϕ in the detector while neglecting detector effects. The PDF can be constructed using these parameters, resulting in

$$\frac{\mathrm{d}p}{\mathrm{d}\cos\theta \mathrm{d}\Delta\tau \mathrm{d}\Sigma\tau} = \frac{\mathrm{d}p_\tau}{\mathrm{d}\Delta\tau \mathrm{d}\Sigma\tau}\frac{\mathrm{d}p_\theta}{\mathrm{d}\cos\theta}, \tag{4.6}$$

where p_θ is the momentum along the θ direction. The differential term is defined as a function only of θ:

$$\frac{\mathrm{d}p_\theta}{\mathrm{d}\cos\theta} = \frac{3}{4}(1 - \cos^2\theta). \tag{4.7}$$

The term containing the momentum's boost direction component p_τ for neutral B mesons can be expressed as

$$\frac{\mathrm{d}p_\tau}{\mathrm{d}\Delta\tau \mathrm{d}\Sigma\tau} = \frac{e^{-\Sigma\tau/\tau}}{2\tau^2}(1 - \cos\Delta m\Delta\tau). \tag{4.8}$$

Next, the step from the true decay time difference $\Delta\tau$ to the measured Δt^{MC} is taken, so the set of parameters undergo the variable change of

$$\Delta\tau, \Sigma\tau, \cos\theta \to \Delta t^{\mathrm{MC}}, \Sigma\tau, \cos\theta. \tag{4.9}$$

The measured decay time difference can be defined as

$$\Delta t^{\mathrm{MC}} = \frac{\Delta z}{c\beta\gamma\gamma_B}, \tag{4.10}$$

where $\beta\gamma \approx 0.29$ the $\Upsilon(4S)$'s boost, $\gamma_B \approx 1.002$ the gamma factor of B in boosted frame [20]. Furthermore, Eq. 4.10 can be expressed in terms of the true decay time difference

$$\Delta t^{\mathrm{MC}} = \Delta\tau + K\Sigma\tau\cos\theta, \tag{4.11}$$

where $K \approx 0.225$ is a beam energy dependent constant defined as $K = \beta_B/\beta$ [20]. In terms of this parameter K, the interval in which Δt^{MC} is defined is now $-\Sigma\tau(1 - K\cos\theta) < \Delta t^{\mathrm{MC}} < +\Sigma\tau(1 + K\cos\theta)$. The PDF from Eq. 4.6 after change of variables now reads:

$$\frac{\mathrm{d}p}{\mathrm{d}\cos\theta \mathrm{d}\Delta t^{\mathrm{MC}}\mathrm{d}\Sigma\tau}(\Delta t^{\mathrm{MC}}, \Sigma\tau, \cos\theta) = \frac{\mathrm{d}p_\tau}{\mathrm{d}\Delta\tau\mathrm{d}\Sigma\tau}(\Delta t(\Delta t^{\mathrm{MC}}, \Sigma\tau, \cos\theta), \Sigma\tau, \cos\theta). \tag{4.12}$$

On the right hand side of Eq. 4.12, the PDF is expressed in terms of the observed decay time difference Δt, accessible by the Resolution Function defined in previous Sec. 4.1.2.

Before the final PDF can be written down, the parameters $\Sigma\tau$ and $\cos\theta$ have to be integrated out. Latter is averaged by an integral in range $(-1, 1)$, while $\Sigma\tau$'s integral covers the range between $\left[\frac{|\Delta t^{\mathrm{MC}}}{1+K\mathrm{sign}(\Delta t^{\mathrm{MC}})\cos\theta}, +\infty\right)$. The resulting function is called the *marginalised PDF*. Lastly, the resolution function $\mathcal{R}(\Delta t - \Delta t^{\mathrm{MC}})$ from Eq. 4.2 is included. The PDF now reads

$$\begin{aligned} P_{\mathrm{obs}}(\Delta t, \sigma_{\Delta t}) &= \int_{-1}^{1} \mathrm{d}\cos\theta \frac{\mathrm{d}p_\theta}{\mathrm{d}\cos\theta} \int_{-\infty}^{+\infty} \mathrm{d}\Delta t^{\mathrm{MC}} \int_{\frac{|\Delta t^{\mathrm{MC}}|}{1+K\mathrm{sign}(\Delta t^{\mathrm{MC}})\cos\theta}}^{+\infty} \mathrm{d}\Sigma\tau \frac{\mathrm{d}p_\tau}{\mathrm{d}\Delta t^{\mathrm{MC}}\mathrm{d}\Sigma\tau}\mathcal{R}(\delta\Delta t) && (4.13) \\ &= T\left[P_{\mathrm{phys}}(\Delta t^{\mathrm{MC}}) \otimes \mathcal{R}(\delta\Delta t, \sigma_{\Delta t})\right], && (4.14) \end{aligned}$$

where first row is the explicit form and the second row the general form with T the operator for the kinematic approximation.

4.1.4 Tag-Side Interference as background of Disentanglement Effects

The TSI effect presented in Sec. 2.3.2 which is, as the name suggest an effect on the tag side, is now relevant for this analysis as the signal channel $B^0 \to D^{(*)-}\pi^+$ suffers from it as well. On the signal-side however, TSI in $B^0 \to D^{(*)-}\pi^+$ decays introduces a term $\propto \sin\Delta m\Delta t$ which acts as a background for disentanglement effects. In principle, the two effects can be distinguished, as shown in a recent study [45]. However, this needs to be tested thoroughly for the specific case of the conditions presented here. For this, an important study will be so-called Pure Toy Monte Carlo studies, where data sets are sampled directly from the model PDFs. That way, different TSI sizes can be tested in a clean environment to predict systematic impacts on mixing studies. In the scope of this thesis, such study has not been performed. Certainly, it has to be included in later studies of systematic uncertainties as an effect on the tag side, if decided against (semi)lepton-tag condition.

4.2 Likelihood Function and Fit Method

To extract physical parameters from the observed Δt distribution, a likelihood-based fitting approach is adopted. The likelihood function $\mathcal{L}(\vec{\theta}; x)$ is defined as a function of a set of parameters $\vec{\theta}$. To retrieve the model that describes the data best, a set of parameters is found that maximizes this likelihood function. In practice, it is numerically more favorable to minimize the negative logarithm of $\mathcal{L}$ instead of maximizing it due to numerical instabilities when multiplying small numbers. Additionally, the computation of derivatives of a sum is simpler than that of a product. Thus, the function minimized for a data set of N events with single event observables x_i (e.g., Δt, tag information), the extended unbinned negative log-likelihood (NLL) is defined as

$$\mathcal{L} = -\sum_{i}^{n} \ln(f(\theta|x_i)), \tag{4.15}$$

where $f(\theta|x_i)$ is the probability density function evaluated at event x_i and parameter θ [46]. In this analysis, the Δt PDF is built from a physics model combined with resolution function, flavor tagging and kinematic effects, presented prior to this section.

In practice, the PDF is constructed using `zfit` [46], a python-based model fitting library based on `TensorFlow` [47]. Here, the unbinned extended negative log-likelihood (NLL) is employed to avoid discretization effects from binning, while simultaneously accounting for both the shape of the Δt distribution and the expected event yield via the extended term. The fit itself is performed using a numerical minimization of the extended unbinned negative log-likelihood using the `Minuit` algorithm implemented within the `iminuit` library [48]. This approach combines the numerical stability of `Minuit` with the flexibility and speed of TensorFlow-backed PDF evaluation.

4.3 Selected decay modes

In this analysis, hadronic decay modes of the neutral B mesons, namely $B^0 \to D^-\pi^+$ and $B^0 \to D^{*-}\pi^+$ are used. The branching fractions for these decays are given by [13]

$$BF(B^0 \to D^-\pi^+) = (2.51 \pm 0.08) \cdot 10^{-3}, \tag{4.16}$$

$$BF(B^0 \to D^{*-}\pi^+) = (2.66 \pm 0.07) \cdot 10^{-3}. \tag{4.17}$$

The signal B is reconstructed in one of four channels:

$$B^0 \to D^-\pi^+$$
$$\quad \hookrightarrow K^+\pi^-\pi^-$$

$$B^0 \to D^{*-}\pi^+$$
$$\quad \hookrightarrow D^0\pi_s^-$$
$$\qquad \hookrightarrow K^-\pi^+\pi^0$$
$$\qquad \hookrightarrow K^-\pi^+\pi^0$$
$$\qquad \hookrightarrow K^-\pi^+\pi^-\pi^+$$

and charge conjugated modes. The subscript in π_s^- denotes so-called *slow* pions. Subsequent decays of the D^- and D^*- which result in a neutral kaon are not included, as reconstruction efficiencies are worse, while not increasing the statistics significantly [44]. In the Signal MC, the relative branching fractions are adjusted to be the same, i.e. B^0 decays 25% of the times in $B^0 \to D^-\pi^+$ and 75% in $B^0 \to D^{*-}\pi^+$. The three subsequent decay modes of D^{*-} are each accounted for with a 1/3 ratio, ensuring the same number of events for each mode. Although this does not represent the reality as $B^0 \to D^{*-}\pi^+$ and $B^0 \to D^-\pi^+$ have about the same size of branching fractions, this is justified since there are no significant differences in these distinct channels in relevant observables [44].

Tab. 4.1 shows the signal efficiencies for each of the four reconstructed channels. Since there were two Signal MC samples generated for entangled and disentangled case, the efficiencies are calculated individually and denoted by subscript QM and SD, respectively. Column *Cut* are divided into *Reconstruction, Selection* and Δt *fit quality cuts*. Prior refers to all cuts during reconstruction and later preselection cuts, as well as final cuts. Δt fit quality cuts refer to criteria applied after the tuple processing.

The total signal efficiency is the best for $B^0 \to D^-\pi^+$, followed by $B^0 \to D^{*-}[\overline{D}^0\pi_s^-]\pi^+$ with $\bar{D}^0 \to K^+\pi^-$, then $\bar{D}^0 \to K^+\pi^-\pi^+\pi^-$, and finally $\bar{D}^0 \to K^+\pi^-\pi^0$, as efficiency scales with number of tracks and clusters to reconstruct. The efficiency is lower for channels including D^{*-} as it contains slow pions (π_s) which do not reach the CDC, thus has lower efficiency itself [49]. In addition, $B^0 \to D^{*-}\pi^+$ with $\bar{D}^0 \to K^+\pi^-\pi^0$ channel's low efficiency is caused by clusters from photons in $\pi^0 \to \gamma\gamma$.

Cut	ε^{sig} [%]
$B^0 \to D^-\pi^+$ **with** $D^- \to K^+\pi^-\pi^-$	
Reconstruction, Selection	45.0
Δt fit quality cuts	89.5
Total	40.2
$B^0 \to D^{*-}\pi^+$ **with** $\bar{D}^0 \to K^+\pi^-$	
Reconstruction, Selection	42.7
Δt fit quality cuts	89.6
Total	37.2
$B^0 \to D^{*-}\pi^+$ **with** $\bar{D}^0 \to K^+\pi^-\pi^0$	
Reconstruction, Selection	16.8
Δt fit quality cuts	90.1
Total	14.5
$B^0 \to D^{*-}\pi^+$ **with** $\bar{D}^0 \to K^+\pi^-\pi^+\pi^-$	
Reconstruction, Selection	31.5
Δt fit quality cuts	89.7
Total	28.7

Table 4.1: Signal Efficiencies ε^{sig} for the four reconstructed channels.

4.4 Event Reconstruction and Selection

In this section the reconstruction process and selection requirements are discussed. The reconstruction of the decay modes $B^0 \to D^{(*)-}\pi^+$ involves multiple steps. The reconstruction process has two main goals: fully reconstruct the signal channel which defines the B_{sig} and find the flavor of the other B_{tag} using a flavor tagger (see Sec. 3.3.5).

4.4.1 B_{sig} reconstruction

The first step of the signal-side event reconstruction is to find D^- and $\bar{D}^0$ meson candidates. This is done combining charged tracks which satisfy specific criteria to ensure they originate from the interaction point:

- Tracks are required to have a polar angle θ within the acceptance of the CDC.
- Impact parameter cuts of $\mathrm{d}z < 3.0$ cm and $\mathrm{d}r < 0.5$ cm are applied.
- A loose kaon identification ($\mathrm{ID}_K > 0.01$) is imposed on the kaon track.

In cases where the decay channel includes π^0, candidates are reconstructed in $\pi^0 \to \gamma\gamma$. There, candidates are formed from ECL clusters not associated with any tracks and several conditions predefined in lists e.g. `eff30_Jan2020`, `eff40_Jan2020` etc. Subsequently, the D^0 or D^- candidate is required to have its invariant mass within a loose window $[1.810,\ 1.895]$ GeV centered asymmetrically around its nominal mass $m_{D^\pm} = (1869.5 \pm 0.4)$ MeV [13]. For D^- candidates, a slow pion (π_s^-) is added to the D^0 candidate. The D^- mass and Q-value, defined as $Q = M(D^{*-}) - M(D^0) - M(\pi^-)$, must satisfy preselection requirements of $Q \in [4.6,\ 7.0]$ MeV, which is centered around the known energy release. Finally, the B_{sig} candidate is formed by combining a $D^{(*)-}$ meson with a π^+ track. Loose selection criteria are applied to the beam-energy-constrained mass (M_{bc}) and the energy difference (ΔE), defined as [20]

$$M_{bc} = \sqrt{E^{*2}_{beam} - p_B^2}, \tag{4.18}$$

where E^{*2}_{beam} is the reconstructed beam energy in rest frame with $E^{*2}_{beam} = \sqrt{s}/2$ and p_B the momentum of reconstructed particle. Furthermore, the energy difference ΔE is defined as

$$\Delta E = E^*_B - E^*_{beam}. \tag{4.19}$$

In theory, correctly reconstructed B meson decays would have $\Delta E = 0$ and $M_{bc} = m_B$, with $m_B = (5279.63 \pm 0.20)$ MeV the invariant B meson mass [13]. Following selection cuts are centered around these nominal values.

- M_{bc} must fall within $5.2 < M_{\text{bc}} < 5.3$ GeV.

- $|\Delta E|$ is constrained to $[-0.10,\ 0.25]$ GeV GeV.

To enhance vertex resolution, a kinematic fit is performed on the B_{sig} decay chain, as explained in Sec. 3.3.4. This fit incorporates constraints from the interaction point and known particle masses, thereby refining the candidate selection.

4.4.2 Tag-side reconstruction

For each event that satisfies the preselection requirements, the remaining tracks and clusters are utilized to reconstruct the B_{tag} candidate. Specific criteria are applied on tag-side tracks:

- Tracks must have impact parameters within $\mathrm{d}z < 2.0$ cm and $\mathrm{d}r < 0.5$ cm.

- Tracks are required to have hits in all sub-detector components: PXD, SVD, and CDC.

- The momentum of each track must exceed 50 MeV/c to suppress contributions from beam backgrounds.

The vertex of the B_{tag} is determined using the vertex fitter `Rave`, which incorporates a beam spot constraint to improve the quality of the vertex fit. This constraint confines the B_{tag} vertex to a tube aligned with the B_{tag} momentum direction. For this, knowledge about the momentum direction from the fully reconstructed signal-side B_{sig} is used which decays back-to-back. These are incorporated to enhance the precision of the Δt measurement.

The decay time difference (Δt) in the lab frame is calculated as:

$$\Delta t = \frac{(z_{B_{\text{sig}}} - z_{B_{\text{tag}}})}{\beta\gamma c}, \tag{4.20}$$

where $z_{B_{\text{sig}}}$ and $z_{B_{\text{tag}}}$ are the reconstructed z-positions of the signal and tag-side vertices, and $\beta\gamma$ represents the Lorentz boost of the system.

To improve the resolution of Δt, the uncertainties in vertex positions are propagated through the covariance matrix obtained from the vertex fit. Events with poorly reconstructed vertices or large Δt uncertainties are excluded to maintain data quality.

Since this work is a Signal MC study further tighter cuts will not be necessary, as a clear signal can be extracted already from loose cuts. This will also help to avoid compromising the sample size.

4.5 First validations of the Signal MC sample

To validate the Signal MC sample generated by a novel `EvtGen` model developed for this analysis, the distributions of key kinematic and event selection variables are compared to their known expected shapes. This step is crucial to ensure that the simulated events accurately represent the physics of $B^0 \to D^{(*)-}\pi^+$ decays and their successful reconstruction and selection. Distributions of variables such as the beam-energy-constrained mass M_{bc}, the energy difference ΔE, the truth Monte Carlo decay time Δt^{MC}, and key flavor tagging parameter qr extracted from GFlaT algorithm are examined. The M_{bc} and ΔE distributions are expected to peak at their nominal values for correctly reconstructed signal events, which are 5.27 GeV/c^2 and $\Delta E = 0$ GeV, respectively. The Δt^{MC} distribution should follow the pure physics PDF's shape shown in Fig. 2.7 for full entanglement (left) and disentanglement (right). To confirm this, a simple fit without physical interpretation is shown for Δt distributions as well as for time-dependent asymmetries.

4.5.1 M_{bc} and ΔE distribution

Parameters M_{bc} and ΔE are crucial for determining the kinematics of a decay. These parameters allow for event selection, as expectations on their values allow for defining variable ranges. In case of ΔE and M_{bc} these value ranges are defined as above in Sec. 4.4.1. For analyses including background or even on data tighter cuts can be defined. The 2D-histogram in the following figures show the variable distribution of M_{bc} and ΔE for full entanglement and disentanglement.

The key takeaway from these Fig. 4.2 showing the M_{bc} and ΔE for full entanglement and disentanglement is that both 2D-histogram show similar shape and peak around the same values for both parameters. As expected, whether B_{tag} and B_{sig} are entangled or not, is a purely quantum mechanical property which does not alter the kinematics.

4.5.2 Flavor tagging parameters

To evaluate the performance of the flavor tagger the variable qr is considered. In the following, two histograms for this variable are shown for both Signal MC samples with full entanglement and disentanglement. Looking at these variables will be one of the validations of the Signal MC samples, since asymmetries between flavors $q_{\mathrm{tag}} = \pm 1$ and also any differences between full entangled sample and disentangled are easily detectable. Finally, Fig. 4.3 shows the qr histogram for full entangled and full disentangled Signal MC data set, respectively. The blue and red histogram show the distribution for $q_{\mathrm{tag}}^{\mathrm{MC}} = \pm 1$, respectively. The combined histogram is shown in black.

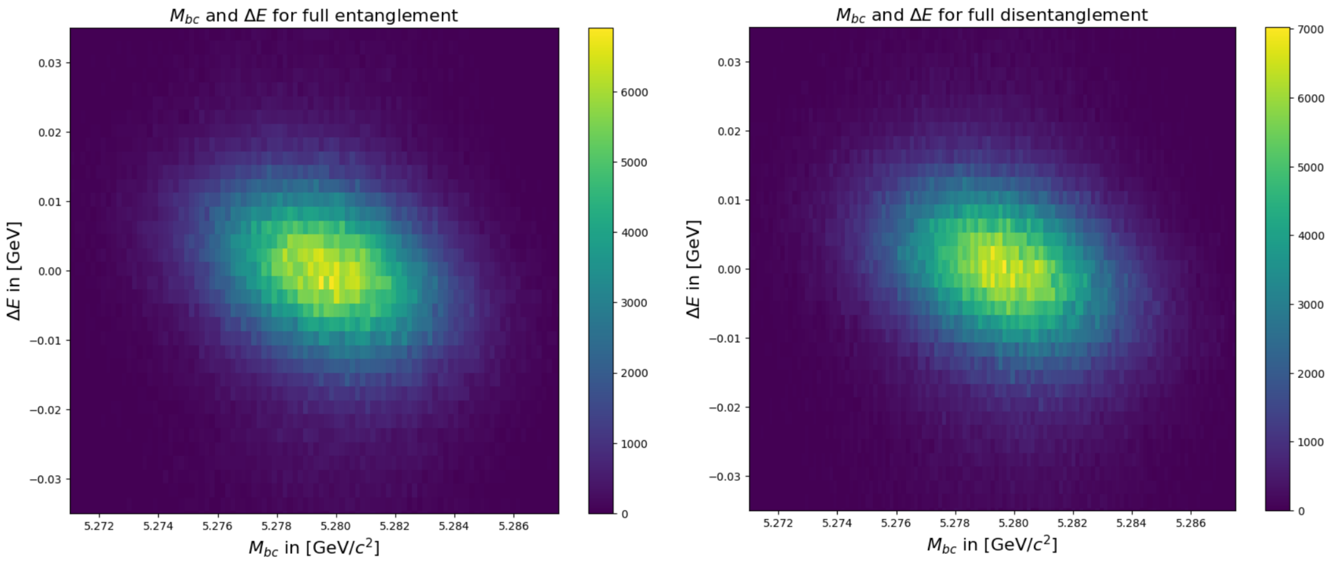

Figure 4.2: 2D-histogram for fully entangled (disentangled) Signal MC parameters M_{bc} and ΔE after loose cuts are applied on the left (right). An expected peak around 5.275 GeV $c^2 < M_{bc}$ < 5.284 GeV c^2 and $|\Delta E| < 0.02$ GeV can be seen.

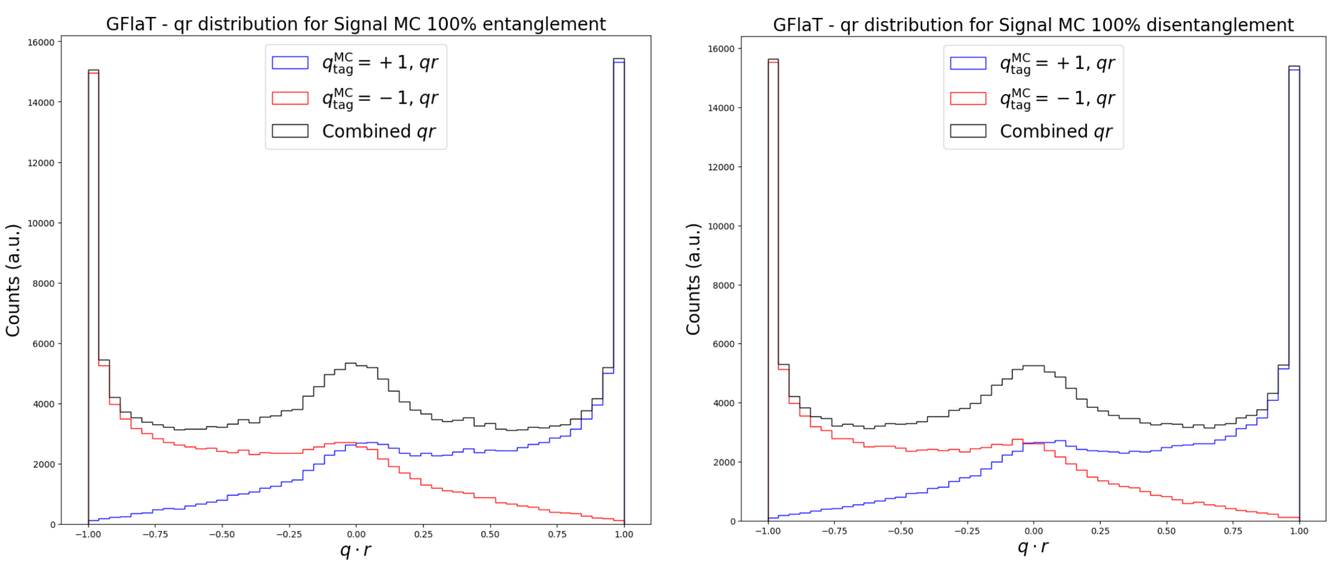

Figure 4.3: Histogram of the qr-distribution in fully disentangled Signal MC data set. Blue and red histograms show the distribution for $q_{\mathrm{tag}}^{\mathrm{MC}} = \pm 1$, respectively. Black histogram shows the combined values.

Both figures show the characteristic shapes of the $q \cdot r$ variables, also seen in Ref. [50], which presents the newly developed Flavor Tagging Algorithm applied in time-dependent CP Violation measurements. As expected, no significant deviation in shape for $q_{\text{tag}}^{\text{MC}}$ can be seen between the two data sets with full (dis)entanglement. Any deviation in that regard would be a hint for either wrong modeling on simulation level or reconstruction, as flavor tagging algorithms are independent of any disentanglement effects. Furthermore, there is a recognizable symmetry for both figures between $q_{\text{tag}}^{\text{MC}} = +1$ and $= -1$ (blue and red histogram). The histograms show a strong peak $|q \cdot r|$-values close to ± 1. This means the qr-bin in intervals 3.12 with highest purity is the most densely populated. For lower $|q \cdot r|$ the blue and red distributions becomes mostly flat until $q \cdot r = 0$. For $q_{\text{tag}}^{\text{MC}} = \pm 1$ and $q \cdot r < 0$ (> 0), drops off but is non-zero due to mistagged events.

4.5.3 Δt^{MC}-distributions

For the analysis at hand, the arguably most important variable is the reconstructed decay time difference Δt. Defined as the decay time difference B_{tag} and B_{sig} in the lab frame, the resulting Δt's distribution has been discussed in Sec. 2.5.1. For the PSD model, the distributions smoothly go from the shape on the left to the shape on the right in Fig. 2.7. The following figures show the Δt^{MC} distributions for the Signal MC data set for full entanglement and disentanglement.

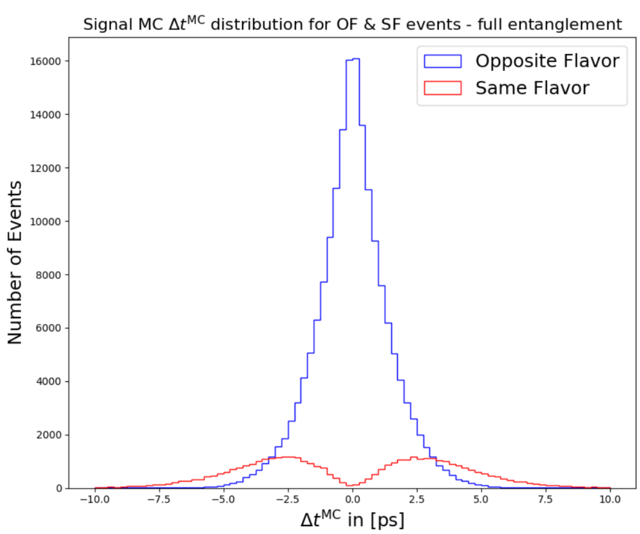

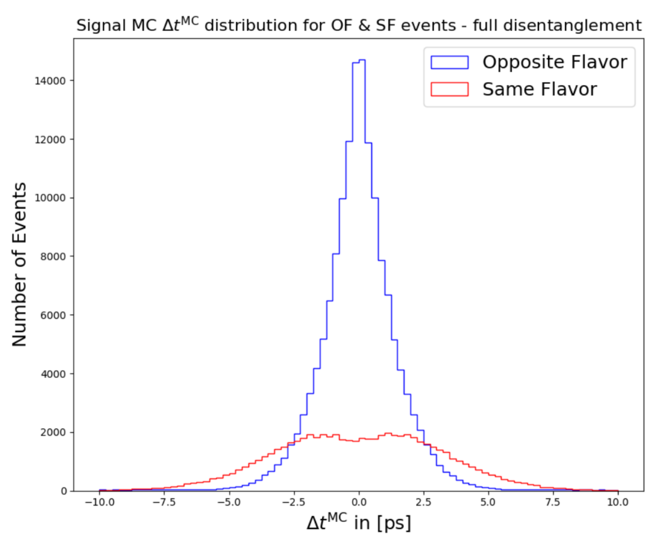

Figure 4.4: Signal MC Δt^{MC}-distribution for full (dis)entanglement on the left (right). Blue and red histograms show the Δt^{MC} for opposite and same flavor events. A difference in the entangled and disentangled case can be seen when looking at Same flavor events. This difference is expected, as already elaborated in Sec. 2.5.1.

Fig. 4.4 show the Δt^{MC} distribution for full entanglement (left) and disentanglement (right) for Opposite Flavor and Same Flavor events in blue and red, respectively. The x-axis shows Δt^{MC} in the range of -10 ps and $+10$ ps, the y-axis shows the number of events. The distributions of the Signal MC follow the expected shape shown in Fig. 2.7, thus are satisfactory. This behavior can be even further validated by laying the physics PDF from Eqs. 2.60 and 2.61 on the Signal MC data for OF and SF events. Additionally, the asymmetry from Eqs. 2.63 and 2.64 is plotted above the data points. Note that this is not a fit but a simple plot, thus do not allow for physical interpretation but the validation of prediction and simulated reconstructed data. Fig. 4.5 show the

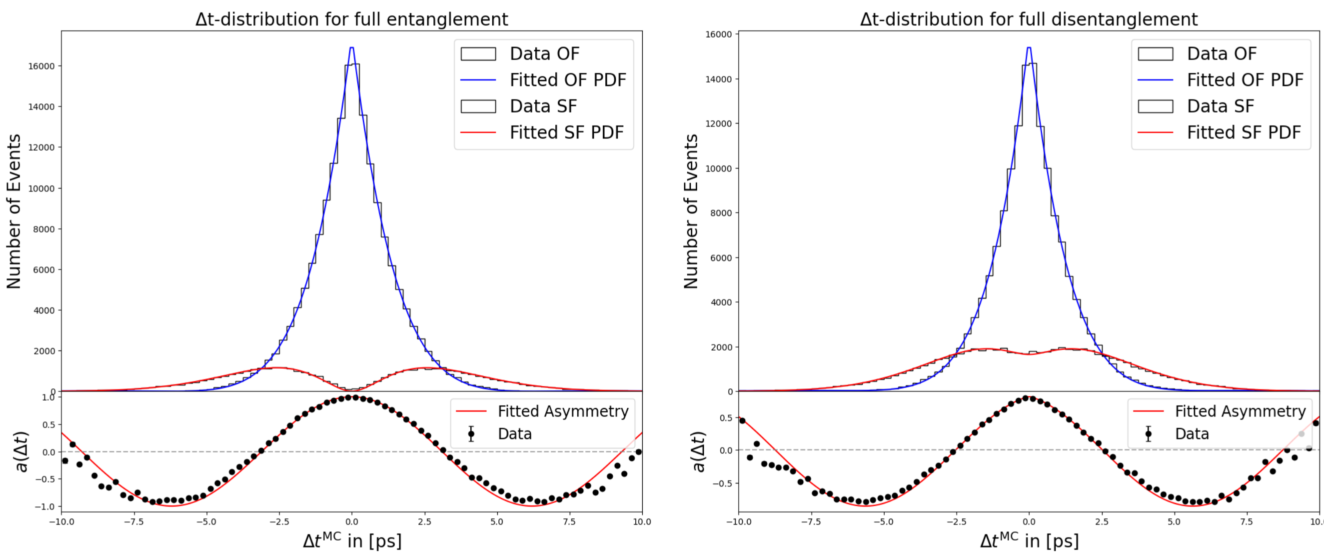

Figure 4.5: Figure on the left (right) shows the Signal MC Δt^{MC}-distribution (upper plot) and time-dependent asymmetry (bottom) for full entanglement (disentanglement). Δt^{MC}-distributions are shown for opposite and same flavor events. The solid lines show the fits of pure physics PDF from Eq. 2.60 (2.61) on the Signal MC data points to validate the parameter's distribution shape. A fit on the time-dependent asymmetry from Eq. 2.63 (2.64) is shown in the bottom plot as well.

fit of the Δt^{MC} distributions of Signal MC data as histograms for OF (blue) and SF events (red) in the upper plot. The lower plot shows the time-dependent asymmetry data points in black. Solid lines are simple plots of purely physical PDFs and asymmetries shapes. As a clear overlap of the plotted curves with the data points can be seen, this naive validation is concluded as successful.

5 Studies of Disentanglement Models on Signal MC

With the analysis framework established, finally the analysis and study of disentanglement effects on Signal MC can be performed. The main goal is to test a framework designed to study the effects and modeling of quantum disentanglement. This is done by fitting the observable Δt to get best fit estimates for parameter ζ, the fraction of PSD. As the PDF contains many variables including resolution function parameters an initial calibration of their values is needed. This is achieved by running so-called residual fits on the observable $\delta\Delta t$ presented in Sec. 5.1.2, before moving on to Δt fits. For Single Δt fits presented in Sec. 5.1.3, the physics parameter ζ is fitted together with resolution function parameters and flavor tagging parameters. In order to test the robustness of the fitter and the value extraction, subsequently a Toy Monte Carlo study is conducted, using two well established methods; the Pure Toy MC study and the Bootstrap method. Lastly, the question whether wrongly neglected small disentanglement effects introduce a bias on time-dependent measurements at Belle II is addressed.

5.1 Fits on Signal MC

The analysis presented in the main part is performed on Signal MC generated for full entanglement and disentanglement. As the real Belle II data size corresponds to an integrated luminosity $\int \mathcal{L}\mathrm{d}t \sim 500\ \mathrm{fb}^{-1}$, each Signal MC sample size is twice the real data's size with an integrated luminosity $\int \mathcal{L}\mathrm{d}t \sim 1\ \mathrm{ab}^{-1}$. The MC data sets with a fraction of disentanglement between 0 and 1, are sampled out of the two original data sets, so that the data sizes correspond to integrated luminosities shown in Tab. 5.1.

5.1.1 ΔE fits

ΔE is primarily influenced by the precision of the reconstructed final-state particles and the detector resolution. Signal events are expected to peak around zero due to energy conservation, whereas

Signal MC with ζ_{gen}	$\int \mathcal{L}\text{d}t$	N (`isSignal == 1`)
0.0	~ 1 ab^{-1}	$\sim 1.9 \cdot 10^5$
0.2	~ 1.2 ab^{-1}	$\sim 2.4 \cdot 10^5$
0.4	~ 1.7 ab^{-1}	$\sim 3.2 \cdot 10^5$
0.6	~ 1.7 ab^{-1}	$\sim 3.2 \cdot 10^5$
0.8	~ 1.2 ab^{-1}	$\sim 2.4 \cdot 10^5$
1.0	~ 1 ab^{-1}	$\sim 1.9 \cdot 10^5$

Table 5.1: Integrated luminosities and approximate number of events after applying condition `isSignal == 1` for Signal MC with fraction of disentanglement ζ_{gen}.

background contributions, particularly those from combinatorial and misreconstructed events, exhibit broader distributions not necessarily peaking around zero. The signal ΔE distribution is modeled by a sum of a Crystal Ball (CB) distribution with left and right tails and a Gaussian. The Crystal Ball function accounts for both asymmetric tails due to energy loss mechanisms and detector resolution effects. Both Gaussian and CB share a common mean but have distinct width parameters to accommodate asymmetry in the distribution. The gaussian distribution is defined already in Eq. A.15. The double-sided Crystal Ball function is defined as follows:

$$f_{\text{CB}}(x;\bar{x},\sigma,\alpha_L,n_L,\alpha_R,n_R) = N \begin{cases} A_L\left(B_L - \dfrac{x-\bar{x}}{\sigma}\right)^{-n_L}, \text{ for } \dfrac{x-\bar{x}}{\sigma} \leq -\alpha_L, \\ \exp\left(-\dfrac{(x-\bar{x})^2}{2\sigma^2}\right), \text{ for } -\alpha_L < \dfrac{x-\bar{x}}{\sigma} < \alpha_R, \\ A_R\left(B_R + \dfrac{x-\bar{x}}{\sigma}\right)^{-n_R}, \text{ for } \dfrac{x-\bar{x}}{\sigma} \geq \alpha_R. \end{cases} \tag{5.1}$$

where

$$A_i = \left(\frac{n}{|\alpha_i|}\right)^n \cdot \exp\left(-\frac{|\alpha_i|^2}{2}\right), \tag{5.2}$$

$$B_i = \frac{n}{|\alpha_i|} - |\alpha_i|, \tag{5.3}$$

with $i = L, R$. The normalization factor for region $-0.10 < \Delta E < 0.15$ GeV [25]:

$$N = \frac{1}{\sigma(C+D)}, \tag{5.4}$$

$$C = \frac{n}{|\alpha|} \cdot \frac{1}{n-1} \cdot \exp\left(-\frac{|\alpha|^2}{2}\right), \tag{5.5}$$

$$D = \sqrt{\frac{\pi}{2}}\left(1 + \text{erf}\left(\frac{|\alpha|^2}{\sqrt{2}}\right)\right). \tag{5.6}$$

The ΔE fit on Signal MC data sets with full entanglement and full disentanglement are shown in Figs. 5.1 and 5.3. Best fit parameters are listed in Table 5.2 and Table 5.3. Fit results for PSD fractions with 20%, 40%, 60% and 80% in the Signal MC can be found in Appendix B.1.

When looking at the shapes and also fit values for Gaussian mean and uncertainty for both full entanglement and disentanglement, no significant change in the kinematics can be observed. The mean values of the Gaussian converge the theoretical value of $\Delta E = 0$ with a precision in the $\mathcal{O}(10^{-5})$. This serves as a confirmation of the assumed invariance of kinematics, regardless of quantum entanglement in the $B^0\overline{B}^0$ system.

Parameter	Mean	Uncertainty
$n_{\Delta E}$	238994	488
$\mu_{\Delta E}$	$-7.8810 \cdot 10^{-5}$	$2.7030 \cdot 10^{-5}$
$\sigma_{\Delta E}$	$8.1893 \cdot 10^{-3}$	$9.0710 \cdot 10^{-3}$
σ_{Gauss}	0.0100	0.0001
f_{Gauss}	0.4314	0.0278
α_L	1.3100	0.0503
α_R	1.5371	0.0459
n_L	1.7759	0.0600
n_R	2.3702	0.0589

Table 5.2: ΔE fit parameters for Signal MC with full entanglement.

Parameter	Mean	Uncertainty
$n_{\Delta E}$	193314	439
$\mu_{\Delta E}$	$-11.8819 \cdot 10^{-5}$	$2.8848 \cdot 10^{-5}$
$\sigma_{\Delta E}$	$8.3116 \cdot 10^{-3}$	$8.2476 \cdot 10^{-3}$
σ_{Gauss}	0.0100	0.0002
f_{Gauss}	0.3496	0.0332
α_L	1.4169	0.04966
α_R	1.6539	0.0480
n_L	1.7283	0.0591
n_R	2.2642	0.0619

Table 5.3: ΔE fit parameters for Signal MC with full disentanglement.

5.1.2 $\delta\Delta t$ Residual Fits

Here, a fit to the Δt residuals $\delta\Delta t$ is performed. The decay time difference's sensitivity is limited by signal-side vertex resolution[1]. As the residual fit on $\delta\Delta t$ is independent of flavor and disentanglement effects this first fit is used to gauge the nuisance parameters needed for later studies. Thus, for all values of ζ_{gen}, no significant deviation in fit parameters are expected, besides statistical fluctuations. The fit to Eq. 4.2 is performed for all qr-bins, while parameters describing main, tail, and exponential parts are shared across qr-bins 0-5 and get a broader range for qr-bin 6. Parameter f_{OL} is shared across all qr-bins.

Figs. 5.1.2 and Figs. 5.1.2 show the shapes for residual fits, and Tab. 5.4 for all seven qr-bins for 0% and 100% PSD fraction in the Signal MC, respectively. Fits to Signal MC with $\zeta_{\text{gen}} = 0.2,\ 0.4,\ 0.6,\ 0.8$ can be found in Appendix B.2. The data points with error bars are

[1] In contrast, in the golden mode $B^0_{\text{sig}} \to J/\psi K^0_S$ the resolution is limited by the tag-side vertex resolution [20].

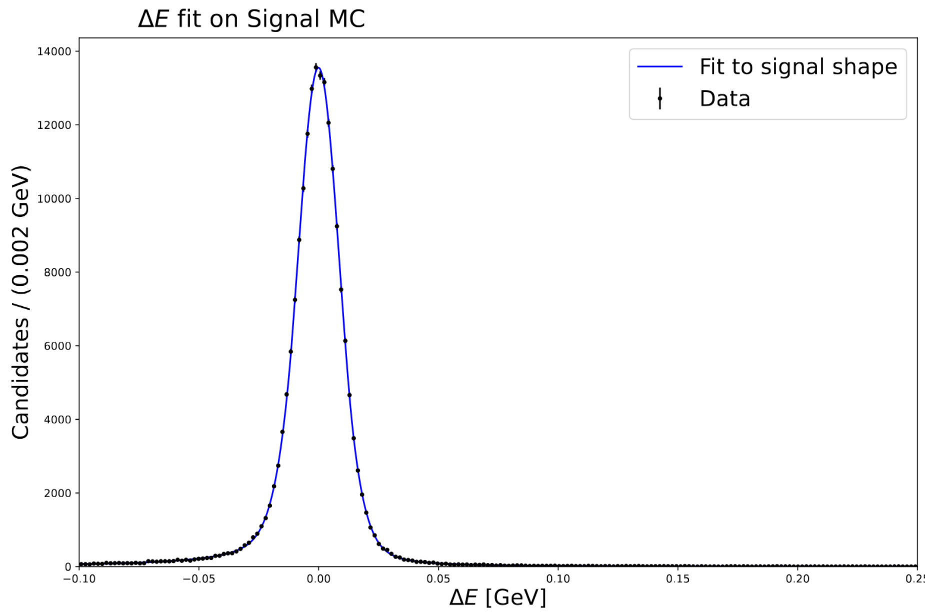

Figure 5.1: Fit to the ΔE distribution Signal MC events with full entanglement, using double-sided Crystal Ball shape.

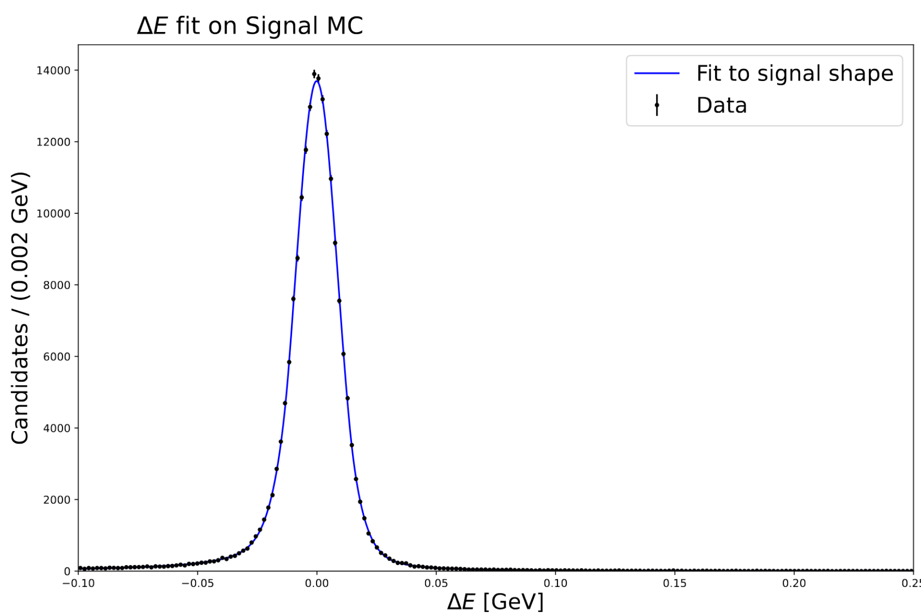

Figure 5.2: Fit to the ΔE distribution Signal MC events with full disentanglement, using double-sided Crystal Ball shape.

shown along with their fits to Eq. 4.2 in solid lines. The lower plots displaying the pulls show the discrepancies between data and fit.

The fits for all MC samples across all qr-bins look reasonable. When looking at the pulls no systematic under-/overshooting of data points visible. As expected, there are no significant deviations in the parameter values between different fractions of disentanglement.

Parameter	Fit estimate
f_{OL}	0.0014 ± 0.0001
μ_{Main}	-0.2395 ± 0.0071
μ_{Tail}	-0.9803 ± 0.0439
σ_{Main}	1.1950 ± 0.0087
σ_{Tail}	2.3456 ± 0.0524
f_{Tail}	0.2898 ± 0.0115
f_{exp}	0.2155 ± 0.0091
c_1 [ps^2]	5.0165 ± 0.1665
$f_{\mathrm{Tail,\ R}}$	0.2573 ± 0.0109
$f_{\mathrm{Tail},\mu}$	0.1916 ± 0.0048
$f_{\mathrm{Tail},\sigma}$	0.0625 ± 0.0059
$\mu^{(6)}_{\mathrm{Main}}$	-0.1804 ± 0.0111
$\mu^{(6)}_{\mathrm{Tail}}$	-0.8157 ± 0.0826
$\sigma^{(6)}_{\mathrm{Main}}$	1.2010 ± 0.0137
$\sigma^{(6)}_{\mathrm{Tail}}$	2.3343 ± 0.1081
$f^{(6)}_{\mathrm{Tail}}$	0.2445 ± 0.0202
$f^{(6)}_{\mathrm{exp}}$	0.2524 ± 0.0197
$c^{(6)}_1$ [ps^2]	5.0281 ± 0.2502
$f^{(6)}_{\mathrm{Tail,\ R}}$	0.2913 ± 0.0212

Parameter	Fit estimate
f_{OL}	0.0013 ± 0.0001
μ_{Main}	-0.2353 ± 0.0072
μ_{Tail}	-0.9737 ± 0.0449
σ_{Main}	1.1921 ± 0.0091
σ_{Tail}	2.3071 ± 0.0516
f_{Tail}	0.2970 ± 0.0121
f_{exp}	0.2199 ± 0.0090
c_1	4.9003 ± 0.1526
$f_{\mathrm{Tail,\ R}}$	0.2625 ± 0.0108
$f_{\mathrm{Tail},\mu}$	0.2003 ± 0.0034
$f_{\mathrm{Tail},\sigma}$	0.0504 ± 0.0043
$\mu^{(6)}_{\mathrm{Main}}$	-0.1816 ± 0.0095
$\mu^{(6)}_{\mathrm{Tail}}$	-0.6649 ± 0.0724
$\sigma^{(6)}_{\mathrm{Main}}$	1.1791 ± 0.0133
$\sigma^{(6)}_{\mathrm{Tail}}$	2.4075 ± 0.1025
$f^{(6)}_{\mathrm{Tail}}$	0.2487 ± 0.0187
$f^{(6)}_{\mathrm{exp}}$	0.2330 ± 0.0167
$c^{(6)}_1$	5.4704 ± 0.2626
$f^{(6)}_{\mathrm{Tail,\ R}}$	0.2095 ± 0.0181

Table 5.4: Parameters from $\delta\Delta t$ residual fit on Signal MC with full (dis)entanglement on the left (right). Superscript 6 represents the 6th qr-bin, which is fitted separately.

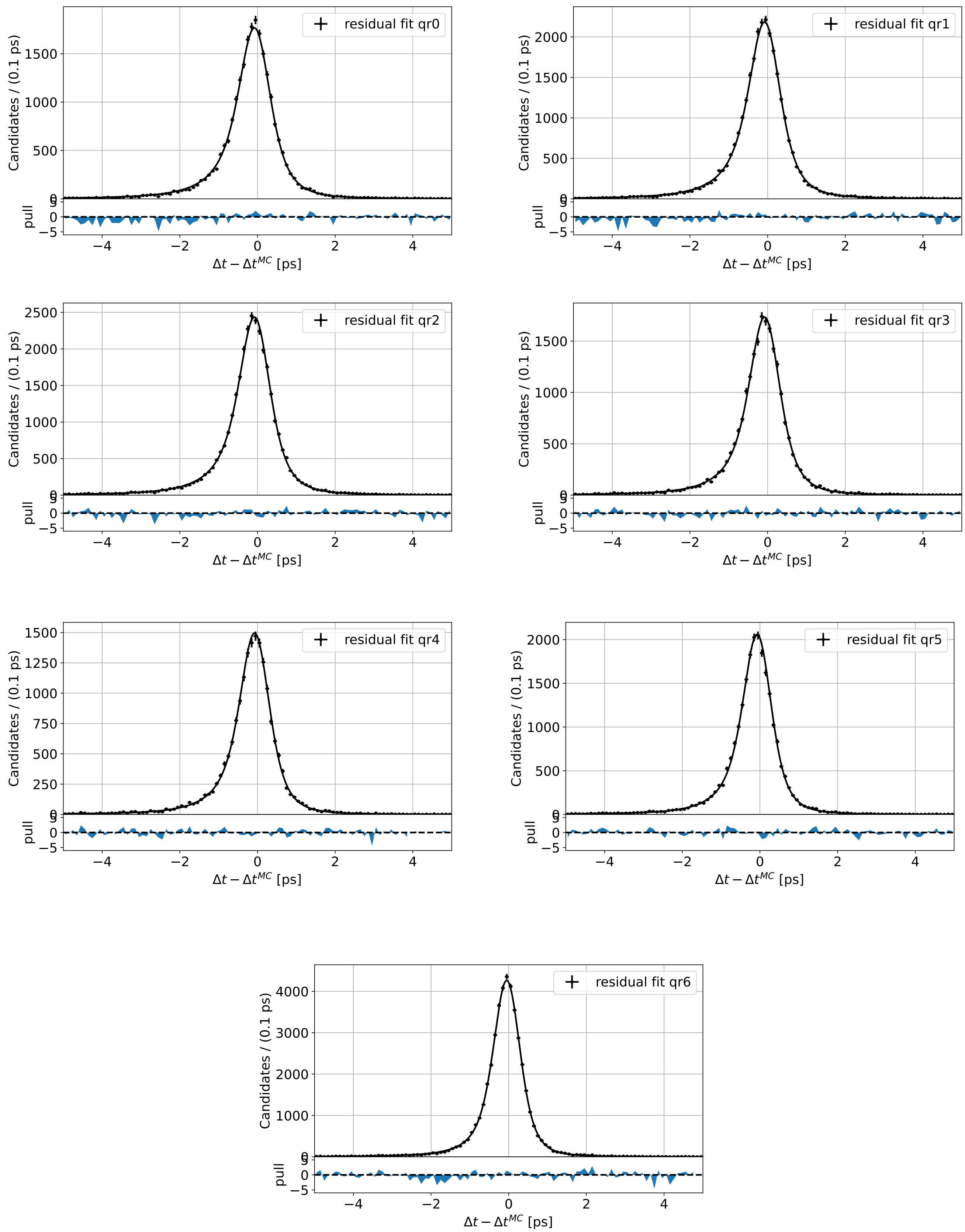

Figure 5.3: Residual fits for Signal MC with full entanglement. Single figures show the fits on different qr-bins 0-6 (left to right, top to bottom).

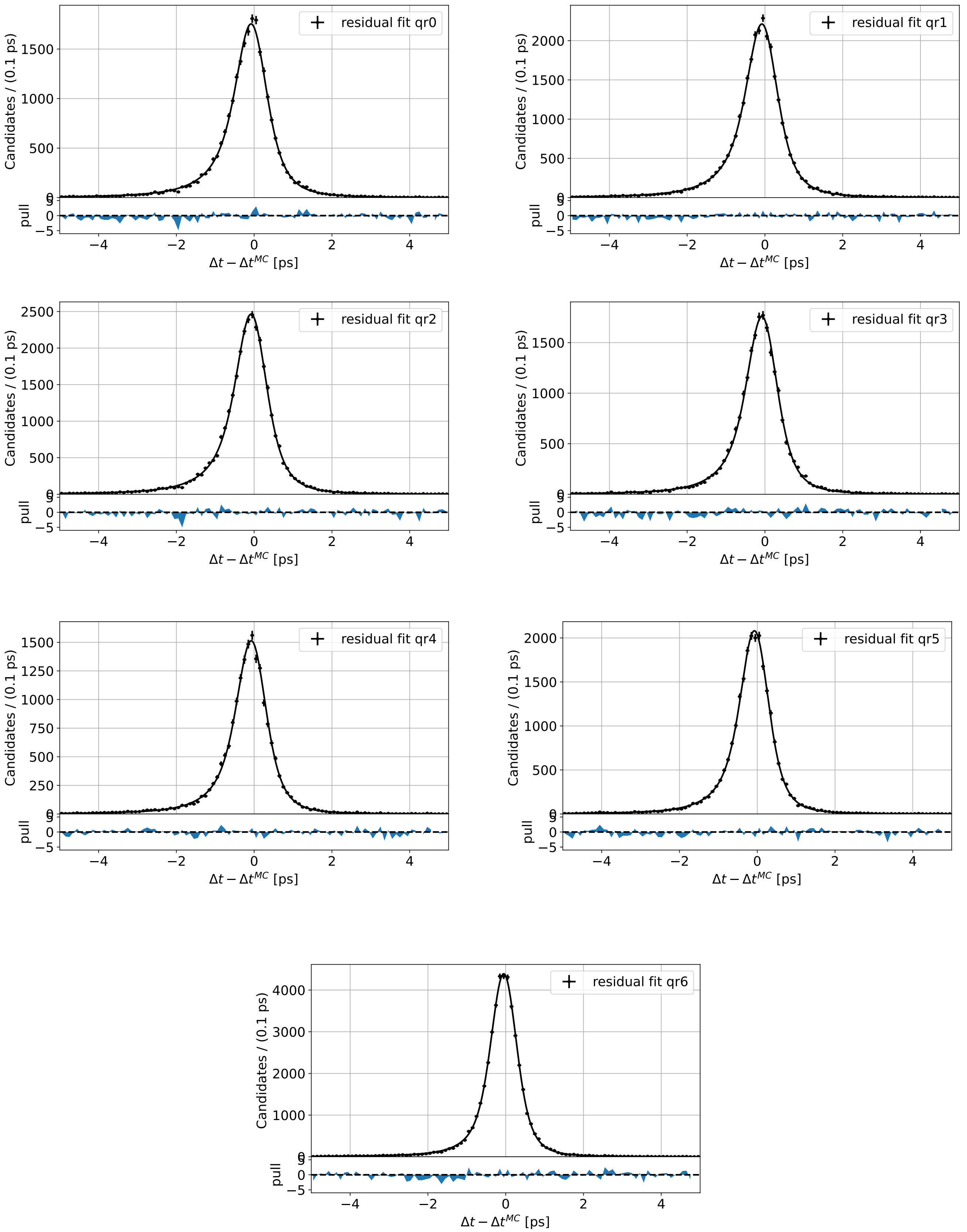

Figure 5.4: Residual fits for Signal MC with full disentanglement. Single figures show the fits on different qr-bins 0-6 (left to right, top to bottom).

5.1.3 Single Δt fits

The main part of the analysis is the fit of the observed PDF's Δt distribution from Eq. 4.14 to the Signal MC data sets, each corresponding to 1 ab^{-1}. This fit can be done to obtain the precise parameter values for mixing parameters such as Δm_d and τ as demonstrated in Ref. [44]. In this case, the special interest and focus will lie on the determination of the value for the fraction of PSD ζ. This is the main physics parameter left to float in the fit, as Δm and τ are fixed to PDG world averages[2] [13]

$$\Delta m_d = (0.5065 \pm 0.0019)\ \mathrm{ps}^{-1}, \quad \tau_B = (1.519 \pm 0.004)\ \mathrm{ps}. \tag{5.7}$$

As OL and Tail parameters (except f_{Tail}) have been fixed in the previous residual fits to values from Tab. 5.4, only core parameters are left free in the resolution function. This is justified by the high sensitivity of mixing parameters, or in this case the fraction of disentangled $B^0\overline{B}^0$ pairs especially to core parameters. To assess possible discrepancies between data and Monte Carlo in studies of systematic uncertainties a alternative resolution function is used where no fixation of certain parameters is necessary [44].

Flavor tagger parameters, such as wrong tag fractions, the uncertainty on the mistag as well as efficiency are also free parameters in the fit. For the fit itself, the data is divided into 7 bins of dilution factor r with intervals given in 3.12, with r-bin 6 having the highest purity of tagging efficiency. In addition, the data is split into four flavor combinations $B^0\overline{B}^0$ and B^0B^0 and charge conjugate. This is done to account more precisely for asymmetries between B^0_{tag} and $\overline{B}^0_{\mathrm{tag}}$, as pointed out in Ref. [51]. The combined parameter $\mu_i = (\varepsilon_{B^0_{\mathrm{tag}}} - \varepsilon_{\overline{B}^0_{\mathrm{tag}}})/(\varepsilon_{B^0_{\mathrm{tag}}} - \varepsilon_{\overline{B}^0_{\mathrm{tag}}})$ is the weighted average of wrong tag fractions with $q_{\mathrm{tag}} = +1$ and -1. This results in a total of 28 qr-bins that are fitted simultaneously. Free parameter ζ, and f_{Tail} are shared across all qr-bins, core parameters and μ_i are shared across respective r intervals and finally $w_i^{\pm}$ are specific for q_{tag}. To avoid the fit to hit parameter limits the allowed parameter space for ζ is extended to $[-0.1,\ 1.1]$.

The plots in Figs. 5.1.3 show the fits to the Signal MC with PSD fraction of 0% for the best quality qr-bin 6, while plots in Figs. 5.1.3 show the fits to the Signal MC with PSD fraction of 100% for the best quality qr-bin 6. The fit parameters for both cases are summarized in Tab. 5.5. For both full entanglement and disentanglement Signal MC, the remaining qr-bin 0-5 alongside fits to the Signal MC samples between 0% and 100% PSD fraction, can be found in the Appendix B.3.

[2]These are also the values which are used for Signal MC generation.

The fitted shapes for same and opposite flavors with q_{tag} both for PSD fraction $\zeta = 0$ and $\zeta = 1$ are consistent with the expectations seen in the physics PDFs in Figs. 2.7. When looking at the pulls displayed in the lower plots, there is no systematic under-/overshooting visible. Moreover, the generated values for PSD fraction ζ are within the fitted ζ's $\pm 1\sigma$ uncertainty for $\zeta_{\text{gen}} = 0$, while for $\zeta_{\text{gen}} = 1$ the fitted value is about 1.15σ away. This will be reviewed in context of bias in Toy MC studies. Remaining parameters for both fits have overlapping 1σ uncertainty regions, although a slight deviation can be seen for μ_6. Shapes between opposite flavor events $B^0\overline{B}^0$ and $\overline{B}^0B^0$ and same flavor events B^0B^0 and $\overline{B}^0\overline{B}^0$ are approximately the same, although a slight deviation can be seen due to different values of $w_6^{\pm}$.

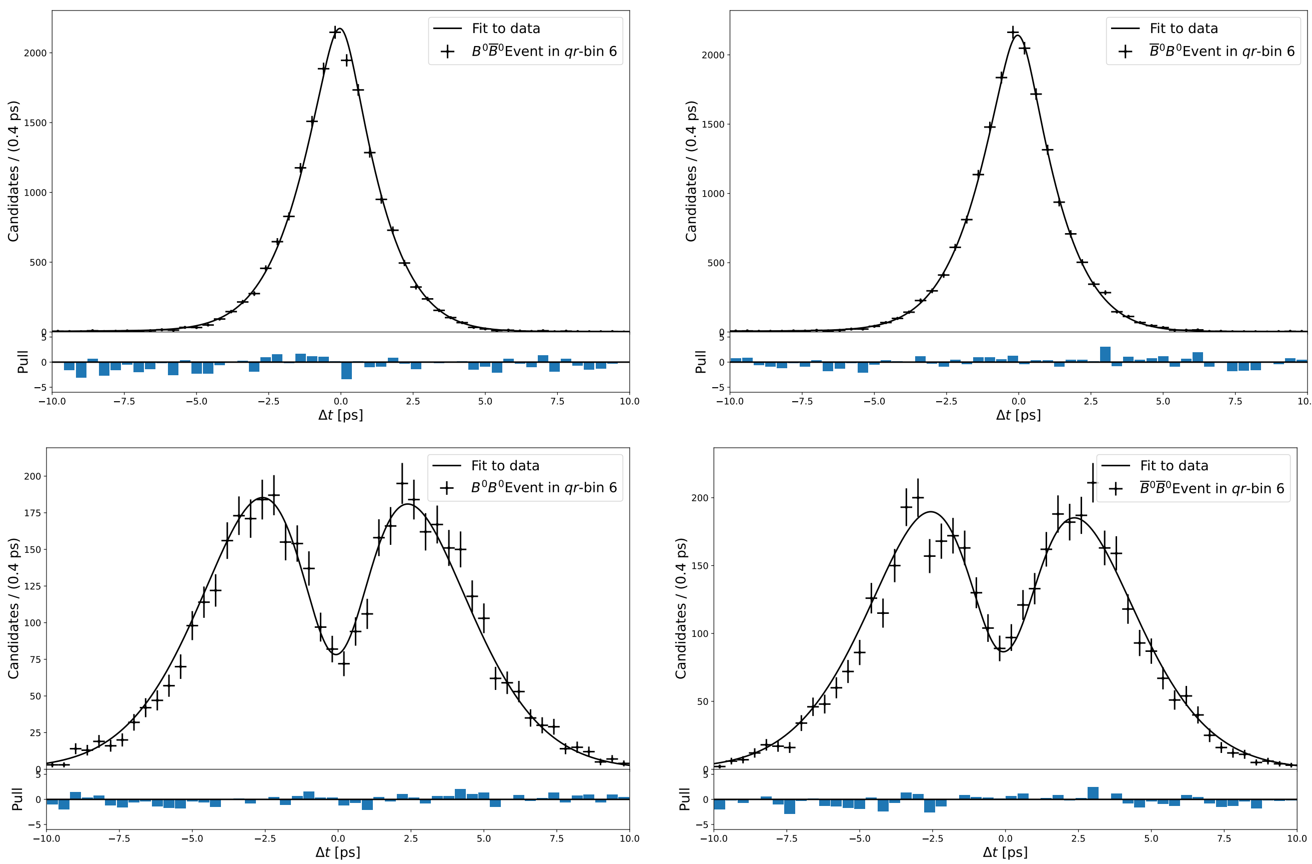

Figure 5.5: Δt-distribution fitted to Signal MC data with full entanglement ($\zeta_{\text{gen}} = 0$). Data points with error bars show Signal MC data for $|qr| > 0.875$ and $\overline{B}^0\overline{B}^0$, solid line shows the fit. The lower plot show the pulls.

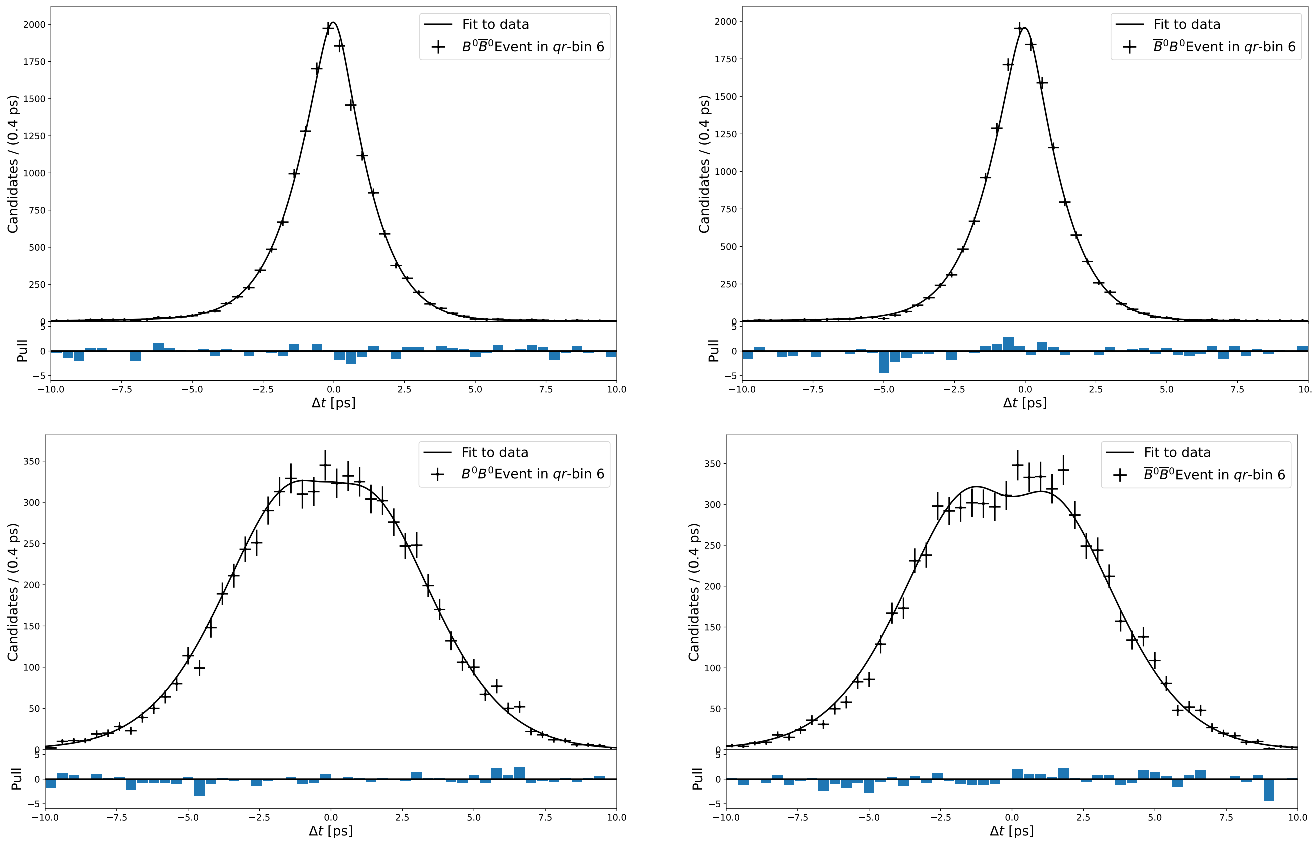

Figure 5.6: Δt-distribution fitted to Signal MC data with full disentanglement ($\zeta_{\text{gen}} = 1$). Data points with error bars show Signal MC data for $|qr| > 0.875$ and $\overline{B}^0\overline{B}^0$, solid line shows the fit. The lower plot show the pulls.

Parameter	Fit estimate	
ζ	0.015	$\pm$ 0.032
$\mu_{M1}^{(6)}$	0.0211	$\pm$ 0.0362
$\sigma_{M1}^{(6)}$	1.1091	$\pm$ 0.0694
f_{Tail}	0.3803	$\pm$ 0.0155
w_6^+	0.0204	$\pm$ 0.0047
w_6^-	0.0166	$\pm$ 0.0046
μ_6	-0.0051	$\pm$ 0.0054

Parameter	Fit estimate	
ζ	1.028	$\pm$ 0.024
$\mu_{M1}^{(6)}$	0.0447	$\pm$ 0.0360
$\sigma_{M1}^{(6)}$	0.9536	$\pm$ 0.0749
f_{Tail}	0.3910	$\pm$ 0.0158
w_6^+	0.0090	$\pm$ 0.0063
w_6^-	0.0203	$\pm$ 0.0060
μ_6	-0.0207	$\pm$ 0.0079

Table 5.5: Δt fit parameters for Signal MC with full entanglement and disentanglement, listed on the left and right, respectively. Sub-/Superscript 6 expresses the parameter's 6th qr-bin specific value. ζ is the fraction of disentanglement and is fit simultaneously across all qr-bins, same for f_{Tail}.

Linearity Test

In the following, the linearity of the fitter's response with respect to parameter ζ is evaluated. Generated values ζ_{gen} are compared to the fitter's best parameter estimates ζ_{fit}. When plotting ζ_{gen} against ζ_{fit} a direct linear relation is expected. Any deviation from linearity would imply either a wrong modeling or a problem in the fitting process.

The fitted values across all qr-bins for single Δt fits on Signal MC ranging from full entanglement to full disentanglement in 20% steps are summarized in Tab. 5.6. Note, that the size of Signal MC on which the fit was performed (Tab. 5.1) changes, with samples with $\zeta_{\text{gen}} = 0.4$ and 0.6 being the largest sample sizes, hence the smaller uncertainties most probably caused by statistical uncertainties. The corresponding figures can be found in Appendix B.3.

Fig. 5.7 shows the dependence of the fitted value ζ_{fit} to ζ_{gen}, where values are taken from 5.6. While error bars show the fitted values with their $\pm 1\sigma$ uncertainty, the solid line shows a linear fit to the points. For $f(\zeta_{\text{gen}}) = a_1 \cdot \zeta_{\text{gen}} + a_2$ the fit gives the values

$$a_1 = 1.006 \pm 0.001, \quad a_2 = 0.009 \pm 0.001,$$

which corresponds to a slope with a deviation from unity in the order of $\mathcal{O}(0.1\%)$. Similarly, for the y-axis intercept, which deviates from zero in the order of $\mathcal{O}(1\%)$. As one can see, besides the value at $\zeta_{\text{gen}} = 0.6$, the linear fit always is within the $\pm 1\sigma$ uncertainty region of the data points. These results provide a first indication of linear behavior, which will be further quantified using toy MC studies.

In all cases, the extracted values of ζ were found to be consistent with the Signal MC value within the statistical uncertainties, indicating correct modeling. The sensitivity for ζ for this specific Signal MC study is determined to be at the few-percent level (3%), demonstrating the viability of the hadronic channels for disentanglement studies despite their relatively low reconstruction efficiency compared to semi-leptonic modes.

5.1.4 Toy Studies

Toy Monte Carlo (Toy MC) studies are an essential tool. This type of study provides a controlled environment in which one can test statistical methods, evaluate biases, and validate fitting procedures by generating pseudo-experiments that mimic events under well-defined assumptions [52]. The core idea behind Toy MC studies is to generate large ensembles of simulated data sets using known PDFs and performing the same fitting procedure multiple times. By doing so, the stability and performance of the model and fitter can be assessed and potential biases in extracted parameters can be determined while assessing statistical uncertainties. Two types of Toy MC studies are

ζ_{gen}	Fit estimate
0%	$(1.5 \pm 3.2)\%$
20%	$(21.3 \pm 2.8)\%$
40%	$(41.7 \pm 2.3)\%$
60%	$(58.1 \pm 2.2)\%$
80%	$(81.7 \pm 2.4)\%$
100%	$(102.8 \pm 2.4)\%$

Table 5.6: Summary of the single Δt fit's estimates on PSD fraction ζ, with respect to PSD fraction in the generated Signal MC (ζ_{gen}).

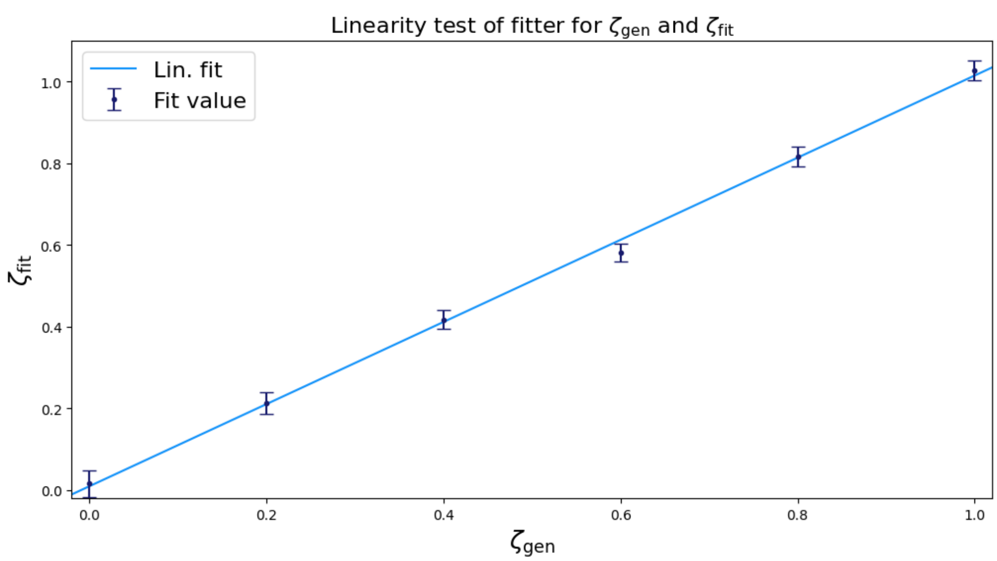

Figure 5.7: Linearity study of the fitter. x-axis and y-axis show ζ_{gen} and ζ_{fit}, respectively. The points with error bars represent the fitted values for ζ, while the solid line represents the linear fit.

used in this analysis, namely the *Pure Toy MC* and *Bootstrap Method*, each having advantages of their own.

The Pure Toy MC approach generates pseudo-experiments directly from an analytical probability density function (PDF). Thereafter, the same model from which the data sets are sampled, is used to fit back the data points. Looking at the individual fit estimates of single fits in the ensemble, the PDF's behavior under statistical fluctuation of parameters can be assessed. Moreover, the bias can be quantified by determining the pull distributions of fit parameters.

In contrast, the Bootstrap method employs data sets bootstrapped from the full Signal MC sample [52]. It is a powerful way of investigating the statistical uncertainty of measurements. The bootstrap method introduces Poisson perturbations which emulate statistical fluctuations in the data. By sampling from the Signal MC data sets, this technique ensures a direct test on the fitting process while being exposed less to systematic uncertainties stemming from the PDF itself. Since these replicas naturally include detector smearing and reconstruction inefficiencies, they provide a way to quantify the extent to which detector effects influence the extracted physics parameters. If a bias in ζ is observed in bootstrapped Toy MC but not in Pure Toy MC, this suggests that the original data set is playing a significant role in the observed bias. Conversely, if a bias appears in both methods, then it is likely that the source of the bias lies in the fitting procedure itself rather than in the detector modeling.

In conclusion, each of these Toy MC approaches have distinct strengths. Pure Toy MC is optimal for isolating biases which stem from the fitting process and testing the statistical behavior of the PDF in a controlled setting, while the bootstrap approach is essential for understanding a bias introduced by modeling while also assessing the statistical uncertainty. The combination of these two methods will provide a comprehensive validation framework, ensuring that the final extracted values of ζ and other parameters are robust and free from artifacts introduced by the analysis method itself.

An important figure of merit for these kind of studies is the so called pull, defined as

$$\text{Pull} = \frac{x_i - \mu_i}{\sigma_i}, \tag{5.8}$$

where x_i is the i-th fit value, μ_i the i-th central generated value and σ_i the i-the uncertainty on the fit value [53]. The calculated pull values can be histogrammed for the number of occurrences. Fitting a Gaussian to the data points would ideally result in a normal distribution with a mean of zero and uncertainty at unity. Significant deviations from nominal values implicate systematic bias.

Pure Toy Studies

To test the robustness of the fitting process itself, Pure Toy MC studies are now performed. For this, 1000 independent samples are generated each corresponding to integrated luminosities given in Tab. 5.1. The starting parameters are combined parameters from residual fits and single Δt fits for flavor tagger parameters. After sampling, the same PDF is refitted to the sampled data sets to get the best fit estimates for each sample, while core and flavor tagging parameters are left float together with ζ. Analogously to single Δt fits in Sec. 5.1.3 tail and OL parameters are fixed to values obtained in residual fits. The resolution function's core parameters, as well as flavor tagger parameters look healthy and unbiased. Thus, the focus only on parameter ζ is justified. Finally, the pull distributions are calculated and then fitted by a Gaussian. Figs. 5.1.4 show the pull distributions for parameter ζ.

Figs. 5.1.4 show the calculated pulls as points with error bars, the fitted Gaussian distribution in orange and the reference line at $x = 0$ as red dotted line. The parameters of the Gaussian are summarized in the following table 5.7. As for the mean values that should be consistent with zero for a normal distribution, that only is true for the last two pull distributions. In those cases however, the uncertainty is inconsistent with one. On the other hand, for the first three pull distribution the uncertainty is indeed consistent with 1, whereas the mean is now deviating from zero with $> 1\sigma$. Only for the generated value of $\zeta_{\text{gen}} = 0.5814$ both mean and uncertainty show a bias. When looking at the plots in the first two rows one can see that the peaks of the data distributions seem to roughly agree with zero, however a tail to the right skews the Gaussian. Thus, there seems to be a biased statistical fluctuation towards positive values, while the correct value is still retrieved most frequently. To see how much the fitted values are really affected by

Generated Value ζ_{gen}	Avg. ζ_{fit}	Pull Mean	Pull Uncertainty
0.0153	0.030 ± 0.061	0.503 ± 0.032	1.003 ± 0.022
0.2126	0.219 ± 0.065	0.293 ± 0.031	0.988 ± 0.022
0.4174	0.428 ± 0.056	0.400 ± 0.031	0.985 ± 0.022
0.5814	0.602 ± 0.059	0.568 ± 0.036	1.126 ± 0.025
0.8167	0.811 ± 0.057	0.027 ± 0.029	0.93 ± 0.021
1.0279	1.018 ± 0.044	-0.142 ± 0.028	0.878 ± 0.020

Table 5.7: Summary of mean and uncertainty of the fitted Gaussian to the pull distribution for Toy MC. The value from which the Toy data is generated is given in the first column.

the bias shown in the pull distribution, the mean of all fitted values for each set of toy samples are plotted. As in the linearity study shown in previous section's Fig. 5.7, this should follow a unitary linear function. Following Fig. 5.9 illustrates the behavior. This linear relation of the fitted value

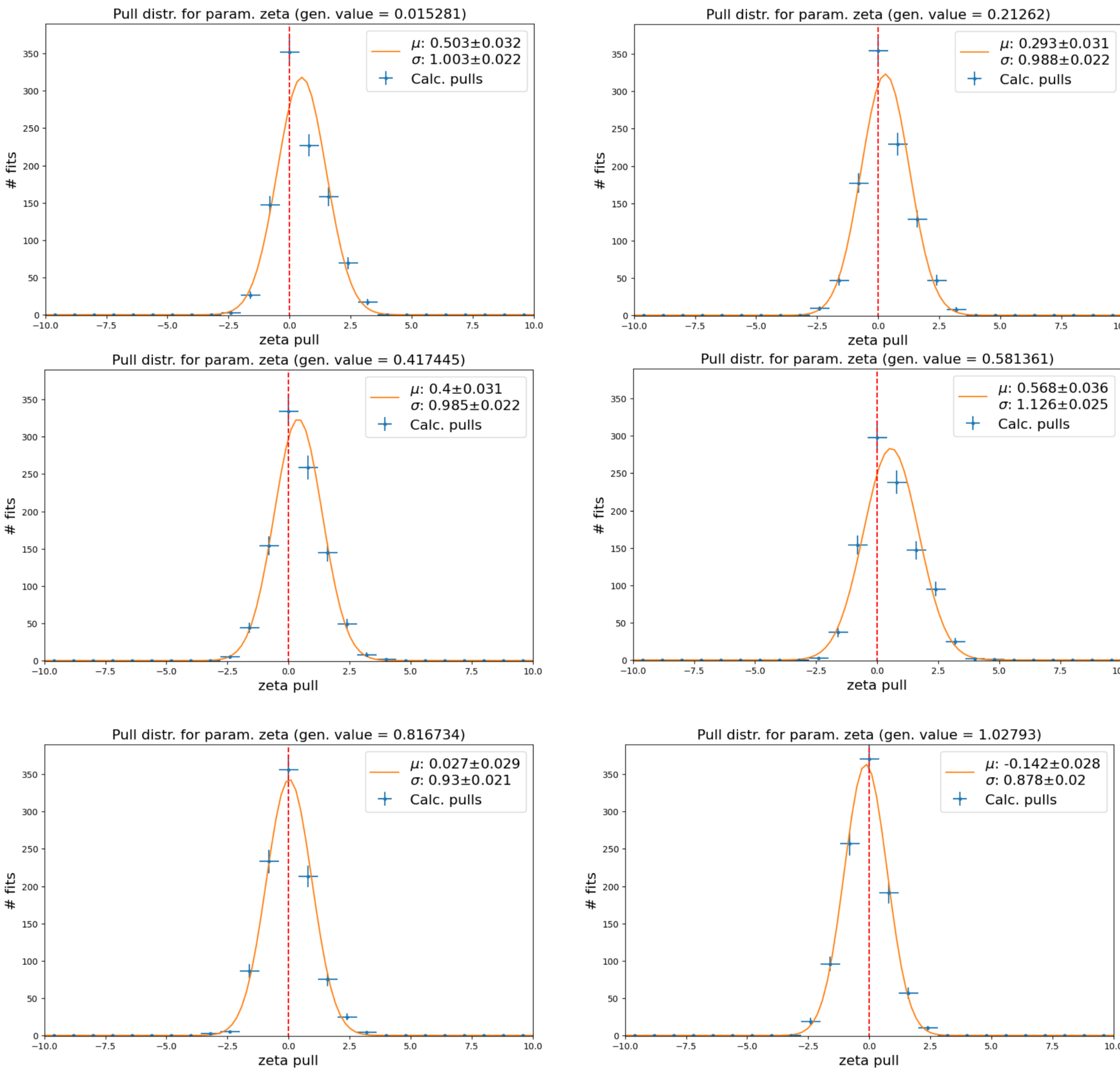

Figure 5.8: Pull distributions for the parameter ζ. Pure Toy MC data sets generated from PDF's with combined fit parameters obtained both from residual $\delta\Delta t$ fits and single Δt fits on Signal MC with PSD fraction written below the individual Figures. The orange curve is the Gaussian fit to the Pull data points shown in blue. The dotted red curve shows the reference point of $x = 0$.

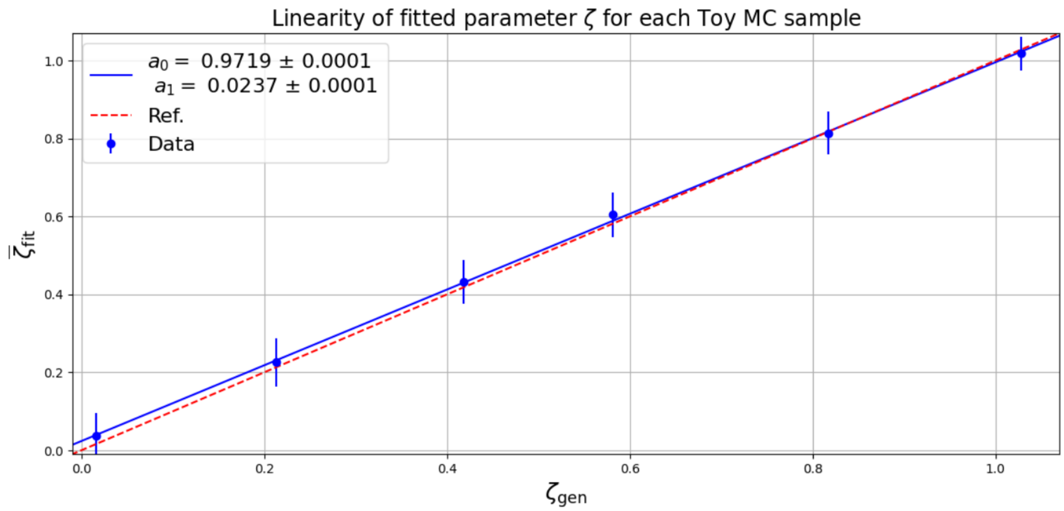

Figure 5.9: Linearity test of the mean value of $\overline{\zeta}_{\mathrm{fit}}$ in each Toy MC generated with ζ_{gen}. The points with error bars represent the mean of $\overline{\zeta}_{\mathrm{fit}}$ in each set of Toy MC samples, the solid blue line is the linear fit with the parameters shown in legend. Red dotted line is the reference line with $a_0 = 1$, $a_1 = 0$.

ζ's mean in each set of Toy MC sample for ζ_{gen} shows that in spite of the bias manifested in Tab. 5.7 the linearity maintains. The reference line (red dotted line) is within the 1σ uncertainty of the fitted ζ's mean values. However, the performed linear fit has a small ($\mathcal{O}(1\%)$) but certain deviation from a slope (a_0) of 1 - the same for the y-intersect (a_1). This is in accordance with the bias observed before when looking at the pulls.

Bootstrapped Toy MC Study

Now, the bootstrap Toy MC study is presented. For this 1000 bootstrapped samples are generated from the Signal MC each corresponding to the integrated luminosities given in Tab. 5.1. For each bootstrap sample the same routine as for single Δt fits in Sec. 5.1.3 is applied. Figs. 5.1.4 show the pull distributions for parameter ζ. The resulting histogram data (blue points with error bars) are then fit with a Gaussian, shown in solid orange lines.

Same as in pure Toy studies, the resolution function's core parameters, as well as flavor tagger parameters look healthy and unbiased. Thus, the focus only on parameter ζ is justified.

The parameter's mean value for each ζ_{gen}, as well as pull distributions' fitted values for mean and uncertainty are summarized in Tab. 5.8. The generated value from MC is always within the mean values' $\pm 1\sigma$ uncertainty, indicating a healthy fit. When turning to the pull's mean and uncertainty, the mean's deviation from zero for $\zeta_{\mathrm{gen}} = 0.8$ and 1.0 are noticeable. Latter bias here reaches almost 60%, while the data points look Gaussian distributed with no one-sided tails (see

Fig. 5.1.4). This could be caused by the parameters' upper limit in the fit bound at an unphysical value of $\zeta_{\max} = 1.2$. For the other sets of bootstrapped toy samples, there does not seem to be a concerning bias.

To further asses the fit's behavior in terms of change under variation of ζ a linearity plot is shown. Fig. 5.11 shows the averaged values across the bootstrapped data sets from Tab. 5.8 with respective uncertainties (error bars). A linear fit (blue line) is performed on the data points which approaches the reference linear line with $a_0 = 1$, $a_1 = 0$ (red dotted line). One can see, the data points' error bars' $\pm 1\sigma$ uncertainty always includes the reference line. This visualizes the linearity of the Δt fit on the bootstrapped sample well, as the linear fit's parameter estimates only deviate in the order of $\mathcal{O}(1\%)$ from reference.

In conclusion one can say, that the pull distributions shown in Figs. 5.1.4 do indicate a bias which need further assessment, while it needs to be pointed out, that the average fitted values do look healthy. A complete analysis including a full study on systematic uncertainties could shed some light on the underlying sources of the remaining biases.

ζ_{gen}	Avg. ζ_{fit}	Pull mean	Pull uncertainty
0%	-0.011 ± 0.047	-0.226 ± 0.033	1.056 ± 0.024
20%	0.197 ± 0.045	-0.055 ± 0.032	1.019 ± 0.023
40%	0.400 ± 0.043	0.026 ± 0.032	1.019 ± 0.023
60%	0.606 ± 0.040	0.192 ± 0.033	1.029 ± 0.023
80%	0.808 ± 0.038	0.240 ± 0.033	1.039 ± 0.023
100%	1.018 ± 0.033	0.598 ± 0.033	1.046 ± 0.023

Table 5.8: Summary of the average fitted ζ value on bootstrapped toy MC, as well as mean and uncertainty of the fitted Gaussian to the pull distribution. First column shows the PSD fraction in the bootstrapped MC samples.

In this section pure and bootstrap Toy MC studies were performed to assess the pull and bias distributions under controlled input conditions. All values extracted for pull and parameter distributions are summarized for pure and bootstrapped in Tabs. 5.7 and 5.8, respectively. For several cases biased pulls could be observed for Pure Toys in $\zeta_{\text{gen}} = 0.,\ 0.6$ at around 0.503 ± 0.032 and 0.568 ± 0.036, respectively. In bootstrapped toys, the sample with $\zeta_{\text{gen}} = 1.$ showed a pull of 0.598 ± 0.033. However, the generated value is in accordance with the averaged mean value's $\pm 1\sigma$ region of the parameter. As both linearity tests in Figs. 5.9 and 5.11 show, there might be some counteractive behavior between model and fitter, indicated by the slight undershoot and overshoot of the slope of 1 for pure (Fig. 5.9) and bootstrapped toys (Fig. 5.11), respectively. With an emphasis on the correctly retrieved average fit values for ζ both in pure and bootstrapped toys, the observed biases call for further investigation.

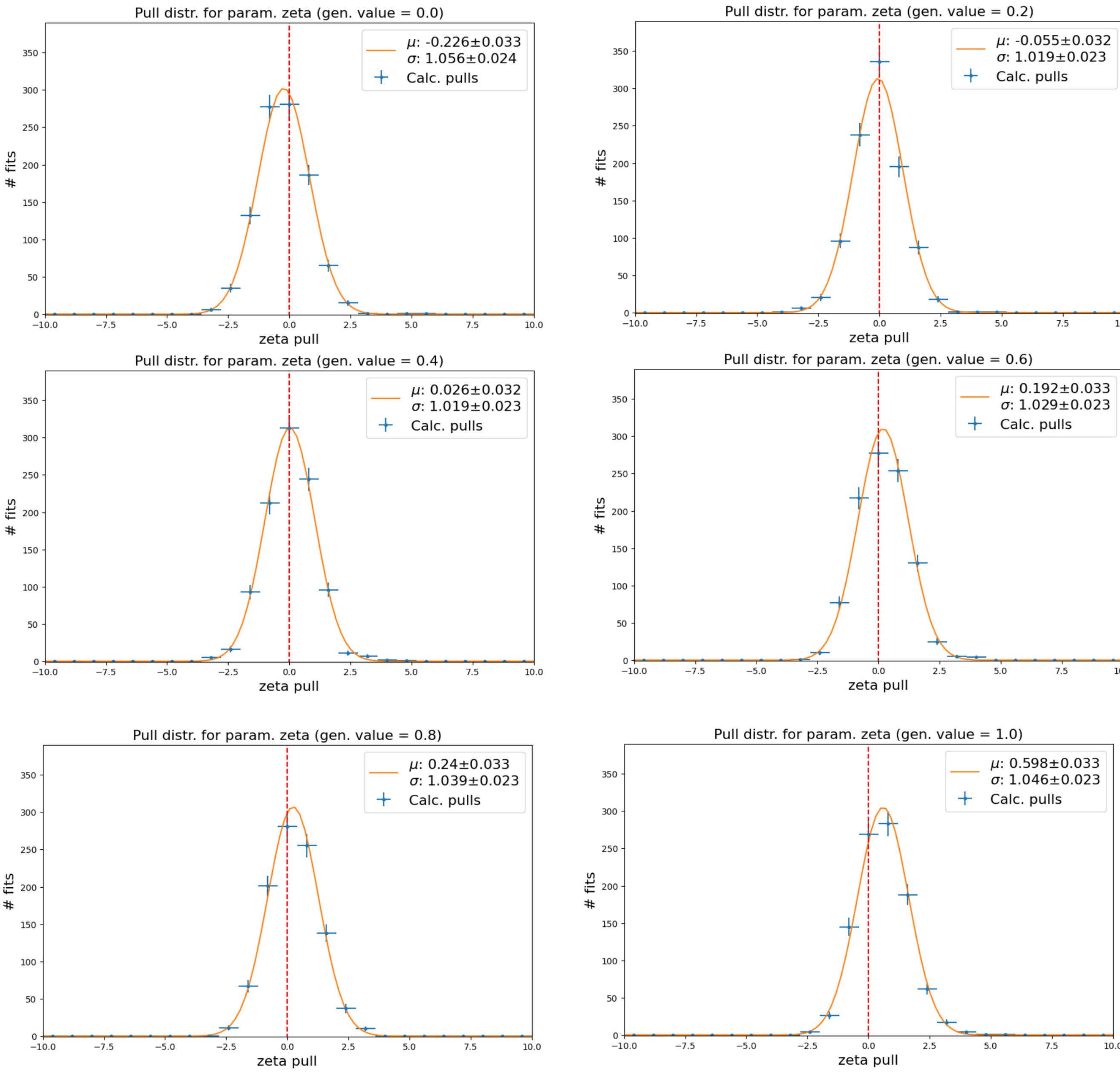

Figure 5.10: Pull distributions for the parameter ζ. Bootstrap Toy MC data sets generated by Poissonian fluctuations of Signal MC sample with combined fit parameters obtained both from residual $\delta\Delta t$ fits and single Δt fits on Signal MC with different values ζ_{gen}, indicated in titles. The orange curve is the gaussian fit to the pull data points shown in blue. The dotted red curve shows the reference point of $x = 0$.

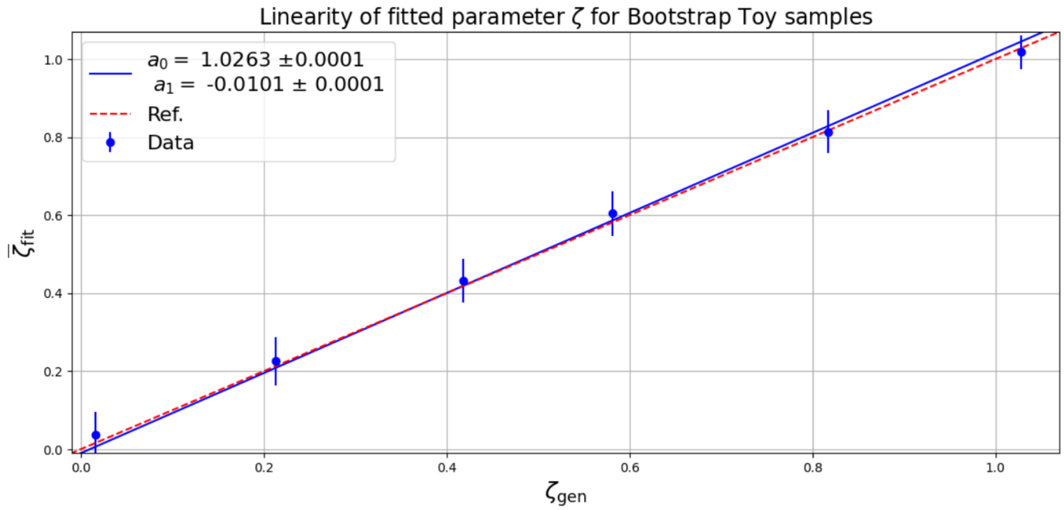

Figure 5.11: Linearity test of the mean value of $\overline{\zeta}_{\text{fit}}$ in each bootstrapped sample generated with ζ_{gen}. The data points with error bars represent the mean of $\overline{\zeta}_{\text{fit}}$ with their uncertainties in each set of samples, the solid blue line is the linear fit with the parameters shown in legend. Red dotted line is the reference line with $a_0 = 1$, $a_1 = 0$.

5.2 Absorption of disentanglement effects resolution and mistag parameters

In this section two types of effects surrounding time-dep. studies are tested: firstly, the resolution functions' and mistag's parameter's impact on disentanglement studies, and secondly, the impact of wrongfully neglecting disentanglement effects. To conceptualize this, two avenues will be explored: the direct impact of said parameters on the parameter ζ, and the behavior of parameters when disentanglement effects are treated incorrectly. Moreover, three questions will be in the center of attention:

- Question 1: Do floating resolution function parameters and wrong tag fractions introduce a bias on the value ζ?
- Question 2: Do floating resolution function parameters absorb disentanglement effects when ζ is assigned a wrong value in the model?
- Question 3: Do unaccounted disentanglement effects introduce a bias on CP violation parameters S_{CP} and A_{CP}?

In fact, the first question can be answered straight forward, as the necessary study has already been performed in Sec. 5.1.4. The interpretation has to be adjusted in this case however. While previously a technical interpretation has been presented, the argument here is going to be of physical nature. Whether floating resolution function and flavor tagging parameters bias the extracted value for ζ can be answered by looking at biases investigated using pure and bootstrapped toy MC. As in Sec. 5.1.4 concluded, a bias has been found both from the modeling and fitting, whether this has purely technical origins or also physical reasoning has unfortunately not been resolved in the scope of this thesis. For further studies a study with calibrated core and flavor tagger is suggested.

Moving on to the second question. As described earlier, the resolution function $R(\delta\Delta t, \sigma_{\Delta t})$ models how detector and kinematic effects smear the time difference Δt^{MC}. In previous publications in which disentanglement effects were neglected, tail and outlier parameters were fixed on entangled Signal MC while core parameters sensitive to mixing parameters Δm_d and τ were left free during the fit on data [54].

In the following, the aim is to study absorption of disentanglement effects by core parameters and mistag. This type of test is relevant for all TDCPV measurements at Belle II which assume full entanglement in $B^0\overline{B}^0$ pairs in flavor tagging. The strategy is the following: First, residual fits are performed on realistically small fractions of PSD in the Signal MC[3]. Analogously as in Sec. 5.1.3, the parameters for OL and tail are fixed from $\delta\Delta t$ fits for further studies while leaving core parameters float. In the next step, mixing parameters Δm and τ are fixed alongside $\zeta = 0$, in spite of the true PSD fraction in the Signal MC being non-zero. This follows the same approach as in Ref. [54], where Δm and τ are fixed in order to retrieve CP violation parameters S_{CP} and A_{CP}. With this, the direct impact of disentanglement effects on TDCPV measurements can be assessed. Conversely, fixing ζ to zero allows to test how resolution function and mistag parameters behave under falsely neglected disentanglement. As a reference, a fit with ζ fixed to the correct MC value is performed as well. These fit values are then used as *nominal* value. Significant deviation from the nominal value can be taken as indication for absorption effects.

Before proceeding to the main part of this study, the nuisance parameters consisting of tail and OL parts have to fixed using residual fits. For this the same technique as before in Sec. 5.1.2 is applied, thus not explained any further in detail here. The residual fit are performed on Signal MC with true PSD fractions of

$$\zeta = [0\%,\ 5\%,\ 10\%,\ 15\%,\ 20\%,\ 30\%,\ 40\%]. \tag{5.9}$$

As already shown earlier residual fits are independent of flavor, therefore also independent of disentanglement effects. This justifies the procedure of using this method to fix the nuisance parameters for further studies sensitive to true ζ values.

[3] *Realistically small* means fraction of PSD should be in the non-excluded region of $\zeta < \mathcal{O}(10\%)$, found in the last disentanglement study in Ref. [26].

Subsequently, the deviation between the first Δt fits with the nominal fits are plotted with respect to the Signal MC's true value. Here, the most compelling parameters are shown, namely the resolution function's main parameters $\mu_{M1}^{(6)}$ and $\sigma_{M1}^{(6)}$ as well as the mistag parameters $w_6^{\pm}$. The latter are shown for both relative deviations from nominal value and for absolute values of the parameters. The remaining parameters for all other qr-bins can be found in Appendix B.4. Fig. 5.16 shows the absolute values of the minimized negative log-likelihood function defined in Eq. 4.15 for both cases, illustrating qualitatively the quality of fit.

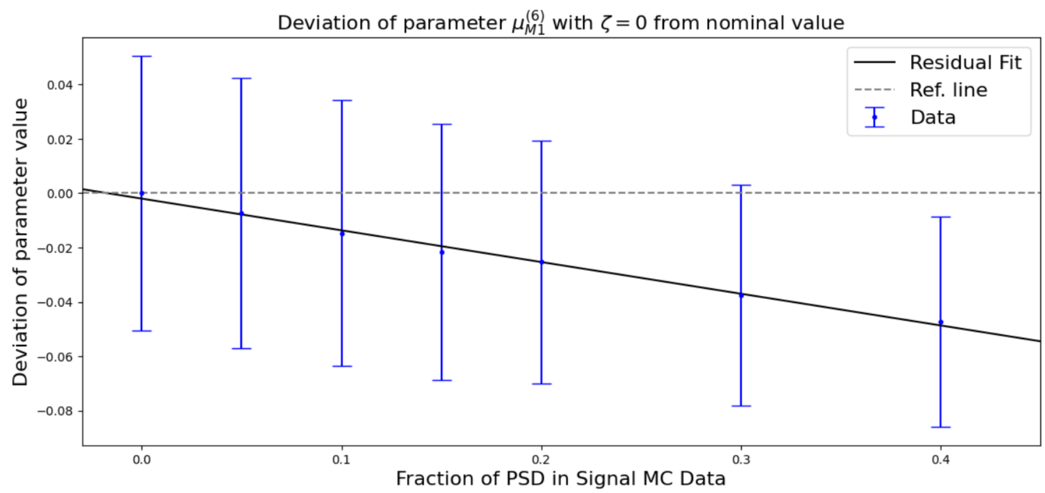

Figure 5.12: Relative deviation of fit value with $\zeta = 0$ from nominal value for parameter $\mu_{M1}^{(6)}$. The dotted line for $y = 0$ shows the relative nominal value, data points with error bars are shown with respect to the true PSD fraction in Signal MC, while the solid line shows a linear fit to the data points.

Figs. 5.12 and 5.13 show a positive linear relation between ζ_{gen} and the deviation of parameter values. However, in the realistic region of below 10%, no significant deviation from zero can be observed. Only above $\zeta_{\text{true}} = 0.3$ a slight deviation from zero above $\pm 1\sigma$ can be seen for parameter $\mu_{M1}^{(6)}$. Although the deviation seems to occur earlier for $\sigma_{M1}^{(6)}$, this is not until $\zeta = 0.2$. Therefore, a conclusion can be drawn that neglected PSD effects in the $\mathcal{O}(1\%)$ do not introduce significant shift in resolution function parameters.

Moving on, the focus is turned to the wrong tag fractions $w_i^{\pm}$. In Fig. 5.14 the wrong tag fraction's relative deviation from the nominal value is shown in dependence of the Signal MC's true ζ value. The wrong tag fraction with positive and negative tag are shown as data points with error bars in orange and blue, respectively. The linear fit manifests the linear relation between ζ_{true} and the relative $w_6^{\pm}$ deviation, which has a steep slope. Even for $\zeta_{\text{true}} = 0.05$, the nominal value is not in the $\pm 1\sigma$ region of the data point anymore. As the trend is linear, the deviation

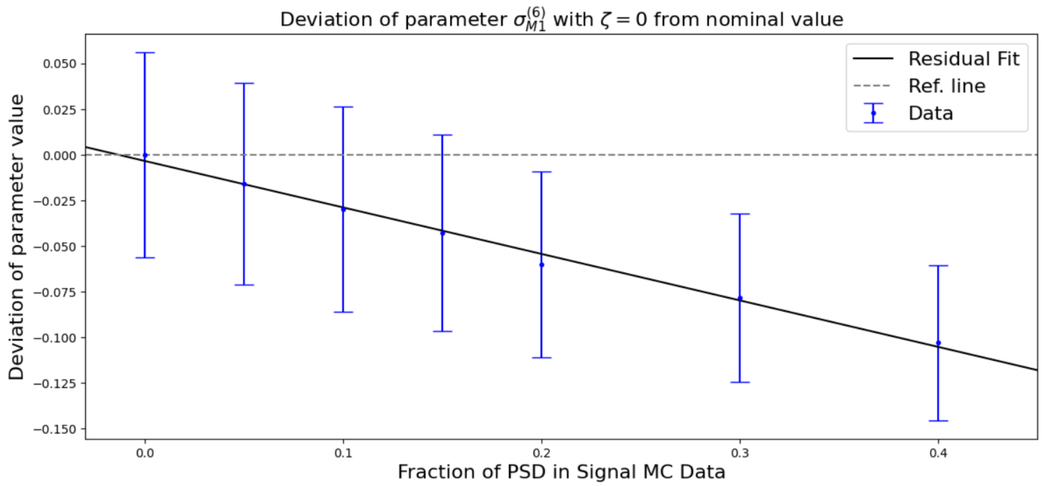

Figure 5.13: Relative deviation of fit value with $\zeta = 0$ from nominal value for parameter $\sigma_{M1}^{(6)}$. The dotted line for $y = 0$ shows the relative nominal value, data points with error bars are shown with respect to the true PSD fraction in Signal MC, while the solid line shows a linear fit to the data points.

Figure 5.14: Relative deviation of fit value with $\zeta = 0$ from nominal value for parameters $w_6^{\pm}$. The dotted line for $y = 0$ shows the relative nominal value, data points with error bars are shown with respect to the true PSD fraction in Signal MC, while the solid line shows a linear fit to the data points. Wrong tag fraction for negative/positive are shown in blue and orange, respectively.

further increases. To gain a better qualitative understanding on the size of this systematic effect this behavior introduces the absolute values of the parameters $w_6^{\pm}$ are investigated, illustrated in Fig. 5.15.

Fig. 5.15 now shows the same effect as before in Fig. 5.14, now in absolute values. The fit for $\zeta_{\text{true}} = 0$ is modeled correctly. $w_6^{\pm}(\zeta_{\text{gen}} = 5\%)$ already deviates more than 1σ from the first value, even more for $w_6^{\pm}(\zeta_{\text{true}} = 10\%)$. Looking at the quantified value given in Fig. 5.14 for $\zeta_{\text{gen}} = 10\%$ deviates by about $1 - 2\%$. Since the flavor tagger should not be directly affected by any PSD effects, a deviation from this value is a clear sign of mismodeling. Moreover, the bias also lies in the same order of magnitude found as a systematic uncertainty on $w_6^{\pm}$ in Ref. [54]. This finding answers Question 3. Although the shift in $w_6^{\pm}$ is a sizable effect, it does not translate to a bias for the CP Violation parameters of A_{CP} and S_{CP} [54]. For the same reason, no bias for key physics parameters are expected due to this absorption effect.

It can also be shown easily that falsely neglecting disentanglement effects indeed leads to mismodeling by showing the achieved fit qualities illustrated in Fig. 5.16. Here, the NLL is the likelihood function in which the PDF is inserted to retrieve a parameter estimation by maximizing it (see Sec. 4.2), thus a higher absolute value implies a better fit. The figure shows the absolute value of NLL's function defined in 4.15 after the fit is performed with increasing ζ_{true}. Orange dots show the value when ζ is fixed to the correct value, while the blue dots show the case for falsely set $\zeta = 0$. The absolute value has no quantitative meaning, however the change in the values throughout different ζ_{true} can be interpreted qualitatively. Expectedly, the quality of the blue points drop for increasing values of ζ while the orange stay about constant. Thus, the fit does indeed experience a drop in and its quality is compromised by having to account for PSD effect.

With all supporting arguments, the main conclusion of this absorption study can be drawn. Although, wrong tag fractions do deviate from nominal values by few percent within the unexcluded ζ region and thereby absorbing disentanglement effects, the effect will have little to no impact on key parameters in time-dependent CP Violation studies such as A_{CP} and S_{CP}. There is a final remark to be made, about an indirect impact of disentanglement effects in processes involving direct and mixing-induced CP violation. The phase shift introduced by PSD could cross-talk between the phase shift caused by CP violation. This will also be subject of further studies.

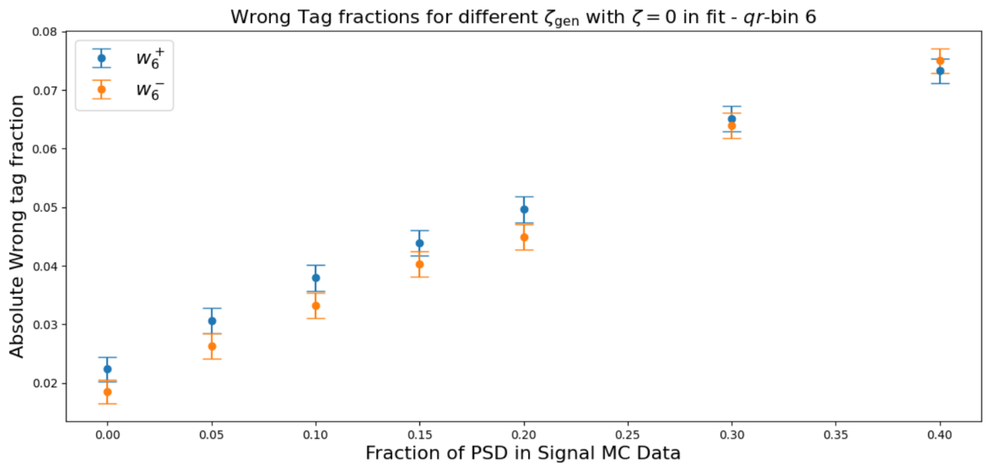

Figure 5.15: Absolute change of wrong tag fractions $w_6^{\pm}$ for $\zeta = 0$ when true PSD fraction in Signal MC increases. Error bars show data points with respect to the true PSD fraction in Signal MC. Wrong tag fraction for negative/positive are shown in blue and orange, respectively.

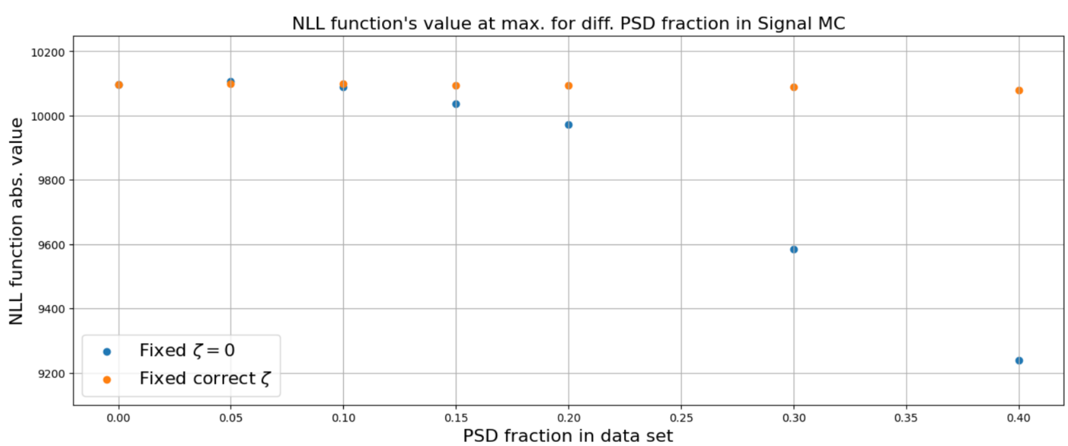

Figure 5.16: Absolute value of NLL function at maximum after fitting process. Fits with correct ζ and false ζ in terms of the true MC value are shown in orange and blue, respectively.

6 Summary and Outlook

In this thesis, a study of quantum entanglement in the neutral B-meson system produced in $\Upsilon(4S) \to B^0\bar{B}^0$ decays has been conducted. The analysis was performed using fully hadronic decay modes $B^0 \to D^{(*)-}\pi^+$, reconstructed with Belle II Signal Monte Carlo. These channels provide excellent vertexing performance, enabling a precise measurement of the proper time difference Δt between the decays of the entangled meson pair.

This work is motivated by the possibility of spontaneous or partial disentanglement of the $B^0\bar{B}^0$ system unexcluded in the 1-10% region on the 90% CL [26], which would manifest as a deviation from the quantum mechanical expectation in the time-dependent flavor asymmetry. Two classes of models were considered: the Spontaneous Disentanglement (SD) model and its generalization, the Partial Spontaneous Disentanglement (PSD) model, characterized by a disentanglement fraction parameter ζ. In PSD Model a fraction of $B^0\overline{B}^0$ pairs disentangles right after production in the $\Upsilon(4S)$ resonance, followed by an independent oscillation and decay. Thus, for a fraction of events the assumption of full entanglement used in flavor tagging does not apply, where B_{tag}'s opposite flavor is assigned to B_{sig} at $\Delta t = 0$, introducing a systematic error.

The data sets generated for this study have been produced locally within `basf2`. A novel `EvtGen` model handling spontaneously disentangled $B^0\overline{B}^0$ pairs has been developed in collaboration with the Belle II group of University of Hawai'i, as described in detail in Sec. 3.3.2. As this thesis presented a successful study using the new `EvtGen` model including a naive Signal MC validation, when moving forward towards a publication a central MC production should be requested. The generated data sets for full entanglement and disentanglement correspond to an integrated luminosity of $\int \mathcal{L}\mathrm{d}t \sim 1\mathrm{ab}^{-1}$, which is twice the available real Belle II data size of $\int \mathcal{L}\mathrm{d}t \sim 500\mathrm{fb}^{-1}$. Thereafter, the generated MC events have undergone reconstruction and selection (Chap. 4).

After the ΔE fits on the Signal MC were shown to be successful, the analysis' initial assumption of disentangled pairs' kinematics does not differ from entangled ones has proven itself to be correct. As first step, nuisance parameter's consisting of resolution function's outlier and tail parts have been fixed for later single Δt fits (Sec. 5.1.3) using $\delta\Delta t$ residual fits (Sec. 5.1.2). Subsequently, single Δt-fits have been performed. The extracted values of ζ summarized in Tab. 5.6 were found to be consistent within uncertainties with the MC values. As the key parameter ζ is sensitive to disentanglement effects, the single Δt fits serve as a proof-of-concept that this framework is in general suitable for such studies at Belle II. When comparing the fitted values' uncertainties in Tab. 5.6 with a Signal MC data set corresponding to 1 ab^{-1} ($\mathcal{O}(2-3\%)$) to the findings of Go *et al.* [26] ($\mathcal{O}(6\%)$), it can be seen that the sensitivity increases on paper. However, one must not forget that the study of Go *et al.* has been performed on a much smaller sample of Belle data corresponding to 152×10^6 $B^0\overline{B}^0$ pairs, while the values showed in this thesis is a pure Signal MC study. Taking this into consideration, the gain in sensitivity is unpromising, thus motivating once more the inclusion of semi-leptonic modes as suggested by several experts in TDCPV working group at Belle II [55, 56, 57].

In the next step, the fitter's robustness and possible bias have been investigated using Pure Toy MC and Bootstrap Toy MC methods. Both approaches have proven the model and fitting process to be consistent across different fractions of PSD to a certain degree when it comes to extracting the correct value for ζ. However, some biases could be observed for parameter ζ both from modeling and fitting. As one can see in the pull distributions for pure toy studies (Fig. 5.1.4) a favored statistical fluctuation towards higher values can be seen. For bootstrapped toys, biases without specific direction has been shown (Fig. 5.1.4). Both effect have to be further investigated for the full analysis.

Finally, the absorption of disentanglement effects by non-physical parameters introduced by detector effects and flavor tagging is investigated. This study serves the purpose of emulating the case of wrongly neglecting a small fraction of PSD in the data and its impact on key CP Violation parameters. It has been found that, the resolution function parameters do not change significantly in the region of $\zeta \sim \mathcal{O}(10\%)$, thus do not play a role in the absorption of disentanglement effects. On the other hand, in the same region for ζ, wrong tag fractions deviated slightly yet significantly, thus absorbing disentanglement effects. The shift however was found to be only by 1% - 2%. A recent study showed that a bias in wrong tag fractions by few percent, do not leak through to CP Violation parameters A_{CP} or S_{CP} [54]. The concern that earlier measurements could be directly affected by falsely assuming full entanglement could therefore be mitigated.

Overall, the results presented in this thesis demonstrate that hadronic decay modes at Belle II provide a viable and sensitive platform to probe quantum entanglement of the $B^0\bar{B}^0$ system. Although, deeper understanding of the model and fitter is necessary the developed methodology and workflow in this thesis ranging from event generation, all the way to fits on physics observables form an analysis framework for the first quantum entanglement study at Belle II.

A Physics

A.1 Derivation Δt distributions for Spontaneous Decoherence Model

The survival probability of a B^0 meson created at time $t = 0$ is given by

$$P(t) = \frac{1}{2} e^{-\Gamma t}(1 \pm \cos \Delta m t), \tag{A.1}$$

where Δm denotes the mass difference between the two mass eigenstates, and Γ the absolute decay width. For same flavor events, two cases and their complex conjugates are considered, in which the B^0 mesons decay with the same flavor. A derivation of the Δt distribution for same flavor events is now performed. The starting point is a case where two completely disentangled B^0 mesons are produced at $t = 0$ from the decay of the $\Upsilon(4S)$ resonance:

$$\begin{aligned} P_{like}(t_1, t_2) = 2 \cdot \frac{1}{2} e^{-\Gamma t_1}(1 + \cos \Delta m t_1) \cdot \frac{1}{2} e^{-\Gamma t_2}(1 - \cos \Delta m t_2) \\ +2 \cdot \frac{1}{2} e^{-\Gamma t_1}(1 - \cos \Delta m t_1) \cdot \frac{1}{2} e^{-\Gamma t_2}(1 + \cos \Delta m t_2), \end{aligned} \tag{A.2}$$

with t_1 and t_2 the absolute times for the first and second B^0 to decay, respectively. The variable t_2 is replaced with $\Delta t = t_1 - t_2$, leading to the expression:

$$P_{like}(t_1, \Delta t) = e^{-\Gamma(2t_1 + \Delta t)}(1 - \cos \Delta m t_1 \cos \Delta m (t_1 + \Delta t)). \tag{A.3}$$

The addition theorem for trigonometric functions, $\cos(\alpha + \beta) = \cos \alpha \cos \beta - \sin \alpha \sin \beta$, is applied to separate t_1 and Δt, yielding

$$P_{like}(t_1, \Delta t) = e^{-\Gamma(2t_1 + \Delta t)}(1 - \cos^2 \Delta m t_1 \cos \Delta m \Delta t + \cos \Delta m t_1 \sin \Delta m t_1 \sin \Delta m \Delta t). \tag{A.4}$$

The trigonometric identities $\cos^2 \alpha = \frac{1}{2}(1 + \cos 2\alpha)$ and $\sin \alpha \cos \alpha = \frac{1}{2} \sin 2\alpha$ are then used:

$$P_{like}(t_1, \Delta t) = e^{-\Gamma(2t_1 + \Delta t)}(1 - \frac{1}{2}(1 + \cos 2\Delta m t_1) \cos \Delta m \Delta t + \frac{1}{2} \sin 2\Delta m t_1 \sin \Delta m \Delta t). \tag{A.5}$$

Integration over t_1 yields the final Δt distribution:

$$P_{like}(\Delta t) = \frac{1}{8} e^{-\Gamma\Delta t}\left[2 - \left(1 + \frac{\Gamma^2}{\Gamma^2 + \Delta m^2}\right)\cos\Delta m\Delta t + \frac{\Gamma\Delta m}{\Gamma^2+\Delta m^2}\sin\Delta m|\Delta t|\right], \tag{A.6}$$

which corresponds to the case of complete spontaneous disentanglement at $t = 0$.

The generalized PDF for same- and opposite flavor events under the spontaneous disentanglement hypothesis is then given by

$$P^{\rm SD}_{\rm like,unlike}(\Delta t) = \frac{1}{8} e^{-\Gamma\Delta t}\left[2 \mp \left(1 + \frac{\Gamma^2}{\Gamma^2 + \Delta m^2}\right)\cos\Delta m\Delta t \pm \frac{\Gamma\Delta m}{\Gamma^2+\Delta m^2}\sin\Delta m|\Delta t|\right]. \tag{A.7}$$

Further integration over time permits the determination of event yields for the given configuration.

A.2 Time-integrated oscillation probabilities

Consider time-integrated oscillation probabilities. For completeness purposes, a generic formalism for disentangled as well as (anti-)symmetric coherent wave functions is kept throughout this calculation. For a time evolution starting from $B^0\bar{B}^0$ at $t = 0$ the wave function reads:

$$\begin{aligned}
|B^0(t_1)\bar{B}^0(t_2)\rangle_\eta &= \frac{1}{\sqrt{2}}\left(|B^0(t_1)\bar{B}^0(t_2)\rangle_0 + \eta\,|\bar{B}^0(t_1)B^0(t_2)\rangle_0\right)\\
&= \frac{1}{\sqrt{2}} e^{-\frac{1}{2}\Gamma(t_1+t_2)} e^{-im(t_1+t_2)} \times\\
&\quad\left[-i\sin\left(\frac{\Gamma z}{2}(t_1+\eta t_2)\right)\left(\eta\frac{p}{q}\,|B^0B^0\rangle + \frac{q}{p}\,|\bar{B}^0\bar{B}^0\rangle\right)\right.\\
&\quad\left. + \cos\left(\frac{\Gamma z}{2}(t_1+\eta t_2)\right)\left(|B^0\bar{B}^0\rangle + \eta\,|\bar{B}^0B^0\rangle\right)\right],
\end{aligned} \tag{A.8}$$

where $z = x + iy = \frac{\Delta m + \frac{i}{2}\Delta\Gamma}{\Gamma}$. The parameter $\eta = \pm1, 0$ which describes symmetric, anti-symmetric or disentangled wave functions, respectively. Now, the time-integrated normalization of these three states is

$$\begin{aligned}
N_\eta &= \int dt_2 \int dt_1 \left[\left|\langle\bar{B}^0B^0|B^0(t_1)\bar{B}^0(t_2)\rangle_\eta\right|^2 \left|\langle\bar{B}^0B^0|\bar{B}^0(t_1)B^0(t_2)\rangle_\eta\right|^2\right.\\
&\quad\left. + \left|\langle B^0B^0|B^0(t_1)\bar{B}^0(t_2)\rangle_\eta\right|^2 + \left|\langle\bar{B}^0\bar{B}^0|\bar{B}^0(t_1)B^0(t_2)\rangle_\eta\right|^2\right]\\
&= \frac{1+\eta y^2}{\Gamma^2(1-y^2)^2}.
\end{aligned} \tag{A.9}$$

Using this normalization, the probabilities of observing a same flavor event can be calculated as follows:

$$\begin{aligned}\mathrm{Prob}(B^0B^0)+\mathrm{Prob}(\bar{B}^0\bar{B}^0) &= \frac{1}{N_\eta}\int dt_2\int dt_1\left(\left|\langle\bar{B}^0B^0|B^0(t_1)\bar{B}^0(t_2)\rangle\right|^2+\left|\langle\bar{B}^0\bar{B}^0|B^0(t_1)\bar{B}^0(t_2)\rangle\right|^2\right)\\ &= \frac{(x^2+y^2)(2+x^2-y^2+\eta(1+x^2y^2))}{2(1+\eta y^2)(1+x^2)^2}.\end{aligned} \tag{A.10}$$

Similarly, the probability for opposite flavor events reads

$$\begin{aligned}\mathrm{Prob}(B^0\bar{B}^0)+\mathrm{Prob}(\bar{B}^0B^0) &= 1-\mathrm{Prob}(B^0B^0)+\mathrm{Prob}(\bar{B}^0\bar{B}^0)\\ &= \frac{1}{N_\eta}\int dt_2\int dt_1\left(\left|\langle\bar{B}^0B^0|B^0(t_1)\bar{B}^0(t_2)\rangle\right|^2+\left|\langle\bar{B}^0\bar{B}^0|B^0(t_1)\bar{B}^0(t_2)\rangle\right|^2\right)\\ &= \frac{x^4+y^4+(2-\eta)(x^2-y^2)+\eta x^2y^2(x^2-y^2+4)+2}{2(1+\eta y^2)(1+x^2)^2}.\end{aligned} \tag{A.11}$$

As a cross check, one can integrate Eq. A.7 over Δt and verify to arrive at the same expression for $\eta=0$ in Eqs. A.10 and A.11. [58]

A.3 Convolution with Resolution function *R*

The convolution here will be discussed in a more general way. The total resolution function consists of the sum of the outlier (OL) and core part, seen here

$$R(\delta\Delta t;\sigma)=(1-f_{\mathrm{OL}})R_{\mathrm{core}}(\delta\Delta t;\sigma)+f_{\mathrm{OL}}R_{\mathrm{OL}}(\delta\Delta t;\sigma), \tag{A.12}$$

with f_{OL} the fraction of outlier events. $R_{\mathrm{core}}(\delta\Delta t;\sigma)$ is a sum of two single Gaussians and a Gaussian convoluted with the right- and left-side exponential tail:

$$\begin{aligned}R_{\mathrm{core}}(\delta\Delta t;\sigma)=&(1-f_{\mathrm{tail}})\cdot G(\delta\Delta t;\mu_{\mathrm{main}}\cdot\sigma,s_{\mathrm{main}}\cdot\sigma)\\ &+f_{\mathrm{tail}}(1-f_{\mathrm{exp}})\cdot G(\delta\Delta t;\mu_{\mathrm{tail}}\cdot\sigma,s_{\mathrm{tail}}\cdot\sigma)\\ &+f_{\mathrm{tail}}\cdot f_{\mathrm{exp}}\cdot G(\delta\Delta t;\mu_{\mathrm{tail}}\cdot\sigma,s_{\mathrm{tail}}\cdot\sigma)\\ &\otimes((1-f_{\mathrm{R}})\mathrm{exp}_{\mathrm{L}}(\delta\Delta t/c\cdot\sigma)+f_{\mathrm{R}}\mathrm{exp}_{\mathrm{R}}(-\delta\Delta t/c\cdot\sigma))\end{aligned} \tag{A.13}$$

We can look at the convolution of the decay probability distribution for variable Δt from equation A.7 with the resolution function in a general way. Due to linearity in the convolution integral it is sufficient to look at one case which is easily extended to a multi-Gaussian resolution function [59]. The integral of interest reads:

$$f(t;\Gamma,\Delta m,\sigma,\mu)=\int_{-\infty}^{+\infty}\mathrm{d}t' P_{\mathrm{SD}}(t')G(t-t',\mu,\sigma), \tag{A.14}$$

with

$$G(t-t',\mu,\sigma)=\frac{1}{\sqrt{2\pi\sigma^2}}e^{-\frac{(t-t'-\mu)^2}{2\sigma^2}}. \tag{A.15}$$

For the following derivation some functions have to be defined first, beginning with the Euler's formula, which states for any real x

$$e^{ix}=\cos x+i\sin x. \tag{A.16}$$

A special functions used frequently are error function (erf), the complementary error function (erfc), and the Faddeeva function (w). The error function, denoted as $\mathrm{erf}(x)$, is defined as:

$$\mathrm{erf}(x)=\frac{2}{\sqrt{\pi}}\int_0^x e^{-t^2}\,\mathrm{d}t, \tag{A.17}$$

and it measures the probability that a normally distributed random variable will fall within the range $[-x,x]$. The complementary error function, $\mathrm{erfc}(x)$, complements $\mathrm{erf}(x)$ and is given by:

$$\mathrm{erfc}(x)=1-\mathrm{erf}(x). \tag{A.18}$$

It is often used in calculations involving Gaussian distributions. Additionally, the Faddeeva function, denoted as $w(z)$, is a complex function related to the error function, commonly used in wave propagation and signal processing, and is defined as:

$$w(z)=e^{-z^2}\left(1+\frac{2i}{\sqrt{\pi}}\int_0^z e^{t^2}\,\mathrm{d}t\right). \tag{A.19}$$

These functions are integral in deriving the final form of the convolution in the following. Using this eq. A.7 can be rewritten in terms of complex exponential functions which forms the convolution integral

$$\begin{aligned} f(t';\Gamma,\omega,\sigma,\mu)=&\frac{1}{\sqrt{2\pi\sigma^2}}\int_0^{+\infty}\mathrm{d}t'\,e^{(\Gamma-i\omega)|t'|}\,e^{-\frac{t+|t'|+\mu}{2\sigma^2}},\quad t'>0, && \text{(A.20)}\\ =&\frac{1}{\sqrt{\pi}}\int_0^{+\infty}\mathrm{d}y\,e^{-x^2+(z-x)^2}e^{-(y-(z-x))^2} && \text{(A.21)}\\ =&\frac{1}{\sqrt{\pi}}e^{-x^2+(z-x)^2}\int_0^{+\infty}\mathrm{d}y\,e^{-(y-(z-x))^2}, && \text{(A.22)}\end{aligned}$$

where substitution $z=(\Gamma-i\omega)\sigma/\sqrt{2}$, $x=(t+\mu)/\sqrt{2\sigma^2}$ and $y=|t'|/\sqrt{2\sigma^2}$ is used. Shifting the integral limits to $(z-x)$ yields

$$\begin{aligned}
f(x;z) =& e^{-x^2+(z-x)^2}\frac{1}{\sqrt{\pi}}\int_{(z-x)}^{+\infty}\mathrm{d}y\, e^{-y^2} && \text{(A.23)}\\
=& e^{-x^2+(z-x)^2}\cdot\frac{1}{\sqrt{\pi}}\frac{\sqrt{\pi}}{2}(\mathrm{erf}(z-x)+1) && \text{(A.24)}\\
=& e^{-x^2+(z-x)^2}\cdot\frac{1}{2}(1+\mathrm{erf}(-(z-x))) && \text{(A.25)}\\
=& e^{-x^2+(z-x)^2}\cdot\frac{1}{2}(1-\mathrm{erf}(z-x)) && \text{(A.26)}\\
=& e^{-x^2}\cdot\frac{1}{2}\,e^{(z-x)^2}\mathrm{erfc}(z-x) && \text{(A.27)}\\
=& e^{-x^2}\cdot\frac{1}{2}\,e^{-(i(z-x))^2}\mathrm{erfc}(z-x) && \text{(A.28)}\\
=& \frac{1}{2}\,e^{-x^2}\cdot w(i(x-z)). && \text{(A.29)}
\end{aligned}$$

Here, the symmetry property of the error function $\mathrm{erf}(-x)=-\mathrm{erf}(x)$ in Eq. A.26 is used. In Eq. A.27 and Eq. A.29 the properties Eq. A.18 and Eq. A.22 are used, respectively.

The total integrated form of the integral is: (getnflav)

$$\frac{\varepsilon n}{4}\cdot\left(1-\alpha\left(1-\frac{\zeta}{2}\right)-\beta\left[\frac{1}{1+\Delta m_d^2\tau^2}-\frac{\zeta}{2}\frac{1-2\Delta m_d\tau}{(1+\Delta m_d^2\tau^2)^2}\right]\right), \qquad \text{(A.30)}$$

with

$$\alpha = q_{tag}(\Delta w+\mu\cdot(1-2w)),$$

and

$$\beta = q_{sig}(\mu(1-q_{tag}\Delta w)+q_{tag}(1-2w)).$$

B Analysis on Signal MC sample

B.1 ΔE fits on Signal MC with 20%, 40%, 60% and 80% PSD

In this section supplementary tables for Sec. 5.1.2 can be found. Tabs. B.5 - B.8 show Δt fit parameters' values for Signal MC with 20%, 40%, 60% and 80% fraction of disentanglement, respectively. As expected, no significant deviations in shapes and fit values across the different Signal MC samples can be observed. Moreover, the fit values are in expected ranges, particularly the mean μ_{DeltaE} for all fits which are in the $\mathcal{O}(10^{-5})$, close to the theoretical value of $\Delta E = 0$.

Parameter	Mean	Uncertainty
$n_{\Delta E}$	238990	488
$\mu_{\Delta E}$	$-7.89 \cdot 10^{-5}$	$2.70 \cdot 10^{-5}$
$\sigma_{\Delta E}$	$8.19 \cdot 10^{-3}$	$0.07 \cdot 10^{-3}$
α_L	1.3100	0.0503
α_R	1.5371	0.0459
n_L	1.7759	0.0600
n_R	2.3702	0.0589
σ_{Gauss}	0.0096	0.0001
f_{Gauss}	0.4314	0.0278

Table B.1: ΔE fit parameters for Signal MC with 20% disentanglement.

Parameter	Mean	Uncertainty
$n_{\Delta E}$	318740	564
$\mu_{\Delta E}$	$-10.2 \cdot 10^{-5}$	$2.34 \cdot 10^{-5}$
$\sigma_{\Delta E}$	$8.25 \cdot 10^{-3}$	$0.08 \cdot 10^{-3}$
α_L	1.3387	0.0488
α_R	1.5647	0.0458
n_L	1.7646	0.0538
n_R	2.3537	0.0552
σ_{Gauss}	0.0097	0.0001
f_{Gauss}	0.4120	0.0287

Table B.2: ΔE fit parameters for Signal MC with 40% disentanglement.

Parameter	Mean	Uncertainty
$n_{\Delta E}$	318920	564
$\mu_{\Delta E}$	$-12.20 \cdot 10^{-5}$	$2.27 \cdot 10^{-5}$
$\sigma_{\Delta E}$	$8.33 \cdot 10^{-3}$	$0.07 \cdot 10^{-3}$
α_L	1.3805	0.0444
α_R	1.6084	0.0422
n_L	1.7353	0.0496
n_R	2.3130	0.0523
σ_{Gauss}	0.0097	0.0002
f_{Gauss}	0.3896	0.0281

Table B.3: ΔE fit parameters for Signal MC with 60% disentanglement.

Parameter	Mean	Uncertainty
$n_{\Delta E}$	239234	489
$\mu_{\Delta E}$	$-12.82 \cdot 10^{-5}$	$2.59 \cdot 10^{-5}$
$\sigma_{\Delta E}$	$8.33 \cdot 10^{-3}$	$0.07 \cdot 10^{-3}$
α_L	1.4172	0.0434
α_R	1.6462	0.0415
n_L	1.7209	0.0526
n_R	2.2779	0.0550
σ_{Gauss}	0.0099	0.0002
f_{Gauss}	0.3572	0.0285

Table B.4: ΔE fit parameters for Signal MC with 80% disentanglement.

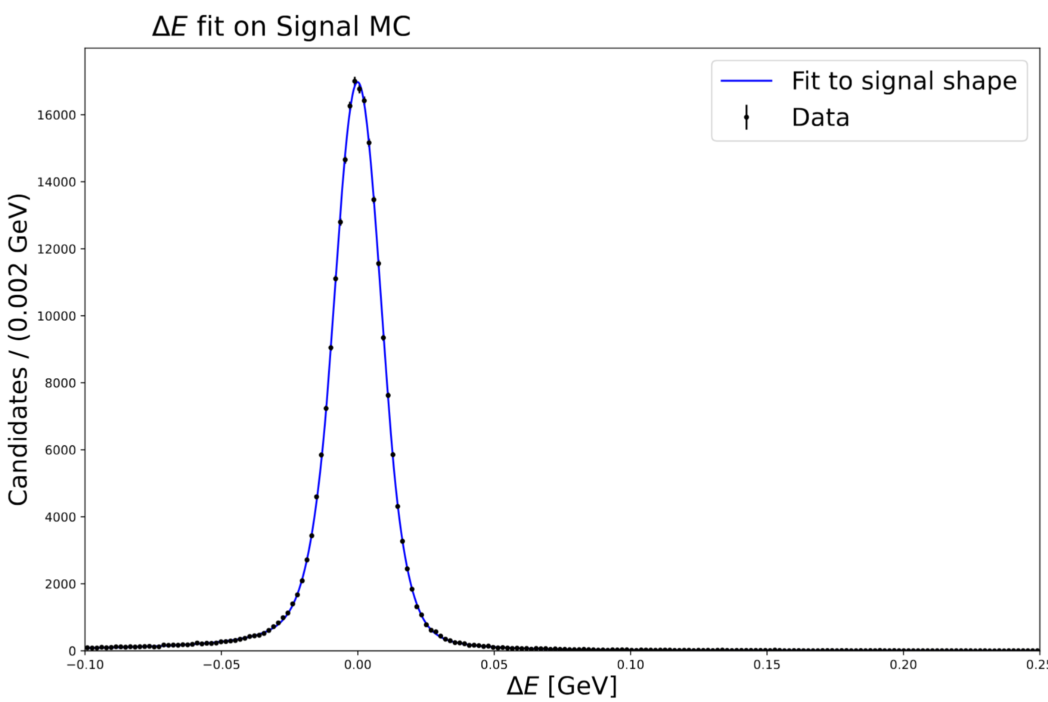

Figure B.1: Fit to the ΔE distribution Signal MC events with 20% disentanglement, using double-sided Crystal Ball shape.

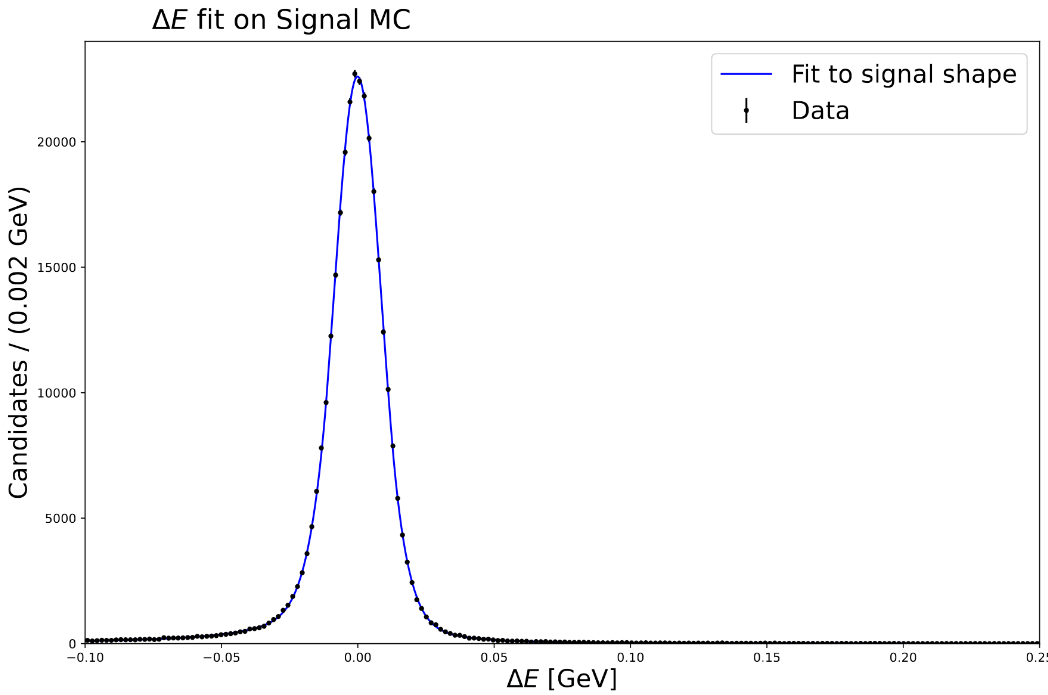

Figure B.2: Fit to the ΔE distribution Signal MC events with 40% disentanglement, using double-sided Crystal Ball shape.

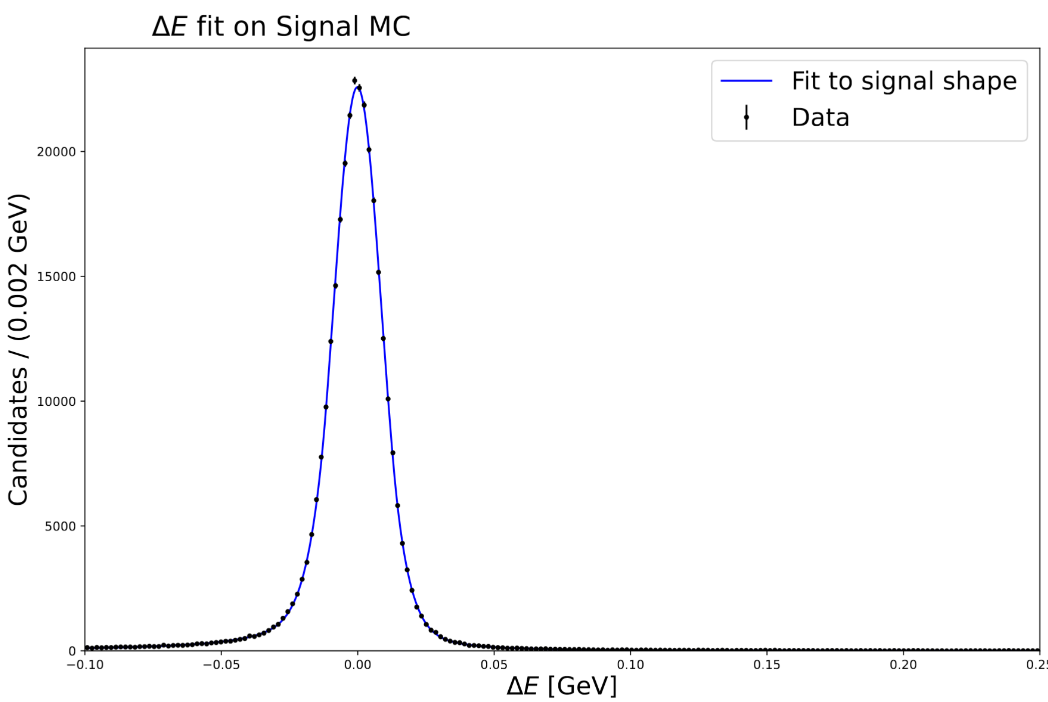

Figure B.3: Fit to the ΔE distribution Signal MC events with 60% disentanglement, using double-sided Crystal Ball shape.

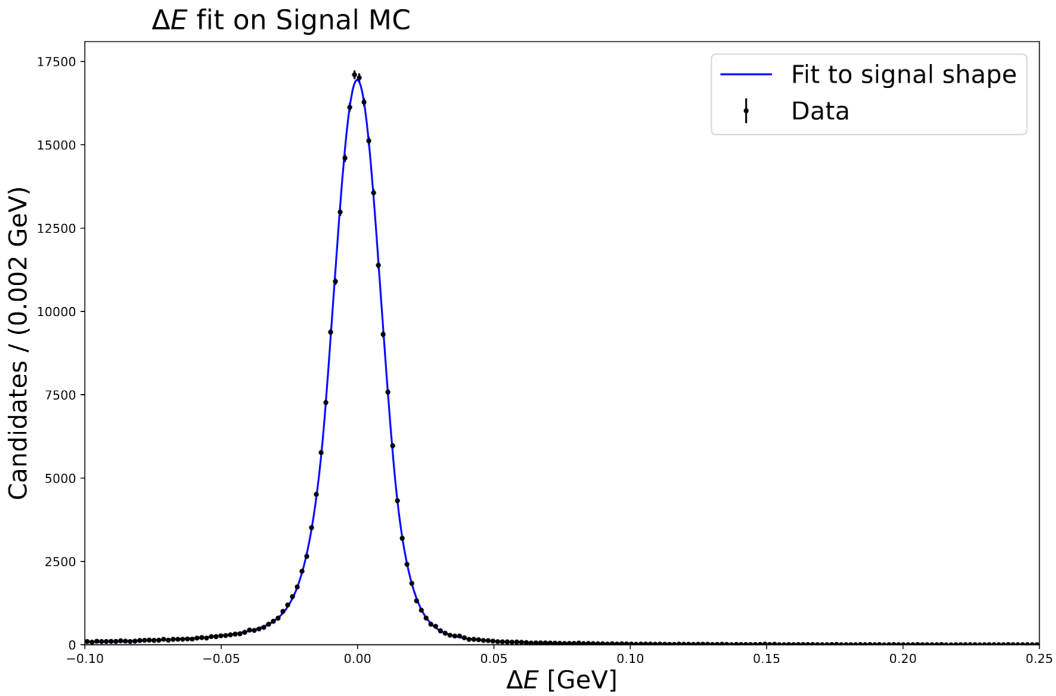

Figure B.4: Fit to the ΔE distribution Signal MC events with 80% disentanglement, using double-sided Crystal Ball shape.

B.2 $\delta\Delta t$ fits on Signal MC with 20%, 40%, 60% and 80% PSD

In this section supplementary tables for Sec. 5.1.2 can be found. Tabs. B.5 - B.8 show the fit parameters' values for Signal MC with 20%, 40%, 60% and 80% fraction of disentanglement, respectively. All fit values are in agreement with corresponding parameter values in fits on different MC samples. This is unsurprising, however an important test to control if there has been any mistakes made during the sampling of data sets.

Parameter	Fit estimate
f_{OL}	0.0014 ± 0.0001
μ_{Main}	-0.2393 ± 0.0064
μ_{Tail}	-0.9911 ± 0.0393
σ_{Main}	1.1959 ± 0.0079
σ_{Tail}	2.3473 ± 0.0466
f_{Tail}	0.2898 ± 0.0102
f_{exp}	0.2142 ± 0.0080
c_1 [ps^2]	5.1032 ± 0.1488
$f_{\text{Tail, R}}$	0.2636 ± 0.0098
$f_{\text{Tail},\mu}$	0.1914 ± 0.0043
$f_{\text{Tail},\sigma}$	0.0611 ± 0.0053
$\mu^{(6)}_{\text{Main}}$	-0.1737 ± 0.0101
$\mu^{(6)}_{\text{Tail}}$	-0.7857 ± 0.0687
$\sigma^{(6)}_{\text{Main}}$	1.1915 ± 0.0128
$\sigma^{(6)}_{\text{Tail}}$	2.3126 ± 0.0920
$f^{(6)}_{\text{Tail}}$	0.2556 ± 0.0190
$f^{(6)}_{\text{exp}}$	0.2360 ± 0.0159
$c^{(6)}_1$ [ps^2]	5.2399 ± 0.2288
$f^{(6)}_{\text{Tail, R}}$	0.2792 ± 0.0180

Table B.5: Parameters from $\delta\Delta t$ residual fit on Signal MC with 20% disentanglement. Superscript 6 represents the 6th qr-bin, which is fitted separately.

Parameter	Fit estimate
f_{OL}	0.0014 ± 0.0001
μ_{Main}	-0.2381 ± 0.0056
μ_{Tail}	-0.9825 ± 0.0339
σ_{Main}	1.1924 ± 0.0069
σ_{Tail}	2.3215 ± 0.0398
f_{Tail}	0.2953 ± 0.0091
f_{exp}	0.2171 ± 0.0070
c_1 [ps^2]	4.9679 ± 0.1229
$f_{\text{Tail, R}}$	0.2632 ± 0.0084
$f_{\text{Tail},\mu}$	0.1954 ± 0.0032
$f_{\text{Tail},\sigma}$	0.0570 ± 0.0040
$\mu^{(6)}_{\text{Main}}$	-0.1853 ± 0.0079
$\mu^{(6)}_{\text{Tail}}$	-0.7420 ± 0.0590
$\sigma^{(6)}_{\text{Main}}$	1.1924 ± 0.0105
$\sigma^{(6)}_{\text{Tail}}$	2.3832 ± 0.0828
$f^{(6)}_{\text{Tail}}$	0.2450 ± 0.0151
$f^{(6)}_{\text{exp}}$	0.2405 ± 0.0139
$c^{(6)}_1$ [ps^2]	5.3139 ± 0.2043
$f^{(6)}_{\text{Tail, R}}$	0.2613 ± 0.0154

Table B.6: Parameters from $\delta\Delta t$ residual fit on Signal MC with 40% disentanglement. Superscript 6 represents the 6th qr-bin, which is fitted separately.

Parameter	Fit estimate
f_{OL}	0.0014 ± 0.0001
μ_{Main}	-0.2374 ± 0.0065
μ_{Tail}	-0.9841 ± 0.0399
σ_{Main}	1.1934 ± 0.0080
σ_{Tail}	2.3024 ± 0.0458
f_{Tail}	0.2954 ± 0.0107
f_{exp}	0.2221 ± 0.0082
c_1 [ps^2]	4.8962 ± 0.1358
$f_{\text{Tail, R}}$	0.2668 ± 0.0098
$f_{\text{Tail},\mu}$	0.1986 ± 0.0032
$f_{\text{Tail},\sigma}$	0.0521 ± 0.0040
$\mu^{(6)}_{\text{Main}}$	-0.1860 ± 0.0087
$\mu^{(6)}_{\text{Tail}}$	-0.6997 ± 0.0696
$\sigma^{(6)}_{\text{Main}}$	1.1883 ± 0.0120
$\sigma^{(6)}_{\text{Tail}}$	2.4169 ± 0.0986
$f^{(6)}_{\text{Tail}}$	0.2394 ± 0.0169
$f^{(6)}_{\text{exp}}$	0.2426 ± 0.0162
$c^{(6)}_1$ [ps^2]	5.3175 ± 0.2339
$f^{(6)}_{\text{Tail, R}}$	0.2263 ± 0.0172

Table B.7: Parameters from $\delta\Delta t$ residual fit on Signal MC with 60% disentanglement. Superscript 6 represents the 6th qr-bin, which is fitted separately.

Parameter	Fit estimate
f_{OL}	0.0014 ± 0.0001
μ_{Main}	-0.2306 ± 0.0055
μ_{Tail}	-0.9267 ± 0.0296
σ_{Main}	1.1830 ± 0.0067
σ_{Tail}	2.2489 ± 0.0342
f_{Tail}	0.9960 ± 0.0614
f_{exp}	0.2193 ± 0.0064
c_1 [ps^2]	4.8201 ± 0.1009
$f_{\text{Tail, R}}$	0.2623 ± 0.0079
$f_{\text{Tail},\mu}$	-0.1002 ± 0.0098
$f_{\text{Tail},\sigma}$	0.2119 ± 0.0055
$\mu^{(6)}_{\text{Main}}$	-0.1640 ± 0.0095
$\mu^{(6)}_{\text{Tail}}$	-0.5955 ± 0.0547
$\sigma^{(6)}_{\text{Main}}$	1.1479 ± 0.0154
$\sigma^{(6)}_{\text{Tail}}$	2.1248 ± 0.0869
$f^{(6)}_{\text{Tail}}$	0.9763 ± 0.1141
$f^{(6)}_{\text{exp}}$	0.2229 ± 0.0134
$c^{(6)}_1$ [ps^2]	4.9543 ± 0.1726
$f^{(6)}_{\text{Tail, R}}$	0.2436 ± 0.0130

Table B.8: Parameters from $\delta\Delta t$ residual fit on Signal MC with 80% disentanglement. Superscript 6 represents the 6th qr-bin, which is fitted separately.

B.3 Single Δt fits

B.3.1 Δt fits on Signal MC with full entanglement and full disentanglement in qr-bin 0-5

In this section the single Δt fits for full entanglement and disentanglement in qr bins 0-5, supplementary to the plots shown in Sec. 5.1.3. The result shown here are fitted simultaneously with results in qr-bin 6 presented in Sec. 5.1.3. Figs. B.3.1 and B.3.1 show the fits for full entanglement and disentanglement, respectively. Tabs. B.9 and B.10 show all fitted parameters, including those already shown in the main Sec. 5.1.3.

Parameter	Mean	Uncertainty
ζ	0.0153	0.0319
μ_{M1}	-0.1977	0.0376
σ_{M1}	1.0767	0.0399
$\mu_{M1}^{(6)}$	0.0211	0.0362
$\sigma_{M1}^{(6)}$	1.1091	0.0694
f_{Tail}	0.3803	0.0155
w_0^+	0.4814	0.0055
w_0^-	0.4764	0.0054
μ_0	-0.0274	0.0087
w_1^+	0.4187	0.0050
w_1^-	0.4071	0.0049
μ_1	-0.0135	0.0078
w_2^+	0.3232	0.0048
w_2^-	0.3198	0.0048
μ_2	-0.0146	0.0074
w_3^+	0.2385	0.0058
w_3^-	0.2400	0.0056
μ_3	-0.0166	0.0087
w_4^+	0.1670	0.0060
w_4^-	0.1685	0.0060
μ_4	-0.0090	0.0094
w_5^+	0.1017	0.0055
w_5^-	0.1050	0.0053
μ_5	-0.0188	0.0080
w_6^+	0.0204	0.0047
w_6^-	0.0166	0.0046
μ_6	-0.0051	0.0054

Table B.9: Single Δt-fit parameters on Signal MC with PSD fraction of $\zeta^{\text{MC}} = 0.$. The superscript 6 for resolution function parameters denotes the 6th qr-bin. The indices $i = 0, ..., 6$ for the flavor tagger parameters denote the i-th qr-bin.

B.3.2 Δt fits on Signal MC with 20% 40% 60% and 80% PSD

This section contains further single Δt fits results presented in Sec. 5.1.3. The results shown here are Signal MC fits with $\zeta_{\text{gen}} = 0.2,\ 0.4,\ 0.6,\ 0.8$ for all qr-bins. Key parameter ζ's fit values are summarized in Tab. 5.6.

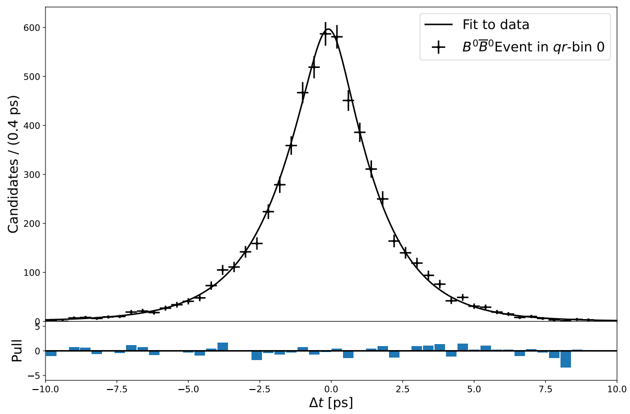
Fit to data
$B^0\overline{B}^0$Event in qr-bin 0
Candidates / (0.4 ps)
Pull
Δt [ps]

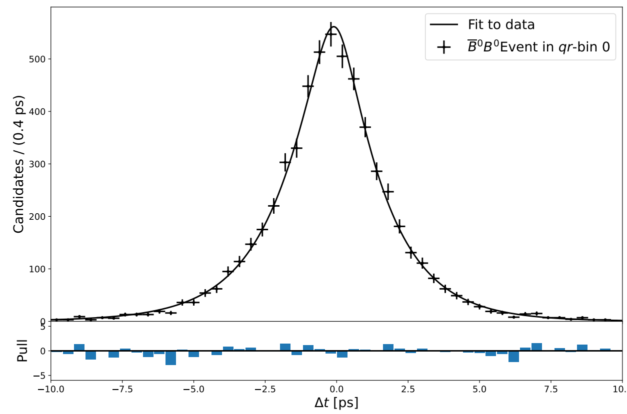
Fit to data
$\overline{B}^0B^0$Event in qr-bin 0
Candidates / (0.4 ps)
Pull
Δt [ps]

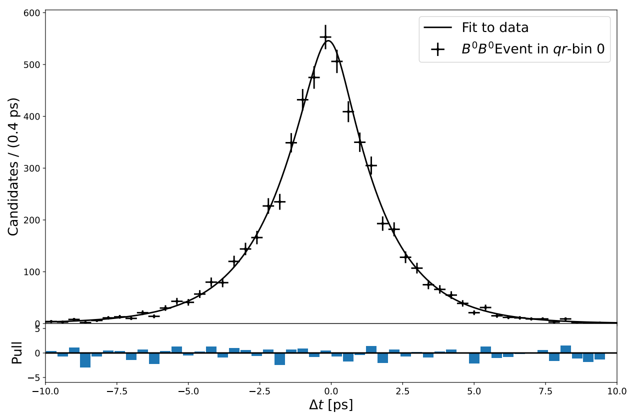
Fit to data
$B^0\overline{B}^0$Event in qr-bin 0
Candidates / (0.4 ps)
Pull
Δt [ps]

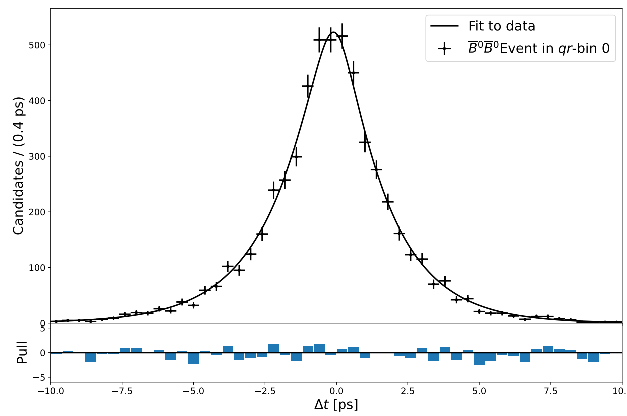
Fit to data
$\overline{B}^0\overline{B}^0$Event in qr-bin 0
Candidates / (0.4 ps)
Pull
Δt [ps]

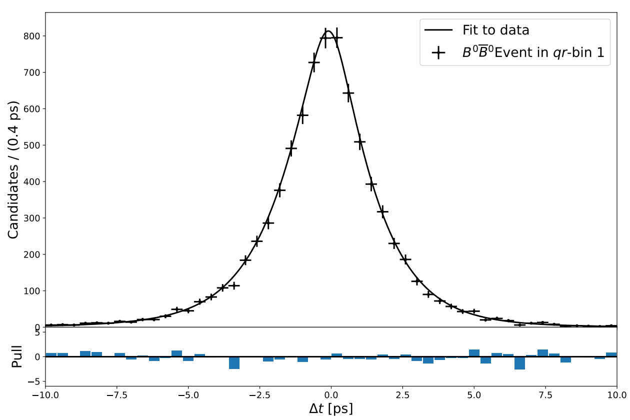
Fit to data
$B^0\overline{B}^0$Event in qr-bin 1
Candidates / (0.4 ps)
Pull
Δt [ps]

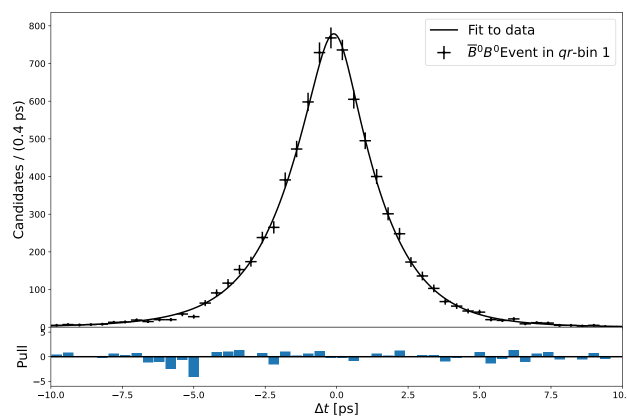
Fit to data
$\overline{B}^0B^0$Event in qr-bin 1
Candidates / (0.4 ps)
Pull
Δt [ps]

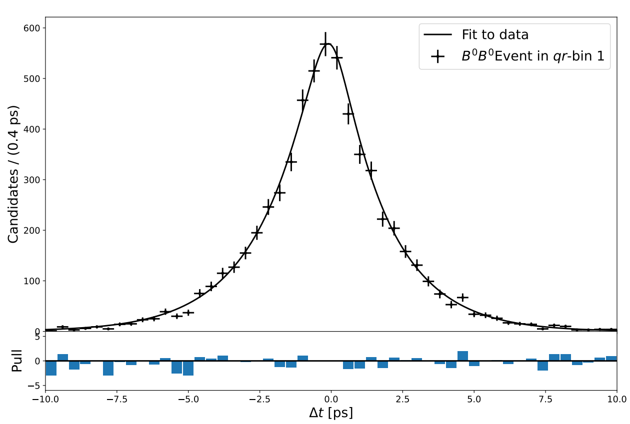
Fit to data
B^0B^0Event in qr-bin 1
Candidates / (0.4 ps)
Pull
Δt [ps]

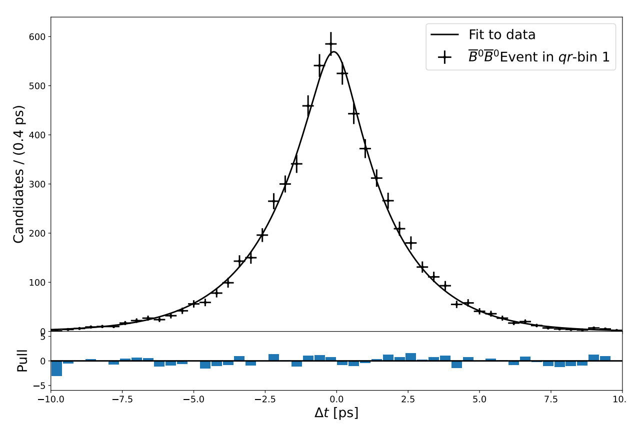
Fit to data
$\overline{B}^0\overline{B}^0$Event in qr-bin 1
Candidates / (0.4 ps)
Pull
Δt [ps]

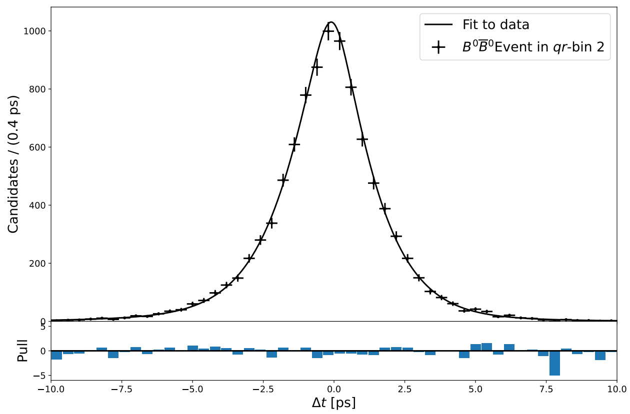
Fit to data
$B^0\overline{B}^0$Event in qr-bin 2
Candidates / (0.4 ps)
Pull
Δt [ps]

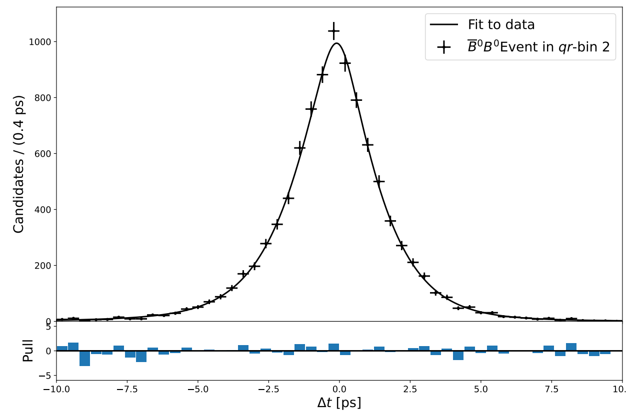
Fit to data
$\overline{B}^0B^0$Event in qr-bin 2
Candidates / (0.4 ps)
Pull
Δt [ps]

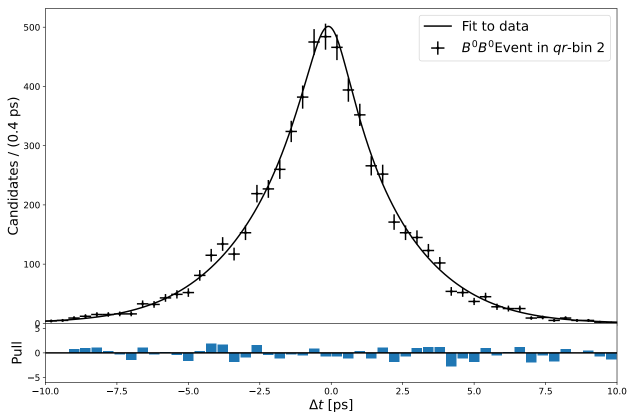
Fit to data
B^0B^0Event in qr-bin 2
Candidates / (0.4 ps)
Pull
Δt [ps]

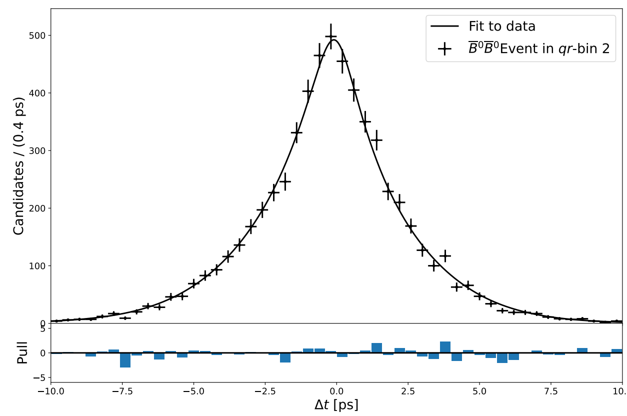
Fit to data
$\overline{B}^0\overline{B}^0$Event in qr-bin 2
Candidates / (0.4 ps)
Pull
Δt [ps]

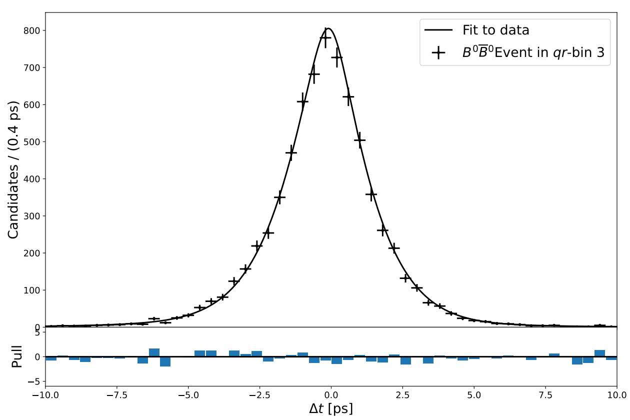
Fit to data
$B^0\overline{B}^0$Event in qr-bin 3
Candidates / (0.4 ps)
Pull
Δt [ps]

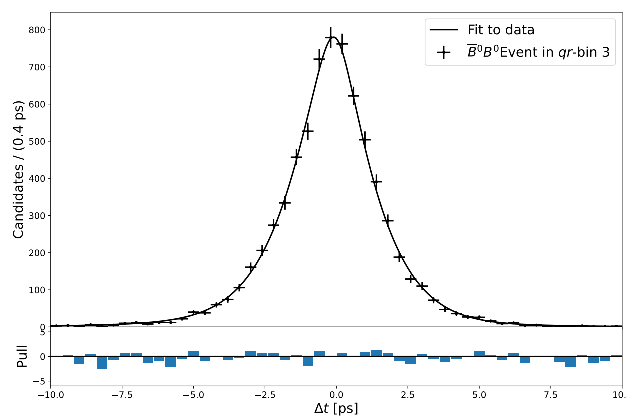
Fit to data
$\overline{B}^0B^0$Event in qr-bin 3
Candidates / (0.4 ps)
Pull
Δt [ps]

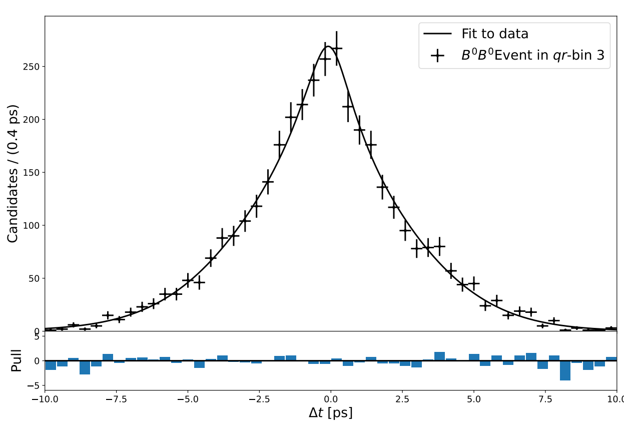
Fit to data
B^0B^0Event in qr-bin 3
Candidates / (0.4 ps)
Pull
Δt [ps]

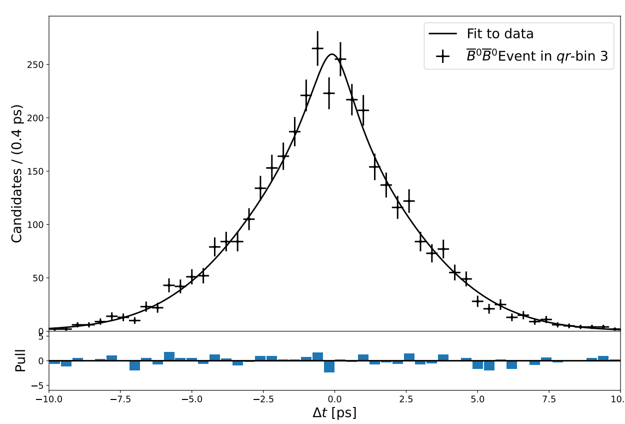
Fit to data
$\overline{B}^0\overline{B}^0$Event in qr-bin 3
Candidates / (0.4 ps)
Pull
Δt [ps]

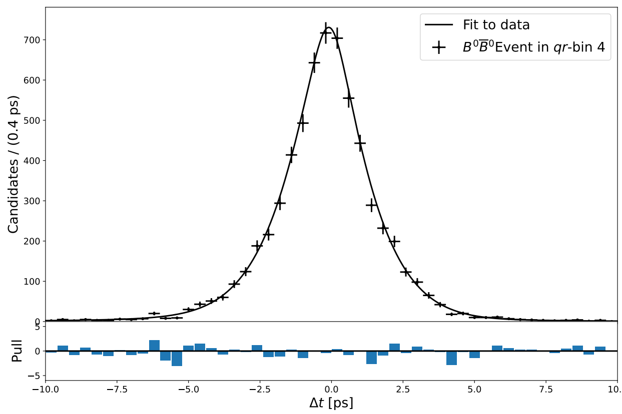
Fit to data
$B^0\overline{B}^0$Event in qr-bin 4
Candidates / (0.4 ps)
Pull
Δt [ps]

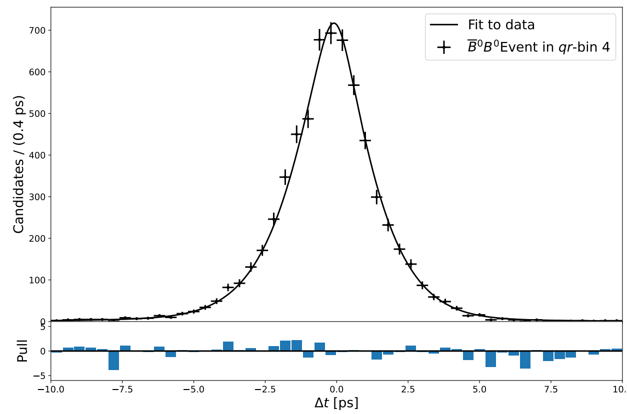
Fit to data
$\overline{B}^0B^0$Event in qr-bin 4
Candidates / (0.4 ps)
Pull
Δt [ps]

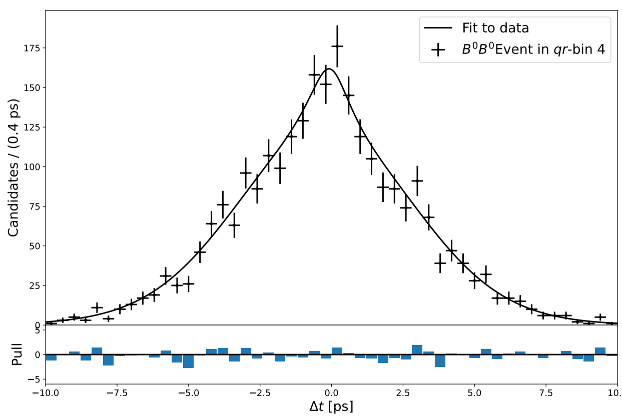
Fit to data
B^0B^0Event in qr-bin 4
Candidates / (0.4 ps)
Pull
Δt [ps]

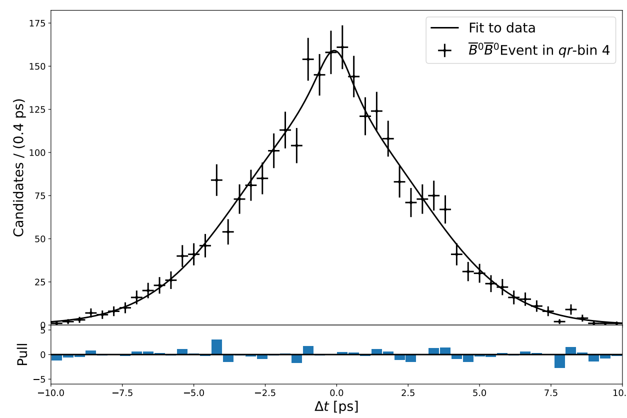
Fit to data
$\overline{B}^0\overline{B}^0$Event in qr-bin 4
Candidates / (0.4 ps)
Pull
Δt [ps]

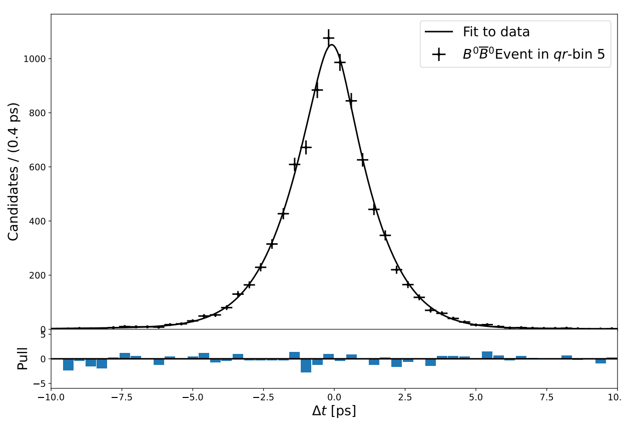
Fit to data
$B^0\overline{B}^0$Event in qr-bin 5
Candidates / (0.4 ps)
Pull
Δt [ps]

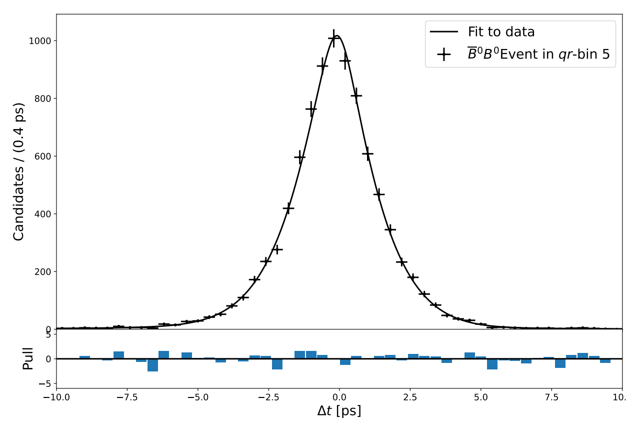
Fit to data
$\overline{B}^0B^0$Event in qr-bin 5
Candidates / (0.4 ps)
Pull
Δt [ps]

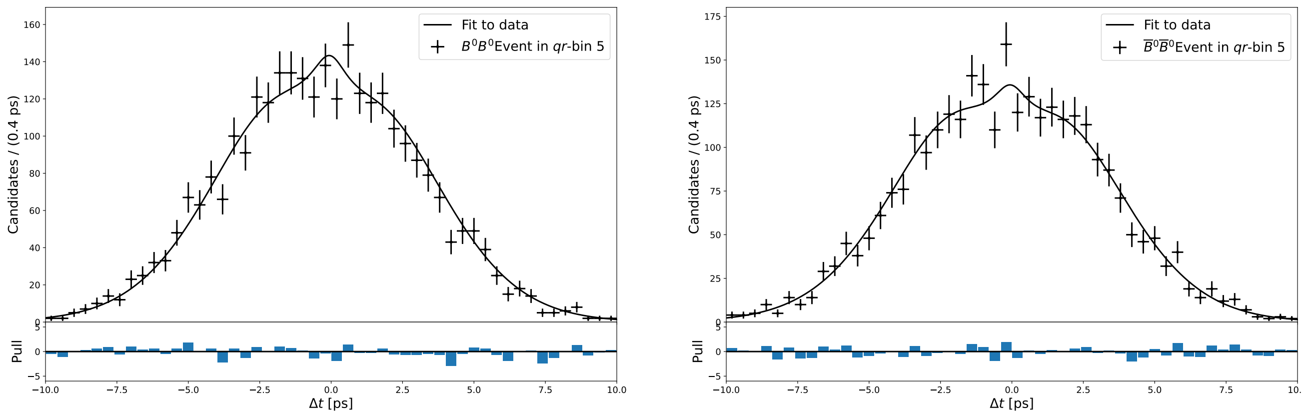

Figure B.5: Δt-distribution fitted to Signal MC data with full entanglement ($\zeta_{\text{gen}} = 0$). Error bars show Signal MC data for qr bins 0-5 (left to right, top to bottom) and solid line shows the fit. The lower plot show the pulls.

Parameter	Mean	Uncertainty
ζ	1.0279	0.0243
μ_{M1}	-0.1625	0.0354
σ_{M1}	1.0137	0.0400
f_{Tail}	0.3910	0.0159
$\mu_{M1}^{(6)}$	0.0447	0.0360
$\sigma_{M1}^{(6)}$	0.9536	0.0749
w_0^+	0.4772	0.0070
w_0^-	0.4772	0.0069
μ_0	-0.0164	0.0122
w_1^+	0.4195	0.0063
w_1^-	0.4063	0.0062
μ_1	-0.0169	0.0109
w_2^+	0.3301	0.0062
w_2^-	0.3309	0.0060
μ_2	-0.0312	0.0103
w_3^+	0.2367	0.0074
w_3^-	0.2344	0.0074
μ_3	-0.0023	0.0122
w_4^+	0.1671	0.0082
w_4^-	0.1750	0.0081
μ_4	-0.0112	0.0132
w_5^+	0.0891	0.0075
w_5^-	0.0945	0.0074
μ_5	-0.0124	0.0113
w_6^+	0.0090	0.0063
w_6^-	0.0203	0.0060
μ_6	-0.0207	0.0079

Table B.10: Single Δt-fit parameters on Signal MC with PSD fraction of $\zeta^{\text{MC}} = 1.$. The superscript 6 for resolution function parameters denotes the 6th qr-bin. The indices $i = 0, ..., 6$ for the flavor tagger parameters denote the i-th qr-bin.

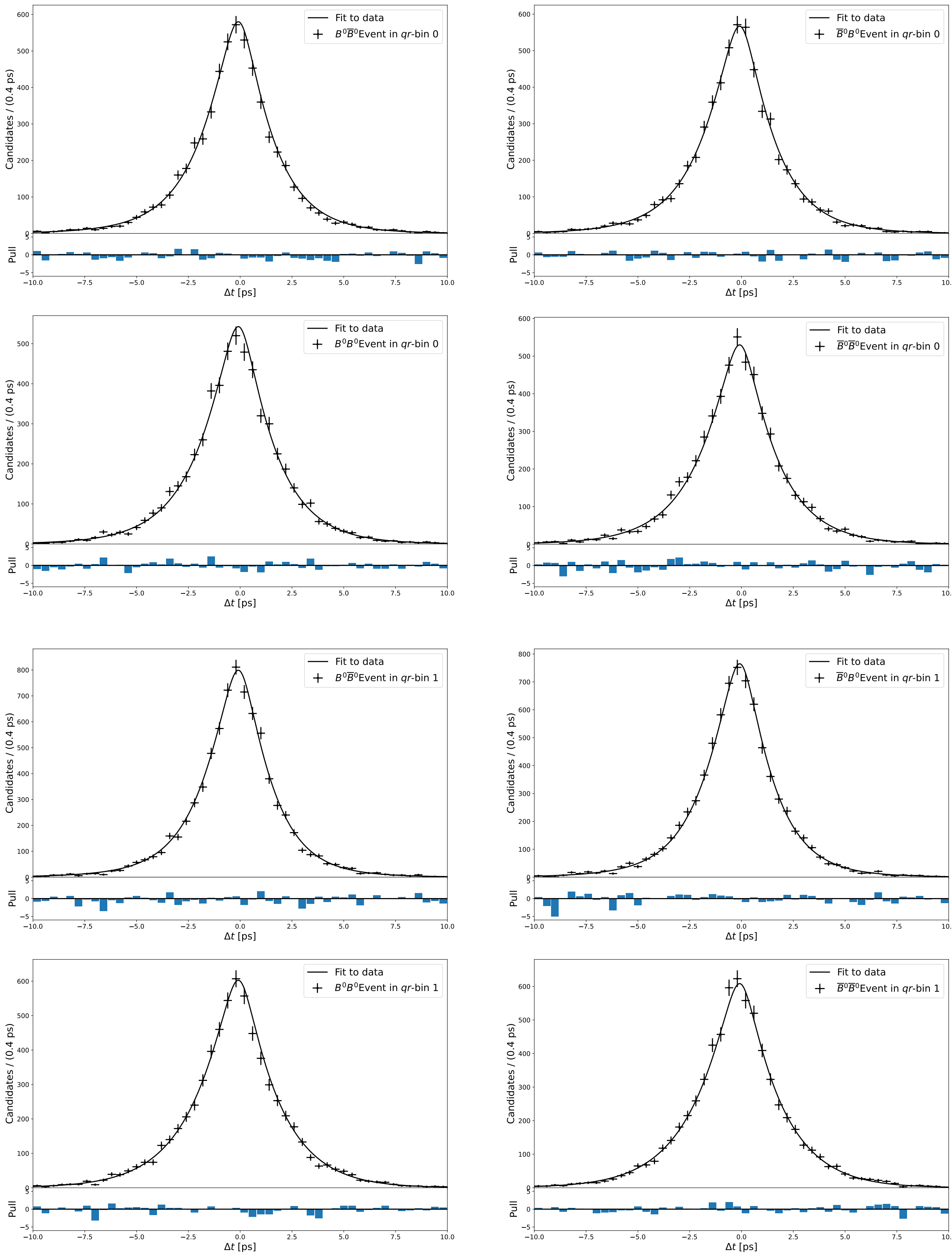

Fit to data
$B^0\overline{B}^0$Event in qr-bin 0
Fit to data
$\overline{B}^0B^0$Event in qr-bin 0
Fit to data
B^0B^0Event in qr-bin 0
Fit to data
$\overline{B}^0\overline{B}^0$Event in qr-bin 0
Fit to data
$B^0\overline{B}^0$Event in qr-bin 1
Fit to data
$\overline{B}^0B^0$Event in qr-bin 1
Fit to data
B^0B^0Event in qr-bin 1
Fit to data
$\overline{B}^0\overline{B}^0$Event in qr-bin 1
Candidates / (0.4 ps)
Pull
Δt [ps]

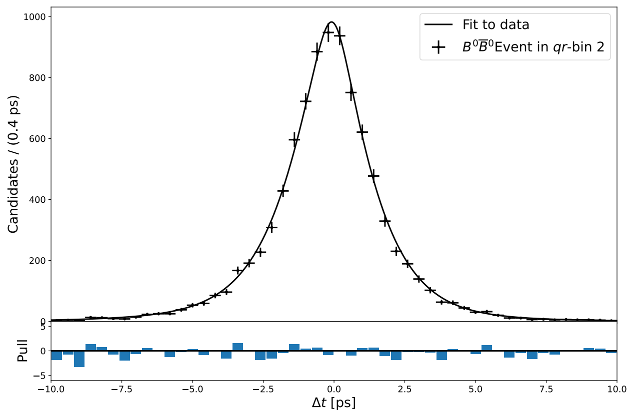
Fit to data
$B^0\overline{B}^0$Event in qr-bin 2
Candidates / (0.4 ps)
Pull
Δt [ps]

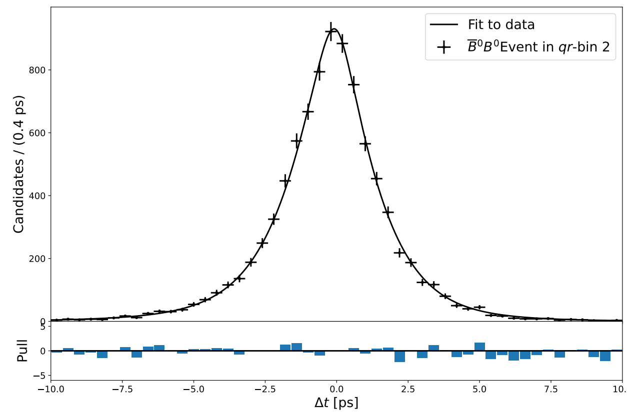
Fit to data
$\overline{B}^0B^0$Event in qr-bin 2
Candidates / (0.4 ps)
Pull
Δt [ps]

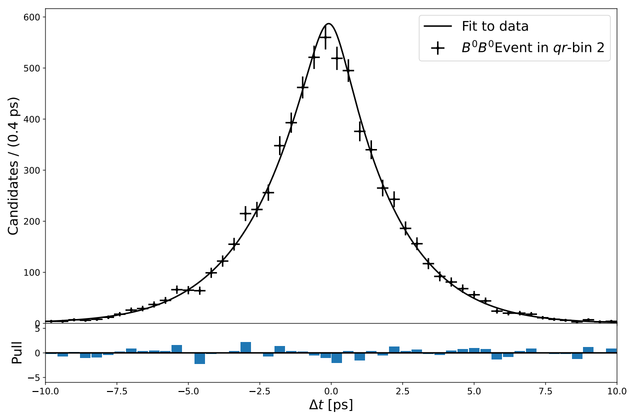
Fit to data
B^0B^0Event in qr-bin 2
Candidates / (0.4 ps)
Pull
Δt [ps]

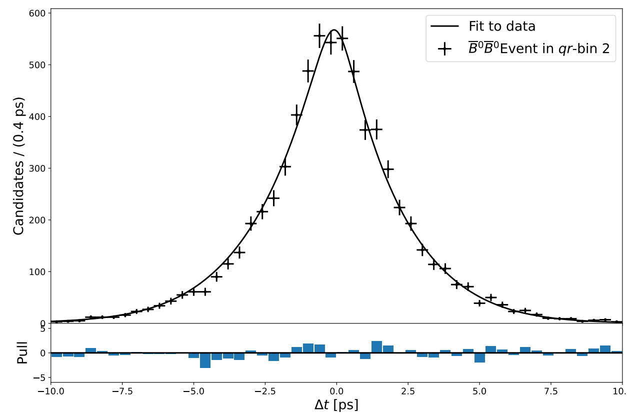
Fit to data
$\overline{B}^0\overline{B}^0$Event in qr-bin 2
Candidates / (0.4 ps)
Pull
Δt [ps]

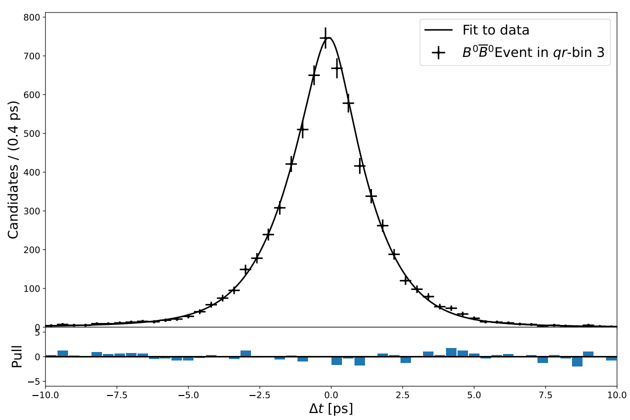
Fit to data
$B^0\overline{B}^0$Event in qr-bin 3
Candidates / (0.4 ps)
Pull
Δt [ps]

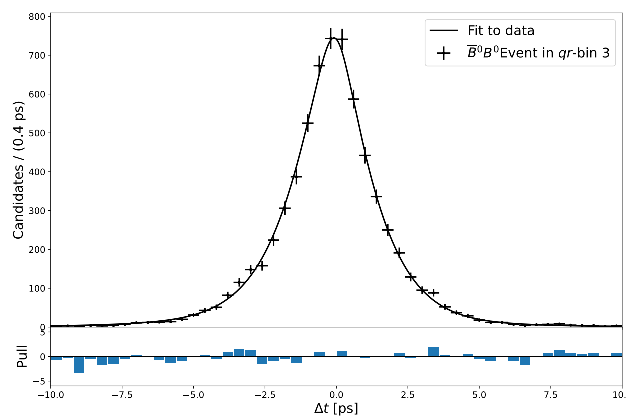
Fit to data
$\overline{B}^0B^0$Event in qr-bin 3
Candidates / (0.4 ps)
Pull
Δt [ps]

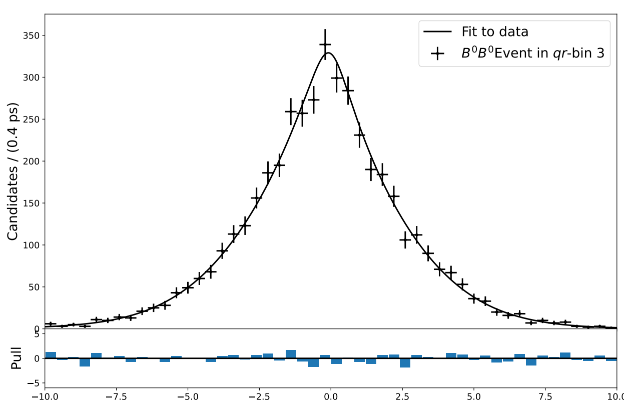
Fit to data
B^0B^0Event in qr-bin 3
Candidates / (0.4 ps)
Pull
Δt [ps]

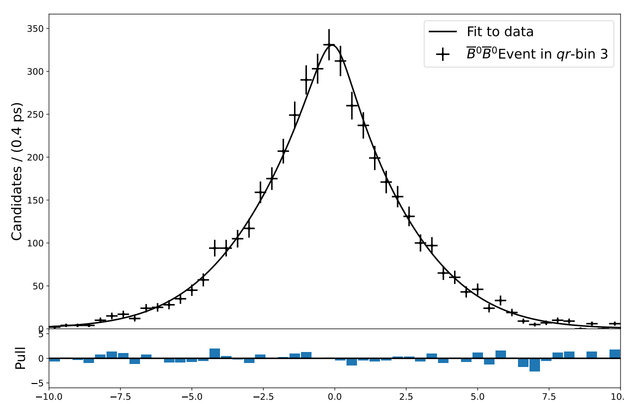
Fit to data
$\overline{B}^0\overline{B}^0$Event in qr-bin 3
Candidates / (0.4 ps)
Pull
Δt [ps]

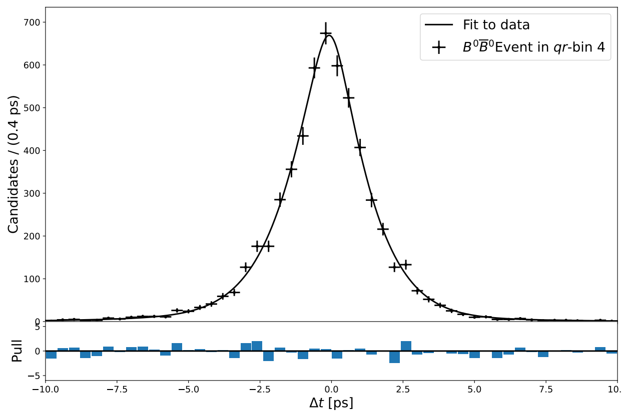
Fit to data
$B^0\overline{B}^0$Event in qr-bin 4
Candidates / (0.4 ps)
Pull
Δt [ps]

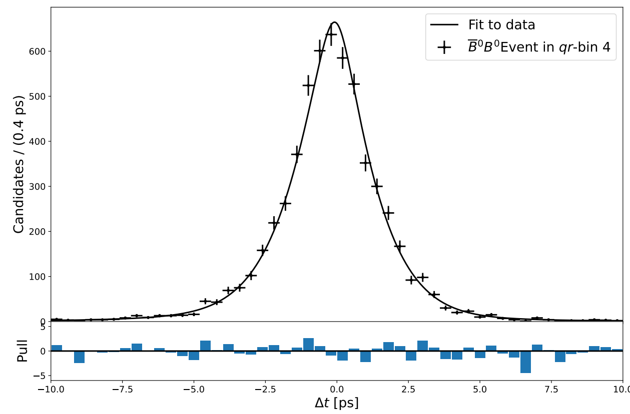
Fit to data
$\overline{B}^0B^0$Event in qr-bin 4
Candidates / (0.4 ps)
Pull
Δt [ps]

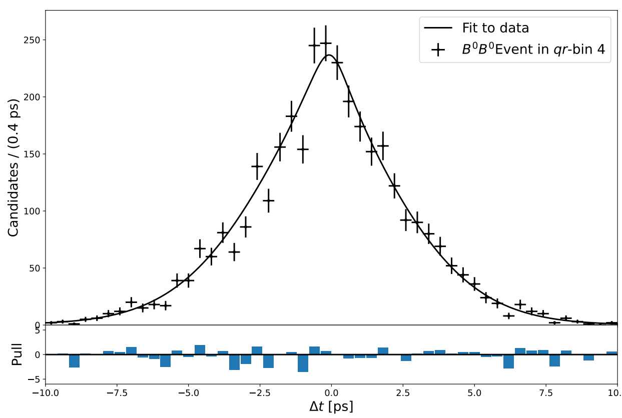
Fit to data
B^0B^0Event in qr-bin 4
Candidates / (0.4 ps)
Pull
Δt [ps]

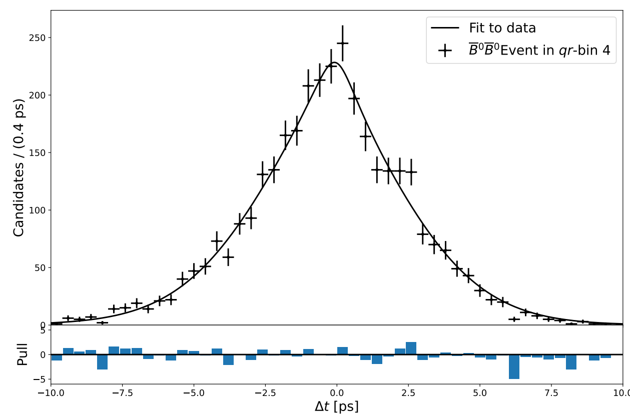
Fit to data
$\overline{B}^0\overline{B}^0$Event in qr-bin 4
Candidates / (0.4 ps)
Pull
Δt [ps]

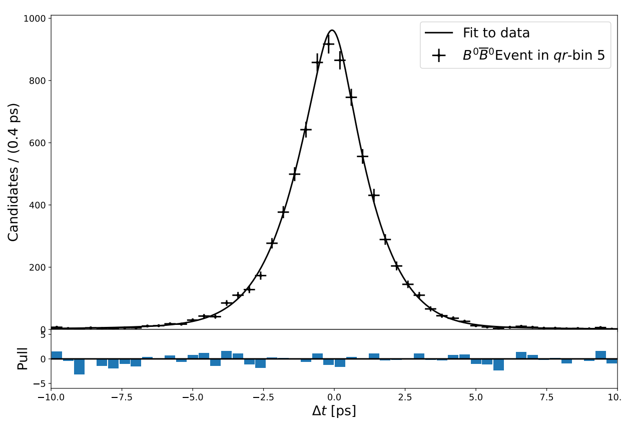
Fit to data
$B^0\overline{B}^0$Event in qr-bin 5
Candidates / (0.4 ps)
Pull
Δt [ps]

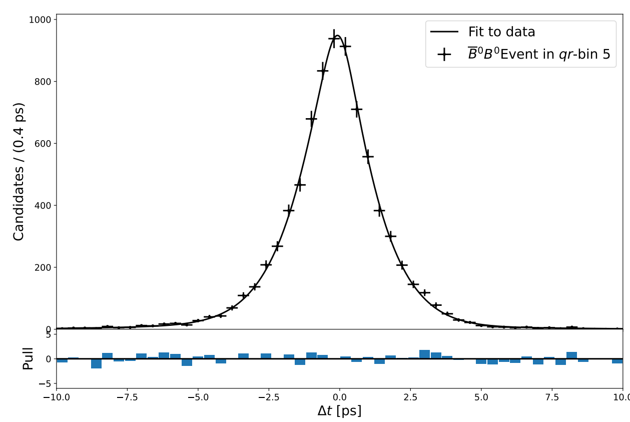
Fit to data
$\overline{B}^0B^0$Event in qr-bin 5
Candidates / (0.4 ps)
Pull
Δt [ps]

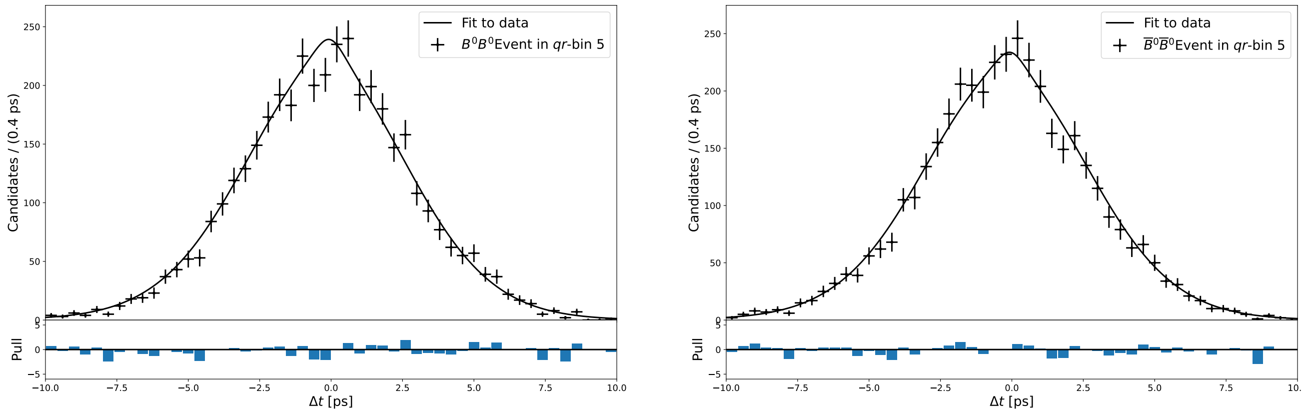

Figure B.6: Δt-distribution fitted to Signal MC data with full disentanglement ($\zeta_{\text{gen}} = 1$). Error bars show Signal MC data for qr bins 0-5 (left to right, top to bottom) and solid line shows the fit. The lower plot show the pulls.

Parameter	Mean	Uncertainty
ζ	0.2126	0.0276
μ_{M1}	-0.1876	0.0344
σ_{M1}	1.0767	0.0366
f_{Tail}	0.3867	0.0138
$\mu_{M1}^{(6)}$	0.0194	0.0325
$\sigma_{M1}^{(6)}$	1.0539	0.0648
w_0^+	0.4797	0.0051
w_0^-	0.4780	0.0050
μ_0	-0.0251	0.0083
w_1^+	0.4194	0.0046
w_1^-	0.4091	0.0046
μ_1	-0.0094	0.0074
w_2^+	0.3254	0.0045
w_2^-	0.3236	0.0044
μ_2	-0.0235	0.0070
w_3^+	0.2379	0.0054
w_3^-	0.2391	0.0053
μ_3	-0.0140	0.0083
w_4^+	0.1692	0.0057
w_4^-	0.1738	0.0057
μ_4	-0.0025	0.0089
w_5^+	0.0990	0.0052
w_5^-	0.1050	0.0051
μ_5	-0.0194	0.0076
w_6^+	0.0215	0.0045
w_6^-	0.0173	0.0044
μ_6	-0.0051	0.0052

Table B.11: Single Δt-fit parameters on Signal MC with PSD fraction of $\zeta^{\text{MC}} = 0.2$. The superscript 6 for resolution function parameters denotes the 6th qr-bin. The indices $i = 0, ..., 6$ for the flavor tagger parameters denote the i-th qr-bin.

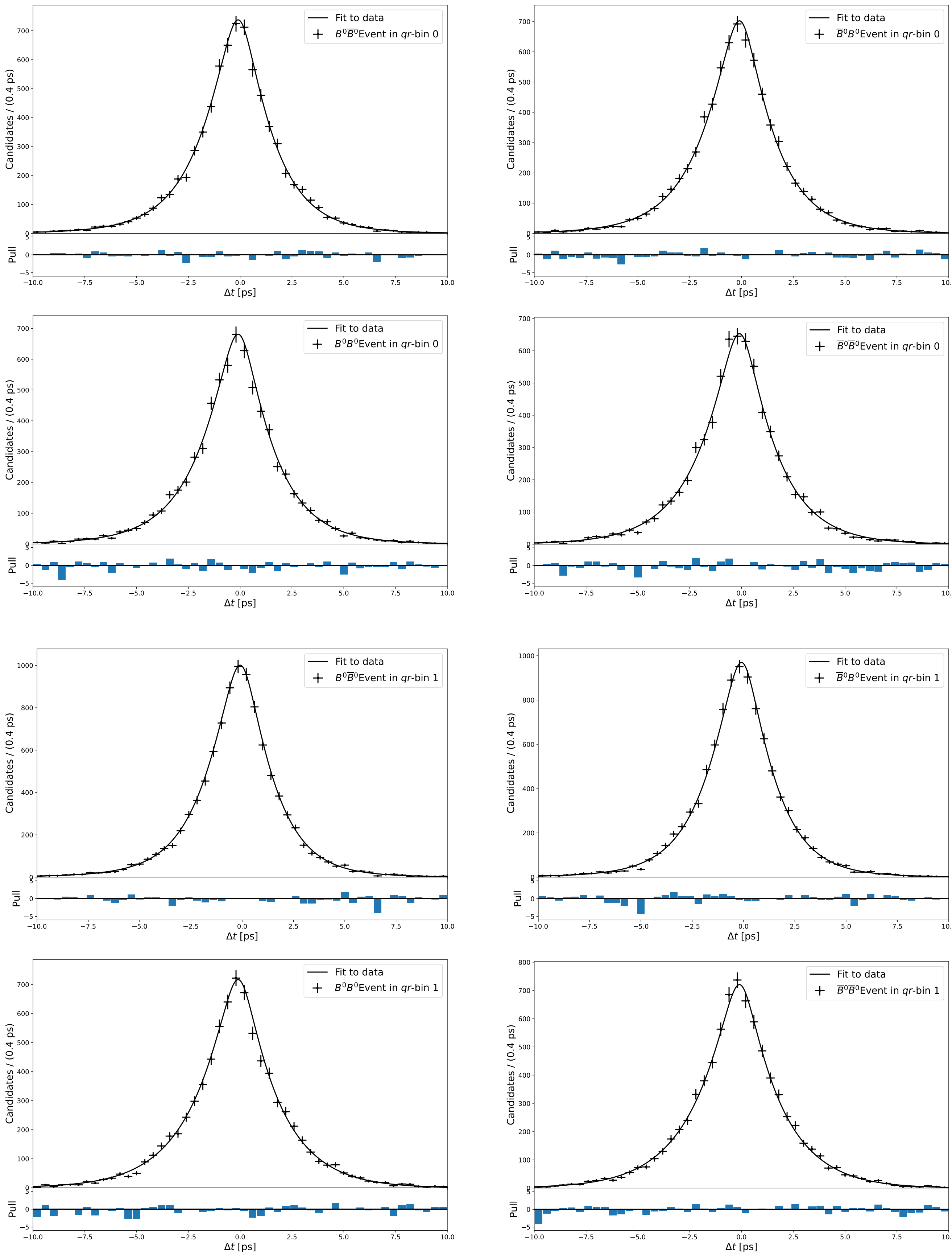
Fit to data
$B^0\overline{B}^0$Event in qr-bin 0
$\overline{B}^0B^0$Event in qr-bin 0
$B^0\overline{B}^0$Event in qr-bin 1
$\overline{B}^0B^0$Event in qr-bin 1
Candidates / (0.4 ps)
Pull
Δt [ps]

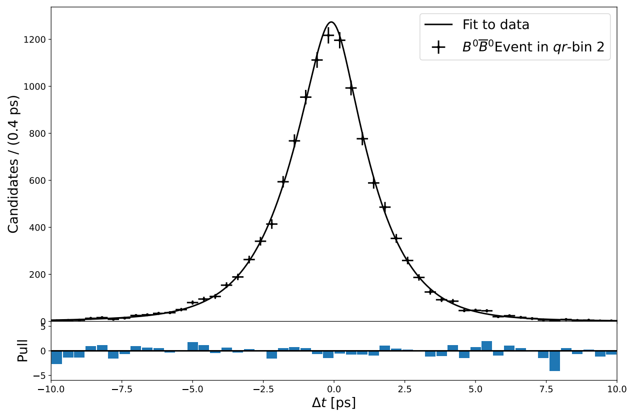
Fit to data
$B^0\overline{B}^0$Event in qr-bin 2
Candidates / (0.4 ps)
Pull
Δt [ps]

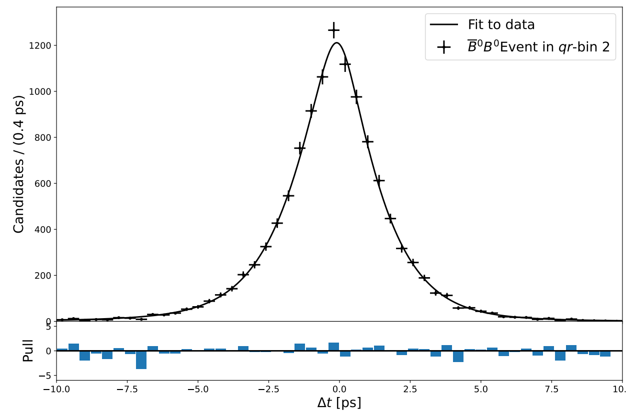
Fit to data
$\overline{B}^0B^0$Event in qr-bin 2
Candidates / (0.4 ps)
Pull
Δt [ps]

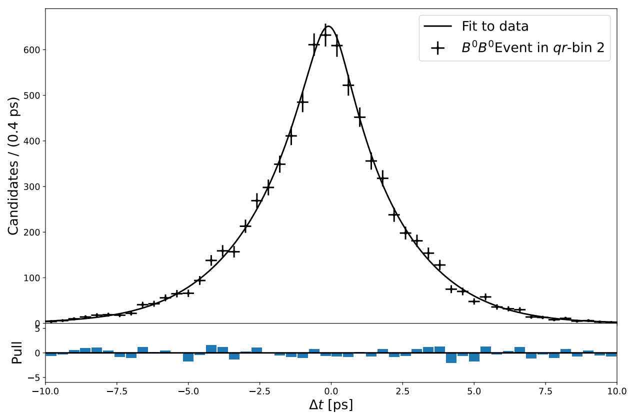
Fit to data
B^0B^0Event in qr-bin 2
Candidates / (0.4 ps)
Pull
Δt [ps]

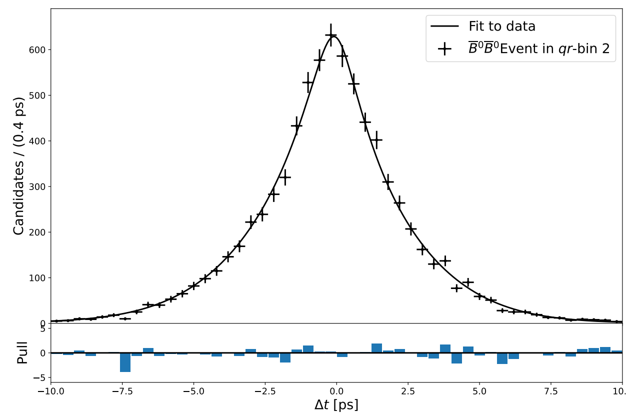
Fit to data
$\overline{B}^0\overline{B}^0$Event in qr-bin 2
Candidates / (0.4 ps)
Pull
Δt [ps]

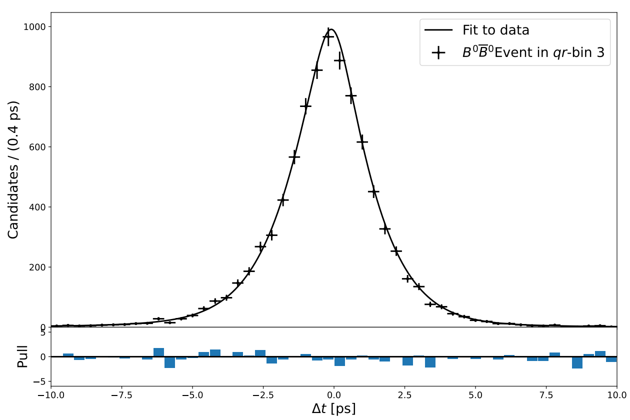
Fit to data
$B^0\overline{B}^0$Event in qr-bin 3
Candidates / (0.4 ps)
Pull
Δt [ps]

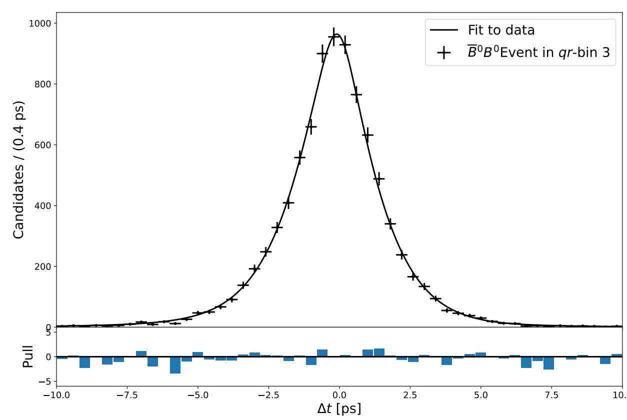
Fit to data
$\overline{B}^0B^0$Event in qr-bin 3
Candidates / (0.4 ps)
Pull
Δt [ps]

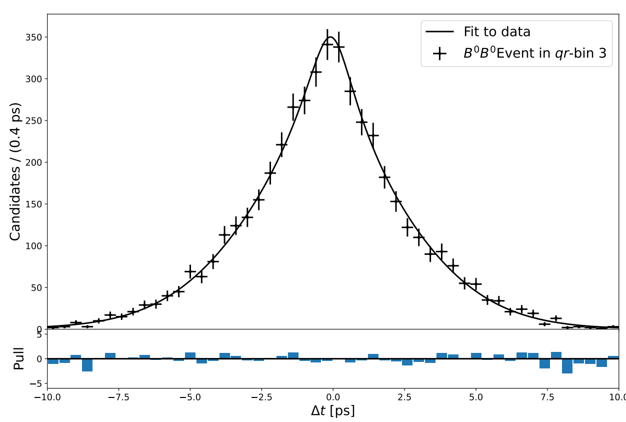
Fit to data
B^0B^0Event in qr-bin 3
Candidates / (0.4 ps)
Pull
Δt [ps]

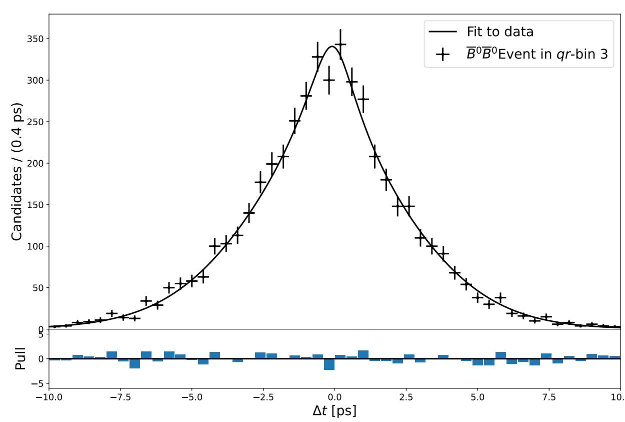
Fit to data
$\overline{B}^0\overline{B}^0$Event in qr-bin 3
Candidates / (0.4 ps)
Pull
Δt [ps]

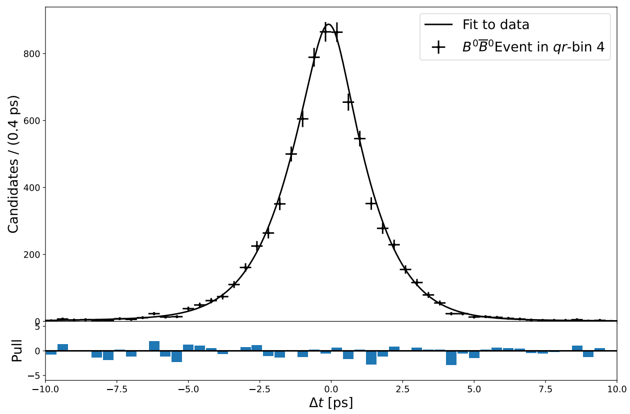
Fit to data
$B^0\overline{B}^0$Event in qr-bin 4
Candidates / (0.4 ps)
Pull
Δt [ps]

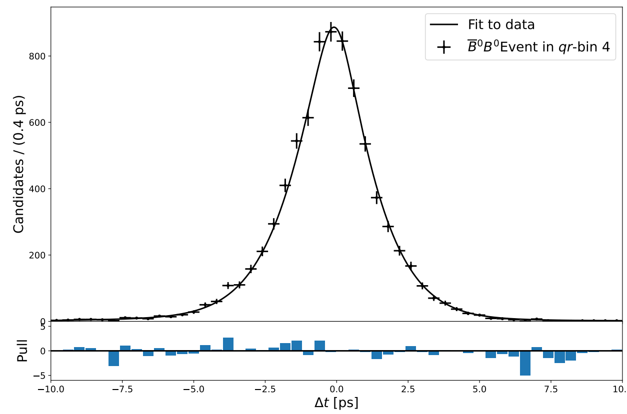
Fit to data
$\overline{B}^0B^0$Event in qr-bin 4
Candidates / (0.4 ps)
Pull
Δt [ps]

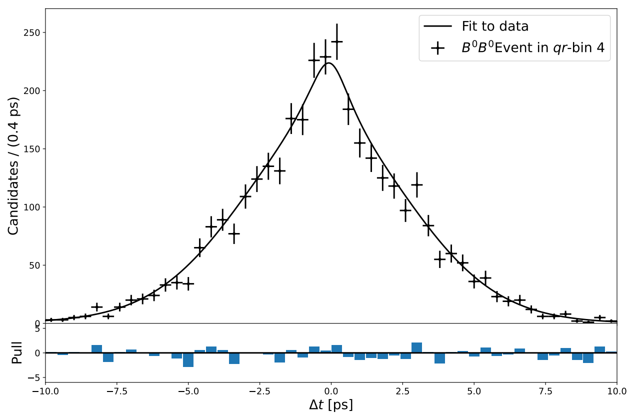
Fit to data
B^0B^0Event in qr-bin 4
Candidates / (0.4 ps)
Pull
Δt [ps]

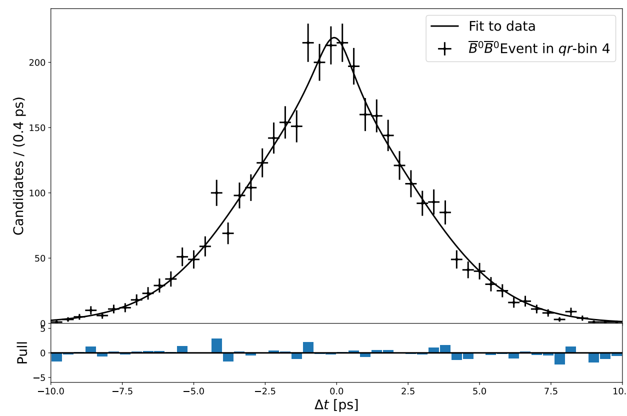
Fit to data
$\overline{B}^0\overline{B}^0$Event in qr-bin 4
Candidates / (0.4 ps)
Pull
Δt [ps]

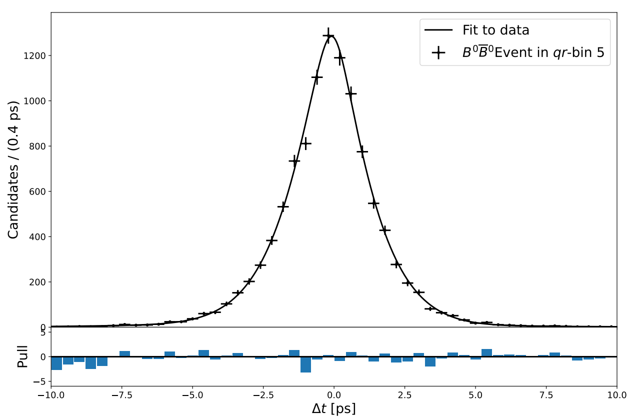
Fit to data
$B^0\overline{B}^0$Event in qr-bin 5
Candidates / (0.4 ps)
Pull
Δt [ps]

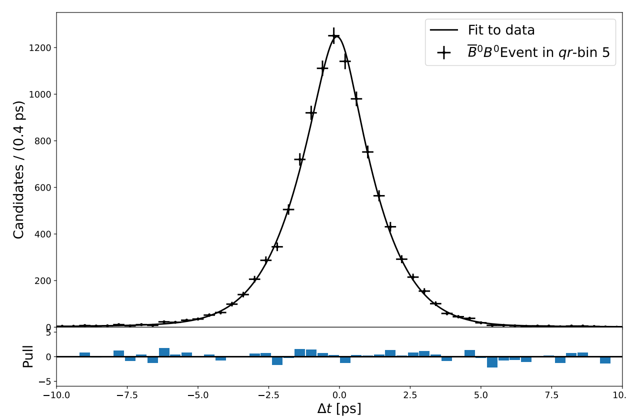
Fit to data
$\overline{B}^0B^0$Event in qr-bin 5
Candidates / (0.4 ps)
Pull
Δt [ps]

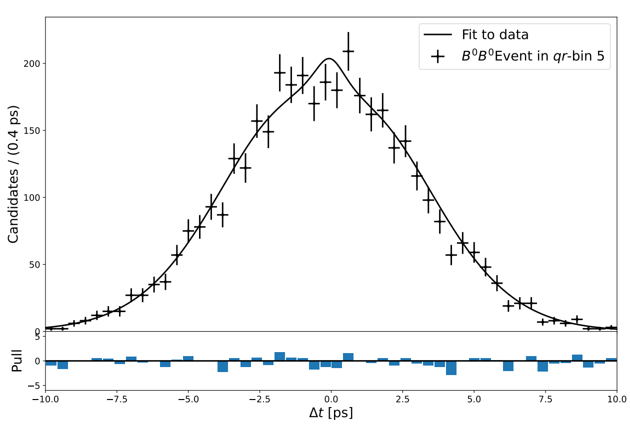
Fit to data
B^0B^0Event in qr-bin 5
Candidates / (0.4 ps)
Pull
Δt [ps]

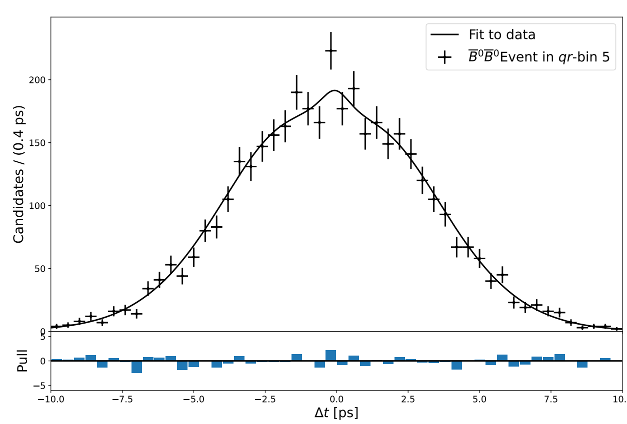
Fit to data
$\overline{B}^0\overline{B}^0$Event in qr-bin 5
Candidates / (0.4 ps)
Pull
Δt [ps]

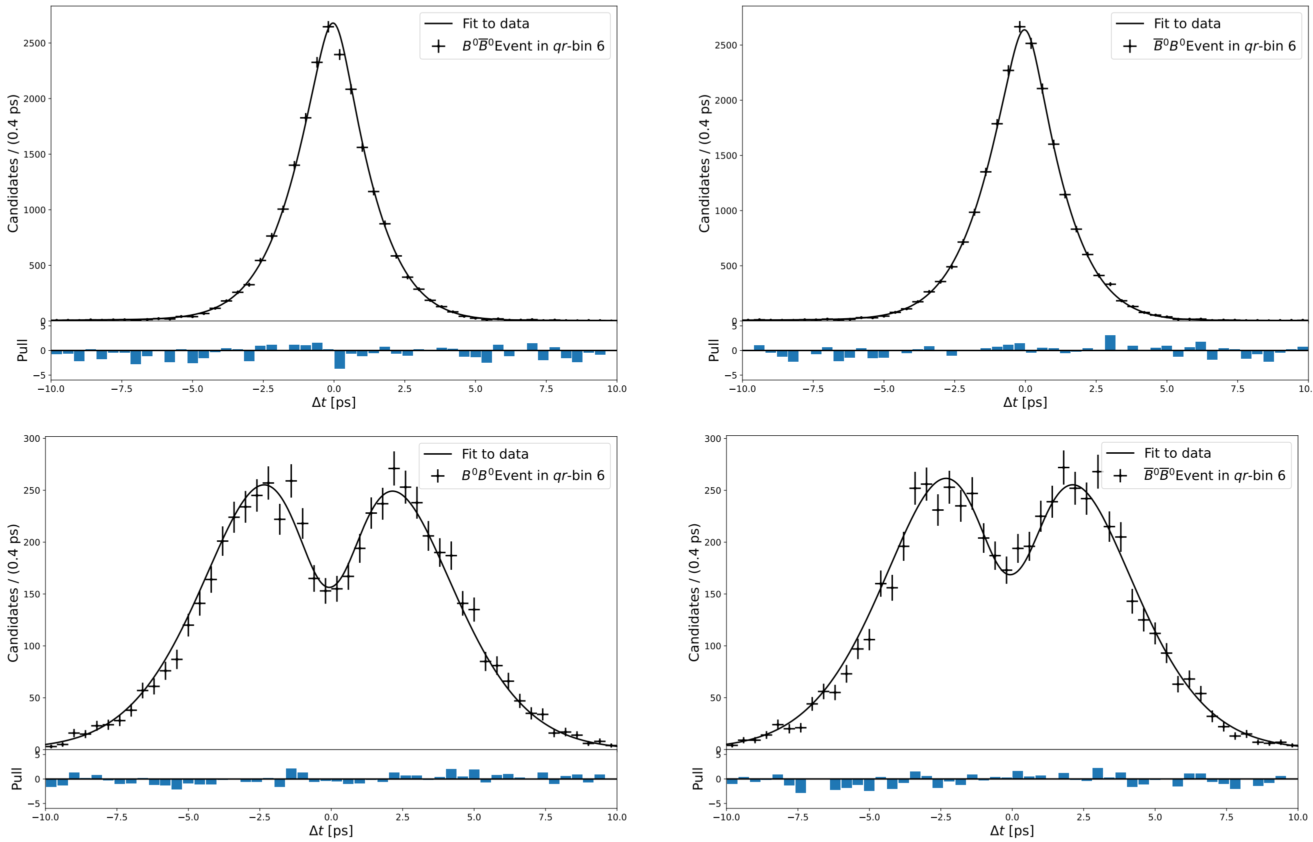

Figure B.7: Δt-distribution fitted to Signal MC data with a fraction of disentanglement ($\zeta_{\text{gen}} = 0.2$) for all qr bins and four flavor combinations (left to right, top to bottom). Error bars show Signal MC data binned in qr bins and solid line shows the fit. The lower plot show the pulls.

Parameter	Mean	Uncertainty
ζ	0.4174	0.0229
μ_{M1}	-0.1879	0.0291
σ_{M1}	1.0516	0.0312
f_{Tail}	0.3900	0.0123
$\mu_{M1}^{(6)}$	0.0290	0.0285
$\sigma_{M1}^{(6)}$	1.0576	0.0563
w_0^+	0.4790	0.0047
w_0^-	0.4766	0.0045
μ_0	-0.0251	0.0076
w_1^+	0.4183	0.0042
w_1^-	0.4070	0.0041
μ_1	-0.0139	0.0069
w_2^+	0.3256	0.0041
w_2^-	0.3259	0.0040
μ_2	-0.0256	0.0065
w_3^+	0.2369	0.0049
w_3^-	0.2364	0.0048
μ_3	-0.0101	0.0077
w_4^+	0.1684	0.0053
w_4^-	0.1728	0.0052
μ_4	-0.0057	0.0083
w_5^+	0.0985	0.0048
w_5^-	0.1003	0.0048
μ_5	-0.0111	0.0071
w_6^+	0.0168	0.0042
w_6^-	0.0208	0.0041
μ_6	-0.0121	0.0049

Table B.12: Single Δt-fit parameters on Signal MC with PSD fraction of $\zeta^{\text{MC}} = 0.4$. The superscript 6 for resolution function parameters denotes the 6th qr-bin. The indices $i = 0, ..., 6$ for the flavor tagger parameters denote the i-th qr-bin.

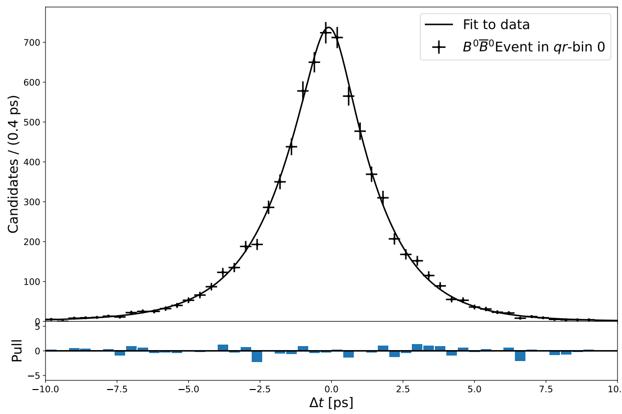
Fit to data
$B^0\overline{B}^0$Event in qr-bin 0
Candidates / (0.4 ps)
Pull
Δt [ps]

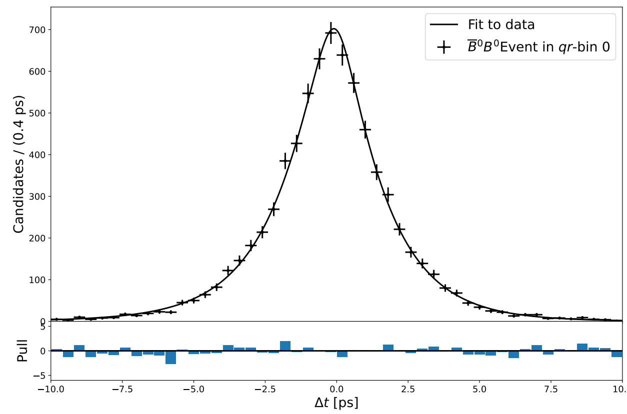
Fit to data
$\overline{B}^0B^0$Event in qr-bin 0
Candidates / (0.4 ps)
Pull
Δt [ps]

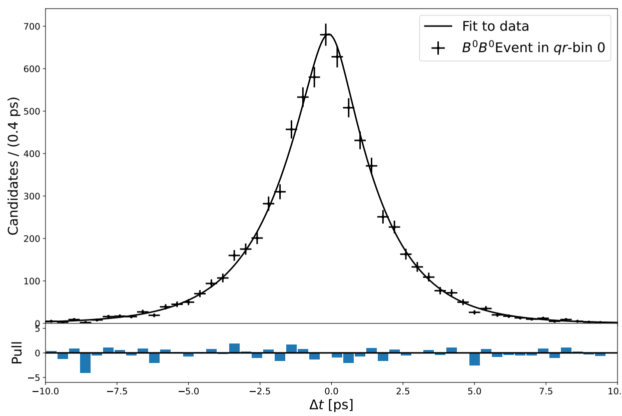
Fit to data
$B^0\overline{B}^0$Event in qr-bin 0
Candidates / (0.4 ps)
Pull
Δt [ps]

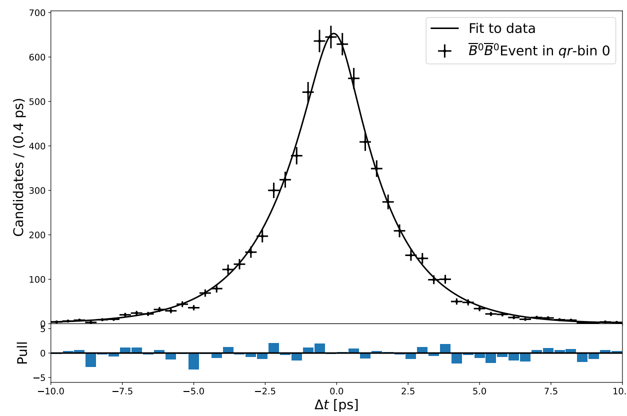
Fit to data
$\overline{B}^0B^0$Event in qr-bin 0
Candidates / (0.4 ps)
Pull
Δt [ps]

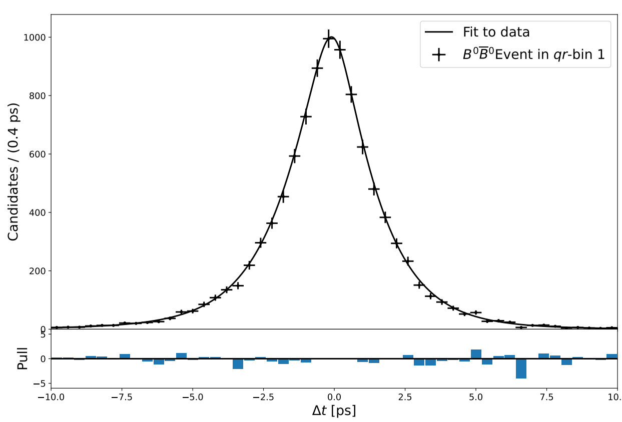
Fit to data
$B^0\overline{B}^0$Event in qr-bin 1
Candidates / (0.4 ps)
Pull
Δt [ps]

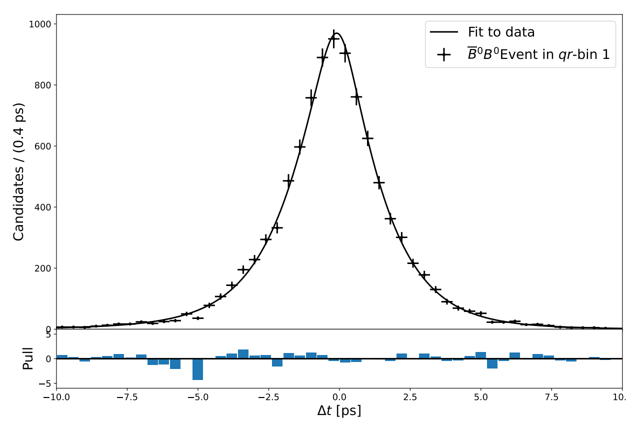
Fit to data
$\overline{B}^0B^0$Event in qr-bin 1
Candidates / (0.4 ps)
Pull
Δt [ps]

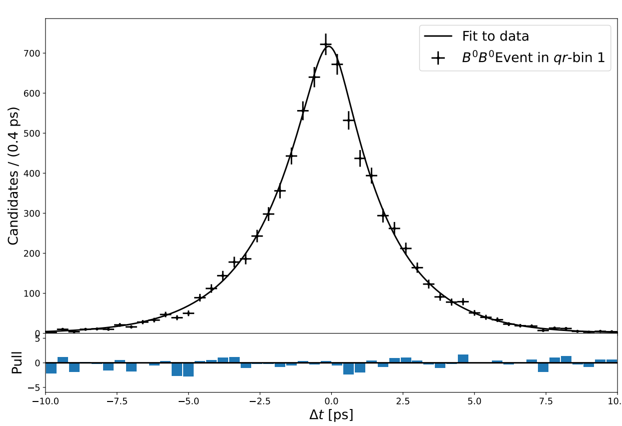
Fit to data
$B^0\overline{B}^0$Event in qr-bin 1
Candidates / (0.4 ps)
Pull
Δt [ps]

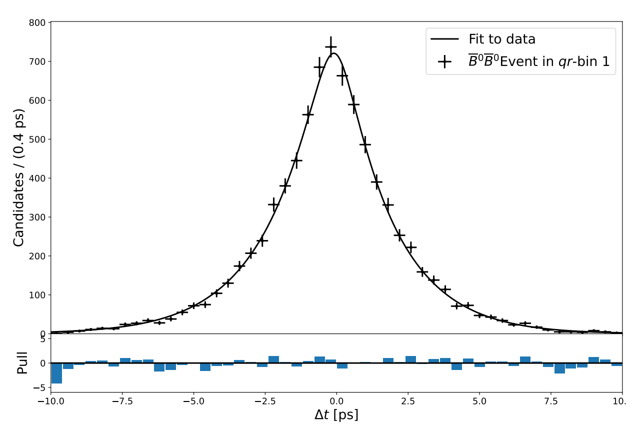
Fit to data
$\overline{B}^0B^0$Event in qr-bin 1
Candidates / (0.4 ps)
Pull
Δt [ps]

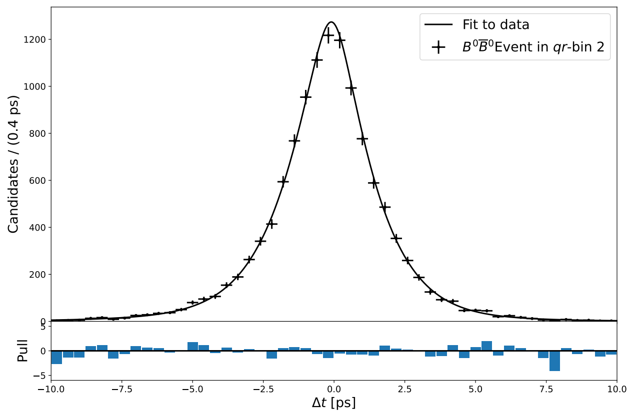
Fit to data
$B^0\overline{B}^0$Event in qr-bin 2
Candidates / (0.4 ps)
Pull
Δt [ps]

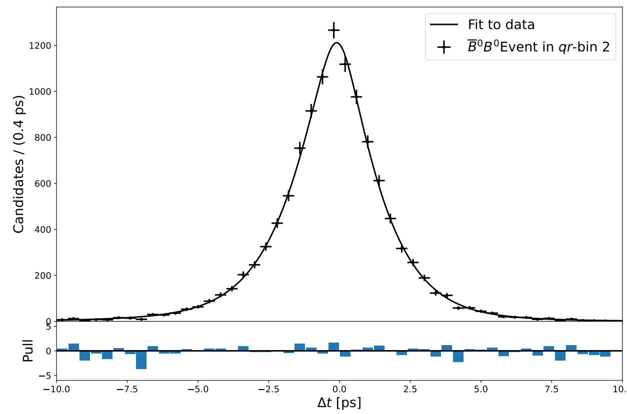
Fit to data
$\overline{B}^0B^0$Event in qr-bin 2
Candidates / (0.4 ps)
Pull
Δt [ps]

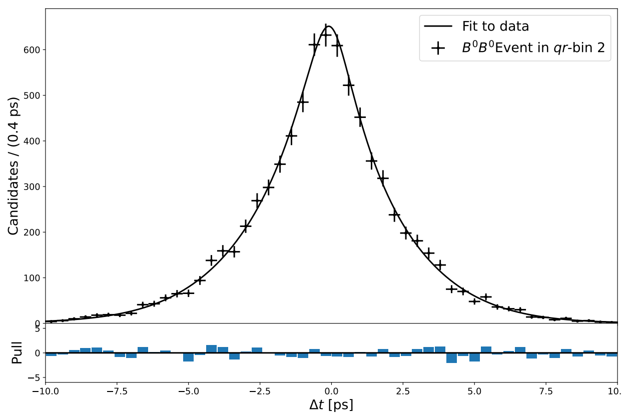
Fit to data
B^0B^0Event in qr-bin 2
Candidates / (0.4 ps)
Pull
Δt [ps]

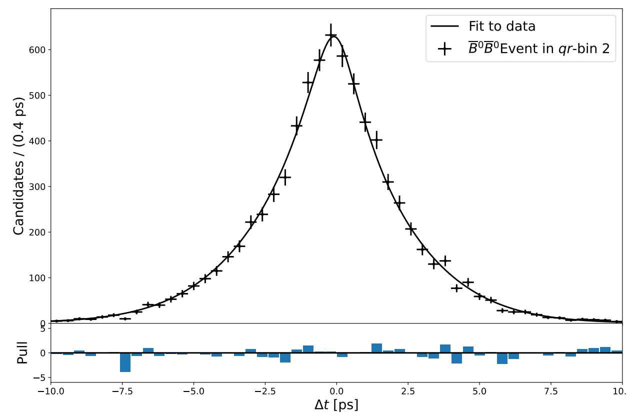
Fit to data
$\overline{B}^0\overline{B}^0$Event in qr-bin 2
Candidates / (0.4 ps)
Pull
Δt [ps]

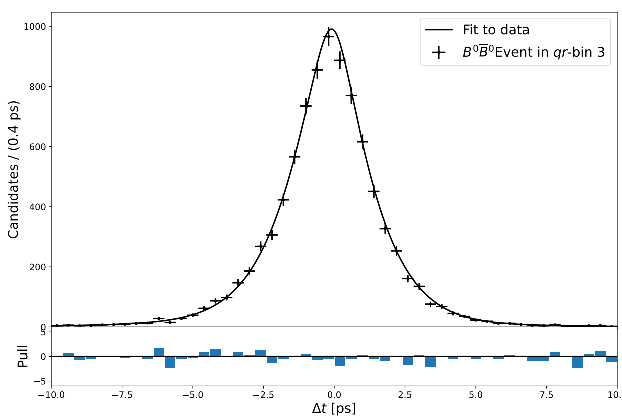
Fit to data
$B^0\overline{B}^0$Event in qr-bin 3
Candidates / (0.4 ps)
Pull
Δt [ps]

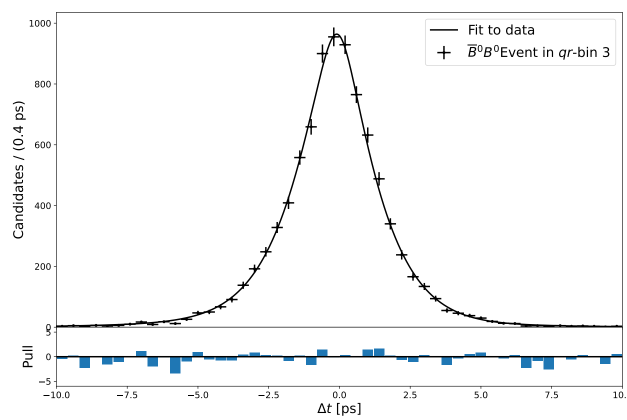
Fit to data
$\overline{B}^0B^0$Event in qr-bin 3
Candidates / (0.4 ps)
Pull
Δt [ps]

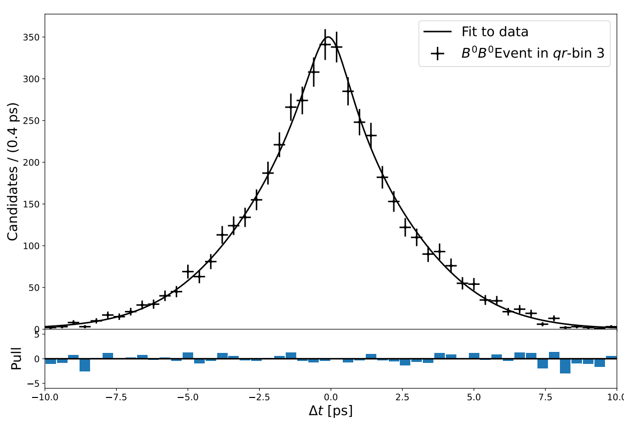
Fit to data
B^0B^0Event in qr-bin 3
Candidates / (0.4 ps)
Pull
Δt [ps]

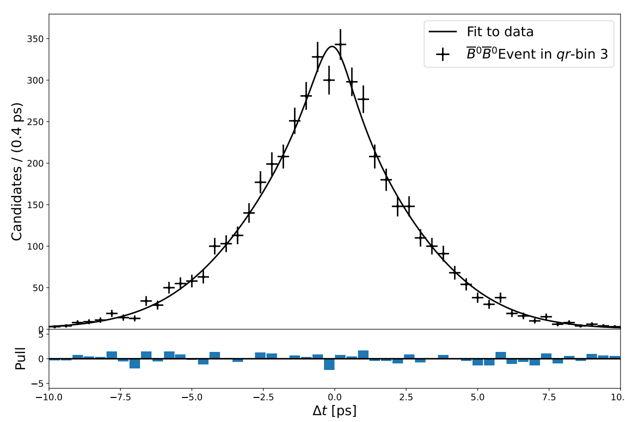
Fit to data
$\overline{B}^0\overline{B}^0$Event in qr-bin 3
Candidates / (0.4 ps)
Pull
Δt [ps]

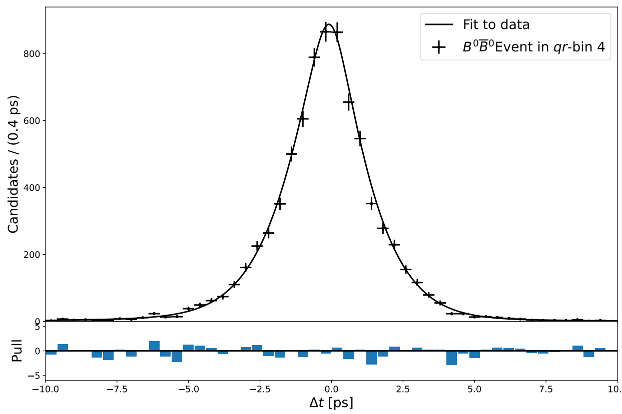
Fit to data
$B^0\overline{B}^0$Event in qr-bin 4
Candidates / (0.4 ps)
Pull
Δt [ps]

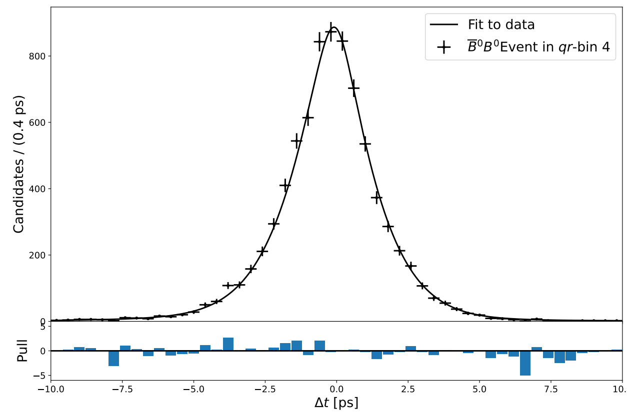
Fit to data
$\overline{B}^0B^0$Event in qr-bin 4
Candidates / (0.4 ps)
Pull
Δt [ps]

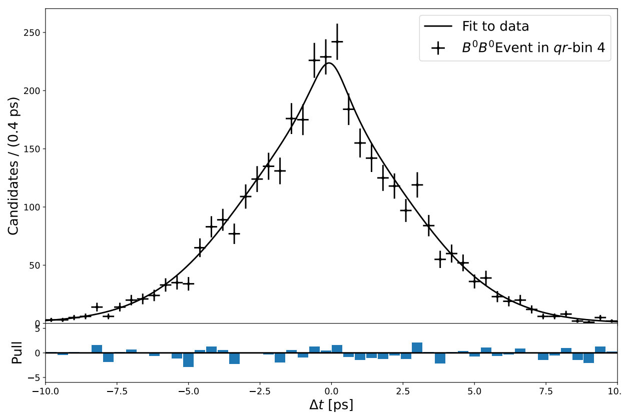
Fit to data
B^0B^0Event in qr-bin 4
Candidates / (0.4 ps)
Pull
Δt [ps]

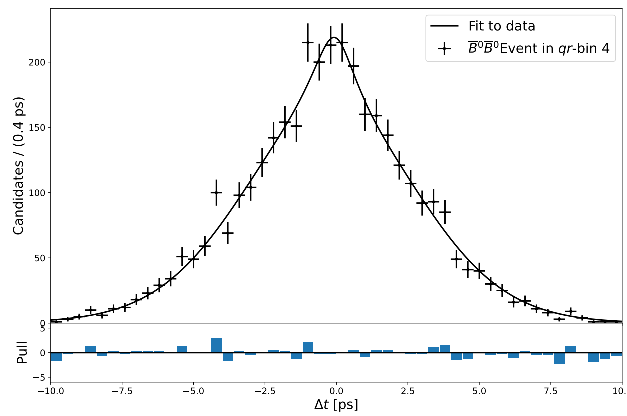
Fit to data
$\overline{B}^0\overline{B}^0$Event in qr-bin 4
Candidates / (0.4 ps)
Pull
Δt [ps]

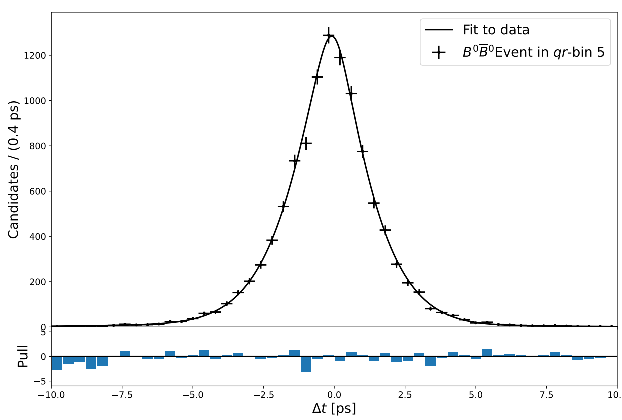
Fit to data
$B^0\overline{B}^0$Event in qr-bin 5
Candidates / (0.4 ps)
Pull
Δt [ps]

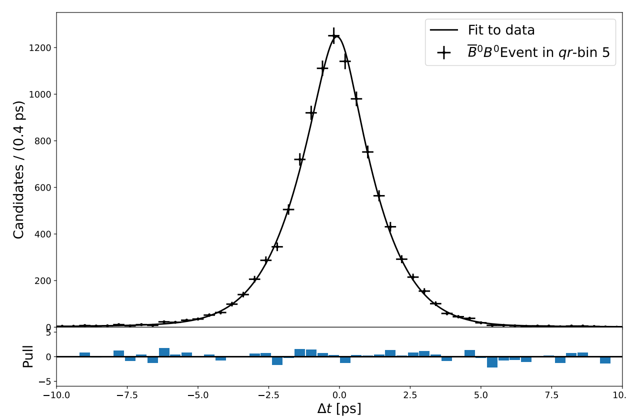
Fit to data
$\overline{B}^0B^0$Event in qr-bin 5
Candidates / (0.4 ps)
Pull
Δt [ps]

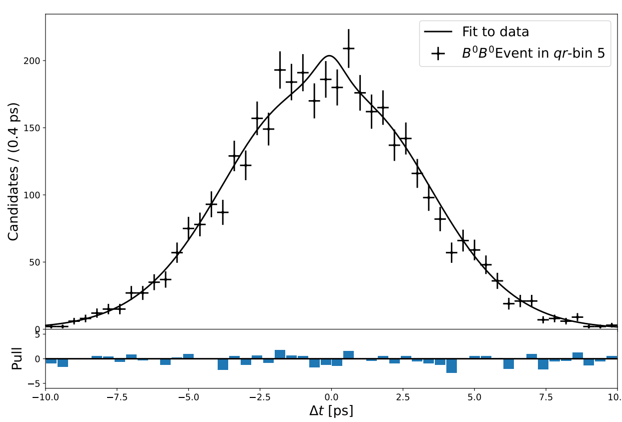
Fit to data
B^0B^0Event in qr-bin 5
Candidates / (0.4 ps)
Pull
Δt [ps]

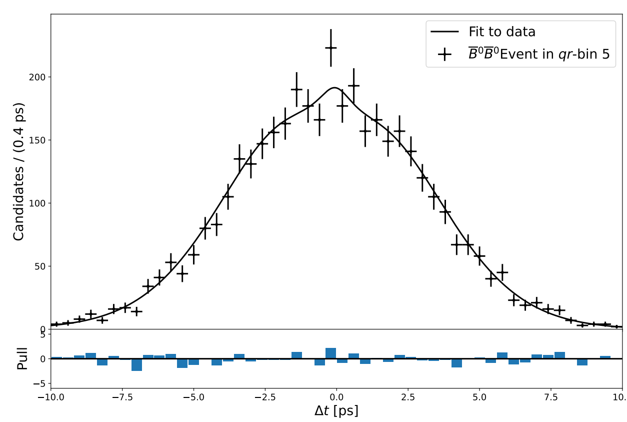
Fit to data
$\overline{B}^0\overline{B}^0$Event in qr-bin 5
Candidates / (0.4 ps)
Pull
Δt [ps]

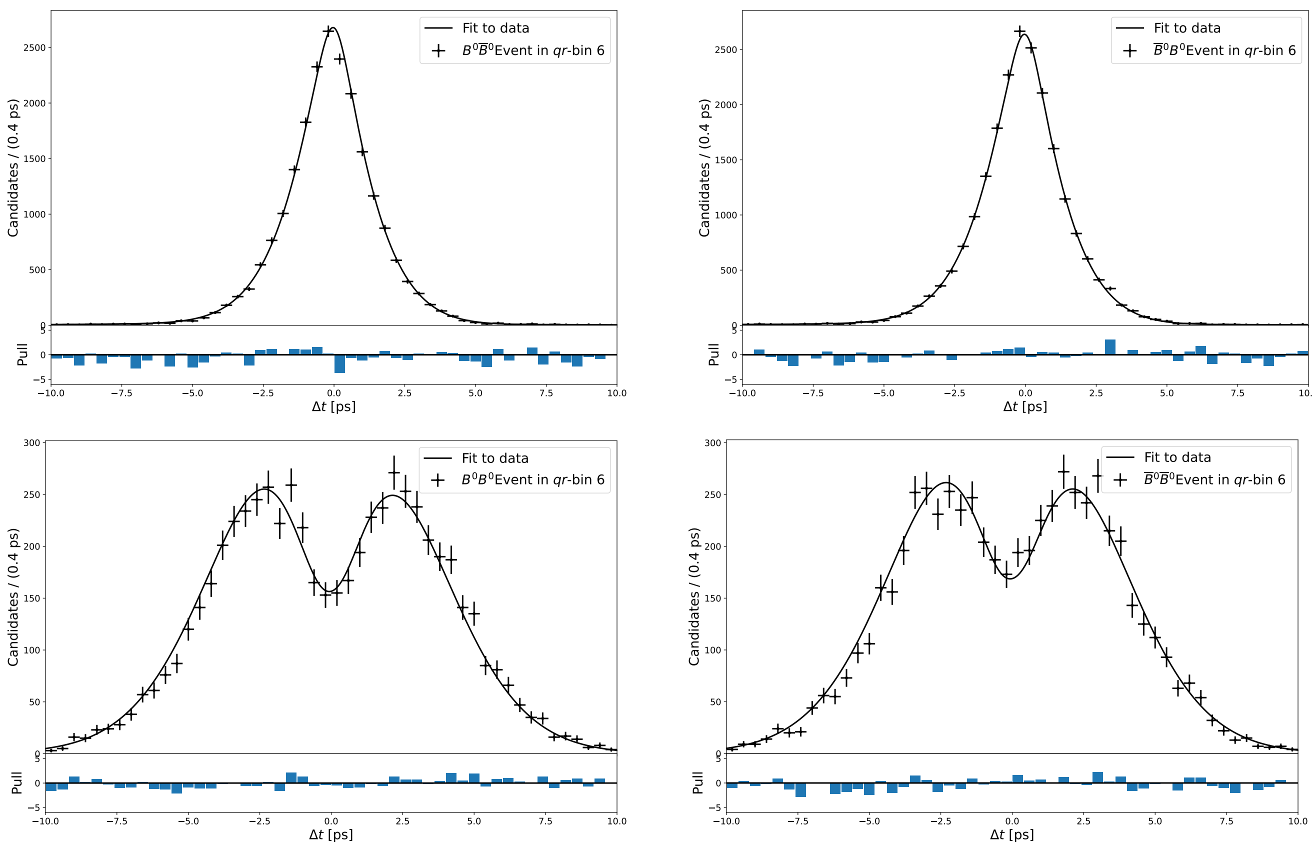

Figure B.8: Δt-distribution fitted to Signal MC data with a fraction of disentanglement ($\zeta_{\text{gen}} = 0.4$) for all qr bins and four flavor combinations (left to right, top to bottom). Error bars show Signal MC data binned in qr bins and solid line shows the fit. The lower plot show the pulls.

Parameter	Mean	Uncertainty
ζ	0.5814	0.0217
μ_{M1}	-0.1958	0.0222
σ_{M1}	1.0761	0.0250
f_{Tail}	1.0000	0.0000
$\mu_{M1}^{(6)}$	-0.0760	0.0234
$\sigma_{M1}^{(6)}$	1.1813	0.0469
w_0^+	0.4817	0.0048
w_0^-	0.4782	0.0047
μ_0	-0.0228	0.0081
w_1^+	0.4219	0.0043
w_1^-	0.4097	0.0043
μ_1	-0.0119	0.0072
w_2^+	0.3292	0.0043
w_2^-	0.3291	0.0041
μ_2	-0.0252	0.0068
w_3^+	0.2420	0.0051
w_3^-	0.2398	0.0050
μ_3	-0.0089	0.0081
w_4^+	0.1726	0.0055
w_4^-	0.1765	0.0055
μ_4	-0.0098	0.0087
w_5^+	0.1018	0.0050
w_5^-	0.1058	0.0049
μ_5	-0.0140	0.0075
w_6^+	0.0236	0.0043
w_6^-	0.0292	0.0041
μ_6	-0.0154	0.0052

Table B.13: Single Δt-fit parameters on Signal MC with PSD fraction of $\zeta^{\text{MC}} = 0.6$. The superscript 6 for resolution function parameters denotes the 6th qr-bin. The indices $i = 0, ..., 6$ for the flavor tagger parameters denote the i-th qr-bin.

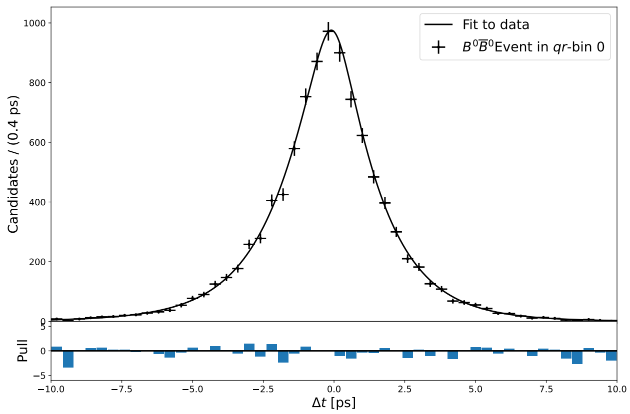
Fit to data
$B^0\overline{B}^0$Event in qr-bin 0
Candidates / (0.4 ps)
Pull
Δt [ps]

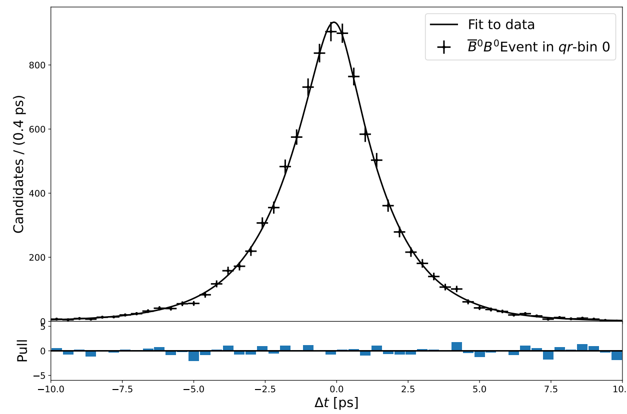
Fit to data
$\overline{B}^0B^0$Event in qr-bin 0
Candidates / (0.4 ps)
Pull
Δt [ps]

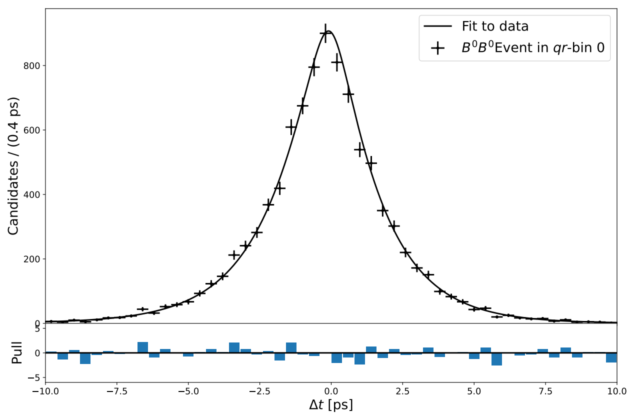
Fit to data
B^0B^0Event in qr-bin 0
Candidates / (0.4 ps)
Pull
Δt [ps]

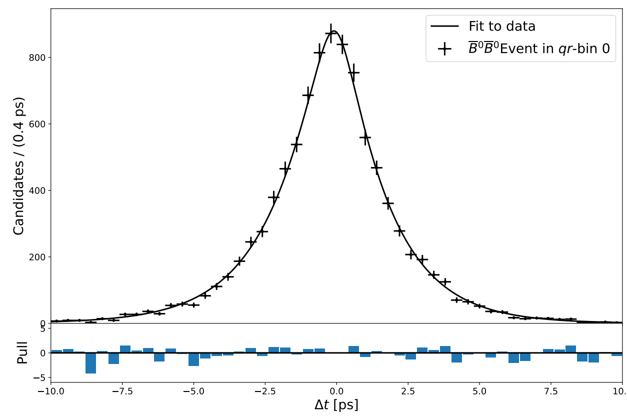
Fit to data
$\overline{B}^0\overline{B}^0$Event in qr-bin 0
Candidates / (0.4 ps)
Pull
Δt [ps]

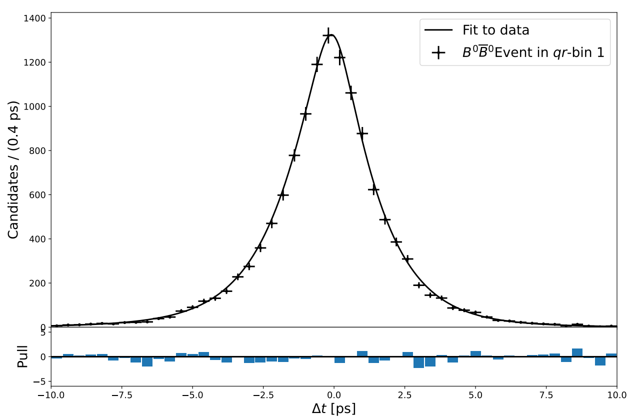
Fit to data
$B^0\overline{B}^0$Event in qr-bin 1
Candidates / (0.4 ps)
Pull
Δt [ps]

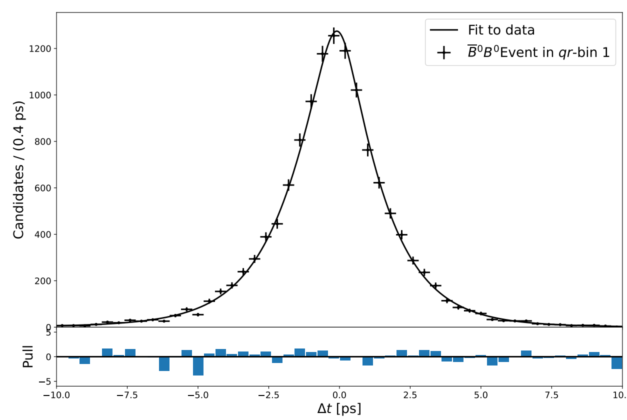
Fit to data
$\overline{B}^0B^0$Event in qr-bin 1
Candidates / (0.4 ps)
Pull
Δt [ps]

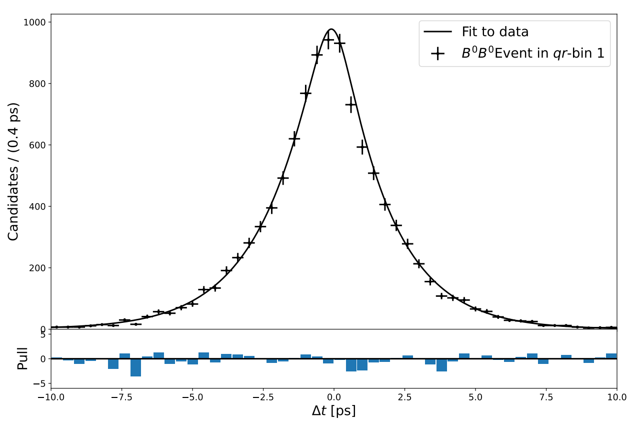
Fit to data
B^0B^0Event in qr-bin 1
Candidates / (0.4 ps)
Pull
Δt [ps]

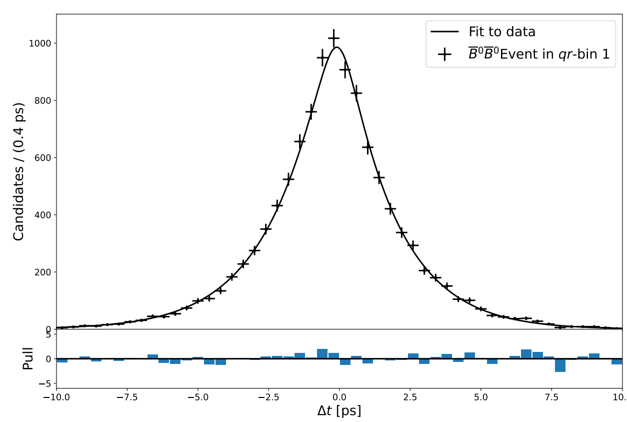
Fit to data
$\overline{B}^0\overline{B}^0$Event in qr-bin 1
Candidates / (0.4 ps)
Pull
Δt [ps]

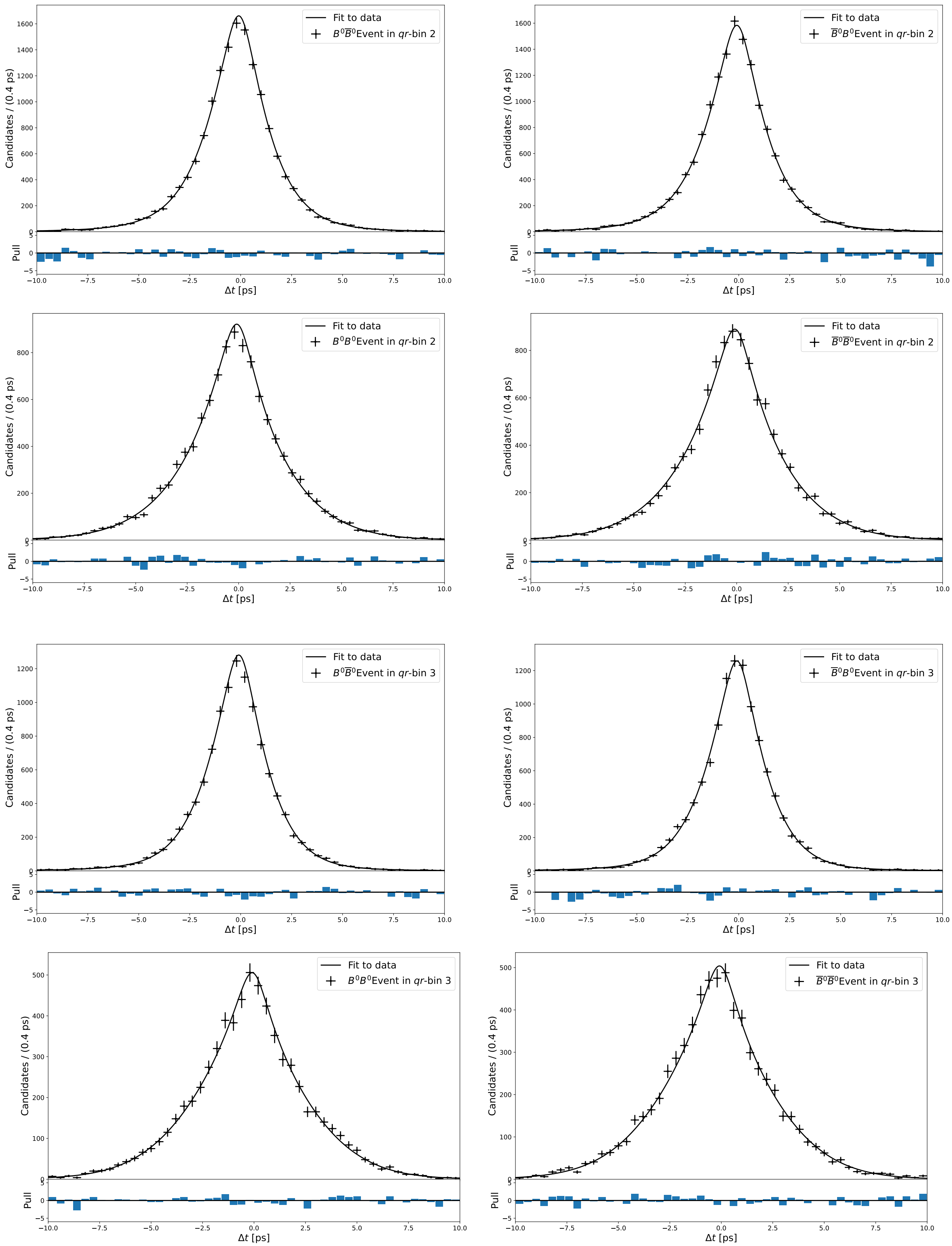
Fit to data
$B^0\overline{B}^0$Event in qr-bin 2
Fit to data
$\overline{B}^0B^0$Event in qr-bin 2
Fit to data
$B^0\overline{B}^0$Event in qr-bin 2
Fit to data
$\overline{B}^0\overline{B}^0$Event in qr-bin 2
Fit to data
$B^0\overline{B}^0$Event in qr-bin 3
Fit to data
$\overline{B}^0B^0$Event in qr-bin 3
Fit to data
B^0B^0Event in qr-bin 3
Fit to data
$\overline{B}^0\overline{B}^0$Event in qr-bin 3
Candidates / (0.4 ps)
Pull
Δt [ps]

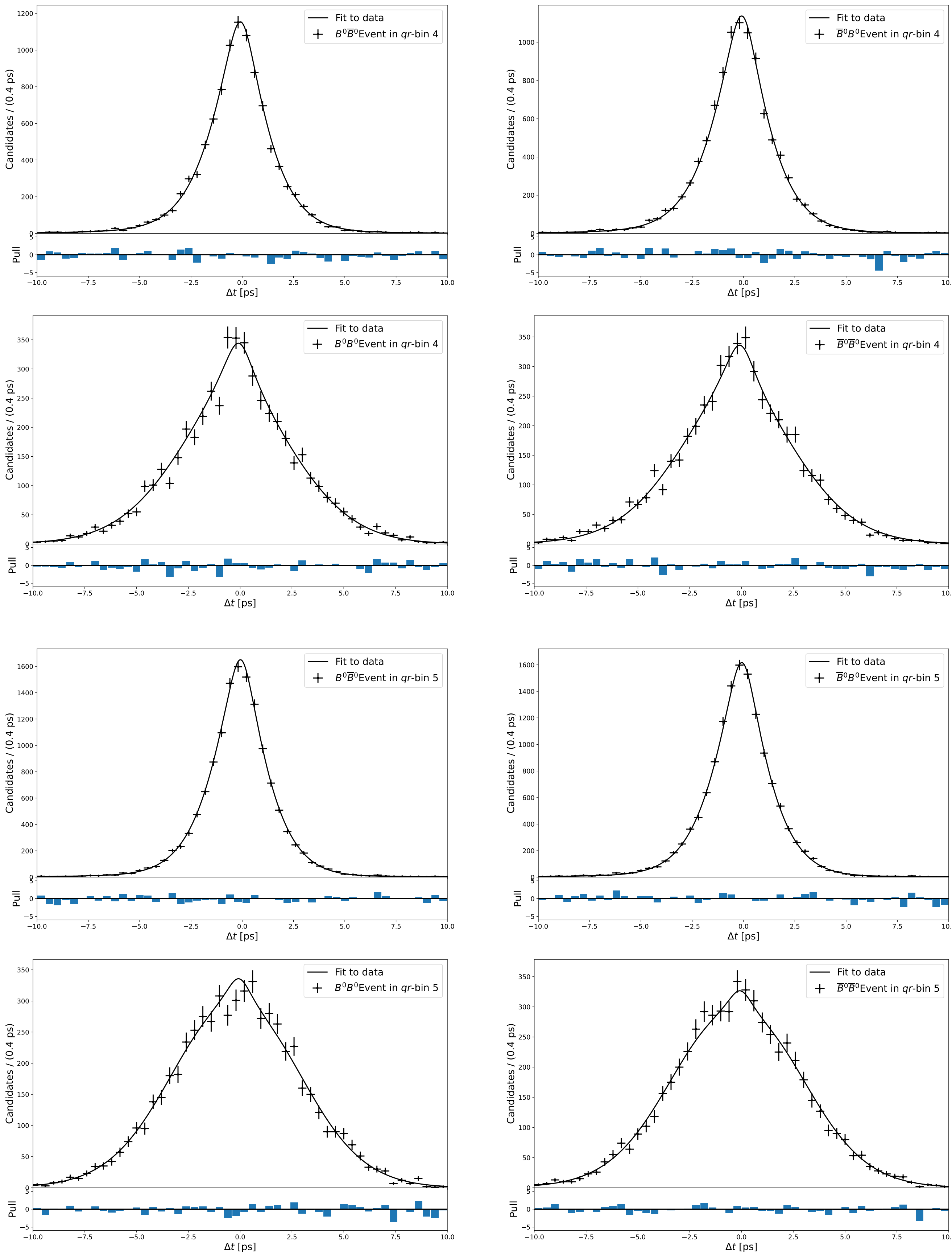
Fit to data
$B^0\overline{B}^0$Event in qr-bin 4
Fit to data
$\overline{B}^0B^0$Event in qr-bin 4
Fit to data
B^0B^0Event in qr-bin 4
Fit to data
$\overline{B}^0\overline{B}^0$Event in qr-bin 4
Fit to data
$B^0\overline{B}^0$Event in qr-bin 5
Fit to data
$\overline{B}^0B^0$Event in qr-bin 5
Fit to data
B^0B^0Event in qr-bin 5
Fit to data
$\overline{B}^0\overline{B}^0$Event in qr-bin 5
Candidates / (0.4 ps)
Pull
Δt [ps]

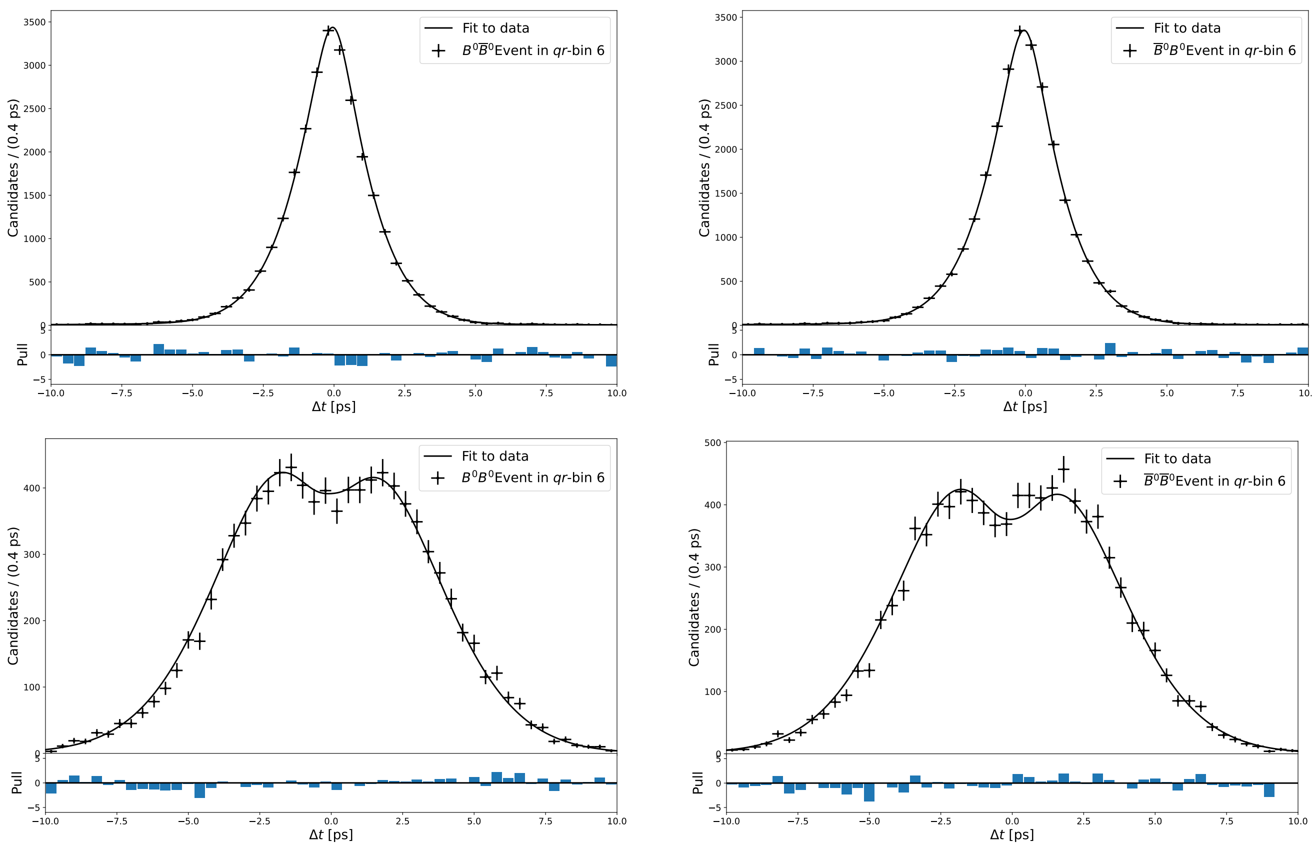

Figure B.9: Δt-distribution fitted to Signal MC data with a fraction of disentanglement ($\zeta_{\text{gen}} = 0.6$) for all qr bins and four flavor combinations (left to right, top to bottom). Error bars show Signal MC data binned in qr bins and solid line shows the fit. The lower plot show the pulls.

Parameter	Mean	Uncertainty
ζ	0.8167	0.0235
μ_{M1}	-0.1623	0.0330
σ_{M1}	1.0410	0.0358
f_{Tail}	0.3816	0.0139
$\mu_{M1}^{(6)}$	0.0418	0.0320
$\sigma_{M1}^{(6)}$	0.9607	0.0657
w_0^+	0.4796	0.0059
w_0^-	0.4780	0.0058
μ_0	-0.0193	0.0101
w_1^+	0.4193	0.0053
w_1^-	0.4057	0.0053
μ_1	-0.0158	0.0091
w_2^+	0.3295	0.0053
w_2^-	0.3304	0.0051
μ_2	-0.0278	0.0086
w_3^+	0.2428	0.0063
w_3^-	0.2377	0.0062
μ_3	-0.0089	0.0102
w_4^+	0.1702	0.0069
w_4^-	0.1757	0.0068
μ_4	-0.0072	0.0110
w_5^+	0.0934	0.0063
w_5^-	0.0952	0.0062
μ_5	-0.0127	0.0094
w_6^+	0.0130	0.0054
w_6^-	0.0222	0.0051
μ_6	-0.0206	0.0066

Table B.14: Single Δt-fit parameters on Signal MC with PSD fraction of $\zeta^{\text{MC}} = 0.8$. The superscript 6 for resolution function parameters denotes the 6th qr-bin. The indices $i = 0, ..., 6$ for the flavor tagger parameters denote the i-th qr-bin.

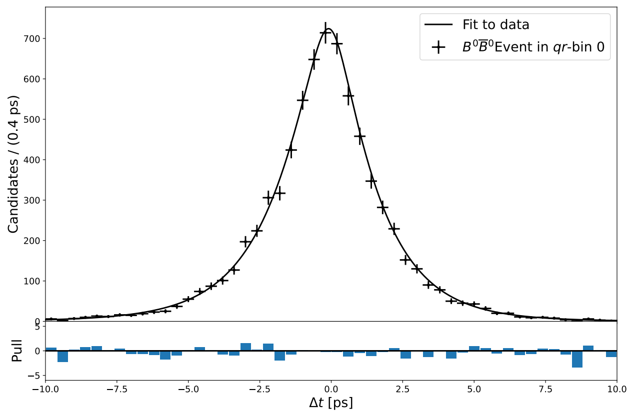
Fit to data
$B^0\overline{B}^0$Event in qr-bin 0
Candidates / (0.4 ps)
Pull
Δt [ps]

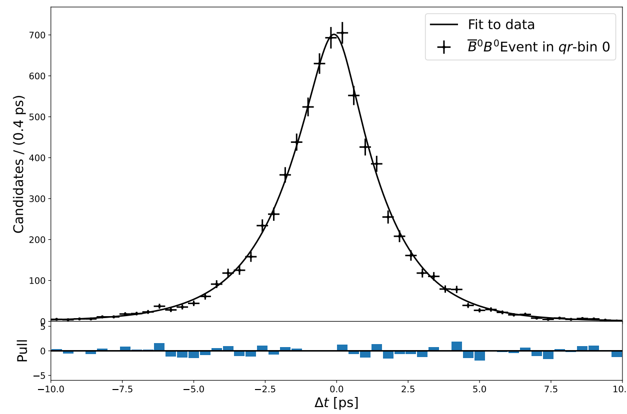
Fit to data
$\overline{B}^0B^0$Event in qr-bin 0
Candidates / (0.4 ps)
Pull
Δt [ps]

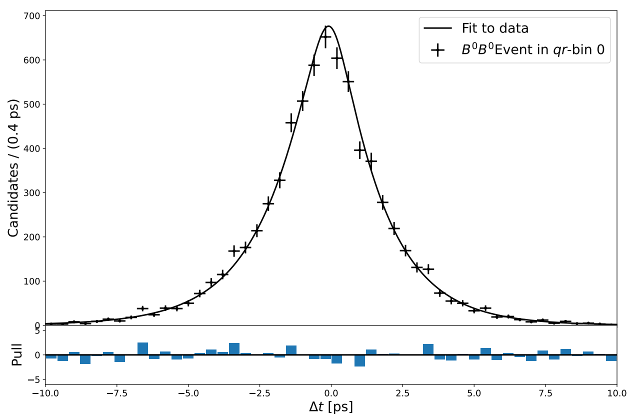
Fit to data
$B^0\overline{B}^0$Event in qr-bin 0
Candidates / (0.4 ps)
Pull
Δt [ps]

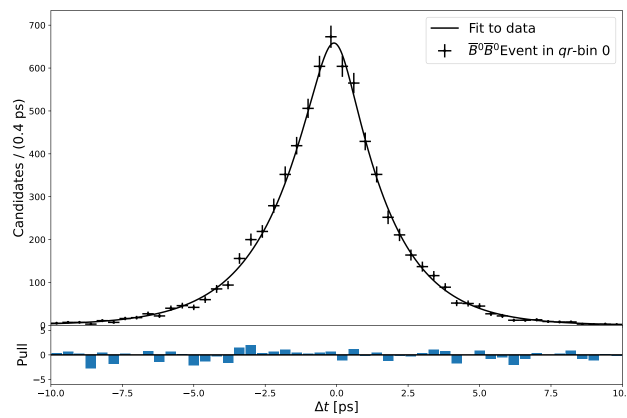
Fit to data
$\overline{B}^0\overline{B}^0$Event in qr-bin 0
Candidates / (0.4 ps)
Pull
Δt [ps]

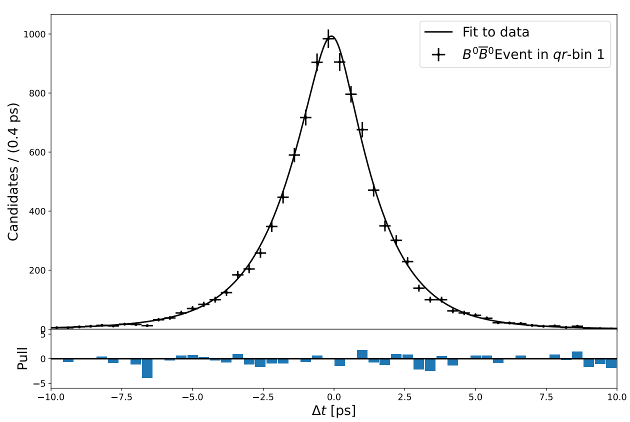
Fit to data
$B^0\overline{B}^0$Event in qr-bin 1
Candidates / (0.4 ps)
Pull
Δt [ps]

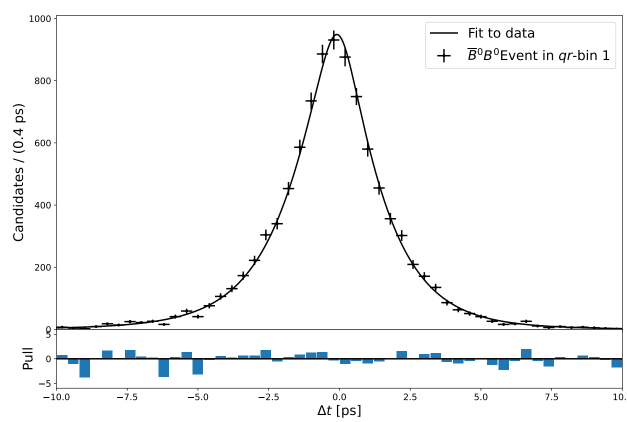
Fit to data
$\overline{B}^0B^0$Event in qr-bin 1
Candidates / (0.4 ps)
Pull
Δt [ps]

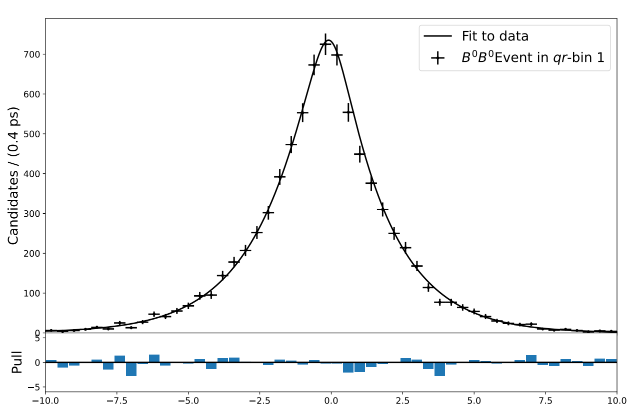
Fit to data
$B^0\overline{B}^0$Event in qr-bin 1
Candidates / (0.4 ps)
Pull
Δt [ps]

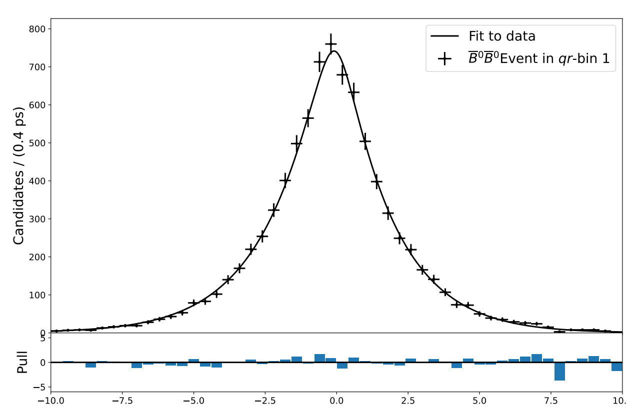
Fit to data
$\overline{B}^0\overline{B}^0$Event in qr-bin 1
Candidates / (0.4 ps)
Pull
Δt [ps]

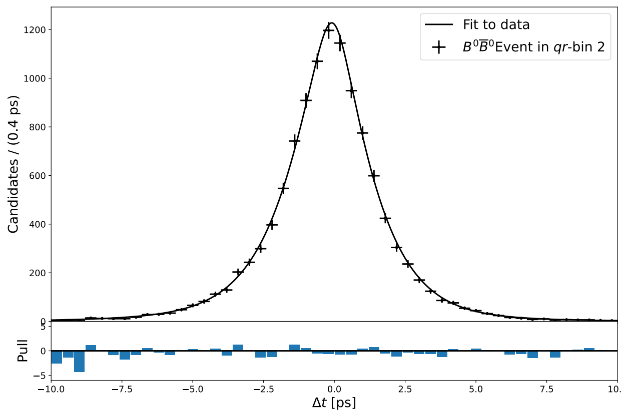
Fit to data
$B^0\overline{B}^0$Event in qr-bin 2
Candidates / (0.4 ps)
Pull
Δt [ps]

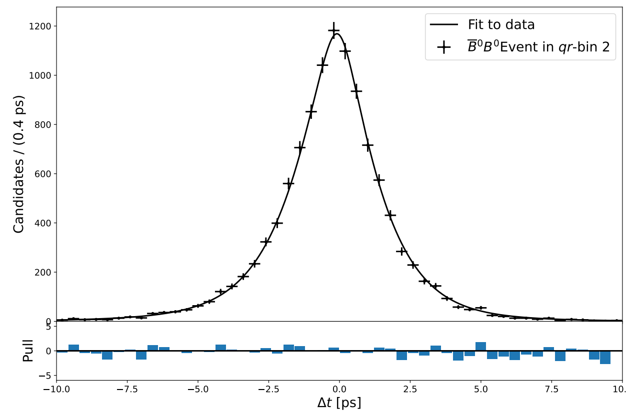
Fit to data
$\overline{B}^0B^0$Event in qr-bin 2
Candidates / (0.4 ps)
Pull
Δt [ps]

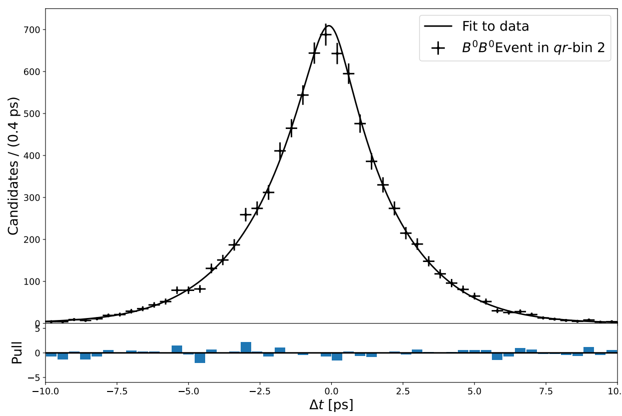
Fit to data
B^0B^0Event in qr-bin 2
Candidates / (0.4 ps)
Pull
Δt [ps]

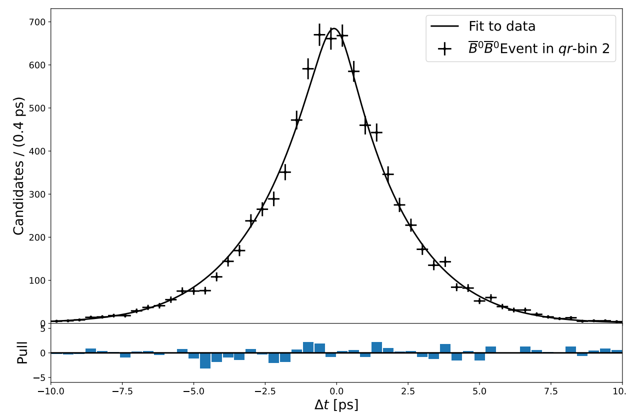
Fit to data
$\overline{B}^0\overline{B}^0$Event in qr-bin 2
Candidates / (0.4 ps)
Pull
Δt [ps]

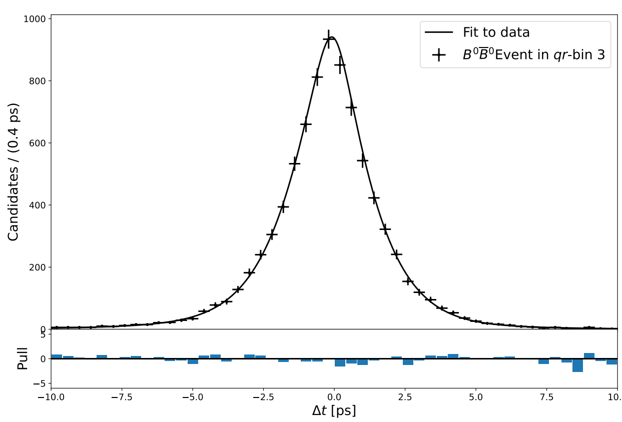
Fit to data
$B^0\overline{B}^0$Event in qr-bin 3
Candidates / (0.4 ps)
Pull
Δt [ps]

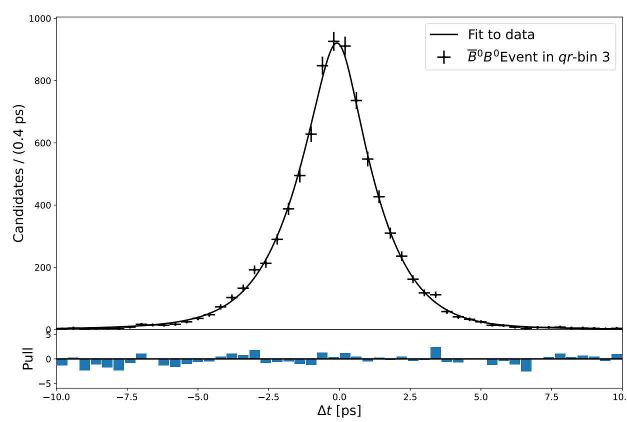
Fit to data
$\overline{B}^0B^0$Event in qr-bin 3
Candidates / (0.4 ps)
Pull
Δt [ps]

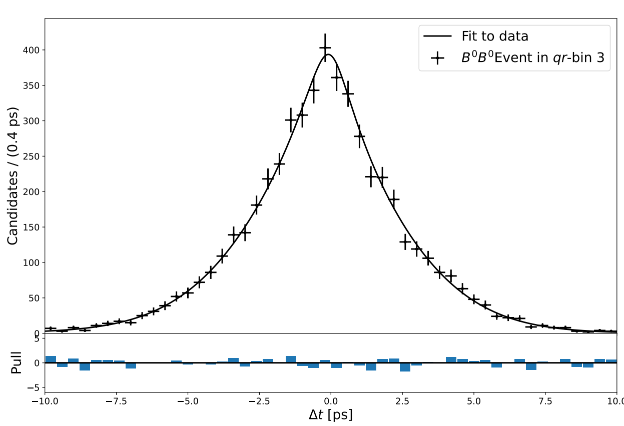
Fit to data
B^0B^0Event in qr-bin 3
Candidates / (0.4 ps)
Pull
Δt [ps]

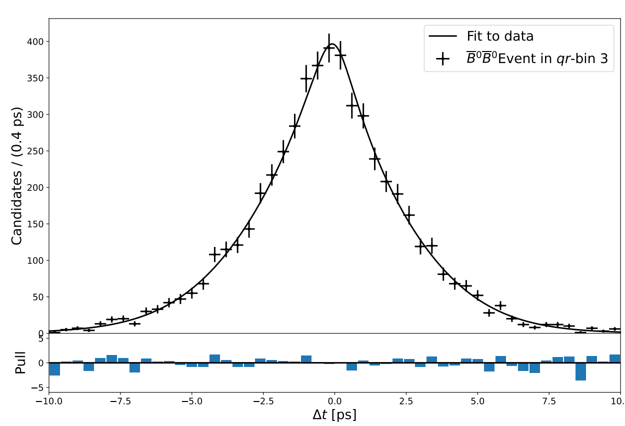
Fit to data
$\overline{B}^0\overline{B}^0$Event in qr-bin 3
Candidates / (0.4 ps)
Pull
Δt [ps]

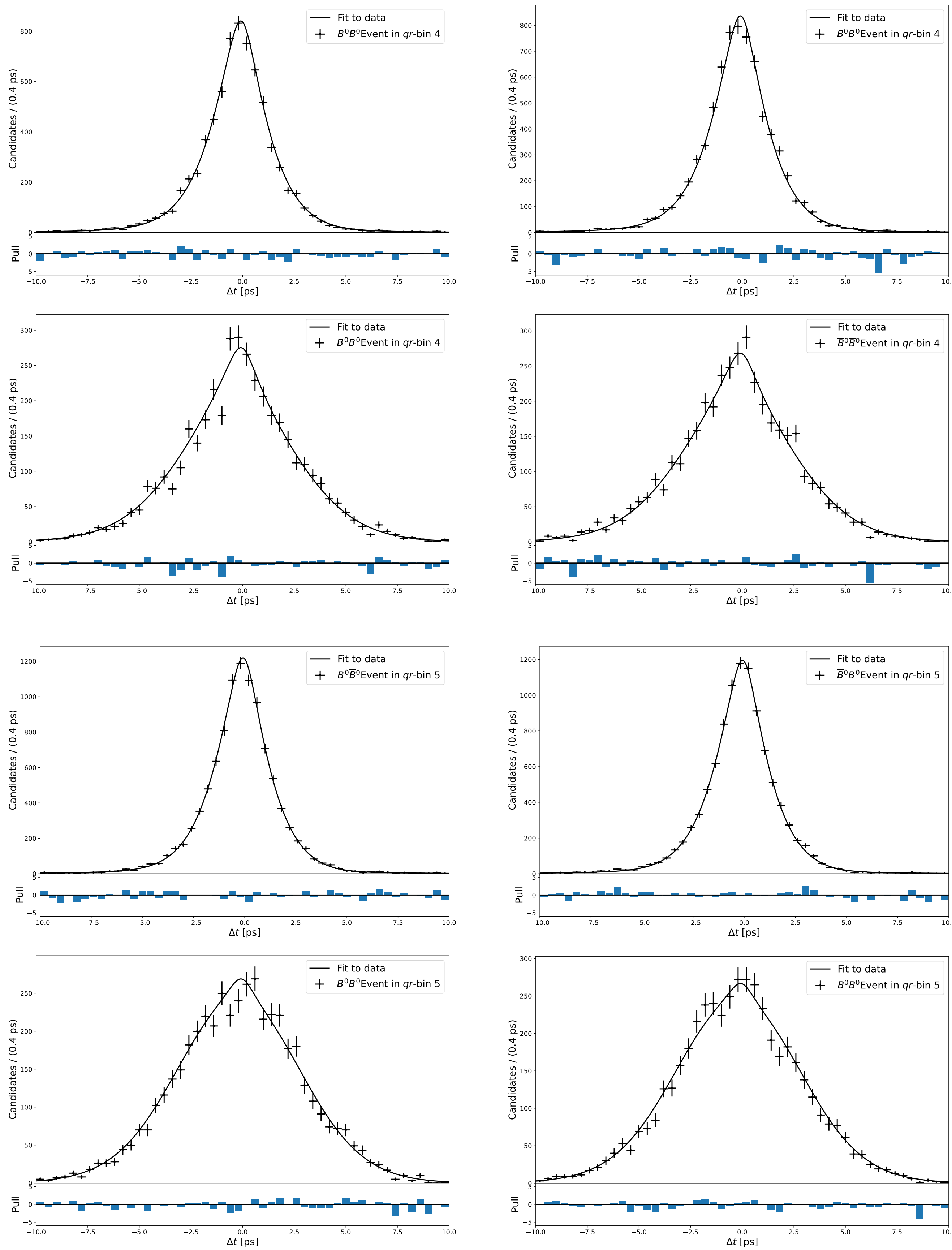
Fit to data
$B^0\overline{B}^0$Event in qr-bin 4
$\overline{B}^0B^0$Event in qr-bin 4
$B^0\overline{B}^0$Event in qr-bin 5
$\overline{B}^0B^0$Event in qr-bin 5
Candidates / (0.4 ps)
Pull
Δt [ps]

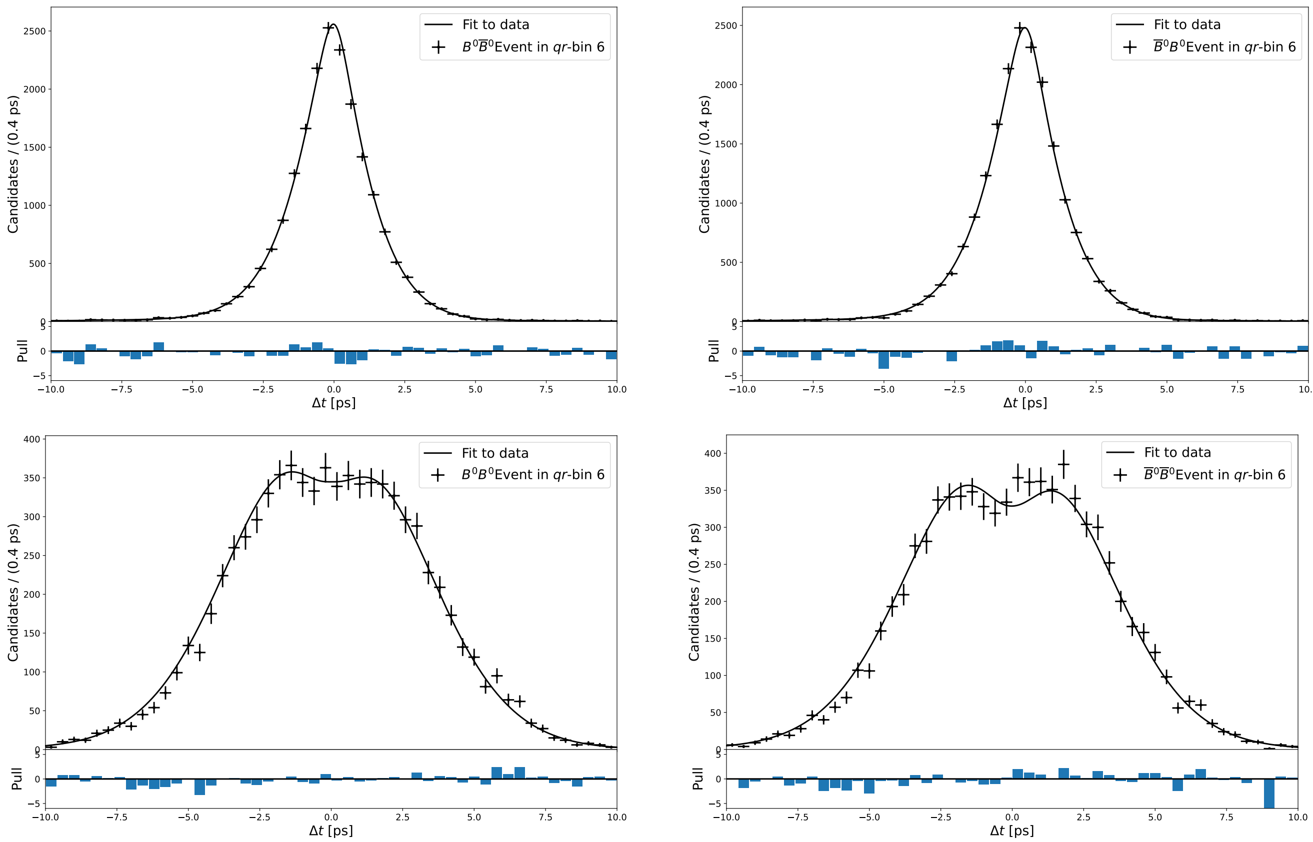

Figure B.10: Δt-distribution fitted to Signal MC data with a fraction of disentanglement ($\zeta_{\text{gen}} = 0.8$) for all qr bins and four flavor combinations (left to right, top to bottom). Error bars show Signal MC data binned in qr bins and solid line shows the fit. The lower plot show the pulls.

B.4 Absorption Studies

In this section, the plots for remaining parameters corresponding to the absorption studies presented in Sec. 5.2 are presented. The figures in the following all show the deviation of respective fit parameters with falsely assumed full entanglement from the nominal value, in dependence of the true value ζ_{gen}. Figs. B.11 and B.12 show the deviations for resolution function parameter μ_{M1} and σ_{M1}, respectively. These are shared parameters across qr-bins 0-5 and fitted simultaneously. Figs. B.13 - B.18 show the deviations for qr-bins 0-5.

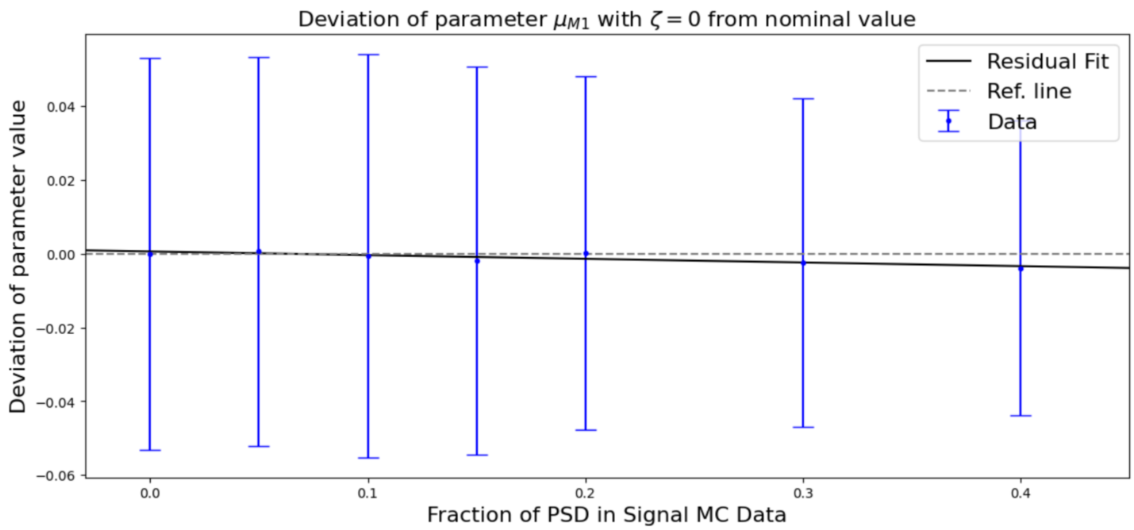

Figure B.11: Relative deviation of fit value with $\zeta = 0$ from nominal value for parameter μ_{M1}. The dotted line for $y = 0$ shows the relative nominal value, data points with error bars are shown with respect to the true PSD fraction in Signal MC, while the solid line shows a linear fit to the data points.

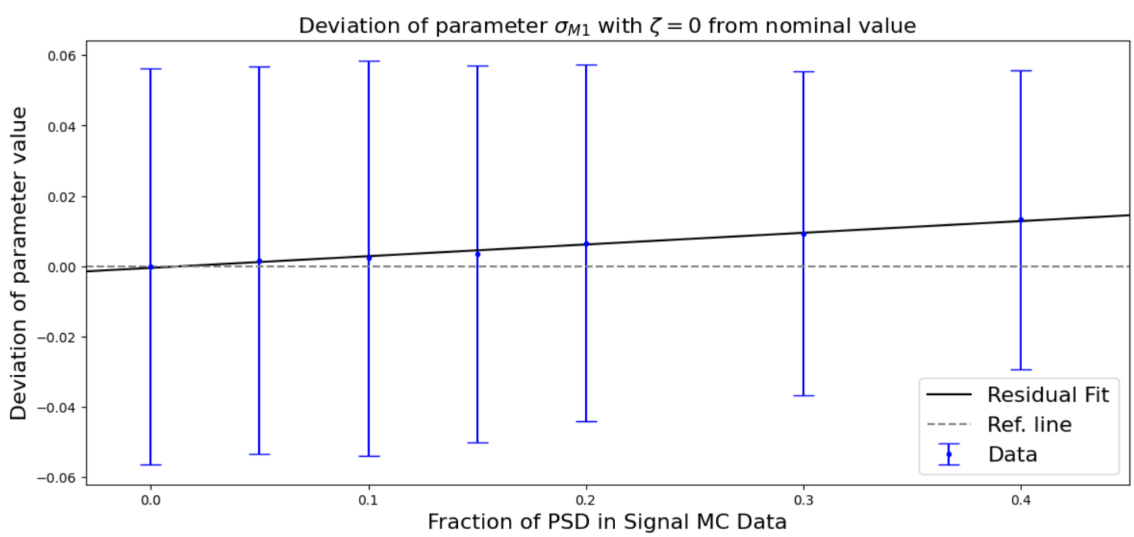

Figure B.12: Relative deviation of fit value with $\zeta = 0$ from nominal value for parameter σ_{M1}. The dotted line for $y = 0$ shows the relative nominal value, data points with error bars are shown with respect to the true PSD fraction in Signal MC, while the solid line shows a linear fit to the data points.

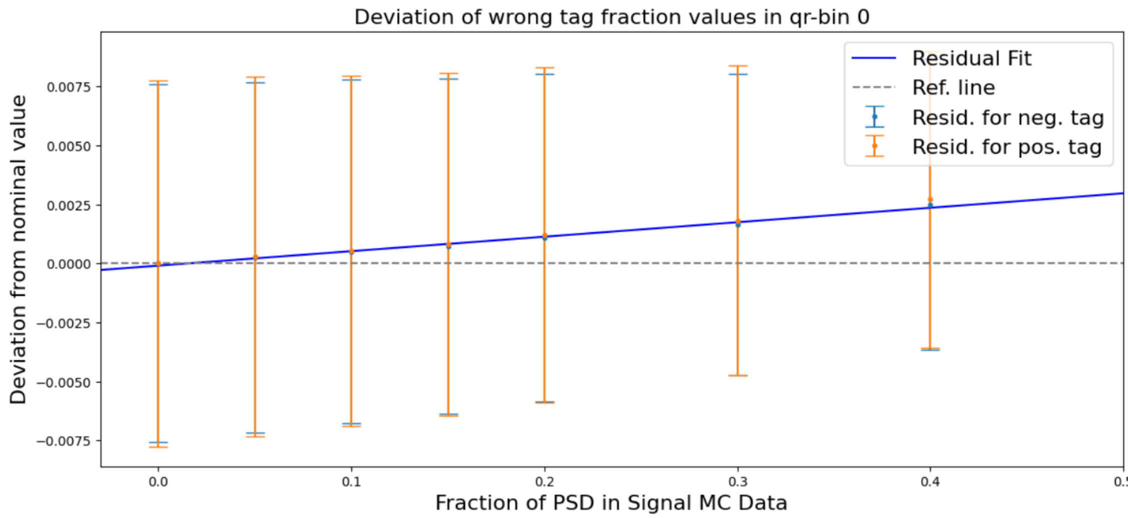

Figure B.13: Relative deviation of fit value with $\zeta = 0$ from nominal value for parameters $w_0^{\pm}$. The dotted line for $y = 0$ shows the relative nominal value, data points with error bars show data points with respect to the true PSD fraction in Signal MC, while the solid line shows a linear fit to the data points. Wrong tag fraction for negative/positive are shown in blue and orange, respectively.

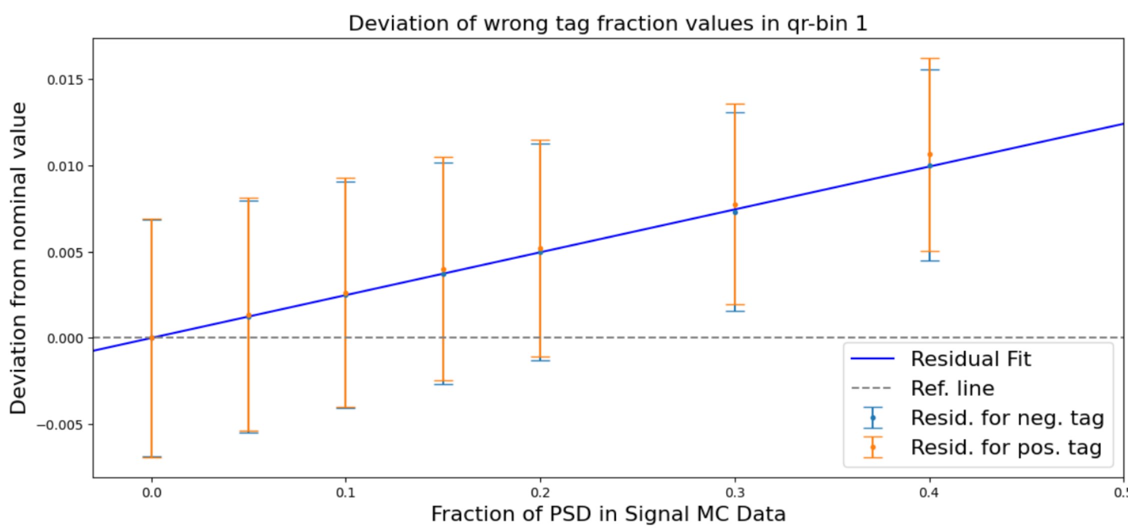

Figure B.14: Relative deviation of fit value with $\zeta = 0$ from nominal value for parameters $w_1^{\pm}$. The dotted line for $y = 0$ shows the relative nominal value, data points with error bars show data points with respect to the true PSD fraction in Signal MC, while the solid line shows a linear fit to the data points. Wrong tag fraction for negative/positive are shown in blue and orange, respectively.

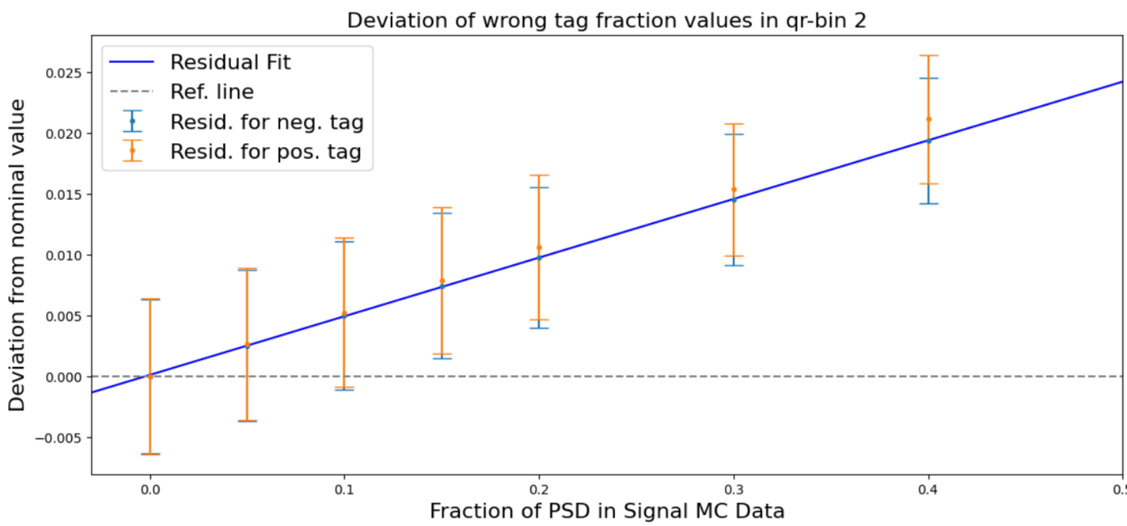

Figure B.15: Relative deviation of fit value with $\zeta = 0$ from nominal value for parameters $w_2^{\pm}$. The dotted line for $y = 0$ shows the relative nominal value, data points with error bars show data points with respect to the true PSD fraction in Signal MC, while the solid line shows a linear fit to the data points. Wrong tag fraction for negative/positive are shown in blue and orange, respectively.

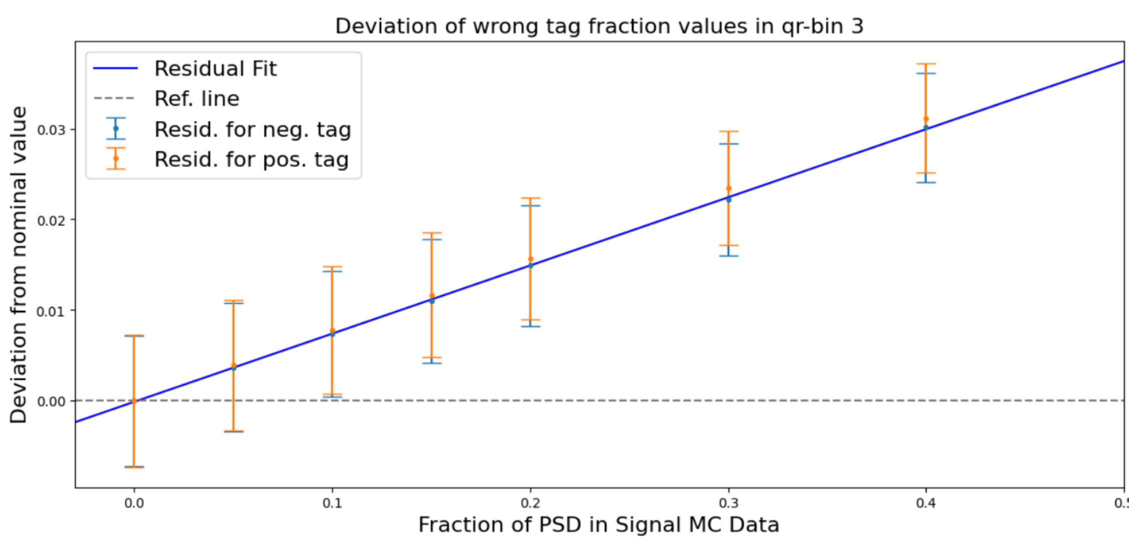

Figure B.16: Relative deviation of fit value with $\zeta = 0$ from nominal value for parameters $w_3^{\pm}$. The dotted line for $y = 0$ shows the relative nominal value, data points with error bars show data points with respect to the true PSD fraction in Signal MC, while the solid line shows a linear fit to the data points. Wrong tag fraction for negative/positive are shown in blue and orange, respectively.

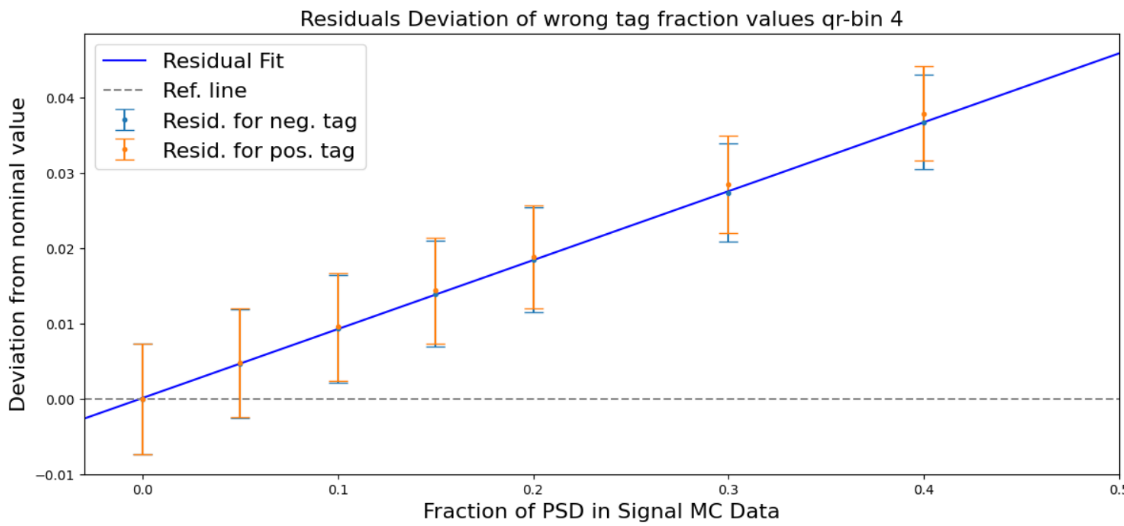

Figure B.17: Relative deviation of fit value with $\zeta = 0$ from nominal value for parameters $w_4^{\pm}$. The dotted line for $y = 0$ shows the relative nominal value, data points with error bars show data points with respect to the true PSD fraction in Signal MC, while the solid line shows a linear fit to the data points. Wrong tag fraction for negative/positive are shown in blue and orange, respectively.

Figure B.18: Relative deviation of fit value with $\zeta = 0$ from nominal value for parameters $w_5^{\pm}$. The dotted line for $y = 0$ shows the relative nominal value, data points with error bars show data points with respect to the true PSD fraction in Signal MC, while the solid line shows a linear fit to the data points. Wrong tag fraction for negative/positive are shown in blue and orange, respectively.

List of Figures

List of Tables

List of Abbreviations

ARICH Aerogel Ring-Imaging Cherenkov Detector
BF branching fraction
BS beam spot
BSM Physics Beyond the Standard Model
CB Crystal Ball
CDC Central Drift Chamber
CHSH Clauser-Horne-Shimony-Holt
CERN Conseil européen pour la recherche nucléaire
CKM Matrix Cabibbo-Kobayashi-Maskawa Matrix
COM center of mass
DEPFET Depleted p-channel Field Effect Transistor
ECL Electromagnetic Calorimeter
EPR Einstein-Podolsky-Rosen
EW Electroweak
FSR final-state-radiation
HER High energy storage ring
IP Interaction Point
KFit Kinematic Fit library
KLM K_L and μ detector
LER Low energy storage ring
LHC Large Hadron Collider
MC Monte Carlo
NLL Negative log-likelihood
NP New Physics
OF opposite flavor
OL Outlier
PDF Probability Density Function
PID Particle identification

PSD Partial Spontaneous Disentanglement

PXD Pixel Vertex Detector

QCD Quantumchromodynamics

QM Quantum Mechanics

Rave Reconstruction in an Abstract Vertices Environment

SD Spontaneous Disentanglement

SSB Spontaneous Symmetry Breaking

SF same flavor

SM Standard Model

(Super)KEKB (Super) KEK B Factory

SVD Silicon Vertex Detector

TOP Time of Propagation detector

TSI Tag-Side Interference

UT Unitarity triangle

vev vacuum expectation value

VXD Vertex detector

Bibliography

[1] Jure Zupan. *Introduction to flavour physics*. 2019. arXiv: 1903.05062 [hep-ph]. URL: https://arxiv.org/abs/1903.05062.

[2] A. Einstein, B. Podolsky, and N. Rosen. “Can Quantum-Mechanical Description of Physical Reality Be Considered Complete?” In: *Phys. Rev.* 47 (10 May 1935), pp. 777–780. DOI: 10.1103/PhysRev.47.777. URL: https://link.aps.org/doi/10.1103/PhysRev.47.777.

[3] J. S. Bell. “On the Einstein Podolsky Rosen paradox”. In: *Physics Physique Fizika* 1 (3 Nov. 1964), pp. 195–200. DOI: 10.1103/PhysicsPhysiqueFizika.1.195. URL: https://link.aps.org/doi/10.1103/PhysicsPhysiqueFizika.1.195.

[4] Guido Bacciagaluppi and Elise Crull. “Note on the Quantum-Mechanical Theory of Measurement”. In: *The Einstein Paradox: The Debate on Nonlocality and Incompleteness in 1935*. Cambridge University Press, 2024, pp. 208–219.

[5] N.E. Mavromatos. “CPT Violation and Decoherence in Quantum Gravity”. In: *Planck Scale Effects in Astrophysics and Cosmology*. Springer-Verlag, pp. 245–320. ISBN: 3540252630. DOI: 10.1007/11377306_8. URL: http://dx.doi.org/10.1007/11377306_8.

[6] Ashutosh Kumar Alok et al. “Probing quantum decoherence at Belle II and LHCb”. In: *Journal of High Energy Physics* 2024.5 (May 2024). ISSN: 1029-8479. DOI: 10.1007/jhep05(2024)124. URL: http://dx.doi.org/10.1007/JHEP05(2024)124.

[7] Bogdan Povh et al. *Teilchen und Kerne*. Berlin, Heidelberg: Springer Sprektrum, 2014. ISBN: 978-3-642-37821-8. DOI: 10.1007/978-3-642-37822-5.

[8] B.R. Martin and G. Shaw. *Particle Physics*. Manchester Physics Series. Wiley, 2017. ISBN: 9781118912164. URL: https://books.google.de/books?id=rulRDQAAQBAJ.

[9] O. Nachtmann. *Elementary Particle Physics*. Springer Berlin, Heidelberg, 1990. ISBN: 978-3-642-61281-7. DOI: https://doi-org.eaccess.ub.tum.de/10.1007/978-3-642-61281-7.

[10] Wikipedia contributors. *Standard Model of Elementary Particles — Wikipedia, The Free Encyclopedia*. [Online; accessed 3-April-2025]. 2024. URL: https://en.wikipedia.org/wiki/File:Standard_Model_of_Elementary_Particles.svg.

[11] Y. Fukuda et al. "Evidence for Oscillation of Atmospheric Neutrinos". In: *Phys. Rev. Lett.* 81 (8 Aug. 1998), pp. 1562–1567. DOI: 10.1103/PhysRevLett.81.1562. URL: https://link.aps.org/doi/10.1103/PhysRevLett.81.1562.

[12] G. Aad et al. "Observation of a new particle in the search for the Standard Model Higgs boson with the ATLAS detector at the LHC". In: *Physics Letters B* 716.1 (Sept. 2012), pp. 1–29. DOI: 10.1016/j.physletb.2012.08.020. URL: https://doi.org/10.1016%2Fj.physletb.2012.08.020.

[13] S. Navas et al. "Review of particle physics". In: *Phys. Rev. D* 110.3 (2024), p. 030001. DOI: 10.1103/PhysRevD.110.030001.

[14] A. J. Bevan et al. "The Physics of the B Factories". In: *The European Physical Journal C* 74.11 (Nov. 2014). ISSN: 1434-6052. DOI: 10.1140/epjc/s10052-014-3026-9. URL: http://dx.doi.org/10.1140/epjc/s10052-014-3026-9.

[15] CKMfitter Group - J.Charles et al. "http://ckmfitter.in2p3.fr". In: (2024). DOI: Eur.Phys.J.C41,1-131(2005)[hep-ph/0406184].

[16] M. Gell-Mann and A. Pais. "Behavior of Neutral Particles under Charge Conjugation". In: *Phys. Rev.* 97 (5 Mar. 1955), pp. 1387–1389. DOI: 10.1103/PhysRev.97.1387. URL: https://link.aps.org/doi/10.1103/PhysRev.97.1387.

[17] J. H. Christenson et al. "Evidence for the 2π Decay of the K_2^0 Meson". In: *Phys. Rev. Lett.* 13 (4 July 1964), pp. 138–140. DOI: 10.1103/PhysRevLett.13.138. URL: https://link.aps.org/doi/10.1103/PhysRevLett.13.138.

[18] C. Albajar et al. "Search for $B^0 - \bar{B}^0$ oscillations at the CERN proton-antiproton collider". In: *Phys. Lett. B* 186.2 (1987). [Erratum: Phys.Lett.B 197, 565 (1987)], pp. 247–254. DOI: 10.1016/0370-2693(87)90288-7.

[19] H. Albrecht et al. "Observation of $B^0 - \overline{B}^0$ mixing". In: *Physics Letters B* 192.1 (1987), pp. 245–252. ISSN: 0370-2693. DOI: https://doi.org/10.1016/0370-2693(87)91177-4. URL: https://www.sciencedirect.com/science/article/pii/0370269387911774.

[20] E Kou et al. "The Belle II Physics Book". In: *Progress of Theoretical and Experimental Physics* 2019.12 (Dec. 2019). DOI: 10.1093/ptep/ptz106. URL: https://doi.org/10.1093%2Fptep%2Fptz106.

[21] C. S. Wu et al. "Experimental Test of Parity Conservation in Beta Decay". In: *Phys. Rev.* 105 (4 Feb. 1957), pp. 1413–1415. DOI: 10.1103/PhysRev.105.1413. URL: https://link.aps.org/doi/10.1103/PhysRev.105.1413.

[22] Andreas Höcker and Zoltan Ligeti. "CP Violation and the CKM Matrix". In: *Annual Review of Nuclear and Particle Science* 56.1 (2006), pp. 501–567. ISSN: 1545-4134. DOI: 10.1146/annurev.nucl.56.080805.140456. URL: http://dx.doi.org/10.1146/annurev.nucl.56.080805.140456.

[23] I. I. Bigi and A. I. Sanda. "$B^0 - \overline{B}^0$ mixing and violations of CP symmetry". In: *Phys. Rev. D* 29 (7 Apr. 1984), pp. 1393–1398. DOI: 10.1103/PhysRevD.29.1393. URL: https://link.aps.org/doi/10.1103/PhysRevD.29.1393.

[24] Owen Long et al. "Impact of tag-side interference on time-dependent CP asymmetry measurements using coherent $B^0\overline{B}^0$ pairs". In: *Physical Review D* 68.3 (Aug. 2003). ISSN: 1089-4918. DOI: 10.1103/physrevd.68.034010. URL: http://dx.doi.org/10.1103/PhysRevD.68.034010.

[25] Fernando Abudinén. "Development of a B^0 flavor tagger and performance study of a novel time-dependent CP analysis of the decay $B^0 \to \pi^0\pi^0$ at Belle II". Oct. 2018. URL: http://nbn-resolving.de/urn:nbn:de:bvb:19-230032.

[26] A. Go et al. "Measurement of EPR-type flavour entanglement in $\Upsilon(4S) \to B^0\overline{B}^0$ decays". In: *Physical Review Letters* 99.13 (Sept. 2007). ISSN: 1079-7114. DOI: 10.1103/physrevlett.99.131802. URL: http://dx.doi.org/10.1103/PhysRevLett.99.131802.

[27] W. Heisenberg. "Über quantentheoretische Umdeutung kinematischer und mechanischer Beziehungen". In: *Original Scientific Papers Wissenschaftliche Originalarbeiten*. Ed. by Walter Blum, Helmut Rechenberg, and Hans-Peter Dürr. Berlin, Heidelberg: Springer Berlin Heidelberg, 1985, pp. 382–396. ISBN: 978-3-642-61659-4. DOI: 10.1007/978-3-642-61659-4_26. URL: https://doi.org/10.1007/978-3-642-61659-4_26.

[28] Stuart Freedman and John Clauser. "Experimental Test of Local Hidden-Variable Theories". In: *Physical Review Letters* 28 (Apr. 1972). DOI: 10.1103/PhysRevLett.28.938.

[29] R.A. Bertlmann et al. "Violation of a Bell inequality in particle physics experimentally verified?" In: *Physics Letters A* 332.5–6 (Nov. 2004), pp. 355–360. ISSN: 0375-9601. DOI: 10.1016/j.physleta.2004.10.006. URL: http://dx.doi.org/10.1016/j.physleta.2004.10.006.

[30] F. Jackl. "Disentanglement Theory". In: *Bachelor Thesis* (2025).

[31] A. Pompili and F. Selleri. In: *Eur. Phy. J. C 14, 469 (2000); Drascati Physics Series Vol.XXVI* 329 (2001).

[32] H. Kakuno et al. “Neutral B Flavor Tagging for the Measurement of Mixing-induced CP Violation at Belle”. In: *Nuclear Instruments and Methods in Physics Research Section A: Accelerators, Spectrometers, Detectors and Associated Equipment* 533.3 (Nov. 2004), pp. 516–531. ISSN: 0168-9002. DOI: 10.1016/j.nima.2004.06.159. URL: http://dx.doi.org/10.1016/j.nima.2004.06.159.

[33] Lindblad G. “On the generators of quantum dynamical semigroups”. In: *Commun.Math. Phys. 48, 119–130* (1976). DOI: https://doi.org/10.1007/BF01608499.

[34] Reinhold A. Bertlmann, Walter Grimus, and Beatrix C. Hiesmayr. “Open-quantum-system formulation of particle decay”. In: *Physical Review A* 73.5 (May 2006). ISSN: 1094-1622. DOI: 10.1103/physreva.73.054101. URL: http://dx.doi.org/10.1103/PhysRevA.73.054101.

[35] T. Abe et al. *Belle II Technical Design Report*. 2010. DOI: 10.48550/ARXIV.1011.0352. URL: https://arxiv.org/abs/1011.0352.

[36] K.A. Olive. “Review of Particle Physics”. In: *Chinese Physics C* 38.9 (Aug. 2014), p. 090001. DOI: 10.1088/1674-1137/38/9/090001. URL: https://doi.org/10.1088/1674-1137/38/9/090001.

[37] KEK. *Electrons and Positrons Collide for the first time in the SuperKEKB Accelerator*. URL: https://www.kek.jp/en/newsroom/2018/04/26/0700/.

[38] Justin Skorupa et al. “Characterization of the Particle Identification of the Belle II Detector with Bhabha Radiation and First Measurement of $\sin(2\phi_1)$ and Δm_d Using Belle II Data”. PhD thesis. München: München, Technische Universität München, 2021.

[39] Jochen Schieck. “DEPFET pixels as a vertex detector for the Belle II experiment”. In: *Nuclear Instruments and Methods in Physics Research Section A: Accelerators, Spectrometers, Detectors and Associated Equipment* 732 (Dec. 2013), pp. 160–163. DOI: 10.1016/j.nima.2013.05.054. URL: https://doi.org/10.1016%2Fj.nima.2013.05.054.

[40] Max-Planck-Institut für Physik. *Belle II: A pixel vertex detector for an updated accelerator*. URL: https://www.mpp.mpg.de/en/research/structure-of-matter/belle-ii-on-the-track-of-the-antimatter-puzzle/belle-ii-a-pixel-vertex-detector-for-an-updated-accelerator.

[41] Benedikt Wach. “Measurement of Branching Fractions and direct CP Violation in $B^0 \to K^+\pi^-$ and $B^0 \to \pi^+\pi^-$ Decays at the Belle II Experiment”. en. PhD thesis. Technische Universität München, 2023, p. 179. URL: https://mediatum.ub.tum.de/1720558.

[42] Anders Ryd et al. *EvtGen - A Monte Carlo Generator for B-Physics*. CERN, 2004. URL: https://evtgen.hepforge.org/doc/EvtGenGuide.pdf.

[43] Andreas Moll. "Comprehensive study of the background for the Pixel Vertex Detector at Belle II". July 2015. URL: http://nbn-resolving.de/urn:nbn:de:bvb:19-191067.

[44] Vladimir Chekelian et al. "Measurement of the B^0 lifetime and mixing frequency using hadronic decays with the Moriond 2022 dataset". In: *Belle II Internal Note* (2022).

[45] O. Eren. "TSI". In: *Bachelor Thesis* (2025).

[46] Jonas Eschle et al. "zfit: Scalable pythonic fitting". In: *SoftwareX* 11 (Jan. 2020), p. 100508. ISSN: 2352-7110. DOI: 10.1016/j.softx.2020.100508. URL: http://dx.doi.org/10.1016/j.softx.2020.100508.

[47] Martín Abadi et al. *TensorFlow: Large-Scale Machine Learning on Heterogeneous Systems*. Software available from tensorflow.org. 2015. URL: https://www.tensorflow.org/.

[48] F. James and M. Roos. "Minuit - a system for function minimization and analysis of the parameter errors and correlations". In: *Computer Physics Communications* 10.6 (1975), pp. 343–367. ISSN: 0010-4655. DOI: https://doi.org/10.1016/0010-4655(75)90039-9. URL: https://www.sciencedirect.com/science/article/pii/0010465575900399.

[49] Oskar Tittel. *Personal communication.*

[50] I. Adachi et al. "New graph-neural-network flavor tagger for Belle II and measurement of $\sin 2\phi_1$ in $B^0 \to J/\psi K^0_S$ decays". In: *Physical Review D* 110.1 (July 2024). ISSN: 2470-0029. DOI: 10.1103/physrevd.110.012001. URL: http://dx.doi.org/10.1103/PhysRevD.110.012001.

[51] Mirco Dorigo, Sebastiano Raiz, and Diego Tonelli. "An updated measurement of the properties of $B^0 \to \pi^0\pi^0$ decays reconstructed in 2019–2022 data". In: *Belle II Internal Note* (2024).

[52] *Evaluating statistical uncertainties and correlations using the bootstrap method*. Tech. rep. Geneva: CERN, 2021. URL: https://cds.cern.ch/record/2759945.

[53] Luc Demortier and Louis Lyons. "Everything you always wanted to know about pulls". In: (2008).

[54] Thomas Czank et al. "Measurement of the CP Violation Parameter $\sin 2\phi_1$ in $B^0 \to J/\psi K^0$ Decay using 189 fb^{-1} data set". In: *Belle II Internal Note* (2022).

[55] Hans-Günther Moser. *Personal communication.*

[56] Thibaud Humair. *Personal communication.*

[57] Michele Veronesi. *Personal communication.*

[58] Remi Léandre Albert Louvot. "Study of B_s^0-meson Production and Measurement of B_s^0 Decays into a $D_s^{(*)-}$ and a Light Meson in e^+e^- Collisions at $\sqrt{s} = 10.87$ GeV". PhD thesis. Lausanne: EPFL, 2012. DOI: 10.5075/epfl-thesis-5213. URL: https://infoscience.epfl.ch/handle/20.500.14299/71143.

[59] Till Moritz Karbach, Gerhard Raven, and Manuel Schiller. *Decay time integrals in neutral meson mixing and their efficient evaluation*. 2014. arXiv: 1407.0748 [physics.data-an]. URL: https://arxiv.org/abs/1407.0748.

Acknowledgments

First, I want to thank Prof. Allen Caldwell for enabling me to carry out my master's research under his supervision. I would also like to express my gratitude to Dr. Hans-Günther Moser for his trust and support, for sparking my interest in Flavor Physics in the first place and now giving me the opportunity to experience working in an international collaboration. Further, I want to extend my gratitude to Dr. Stefan Wallner for his expertise and guidance.

I would like to express my appreciation for the members of the Belle II group at the Max-Planck-Institute for Physics, especially Sagar Hazra PhD and Dr. Ben Wach. I want to thank Prof. Thibaud Humair for the encouraging support and for providing me with his knowledge and repositories.

Oskar Tittel, thank you for taking me under your wing and offering your support and time when I was feeling helpless. You really steered me in the right direction and got me back on track with my analysis. As a homage to our Japan trip I will never not order extra pass-out for Ramen in the future.

Thank you Cosmo, Vanessa and Claudia for the time together. Vanessa, I was happy to have a peer at the group - I wish you luck and endurance for the rest of your master's research.

I would like to thank Luna Laufer for always being there for me. I am sorry that you had to listen every day for an entire year to my desperate complaints about my jobs on KEKcc not running properly. You were right after all; It did work out in the end and I did not end up being the worst physics student the world has seen.

Finally, thank you to my mom and brother. Even in times where we would not talk much or see much of ourselves I can always feel you having my back. Without your unwavering support I would not have been able to pursue my dream. I am nothing but grateful for you.